

Doctoral Thesis

# Low-Cost Receivers for EMC Measurements

submitted in satisfaction of the requirements for the degree  
Doctor of Science in Electrical Engineering  
of the TU Wien, Faculty of Electrical Engineering and Informations Technology

---

Dissertation

## Kostengünstige Messempfänger für EMV Messungen

ausgeführt zum Zwecke der Erlangung des akademischen Grads  
Doktor der technischen Wissenschaften  
eingereicht an der TU Wien, Fakultät für Elektrotechnik und Informationstechnik

Dipl.-Ing. **Christian Spindelberger**, BSc

Matr.Nr.: 01226143

Supervisor: Assoc. Prof. Dipl.-Ing. Dr. techn. **Holger Arthaber**  
Institute for Electrodynamics Microwave and Circuit Engineering  
TU Wien

Reviewer: Univ. Prof. Dipl.-Ing. Dr. techn. **Bernd Deutschmann**  
Institute for Electronics  
TU Graz

Reviewer: Univ. Prof. Ing. Dipl.-Ing. Dr. -Ing. **Christoph Mecklenbräuer**  
Institute of Telecommunications  
TU Wien

Vienna, February 2024

---

---

# Kurzfassung

---

Diese Arbeit untersucht die Anwendbarkeit von Software-Defined Radios (SDRs) als Messempfänger für elektromagnetische Interferenzen (EMIs). SDRs sind aufgrund ihrer niedrigen Kosten, vielfältigen Konfigurationsmöglichkeiten und vollen Funktionsfähigkeit mit Hilfe eines PCs eine interessante Alternative zu teuren EMI Empfängern. Als Testmethode wird für abgestrahlte Emissionsmessungen im *CISPR* Band C/D (30 MHz–1 GHz) auf transversal elektromagnetische (TEM) Zellen zurückgegriffen. In diesem Band werden meist der Spitzen- und Quasi-Spitzenwert Detektor angewendet. Der Letztere stellt die höchsten Anforderungen an die Messdynamik.

Berechnungen, die auf der Empfänger Norm *CISPR 16-1-1* beruhen, zeigen, dass SDRs mit verstimmbaren anti-aliasing Filtern (AAF<sub>n</sub>) normgerechte elektromagnetische Verträglichkeits- (EMV)-Messungen erlauben. Solche Low-Cost Geräte (< 2 k€) verwenden oftmals Empfänger, die in einen einzelnen Chip integriert sind. Ein bekanntes Beispiel, das in vielen SDRs Gebrauch findet, ist die RFIC Serie *AD936x* von Analog Devices. Da der *USRP B200mini* von Ettus Research diesen Chip verwendet und zu den gewünschten Konditionen verfügbar ist, wird dieser SDR für eine genaue Analyse herangezogen.

Erste Evaluierungen mittels standardisierter Testsignale haben zwei fundamentale Probleme des homodynen SDRs zum Vorschein gebracht, die konforme EMV Messungen unmöglich machen. Einerseits wurden mittels einzelner Trägersignale unerwünschte Mischprodukte nachgewiesen, die zu Normverletzungen führen. Andererseits ist die Messdynamik des SDRs unzureichend, um Breitbandimpulse mit dem Quasispitzenwertdetektor bewerten zu können.

Die genannten Probleme werden mittels einer eigens konstruierten hoch linearen Mischerstufe gelöst, was konforme EMV Messungen mit dem SDR nach *CISPR 16-1-1* ermöglicht. Der zu messende Frequenzbereich wird auf eine höhergelegene Mittenfrequenz gemischt und schmalbandig gefiltert, bevor das Signal den SDR passiert. Aufgrund der reduzierten Bandbreite am SDR Eingang werden unerwünschte Mischprodukte hinreichend unterdrückt und die Vorteile von verstimmbaren AAF<sub>n</sub> zugänglich, um den Anforderungen des Quasispitzenwert Detektors nachzukommen. Spitzenwertmessungen sind bei voller AAF Bandbreite von 22.5 MHz möglich und erlauben einen schnellen initialen Frequenzbanddurchlauf. Bei Anwendung des Quasi-Spitzenwert Detektors ist eine Reduktion auf 1 MHz notwendig, was den Durchlauf signifikant verlangsamt. Um die Effizienz zu steigern, wird mit einer speziell entwickelten automatischen Verstärkungsregelung, die sich zwischen Mischerstufe und SDR befindet, gearbeitet. Durch die aktive Regulation von Impulsen, mittels eines Hochgeschwindigkeitsabschwächers, wird die Messdynamik verbessert und eine erhöhte AAF Bandbreite erzielt, während standardisierte Toleranzen eingehalten werden.

Abschließend wird ein Testobjekt mit dem SDR basierten Messempfänger und einer für diese Anwendung konstruierten und kostengünstigen TEM Zelle charakterisiert. Mit Hilfe von Vergleichsmessungen aus EMV Testhäusern kann gezeigt werden, dass zuverlässige Emissionsmessungen für ein Budget von ~ 1.9 k€ möglich sind. Des Weiteren ist die erzielbare Dynamik vergleichbar mit dem EMI Empfänger MXE *N9038A* von Keysight Technologies. Dieser muss jedoch auf hochpreisige Filterbänke zurückgreifen, um die Werte zu erreichen.

---

# Abstract

---

Within this thesis, the suitability of software-defined radios (SDRs) as an electromagnetic interference (EMI) receiver is investigated. SDRs are a promising alternative to expensive EMI receivers as they are low in costs, highly configurable, and working out-of-the-box with a host PC. As measurement method, transverse electromagnetic (TEM) cells are taken into account for radiated emission testing in *CISPR* band C/D (30 MHz–1 GHz). In this band, the peak and quasi-peak detectors are most frequently applied. The latter one poses the highest receiver requirements in terms of dynamic range.

Analytical derivations, based on the EMI receiver norm *CISPR 16-1-1*, indicate that SDRs with tunable anti-aliasing filters (AAFs) presumably allow for compliant electromagnetic compatibility (EMC) measurements. Low-cost devices (<2 k€) offering this feature often deploy analog receiver frontends integrated in a single chip. For instance, Analog Devices' popular RFIC series *AD936x* is used in many SDRs ranging in the target price category. As the SDR *USRP B200mini* from Ettus Research incorporates this chip, it is chosen for a rigorous suitability analysis.

An initial performance evaluation utilizing standardized test stimuli, i.e., a continuous wave and broadband impulses, indicates two major problems of the homodyne SDR making compliant EMC measurements out-of-the-box impossible. Firstly, unintended downconversion products cause significant signal distortions, especially at low tuning frequencies. Secondly, the SDR's analog frontend does not provide sufficient dynamic range for measuring impulses with the quasi-peak detector.

To overcome the mentioned problems, a highly-linear upconversion stage is designed enabling compliant EMC measurements with the SDR in accordance to *CISPR 16-1-1*. The frequency content of *CISPR* band C/D is mixed upwards to a static center frequency and filtered with a narrowband bandpass filter before reaching the *USRP B200mini*. Because of the lowered bandwidth at the SDR input, the benefits of tunable AAFs can be exploited for achieving quasi-peak detector requirements and disturbing mixing products are suppressed sufficiently. Peak detector measurements are possible at full AAF bandwidth, i.e., 22.5 MHz, allowing for a fast initial frequency scan. For the quasi-peak detector, the bandwidth must be reduced to 1 MHz, degrading the scan speed severely. To tackle this problem, a certain feed-forward automatic gain control is developed and inserted between the upconversion stage and the SDR. By leveling impulses with a high-speed attenuator, the available dynamic range of the SDR is increased and allows for a larger AAF bandwidth while fulfilling standardized accuracy requirements.

Finally, a test device is characterized utilizing the SDR-based receiver in conjunction with a low-cost TEM cell designed for this task. Comparing the results of this setup, available for a budget of ~ 1.9 k€, with professional test houses demonstrates the feasibility of reliable radiated emission spectra estimates in advance. Moreover, it shows that the available dynamic range of the developed system is in the same range as for a professional EMI receiver, i.e., Keysight Technologies' MXE *N9038A*, which utilizes expensive preselector filterbanks to achieve this benchmark.

---

# Acknowledgement

---

Viewed retrospectively, the last four years I have spent for my doctoral thesis went by in the blink of an eye. It was a highly interesting time where I had to face numerous challenges demanding my full commitment and lifeblood. The gained experiences strongly evolved my technical skills and personal competences I can always refer to and which I would have probably never undergone in a different environment. Therefore, I would like to acknowledge the most important persons who contributed to this successful time.

My personal thanks go to Assoc. Prof. Dipl. Ing. Dr. techn. Holger Arthaber for always finding the perfect mixture between motivation and restraint as a supervisor. I have never met a comparable character having such a deep passion for RF research and the intuitive ability of imparting his knowledge to students in a simple and concise manner.

Next, I would like to appreciate the support I have received from Christian Bauer who gave me my first job when I was a young student and brought me into touch with the world of RF engineering. With his help and broad connections to industry, I organized an event where the content of my thesis was disseminated to a large community beyond research institutions.

I also want to acknowledge all colleagues I was working together with. Thanks to Giacomo Giannetti and Dimitirios Kalodikis for helping me to realize some of the hardware developments I have used in my thesis.

The last thanks are dedicated to the most important people in my life. Lena deserves my highest gratitude as I would have probably quit a several times without her continuous encouragement and guidance through times of ups and downs. Furthermore, I want to express my special thanks to my parents for coining me with a deep confidence of unconditional support and the firm conviction I can achieve any goal that I desire.

---

# Contents

---

<b>List of Acronyms</b>	<b>vii</b>
<b>List of Figures</b>	<b>xi</b>
<b>List of Tables</b>	<b>xii</b>
<b>1 Introduction</b>	<b>1</b>
1.1 General Radiated Emission Measurement Setup . . . . .	2
1.2 Pre-Compliance Utilities . . . . .	4
1.2.1 Measurement Methods . . . . .	4
1.2.2 Receivers . . . . .	6
1.3 Thesis Organization . . . . .	9
<b>2 Theoretical System Analysis</b>	<b>10</b>
2.1 Using a TEM Cell for EMC Measurements . . . . .	11
2.1.1 Total Radiated Power Estimate . . . . .	11
2.1.2 Equivalent Far Field Representation . . . . .	15
2.1.3 Usable Test Volume . . . . .	16
2.2 Concept Analysis of the EMI Receiver . . . . .	18
2.2.1 Generic Receiver Elements . . . . .	18
2.2.2 Suitability of Software-Defined Radios . . . . .	23
2.2.3 Digital IF Implementation . . . . .	27
2.2.4 Broadband Receiver Frontends . . . . .	31
<b>3 SDR Performance Evaluation</b>	<b>33</b>
3.1 SDR Selection . . . . .	33
3.1.1 Tuning Range and Accuracy . . . . .	35
3.1.2 Test Signal Considerations . . . . .	35
3.1.3 Decision for the <i>USRP B200mini</i> . . . . .	39
3.2 Continuous Wave Analysis . . . . .	41
3.2.1 Out-of-Band Carrier Suppression . . . . .	44
3.2.2 Sensitivity and Spurious Emission . . . . .	45
3.2.3 Matching . . . . .	47
3.3 Transient Analysis . . . . .	47
3.3.1 Coherent Detection of <i>CISPR</i> Pulses . . . . .	48
3.3.2 Broadband Performance . . . . .	52
<b>4 Improving the Performance</b>	<b>55</b>
4.1 Benefits of a Heterodyne Design . . . . .	55

4.2	Feasibility Analysis of an Upconversion Stage . . . . .	57
4.2.1	Implementation Considerations . . . . .	58
4.2.2	Design Criteria Evaluation . . . . .	60
4.2.3	LO Signal Generation . . . . .	64
4.3	Final Prototype Design . . . . .	64
4.3.1	Transfer Characteristics . . . . .	66
4.3.2	Sensitivity and LO Design . . . . .	68
4.3.3	Broadband Performance . . . . .	69
4.4	Enhancements . . . . .	70
4.4.1	Available Dynamic Ranges . . . . .	70
4.4.2	Available Analysis Bandwidths . . . . .	72
4.4.3	Discussion of Further Improvements . . . . .	73
4.5	Gain Control . . . . .	74
4.5.1	Application of a Feed-Forward AGC . . . . .	75
4.5.2	Signal Reconstruction . . . . .	75
4.5.3	System Design . . . . .	78
4.5.4	System Verification . . . . .	80
<b>5</b>	<b>System Verification</b>	<b>83</b>
5.1	Classic Single Frequency Metering . . . . .	83
5.1.1	Detector Implementation . . . . .	83
5.1.2	Absolute Accuracy . . . . .	84
5.1.3	Relative Accuracy . . . . .	85
5.1.4	Overload Detection . . . . .	87
5.2	Broadband IF Capabilities . . . . .	88
5.2.1	Spectral Purity . . . . .	88
5.2.2	Usable Analysis Bandwidth . . . . .	90
5.3	Performance Comparison Against Accredited Test-Houses . . . . .	91
5.3.1	Pre-Compliance Setup . . . . .	92
5.3.2	Measurement Results Comparison . . . . .	93
5.4	Overall Budget Estimate . . . . .	96
<b>6</b>	<b>Conclusion and Outlook</b>	<b>98</b>
	<b>References</b>	<b>101</b>
<b>A</b>	<b>TEM Cell Characterization</b>	<b>107</b>
A.1	S-Parameters . . . . .	108
A.2	Field Homogeneity . . . . .	109

---

# List of Acronyms

---

<b>AAF</b>	anti-aliasing filter
<b>ADC</b>	analog-to-digital converter
<b>AGC</b>	automatic gain control
<b>CW</b>	continuous wave
<b>DR</b>	dynamic range
<b>DSO</b>	digital sampling oscilloscope
<b>EMC</b>	electromagnetic compatibility
<b>EMI</b>	electromagnetic interference
<b>ENOB</b>	effective number of bits
<b>EUT</b>	equipment under test
<b>FAC</b>	fully-anechoic chamber
<b>FFT</b>	fast Fourier transform
<b>IF</b>	intermediate frequency
<b>IoT</b>	internet of things
<b>LNA</b>	low-noise amplifier
<b>LO</b>	local oscillator
<b>NF</b>	noise figure
<b>OATS</b>	open-area test site
<b>OVF</b>	overload factor
<b>PC</b>	personal computer
<b>PLL</b>	phase-locked loop
<b>PN</b>	pseudo noise
<b>RF</b>	radio frequency

- RL** return loss
- RVC** reverberation chamber
- SAC** semi-anechoic chamber
- SDR** software-defined radio
- STFT** short-time Fourier transform
- TEM** transverse electromagnetic
- UTV** uniform test-volume
- VSG** vector signal generator
- VSWR** voltage standing wave ratio

---

# List of Figures

---

1.1	Professional radiated emission measurement setup using an SAC with a distance of $s = 3$ m for frequencies between 30 MHz–1 GHz. . . . .	2
1.2	Near field measurement setup using a small antenna probe to scan emissions of an EUT (left) [11]. For improved measurement repeatability, the probe is mounted on linear axes (right) [12]. . . . .	5
1.3	Comparison of a professional hybrid log-periodic antenna (left, Aaronia <i>HyerLOG 20300</i> , width: 1.3 m) with a pre-compliance broadband biconical dipole (right, Aaronia <i>Bicolog 30100</i> , width: 20 cm). Both taken from Aaronia AG webpage. . . . .	6
1.4	Overview of a professional GTEM cell Teseq <i>500</i> (left) with an open TEM cell Tekbox <i>TBTC3</i> (right) for pre-compliance purposes. Both pictures are taken from the manufacturers' webpages. . . . .	7
1.5	Overview of different receiver categories (pre-compliance/full-compliance) for EMC purposes over budget vs. frequency range. . . . .	8
2.1	Visualization of a TEM-cell-based radiated emission measurement setup. . . . .	10
2.2	Magnetic vector potential description of a general current density distribution $\vec{J}$ in $\mathcal{V}'$ observed from point $\mathcal{P}$ with the origin $\mathcal{O}$ . . . . .	11
2.3	EUT rotations to estimate the total radiated power with a TEM cell. . . . .	13
2.4	Side view (left) and cross section (right) of a generic transverse electromagnetic (TEM) cell sketching significant dimension parameters for calculating the field factor $e_{0y}(x, y, z)$ . . . . .	14
2.5	Mirrored EUT scenario modeling the reflecting ground plane in an SAC. . . . .	15
2.6	Electric field strength $E_y$ in vertical direction for different cross sections of the TEM cell from [20] (top) at 30 MHz (left) and 920 MHz (right), measured with a field probe. . . . .	17
2.7	Generic block diagram of an EMI receiver in accordance to the analytically derived signal model. Complex signals are indicated by two parallel connection wires. . . . .	19
2.8	IF filter response of (2.24) fulfilling the spectral mask specified in <i>CISPR 16-1-1</i> . . . . .	20
2.9	Visualization of the direct envelope quasi-peak detector circuit (left) and the transient response (right). . . . .	21
2.10	Relative detector outputs for recurrent impulses in <i>CISPR</i> band C/D. . . . .	22
2.11	Broadband extension of the IF section performing simultaneous signal detection over multiple independent paths. . . . .	23
2.12	Blockdiagram of a generic SDR connected to a host PC. . . . .	24
2.13	Generic description of a homodyne receiver (left) and the downconverted signal represented in frequency domain (right). . . . .	25
2.14	Low-IF signal processing procedure in discrete time domain to access the LSB of the sampled signal for $f_{IF} = -f_s/4$ . . . . .	26

2.15	Visualization of the amplitude uncertainty problem due to sampling the IF filter's impulse response $h_{\text{IF}}[k]$ with finite time resolution. . . . .	28
2.16	Maximum amplitude uncertainty in time domain (left) and frequency domain (right) for the IF filter definition from (2.34) using the STFT-based analysis approach. . . . .	29
2.17	Visualization of an impulse amplitude over time and frequency using the STFT-based method (left) and the time domain signal of certain frequency bins (right). . . . .	30
2.18	Advanced receiver concepts: Gauss Instruments (left) and Rohde & Schwarz (right). . . . .	31
2.19	Noise floor over frequency of the <i>RFSoc</i> at full sampling rate with terminated input. The indicated signals are relative to the full-scale power level (dBFS). . . . .	32
3.1	Available DR using an idealized ADC for measuring a single CW tone. . . . .	36
3.2	Available DR using an idealized ADC for measuring broadband impulses. . . . .	37
3.3	Estimated measurement uncertainty using the peak detector for different standard deviation ( $\sigma$ ) intervals of thermal noise. . . . .	38
3.4	Broadband DR limitations of a typical analog frontend incorporated in an SDR for different preselector bandwidths. . . . .	38
3.5	Visualization of the <i>USRP B200mini</i> with enclosure (left), unboxed (middle), and a blockdiagram describing the main functionalities (right). . . . .	40
3.6	Measurement setup for continuous wave (CW) analysis of the SDR <i>USRP B200mini</i> . . . . .	42
3.7	Measured dynamic range (DR) for continuous wave (CW) signals over input power at different gain settings: $f_0 = 750$ MHz, $f_{\text{IF}} = -12$ MHz. . . . .	43
3.8	Noise power measurement over $f_{\text{IF}}$ at different gains and $f_{\text{LO}} = 762$ MHz. . . . .	44
3.9	RF-IF leakage and image frequency suppression over LO frequency. . . . .	45
3.10	Suppression of downconversion products due to frequency content located at $f_{\text{RF}} = n f_{\text{LO}} \pm f_{\text{IF}}$ . . . . .	46
3.11	Peak detected noise floor over <i>CISPR</i> band C/D for different gain settings. . . . .	47
3.12	VSWR of the <i>USRP B200mini</i> measured at the input connector <i>RX2</i> . . . . .	48
3.13	Measurement setup for broadband linearity analysis of the SDR <i>USRP B200mini</i> measuring <i>CISPR</i> impulses. . . . .	49
3.14	Coherent overlay of measured <i>CISPR</i> impulses followed by the PN sequence. . . . .	50
3.15	Phase drift over time of a single tone measured at $f_0 = 500$ MHz. . . . .	51
3.16	Measured DR for <i>CISPR</i> impulses over input power at different gain settings: $f_0 = 500$ MHz, $f_{\text{IF}} = -12$ MHz. . . . .	53
3.17	Absolute error evaluation according to <i>CISPR 16-1-1</i> in comparison to compressions from linear gain. . . . .	53
4.1	Visual description in frequency domain (left) of the target upconversion stage (right), connected to the SDR <i>USRP B200mini</i> . . . . .	56
4.2	Initial upconversion stage design showing the block diagram (top) and the realization (bottom). . . . .	59
4.3	Noise figure measurement setup situated in a shielded environment, i.e., a GTEM cell, performing the Y-factor method. . . . .	60
4.4	Modified network analyzer setup for S-parameter and 1-dB compression measurements. . . . .	62
4.5	Prototype performance over frequency measured at $f_c = 1090$ MHz, $P_{\text{LO}} = 20$ dBm. . . . .	63
4.6	Redesigned upconversion stage: Block diagram (top) and the realization with and without a brass shielding (bottom). . . . .	65

4.7	Conversion gain and matching of the redesigned upconversion stage having the 40-MHz path configured. . . . .	67
4.8	IF response of the redesigned upconversion stage, $f_c = 1227$ MHz. . . . .	67
4.9	NF of the redesigned upconversion stage measured with internal and external LOs. . . . .	68
4.10	Broadband DR of the upconversion stage measuring <i>CISPR</i> impulses: power sweep at constant frequency (left) and frequency sweep at constant power (right). The absolute error was evaluated by $ \hat{\mathcal{I}}_{f_c CW} - \hat{\mathcal{I}}_{f_c IMP} $ . . . . .	69
4.11	Broadband DR of the SDR-based receiver at $f_0 = 60$ MHz, $f_{IF} = -500$ kHz, and full anti-aliasing filter (AAF) bandwidth. The absolute error was evaluated relative to a linearly increasing trace fitted to the measurement data. . . . .	71
4.12	Broadband DR of the SDR-based receiver at $f_0 = 60$ MHz, $f_{IF} = -500$ kHz, and minimum AAF bandwidth. The absolute error was evaluated relative to a linearly increasing trace fitted to the measurement data. . . . .	72
4.13	Analytically calculated AAF bandwidths vs. DR of the SDR-based receiver. . . . .	73
4.14	IF response comparison of the designed upconversion stage versions. . . . .	74
4.15	Blockdiagram of a classic analog fed back AGC (left) and a digital feed-forward approach (right). . . . .	75
4.16	Time domain excerpt of the downconverted signals used in (4.10). . . . .	76
4.17	Spectral broadening due to the finite trigger response time of DU to asynchronously detected events, $f_c = 1227$ MHz. . . . .	77
4.18	Recovered signal spectrum taking the timing uncertainty into account. . . . .	78
4.19	Block diagram of the feed-forward AGC implementation approach [71] © 2023 IEEE. . . . .	79
4.20	Measurement setup for characterizing the feed-forward AGC. . . . .	80
4.21	Normalized step responses of the attenuator for modeling $\alpha[k]$ at $f_s = 56$ MSa/s [71] © 2023 IEEE. . . . .	81
4.22	Measurement results of the AGC over $f_{IF}$ indicating peak detected impulse spectra (left) and the RMS noise power spectra (right) [71] © 2023 IEEE. . . . .	82
5.1	Absolute detector accuracy $\epsilon$ of the peak and quasi-peak detector over frequency. . . . .	85
5.2	Relative accuracy of the envelope quasi-peak detector at gain setting $G = 30$ . . . . .	86
5.3	Relative accuracy of the envelope quasi-peak detector at gain setting $G = 40$ . . . . .	86
5.4	Available DR comparison with fully-compliant EMI receiver Keysight Technologies <i>MXE N9038A</i> . . . . .	87
5.5	Intermodulation distortion measurement using a two-tone with a distance of 1 MHz. . . . .	88
5.6	Spectral regrowth measurement using a notch filtered impulse. . . . .	89
5.7	Peak detected spectra of absolute calibration procedure and the corresponding amplitude error over frequency $f_{IF}$ . . . . .	90
5.8	Realized test EUT: top view (left), bottom view (middle), and side view (right). . . . .	91
5.9	Low-cost measurement setup placed in an anechoic chamber. In the lower right, the test EUT is magnified. . . . .	92
5.10	Alternative criteria evaluation in unloaded and loaded conditions of the used low-cost TEM cell. . . . .	93
5.11	Calculated vs. measured field factor of a Teseq <i>500</i> GTEM cell and the used low-cost TEM cell. . . . .	94

5.12	Comparison of the radiated emission spectra from the 3 m FAC (top left), 3 m SAC (top right), and the 5 m SAC (bottom) with the measurements made using a Teseq 500 GTEM cell and the proposed low-cost setup. The results of the 5 m SAC have been transformed by the EMC test house to a hall with 10 m distance. The maximum field strength of the traces is emphasized by visualization of the spectrum peaks separated by at least 1 MHz. . . . .	95
A.1	Picture of the developed asymmetric TEM cell from [20]. . . . .	107
A.2	S-parameter measurement of the empty low-cost TEM cell from [20] placed in an anechoic chamber as in Fig. 5.9. . . . .	108
A.3	Definition of the cubic UTV placed in the central of a TEM cell. . . . .	109
A.4	Automatized measurement setup for characterizing the field homogeneity of the developed TEM cell with a field probe. . . . .	110
A.5	Horizontal sweep of the field probe along the TEM cell's cross section $z = 0$ measured at the constant height of $y = h_s/2 = 15$ cm and frequency of 30 MHz. . . . .	111
A.6	Field homogeneity criteria evaluation in accordance to <i>DIN EN 61000-4-20</i> . While on the left hand side, the simulation-based results are evaluated, the right hand side represents for the measured values. The y-axis of the plots denote the investigated criteria and the belonging field components. Longitudinal stands for the evaluation of $E_{ij}^{(z)}/ \vec{E}_{ij} $ and horizontal for $E_{ij}^{(x)}/ \vec{E}_{ij} $ . For the simulation and the measurement, 0.3 % and 1.3 % of the investigated frequencies are failing the second requirement respectively. . . . .	112

---

# List of Tables

---

3.1	Popular SDRs of different budget and capabilities. The specifications for the <i>USRP X310</i> is given in conjunction with a single frontend, i.e., the <i>TwinRX</i> . AAF bandwidth definition refers to complex baseband taking both sidebands into account. . . . .	34
4.1	Examples of high dynamic range mixer specifications. . . . .	57
4.2	Harmonic table of the used mixer <i>SYM-30DHW+</i> from Mini-Circuits. . . . .	59
4.3	Key component list of the redesigned upconversion stage. . . . .	65
5.1	Overall budget estimate of the low-cost measurement system. Alternative or not mandatory options are denoted with *. PCB assembly costs are derived for a single unit production size. . . . .	96

## Introduction

---

Electronic devices serve for plenty of purposes making them indispensable in the modern world we are living in. Depending on the product complexity, several different modules are implemented, e.g., switch-mode power supplies, electrical engines, or displays. Such modules inherently emit electromagnetic fields interfering with the environment. To ensure the reliability of end-consumer products in co-existence with other devices from an electromagnetic perspective, compatibility norms have been developed.

If an electronic product wants to be commercialized, several country specific certifications must be passed. In Europe, the international special committee on radio interference (*CISPR*) specifies most of these regulations and is taken as reference within this work. Many of the specified procedures are similar to other committees, e.g., the federal communications commission (*FCC*) applied in the USA, and can be split mainly into two categories termed emission and immunity testing. The goal is to characterize the equipment under test (EUT) under realistic operating conditions to check if certain requirements in terms of emitting and resisting electromagnetic fields are fulfilled. Compliance of an EUT is verified via two access media which are cables (conducted) and over the air (radiated), in defined frequency ranges. Conducted tests refer to couplings of the EUT with peripherals, e.g., the power supply, in a frequency range between 9 kHz–30 MHz. The radiated part extends over a frequency range between 30 MHz–18 GHz, investigating the wireless integrity of a device [1].

Accredited electromagnetic compatibility (EMC) test houses utilize large anechoic chambers to characterize an EUT under controlled conditions. The necessary test site and measurement equipment to verify compliance is extremely expensive and has to fulfill strict norms. Furthermore, EMC laboratories have to put great effort into maintenance by conducting periodic calibrations of their test sites to guarantee accurate and comparable results. Depending on the test object and related standards, the certification process can become a time-consuming and costly task as several different tests must be carried out. It is not unusual that a redesign of an EUT is required due to norm violations which cannot be solved by simply applicable modifications. Design iterations are always a setback in time and financial goals of bringing a product from prototyping phase to market. A new certification attempt may be involved with significant idle times due to several impacts, such as, limited availability of test houses or setup preparations. To achieve a competitive time schedule for releasing products, EMC measurements in advance of certification, i.e. pre-compliance testing, has gained a lot of popularity by the industry.

The high investment costs for a professional pre-compliance test setup usually exceed financial reserves of small companies, especially start-ups. Thus, the goal of this thesis is to elaborate on low-cost solutions for pre-compliance purposes supporting entrepreneurs to launch their developments. As this is a highly diverse topic, the main focus is put on radiated emission testing

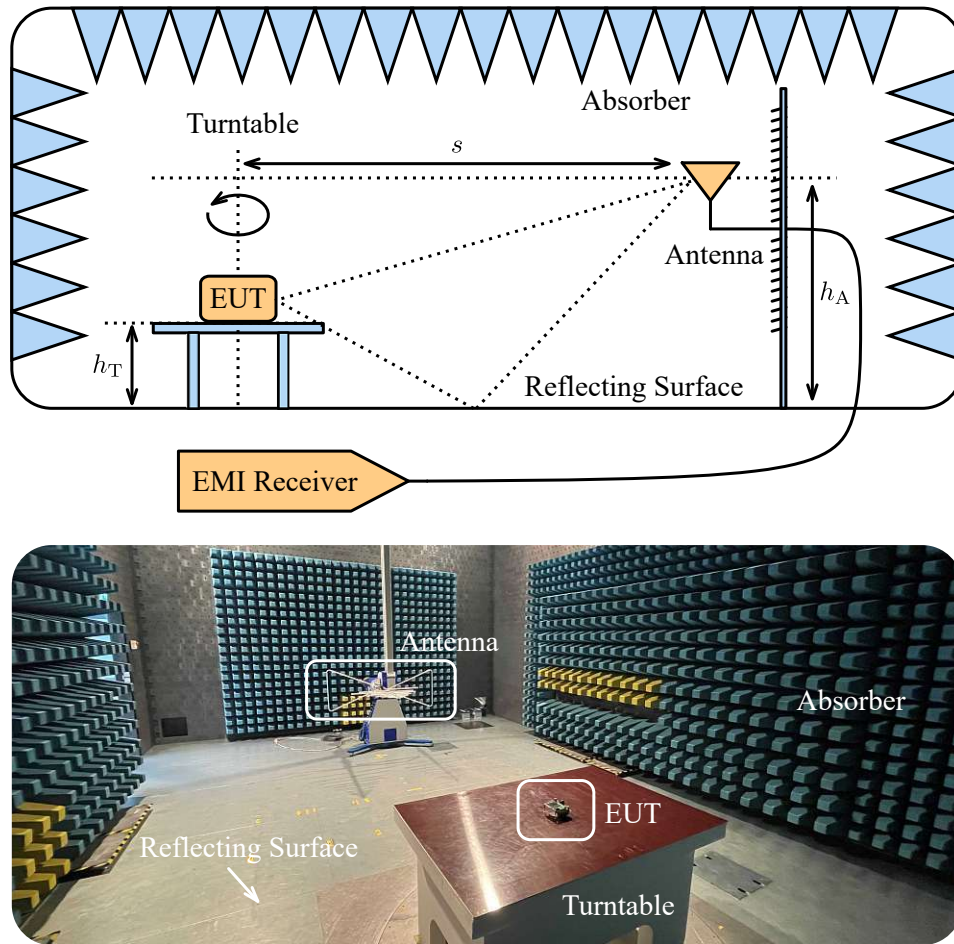


**Fig. 1.1:** Professional radiated emission measurement setup using an SAC with a distance of  $s = 3$  m for frequencies between 30 MHz–1 GHz.

in laboratory conditions of battery-powered devices which represents a typical use case in the internet of things (IoT) branch. According to received resonances from industry partners, EMC consultants, and test houses, the frequency range causing the most certification fails is between 30 MHz–1 GHz (*CISPR* band C/D) and hence investigated in this work. Later in this chapter, it will be shown that a lot of successful research has been already made towards cost-effective measurement solutions. The still unexplored part in terms of performance, accuracy, and costs is the electromagnetic interference (EMI) receiver. Therefore, the focus of this thesis is further narrowed down to the measuring apparatus. In particular, the suitability of low-cost receivers for pre-compliance measurements shall be investigated and if standardized EMC requirements can be met.

## 1.1 General Radiated Emission Measurement Setup

A typical test site for radiated emission testing in *CISPR* band C/D is the semi-anechoic chamber (SAC). In Fig. 1.1, a typical configuration of such a chamber with a measurement distance of  $s = 3$  m is depicted. To reduce electromagnetic reflections by the sidewalls, absorbers and ferrites are applied. A test device, called EUT, is placed on a turntable with a height of  $h_T$ , apart from

the receiving antenna at the constant horizontal distance  $s$ . While the EUT is energized, the antenna is used to capture the electric field, radiated during a typical use case emulation. The antenna forwards the signal directly to the EMI receiver placed outside the anechoic chamber. After correcting the measurement data with setup specific calibrations, the absolute field strength emitted by the EUT is derived and compared to a certain threshold defined for  $s$ . If the measured field strength is in excess of this threshold at any frequency, the EUT has failed the test.

### Anechoic Chamber

The most significant part in EMC measurements is the test site. In test houses, the SAC is used most often. Some institutions still make use of an open-area test site (OATS) representing the same method with the only difference that they do not require absorbers to dampen sidewall reflections. As the OATS is prone to interference from, e.g., base-stations and the availability depends on the weather, SACs have become more popular. For measurements below 1 GHz, these chambers incorporate a metal plane on the ground taking potential reflecting surfaces of real scenarios into account, e.g., reinforced concrete. The horizontal distance  $s$  between the antenna and the EUT is constant and ranges typically between 3–10 m while the turntable has a height of  $h_T = 0.8$  m [2]. To capture the maximum emitted field strength over frequency, the receiving antenna scans the EUT's field pattern by rotating it (turntable) and performing a height scan between  $h_A = 1$ –4 m. To take different polarizations of the EUT into account, the height scan is performed in vertical and horizontal position of the receiving antenna.

The absolute measurement results of radiated emission tests highly depend on the used chamber type and cannot always be directly compared. There are two more types which are frequently used. Firstly, the fully-anechoic chamber (FAC) which is simply the same setup as for the SAC except that the ground surface is covered with absorbers and ferrites. Due to the elimination of ground reflections, it is assumed that the maximum emitted field strength can be captured at a constant antenna height. For accessing the entire radiation pattern, the EUT is rotated on the turn table taking different positionings into account. Secondly, and currently the most popular research topic regarding EMC test sites, the reverberation chamber (RVC) [3, 4]. These chambers are large cavities making use of higher order mode propagation to perform radiated tests. By changing the boundary conditions with a mode stirrer, different field patterns are excited and changed over time. Averaging the received signal allows to estimate the total radiated power of an EUT. To gain equivalent field strength values in far field conditions, the measurement data is further processed by a standardized analytical scheme [5]. As RVCs require even more space than a 3-m SAC or FAC in the target frequency range, they are less used [6].

### Antenna

The typical EMI antenna in EMC laboratories is a hybrid log-periodic dipole antenna. To cover low frequency ranges of radiated emission measurements starting from 30 MHz, EMI antennas are relatively large with a dipole length in the range of one meter. The measured power relates to the equivalent electric field strength at the specified distance  $s$  of the test site by multiplying the measurement data with the antenna factor. During the height scan, the antenna may be operated in an SAC very close to the reflecting floor. This causes significant deviations of the antenna's transfer characteristics, e.g., the 3 dB-opening-angle [7]. As the dipole tip is only a few ten of centimeters above ground in vertical polarization, accurate and comparable measurements are in general difficult if the maximum field strength occurs at this specific height.

### EMI Receiver

The EMI receiver is quite similar to the classic swept-spectrum analyzer with the main difference that it stays tuned to a certain frequency until the signal has been detected properly. The stepped sweep ensures that transient signals are not missed when analyzing a certain frequency

range of interest. Electronic devices incorporate several different modules, e.g, power supplies, producing switching currents and thus, transient signals with large bandwidths. According to *CISPR 16-1-1*, the EMI receiver has to measure specified test impulses with sufficient accuracy proving the unrestricted use for EMC measurements. Usually, fully compliant analyzers come with costly preselection filterbanks to avoid an overload of the analog frontend for this test case. Due to narrowband preselection, the instantaneous analysis bandwidth is limited which directly affects the frequency scan speed.

Modern receivers perform signal analysis in the time domain using a broadband architecture consisting of multiple samplers. The main benefit of such receivers is that frequency scans with exceptional speed are possible, allowing to analyze, e.g., the entire *CISPR* band D (300 MHz–1 GHz) instantaneously by making a single recording [8–10]. To avoid saturation in case of the broadband test impulses, the analog frontend of such instruments differs from a traditional filterbank-based concept. State-of-the-art receivers split the incoming signal up into several paths either limited to certain frequency or amplitude ranges. Each of the paths is foreseen with a separate sampler. The split signals are recombined in discrete time domain enabling these fast instantaneous frequency scans without running into saturation by the analog frontend. Additional information about such architectures is given in Sec. 2.2.4.

## 1.2 Pre-Compliance Utilities

The aim of pre-compliance measurements is to verify an EUT in advance of attempting the EMC certification process in a test house. In principle, any equipment or method may be used for this purpose, even if not accepted by relevant standards. In some cases, the measurement results cannot be related to absolute field strength values in far field conditions and only relative measurements are possible for design change investigations. A further problem in this field is that the measurement accuracy and repeatability is not given out-of-the-box and requires additional verification steps, if they are even applicable.

In comparison, accredited EMC test houses perform measurements with methods and equipment which fully complies with the target norms. This includes that the system performance and responsible personnel has been verified as a whole to guarantee accurate and comparable measurements in any specified use case.

Within this section, the most common pre-compliance utilities are discussed and compared to professional equipment and test methods. The goal is to identify the most promising solutions, further investigated in this work and potentially fully complying with standardized measurement accuracy requirements. Although, focus in this thesis is put on the EMI receiver, it is elaborated as well on measurement methods for taking specific requirements into account. Financially limited companies, developing battery-powered devices in the IoT branch, are addressed. Thus, the content refers to cost-effective measurement techniques applicable to indoor scenarios in laboratory conditions.

### 1.2.1 Measurement Methods

To measure the radiated emission spectra of an EUT in advance, several different methodologies have been developed [13]. In the following, the most common ones are discussed and evaluated in terms of financial costs, compliance, and absolute measurement accuracy. Beforehand, it shall be noted that it is not elaborated on RVCs. Due to the large space required for measurements down to 30 MHz, this method does not fit typical development laboratory conditions.

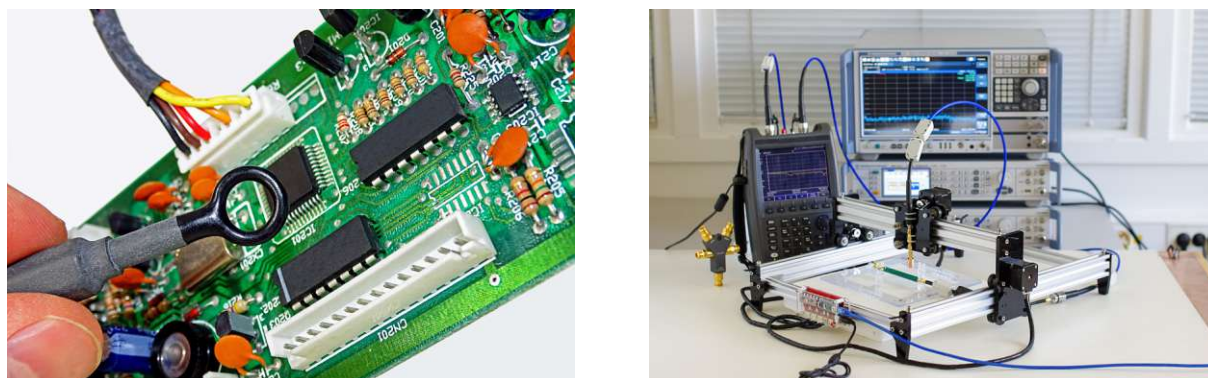


**Fig. 1.2:** Near field measurement setup using a small antenna probe to scan emissions of an EUT (left) [11]. For improved measurement repeatability, the probe is mounted on linear axes (right) [12].

### Near Field Probing

In hardware engineering, it is common practice to identify EMI radiation spots by using a near field probe. The EUT is scanned with a small hand-held loop antenna to discover potentially critical areas or components. As this method underlies significant uncertainties due to the limited repeatability of, e.g., the height between the antenna and the EUT, this technique has been improved by mounting the probe statically on linear axis. This allows to move the probe over a defined trajectory enabling repeatable measurements, see Fig. 1.2. The main problem of this method is that information on the absolute radiated field strength is neither directly accessible nor is it compliant to any emission standard. Although, there are works on near to far field transformations to estimate absolute electric field strengths with such a setup, the results suffer from difficulties in measuring the entire radiation pattern taking time dependencies into account and the cabling of a device when it is placed in a measurement chamber [14–16]. Anyways, this method is attractive to verify design changes of an EUT by performing relative measurements. Because of the simple setup, composed of a small antenna and two linear axes, the required budget is rather low, easy to build, and adjustable.

### Antennas

It is obvious to measure the emission spectra of an EUT with the same approach as in test houses using an antenna. Professional antennas achieve high sensitivities at low frequencies coming by without any pre-amplification due to large dipole widths, see Fig. 1.3. There are several low-cost and broadband antennas specified for the desired frequency range of 30 MHz–1 GHz. The classic biconical dipole antenna is used most frequently for such measurements. Although these antennas come with calibration data, they suffer from an insufficient sensitivity at a measurement distance above 3 m due to constructional limits. Especially at low frequencies, the antenna gain degrades and requires to apply a high performance low-noise amplifier (LNA) directly at the antenna output to achieve the required noise power level. The main problem of this approach is that LNAs usually do not provide sufficient dynamic range (DR) to preserve full compliance of the EMI receiver [1]. Besides the limited sensitivity, the setup suffers from test site related deviations through, e.g., undefined reflections from the ground and sidewalls, and interference, if no suitable anechoic chamber is available. To conclude, these low-cost antennas are a helpful and easily applicable pre-compliance tool. As full compliance is violated due to required pre-amplification and uncontrolled site reflections, the absolute accuracy of the measurement results cannot be

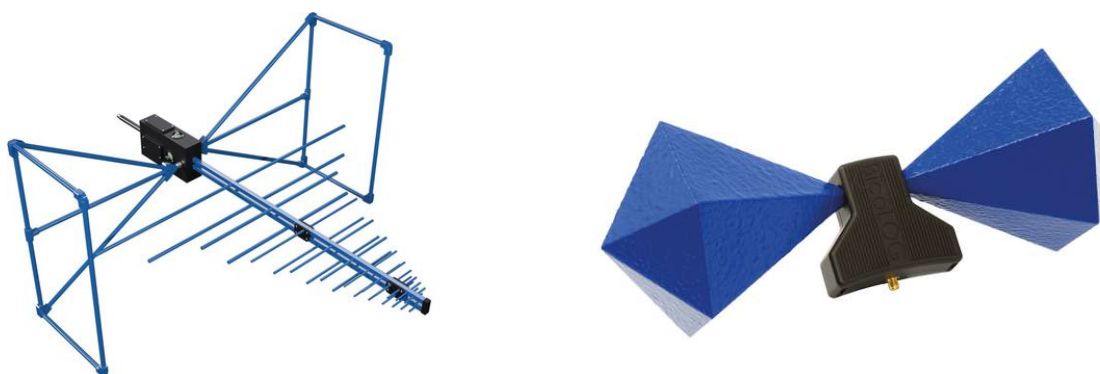


**Fig. 1.3:** Comparison of a professional hybrid log-periodic antenna (left, Aaronia *HyerLOG 20300*, width: 1.3 m) with a pre-compliance broadband biconical dipole (right, Aaronia *Bicolog 30100*, width: 20 cm). Both taken from Aaronia AG webpage.

compared to accredited test houses and shall be used for relative measurements during the design process only.

### TEM Cells

The probably most referred pre-compliance site is the transverse electromagnetic (TEM) cell [17]. In this method, the EUT is placed in a large stripline, filled with air, coupling the emitted field into the waveguide which is directly delivered to a connected receiver. This technique is also a kind of near field sensing and requires to transform the measurement results for gaining equivalent values in far field conditions [18, 19]. The main advantage of TEM cells is that they are fully compliant and they are accepted in several EMC norms, such as, *CISPR 32* which is frequently applied for multimedia-based IoT products [2]. As the usable frequency range of the classic TEM cell is limited due to constructional limitations, an evolved approach called Gigahertz-TEM cell has been developed to extend the frequency range, see Fig. 1.4. Commercially available cells are usually closed and thus, not affected by interference. Although there are a lot of points speaking for such waveguides, there are a few drawbacks limiting their use cases: Firstly, the maximum dimensions of the EUT are proportionally coupled to the usable frequency range of the cell. Secondly, it is not allowed to route any EUT cabling in the inner of the cell as this may lead to field resonances. And lastly, to scan the entire field pattern of the EUT, it must be rotated vertically and horizontally which is not applicable to each object.

In this thesis, the focus is put on radiated emission testing of IoT products. As devices in this branch are rather compact in size and wireless, they are usually battery-powered and fit the testing capabilities of a TEM cell very well. It has been shown in [20] and [21] that open do-it-yourself cells can be easily built for a budget below 500 €. Even if these cells are open structures and prone to interference, they have one major advantage compared to the previously presented methodologies. As TEM cells are fully compliant to EMC norms, it is possible to characterize the absolute radiated emission spectra in advance which is the target of this thesis. Consequently, the primary focus of this work is on a TEM-cell-based measurement setup.

### 1.2.2 Receivers

While a lot of research has been made towards pre-compliance testing methods, there is a lack of knowledge on low-cost EMI receivers. Although, the successful use of a standard digital sampling oscilloscope (DSO) for conducted tests has been demonstrated in [22] and [23], the radiated part



**Fig. 1.4:** Overview of a professional GTEM cell Teseq 500 (left) with an open TEM cell Tekbox TBTC3 (right) for pre-compliance purposes. Both pictures are taken from the manufacturers' webpages.

has not been tackled yet according to actual norms using low-cost alternatives. The problem with radiated emission testing is that large frequency ranges must be covered exceeding the bandwidth and DR of such a standard DSO. Furthermore, the acquisition time vs. analysis bandwidth is limited which is crucial for EMC measurements where recordings of up to 15 s have to be made. Available instruments covering the target frequency range of interest 30 MHz–1 GHz are discussed in terms of compliance, frequency range, and budget. In Fig. 1.5, one can find a comparison of different analyzer categories referring to their respective budget and frequency range.

### Fully-Compliant Equipment

The manufacturer with the largest product range of professional EMI receivers is Rohde & Schwarz. Other popular brands are Keysight Technologies and Gauss Instruments. All these receivers are fully compliant, provide broadband signal analysis, and make frequencies up to 44 GHz accessible. The budget for such instruments starts from 50 k€ and goes, depending on configurable options, above 100 k€. Besides the target application as an EMI receiver, these analyzers can be utilized for many other measurement problems as well. In 2023, the company Narda has launched a fully compliant solution for frequencies up to 3 GHz. As the use case of the *N9000A* is limited to EMI receiver purposes only and requires a personal computer (PC) for data analysis, the budget for this device is much lower starting from about 18 k€.

### Entry-Level Spectrum Analyzers

The next lower category are entry-level spectrum analyzers which are often used for pre-compliance purposes. In the world of EMC, certain analysis filter bandwidths, frequency scan settings, and detectors are defined which are not always fully supported by low-cost analyzers. A prime example is the *BB60C* from Signal Hound, usable in a frequency range of 10 MHz–6 GHz and available for a budget of approx. 4 k€. This receiver provides a graphical user interface with an EMI analyzer mode which is accessible in conjunction with a host PC, where also the measurement data is processed. Although superficial measurements are possible with this device, certain limitations in recording times, DRs, and limited analysis bandwidths depending on the utilized detector have to be expected.

### Software-Defined Radios

A promising low-cost alternative to the presented analyzers are software-defined radios (SDRs) [24]. These highly configurable transceivers suit various applications, e.g., radar, medical imaging,

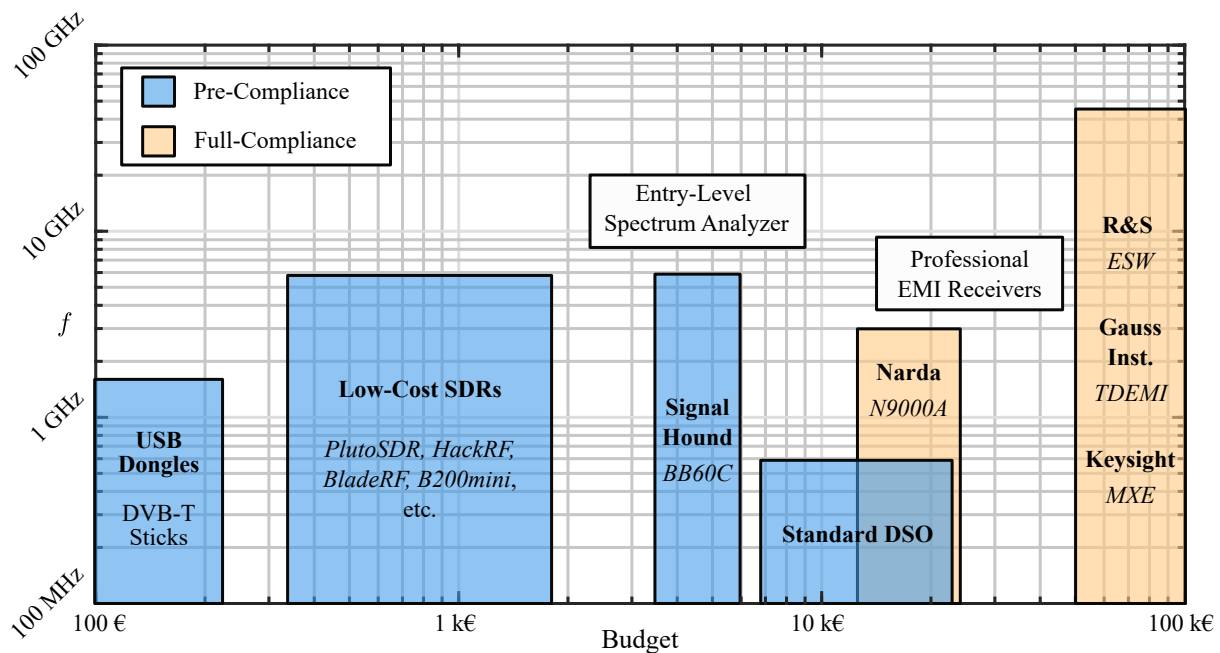


**Fig. 1.5:** Overview of different receiver categories (pre-compliance/full-compliance) for EMC purposes over budget vs. frequency range.

or localization [25–27]. Low-cost SDRs often come as an evaluation board with limited software support and usually cover frequencies up to 6 GHz. As for the *BB60C*, a PC is required to control the SDR and access the measurement data. Necessary signal processing units to perform a frequency scan have to be implemented mostly by the user. State-of-the-art radios incorporate digital resources allowing to allocate real-time processing on the measurement data and reducing computational resources on the host PC. Depending on the receiver complexity, performance, and manufacturer, the price of medium to low budget SDRs ranges between 300 €–2 k€. Popular SDRs and the *BB60C* have been analyzed out-of-the-box in terms of radiated pre-compliance measurements in the target frequency range of *CISPR* band C/D by the author of this thesis in [28]. The results indicate the potential of SDRs to be used as an EMI receiver, though, some of the low-budget devices showed a slightly worse performances compared to the *BB60C*. As SDRs offer significant advantages over entry-level spectrum analyzers in terms of signal processing capabilities and budget, they are analyzed in this thesis regarding their applicability for EMC measurements.

### USB Dongles

To complete the research on available low-cost solutions, USB dongle based receivers are discussed. The target application of these dongles is, in principal, the demodulation of FM radio and DVB-T frequency bands. As the signal demodulation is usually conducted on a host PC, the transmitted baseband data can be used for other purposes as well, similar to SDRs and the *BB60C*. The budget for such USB sticks starts below 100 €. Inherent with the low price is the simple receiver topology representing the lower end of low-cost receivers in terms of performance. Because of concept-related limitations regarding the usable frequency range, signal distortion, missing real-time capable signal processing units, and build quality, this class of low-cost receivers is not further covered in this thesis and only mentioned for the sake of completeness.

### 1.3 Thesis Organization

After a thorough discourse on low-cost EMC pre-compliance tools, the objectives of this thesis and the corresponding research organization towards an SDR-based measurement solution are discussed. Because of their applicability to the dedicated use case of rather small battery-powered EUTs and full compliance according to relevant radiated emission norms, the content refers to TEM cells as a test environment and method. In total, the investment costs of the entire setup, comprising the cell and the receiver, shall not exceed the budget which is required for a single certification attempt in an accredited EMC test house verifying an EUT in *CISPR* band C/D.

In Ch. 2, the necessary theory to understand the basic principles of TEM cells for EMC testing is given. It is started with an analytical description of a far field transformation algorithm delivering absolute field strength values comparable to anechoic-chamber-based test sites. Further analysis on operating limits considering the usable test volume of a TEM cell shall complement the required knowledge for further requirement derivations of an SDR-based analyzer. In a next step, the functional blocks and operating principles of a generic EMI receiver are examined. Based on this, the suitability of low-cost SDRs is investigated including important digital signal processing techniques which are used throughout this thesis.

Next, in Ch. 3, available low-cost SDRs are evaluated in terms of theoretically derived *CISPR* norm requirements. The chosen device is then investigated rigorously using specified test signals to identify and describe potential performance limitations.

After exploring the problems of the chosen SDR, it is proceeded in Ch. 4 with performance improvements aiming to satisfy failed *CISPR* requirements. Therefore, a highly-linear hardware extension is designed and characterized in conjunction with the low-cost SDR. Furthermore, the applicability of a certain gain control approach is analyzed which shall further increase the measurement speed and DR of the system.

In Ch. 5, the measurement accuracy of the SDR-based solution is verified in a two step procedure over the entire *CISPR* band C/D. At first, the receiver is investigated alone, performing specified test methods professional EMI receivers have to fulfill as well. In the second step, the low-cost receiver is used in conjunction with a do-it-yourself TEM cell for measuring the emission spectra of a test EUT. For comparison purposes, the test EUT was characterized in three accredited EMC test houses using different test methods. The chapter is completed with an overall budget estimate of the used measurement setup for a final justification regarding the relevance of this work.

A final conclusion of the entire thesis, discussing the main results and open research questions, is given in Ch. 6. Furthermore, in App. A, one can find construction and performance based details on the used do-it-yourself TEM cell which has been specifically designed for this work by the author.

## Theoretical System Analysis

For characterizing the radiated emission spectra of battery-powered EUTs in *CISPR* band C/D, a measurement setup consisting of an SDR-based EMI receiver and a TEM cell is pursued in this thesis. In Fig. 2.1, the addressed low-cost setup while performing a radiated emission measurement is depicted. The cell is a two-port and terminated with a  $50\text{-}\Omega$  load on the left hand side to prevent from unintended reflections affecting the signal which is measured by the EMI receiver. Goal of this chapter is to elaborate on relevant theoretical aspects to understand such a measurement system in detail and important configurations, adopted throughout this thesis.

The application of TEM cells has been identified as a promising solution for radiated pre-compliance testing for the target use case of this work. As they are a kind of near field sensing method, measurement values must be transformed analytically for making them directly comparable to professional anechoic chamber sites. Within this chapter, an analytical and standardized procedure is presented which allows to transfer TEM-cell-based measurements into far field conditions of such chambers. The derived content is used throughout this work for EMI receiver requirement definitions and supporting the clarity of verification task restrictions.

Subsequently, the EMI receiver is explained, based on a generic block diagram and a belonging analytic framework, covering all significant sections. In particular, it is focused on the analog signal path and certain detection units which are required to measure radiated emission spectra in accordance to EMC norms. Based on the gained knowledge, the applicability of SDRs as an EMI receiver is investigated and how necessary functional blocks can be integrated. The primary focus is on state-of-the-art devices requiring to conduct signal detection in discrete time domain. Furthermore, modern EMI receiver concepts are compared to the capabilities of low-cost SDRs,

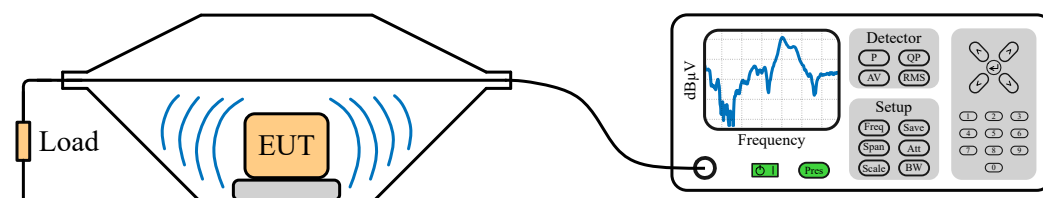
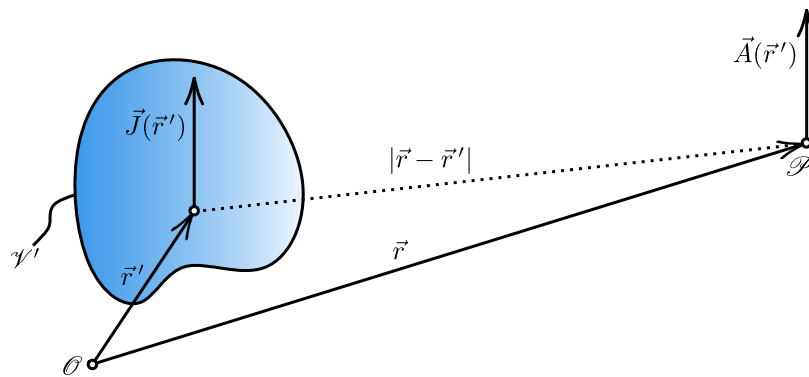


Fig. 2.1: Visualization of a TEM-cell-based radiated emission measurement setup.



**Fig. 2.2:** Magnetic vector potential description of a general current density distribution  $\vec{J}$  in  $\mathcal{V}'$  observed from point  $\mathcal{P}$  with the origin  $\mathcal{O}$ .

especially focusing on the frequency scan speed. The introduced definitions and descriptions are used supportive in consecutive chapters of this work.

Parts of the theoretic investigations and corresponding graphs are based on the author's publications [29, 30].

## 2.1 Using a TEM Cell for EMC Measurements

The history of TEM cells goes back into the 1970s when *Crawford* published an initial work on such a simple stripline to generate uniform field patterns [17]. Since then, the enormous potential of TEM cells for EMC measurements has been recognized as they either can be used for immunity testing where the EUT is exposed to a certain field stimulus or for measuring radiated emissions [31]. For the latter purpose, in [19], a method has been developed to describe the radiation pattern of an EUT using electrodynamic potentials. These definitions are then transferred to environmental conditions of a waveguide for estimating the total radiated power of an object with a TEM cell. In a further step, this estimate is transformed to free space test sites enabling reliable radiated emission measurements in advance. This algorithm and its limitations has been standardized in *DIN EN 61000-4-20* and is explained in what follows [18]. As the focus in this thesis is on the use of low-cost receivers applying TEM cells as a measurement method, design specific limitations are not further discussed. For the interested reader, derivative work can be found in [20, 32, 33].

### 2.1.1 Total Radiated Power Estimate

The radiated emission measurement procedure using TEM cells relies on analytical descriptions and several assumptions which are used to estimate the total radiated power of a certain EUT. As a starting point, one of the complex electrodynamic potentials, either the magnetic vector potential  $\vec{A}(\vec{r})$  or the electric potential  $\varphi(\vec{r})$ , can be used. A detailed analysis and derivation of the electrodynamic potentials is given in [34]. In the following, the magnetic vector potential is taken for further investigations as it is used most often in referred literature. The retarded notation:

$$\vec{A}(\vec{r}) = \frac{\mu_0}{4\pi} \int_{\mathcal{V}'} \vec{J}(\vec{r}') \frac{e^{-jk_0|\vec{r}-\vec{r}'|}}{|\vec{r}-\vec{r}'|} dV' \quad (2.1)$$

relates to the magnetic induction by  $\vec{B} = \vec{\nabla} \times \vec{A}$  where  $k_0 = 2\pi/\lambda$  and  $\mu_0$  denotes the permeability

in vacuum. With (2.1), the magnetic vector potential  $\vec{A}$  of a general current density distribution  $\vec{J}$ , covered in the volume  $\mathcal{V}'$ , is described at the observation point  $\mathcal{P}$ . This volume represents an arbitrary EUT including all occurring current flows. To solve this equation, the integral must be evaluated over the complete volume  $\mathcal{V}'$  in dependence on  $\vec{r}'$ , see Fig. 2.2. Increasing the distance  $|\vec{r}| \gg |\vec{r}'|$  allows significant simplifications of (2.1). Because of the large observation distance, the origin  $\mathcal{O}$  may be placed to the edge of  $\mathcal{V}'$  justifying two assumptions. Firstly, the denominator  $|\vec{r} - \vec{r}'|$  is reduced to  $|\vec{r}| = r$  as small deviations of the magnitude have a negligible influence on the overall result. Secondly, the vectors  $\vec{r} - \vec{r}'$  and  $\vec{r}$  are assumed to be parallel. As the phase term has a much higher impact on  $\vec{A}(\vec{r})$ , the complex exponent is approximated by  $|\vec{r} - \vec{r}'| = r - \hat{r} \cdot \vec{r}'$ , where  $\hat{r}$  denotes the unit vector of  $\vec{r}$ . Applying these assumptions yields the well known magnetic vector potential in far field conditions [35]:

$$\vec{A}(\vec{r}) \cong \frac{\mu_0}{4\pi} \frac{e^{-jk_0 r}}{r} \int_{\mathcal{V}'} \vec{J}(\vec{r}') e^{jk_0 \hat{r} \cdot \vec{r}'} dV'. \quad (2.2)$$

If the sphere diameter covering  $\mathcal{V}'$  is small compared to the wavelength  $\lambda$ , (2.2) can be rewritten with a multipole expansion by superposing known electric and magnetic moments [34]:

$$\vec{A}(\vec{r}) \cong \frac{\mu_0}{4\pi} \frac{e^{-jk_0 r}}{r} \left( \vec{P} - jk_0 \hat{r} \times \vec{M} + \frac{1}{2} jk_0 \underline{Q} \cdot \hat{r} \right). \quad (2.3)$$

In the standard, it is assumed that the electric ( $\vec{P} = \int_{\mathcal{V}'} \vec{J}(\vec{r}')$ ) and magnetic ( $\vec{M} = 1/2 \int_{\mathcal{V}'} \vec{r}' \times \vec{J}(\vec{r}')$ ) dipole moments are sufficient to describe electrically small radiation sources [18]. Hence, the quadrupole tensor  $\underline{Q}$  is neglected in derivative calculations.

It is shown in [36], that the total radiated power of a radiation source according to (2.3) can be characterized by:

$$P_0 = 10k_0^2 (|\vec{P}|^2 + k_0^2 |\vec{M}|^2). \quad (2.4)$$

For estimating the total radiated power  $P_0$  with a TEM cell, the current density distribution  $\vec{J}$  covered in  $\mathcal{V}'$  is placed in a waveguide and brought into context with (2.4). The corresponding electric and magnetic field can be described by forward and backward traveling waves as a superposition of existing modes [37]:

$$\vec{E}^\pm = \sum_n \begin{pmatrix} a_n \\ b_n \end{pmatrix} \vec{E}_n^\pm \quad \vec{H}^\pm = \sum_n \begin{pmatrix} a_n \\ b_n \end{pmatrix} \vec{H}_n^\pm \quad (2.5)$$

$$\vec{E}_n^\pm = (\vec{e}_{n_t} \pm \hat{z} e_{n_z}) e^{\mp jk_n z} \quad \vec{H}_n^\pm = (\pm \vec{h}_{n_t} + \hat{z} h_{n_z}) e^{\mp jk_n z}. \quad (2.6)$$

In (2.5), the superposition of existing field modes is described by the coefficients  $a_n$  and  $b_n$  denoting the forward and backward propagation direction of each mode in accordance to the  $\pm$  sign. With (2.6), the definition of the mode specific normalized field vectors in transverse and longitudinal direction is given. While the direction of propagation along the waveguide is described by the longitudinal component in  $z$ -direction,  $x$  and  $y$  directions are united in the transverse vectors  $(\vec{e}_{n_t}, \vec{h}_{n_t})$  pointing in horizontal and vertical direction respectively. The constant  $k_n$  takes the respective wave number into account. The coefficients  $a_n$  and  $b_n$  refer to normalized power waves defined by the integral:

$$\begin{pmatrix} a_n \\ b_n \end{pmatrix} = -\frac{1}{2} \int_{\mathcal{V}'} \vec{J}(\vec{r}) \cdot \vec{E}_n^\mp(\vec{r}) dV'. \quad (2.7)$$

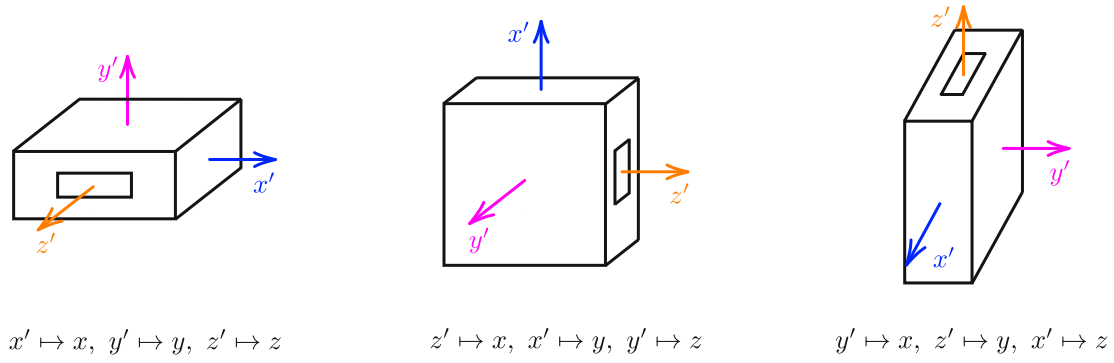


**Fig. 2.3:** EUT rotations to estimate the total radiated power with a TEM cell.

If  $\mathcal{V}'$  is uniformly covered by the mode of interest, the electric field may be approximated by a Taylor series developed in the origin  $\mathcal{O}$ , local to the volume, after truncation of the second element by:

$$\vec{E}_n^\pm(\vec{r}) = \vec{E}_n^\pm(\mathcal{O}) + \vec{r} \cdot \vec{\nabla} \vec{E}_n^\pm(\mathcal{O}). \quad (2.8)$$

Setting (2.8) into (2.7) allows to reformulate the integral. Due to the assumption that the radiation source is electrically small, it is possible to use a description of electric and magnetic dipole moments, as for (2.3), resulting in:

$$\begin{aligned} \begin{pmatrix} a_n \\ b_n \end{pmatrix} &= -\frac{1}{2} \left\{ \vec{E}_n^\pm(\mathcal{O}) \int_{\mathcal{V}'} \vec{J}(\vec{r}) dV' + \int_{\mathcal{V}'} [\vec{r} \cdot \vec{\nabla} \vec{E}_n^\pm(\mathcal{O})] \cdot \vec{J}(\vec{r}) dV' \right\} \\ &= -\frac{1}{2} \left\{ \vec{E}_n^\pm(\mathcal{O}) \cdot \vec{P} - jk_0 \eta_0 \vec{H}_n^\pm(\mathcal{O}) \cdot \vec{M} \right\}. \end{aligned} \quad (2.9)$$

For measurements with a TEM cell, it is important that the dominating mode is, as the name imposes, the TEM mode. Higher order modes lead to resonances of the field in the cell and impede accurate measurements. Hence, such cells are usually operated below the cutoff frequency of undesired modes. For  $n = 0$ , the normalized electric fields from (2.6) result in transverse components only:

$$\vec{E}_0^\mp(\mathcal{O}) = \hat{x}e_{0_x}(\mathcal{O}) + \hat{y}e_{0_y}(\mathcal{O}), \quad \eta_0 \vec{H}_0^\mp(\mathcal{O}) = \pm \hat{x}e_{0_y}(\mathcal{O}) \mp \hat{y}e_{0_x}(\mathcal{O}) \quad (2.10)$$

with  $\eta_0 = 377 \Omega$ . Putting (2.10) into (2.9) and assuming that the EUT, i.e.,  $\mathcal{V}'$ , is placed in the middle of the cell's cross section reduces  $e_{0_x}$  to zero:

$$\begin{aligned} \begin{pmatrix} a_0 \\ b_0 \end{pmatrix} &= -\frac{1}{2} \{ [P_x \pm jk_0 M_y] e_{0_x}(\mathcal{O}) + [P_y \mp jk_0 M_x] e_{0_y}(\mathcal{O}) \} \\ &= -\frac{1}{2} [P_y \mp jk_0 M_x] e_{0_y}(\mathcal{O}). \end{aligned} \quad (2.11)$$

The coefficients  $a_0$  and  $b_0$  denote the forward and backward traveling waves of the TEM mode in the waveguide. As the proposed cell from Fig. 2.1 has two ports, one of the coefficients can be used to relate the power at the connector output to, e.g.,  $|b_0|^2 = (P_y^2 + k_0^2 M_x^2) e_{0_y}^2 / 4$ . Thus, it is now possible to measure the remaining components  $P_x$ ,  $P_z$ ,  $M_y$ , and  $M_z$  by rotating the EUT according to Fig. 2.3. These three depicted positions are only sufficient as long as the dipole moments are radiating in phase and the EUT either is a dominantly electric ( $|\vec{P}| \gg k_0 |\vec{M}|$ )

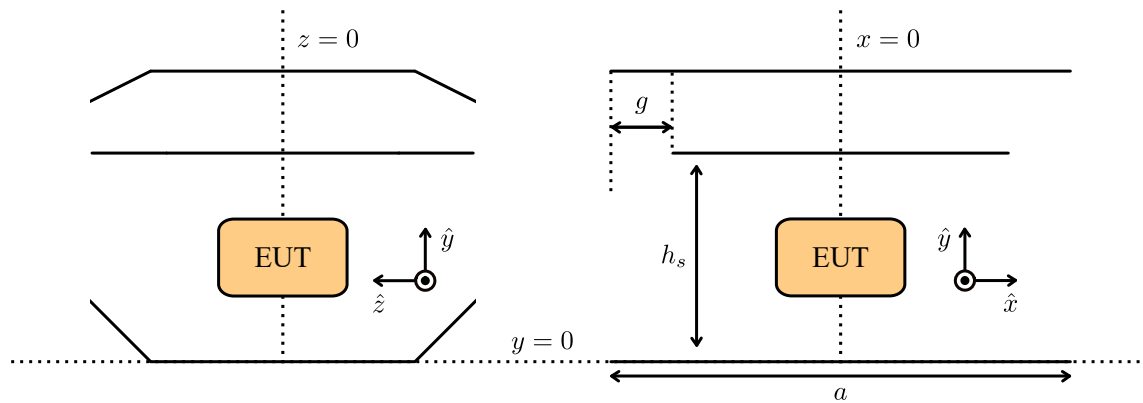


**Fig. 2.4:** Side view (left) and cross section (right) of a generic TEM cell sketching significant dimension parameters for calculating the field factor  $e_{0y}(x, y, z)$ .

or magnetic ( $k_0|\vec{M}| \gg |\vec{P}|$ ) source. In addition, the waveguide coordinate system must be sufficiently aligned with the orthogonal moments which is also assumed in the applied standard. After measuring each EUT position and taking (2.4) into account, the desired total radiated power estimate results in:

$$P_0 = 10k_0^2(|b_{01}|^2 + |b_{02}|^2 + |b_{03}|^2). \quad (2.12)$$

In the calculations, the phase center of the EUT is defined for the middle of the TEM cell's cross section, see Fig. 2.4. Even if an extremely small dipole radiator is located apart from this geometrical origin, higher order terms, e.g., the quadrupol moment, are necessary for an accurate analytical modeling of (2.9). As for EMC measurements rather the maximum emitted field is of interest than side lobes of the field pattern, the accuracy of this method is accepted and utilized by international standards. Differential techniques using both TEM cell ports exist and enable measurements with less uncertainties. As the main EMC norm for TEM cells, i.e., *DIN EN 61000-4-20*, specifies the presented one-port based technique, two-port measurements have been discarded and are not considered in this thesis.

The normalized field factor  $e_{0y}$  describes the relation between measured power values at the output port of the TEM cell and the absolute electric field strength radiated by the EUT. Professional manufacturers usually provide this frequency dependent factor by simply measuring the generated vertical field strength  $E_y(x, y, z)$  with a field probe at known input power  $P_{in}$ :

$$e_{0y} = \frac{E_y(x, y, z)}{\sqrt{P_{in}}}. \quad (2.13)$$

The coordinates  $x$ ,  $y$ , and  $z$  stand for the central of the target test volume.

If factory calibrations are not accessible, it is common practice to use an analytical approximation of  $e_{0y}$ , depending on the positioning of the EUT in the cell using [38]:

$$e_{0y} = \frac{4}{a} \sqrt{Z_0} \sum_{m=1,3,\dots}^{\infty} \frac{\cosh(My)}{\sinh(Mh_s)} \cos(Mx) \sin\left(\frac{Ma}{2}\right) J_0(Mg), \quad (2.14)$$

where  $M = m\frac{\pi}{a}$  with  $m = 1, 3, 5, \dots$ ,  $J_0$  is the zero-order Bessel function, and  $Z_0 = 50 \Omega$ . The remaining geometric parameters used in (2.14) are depicted in Fig. 2.4.

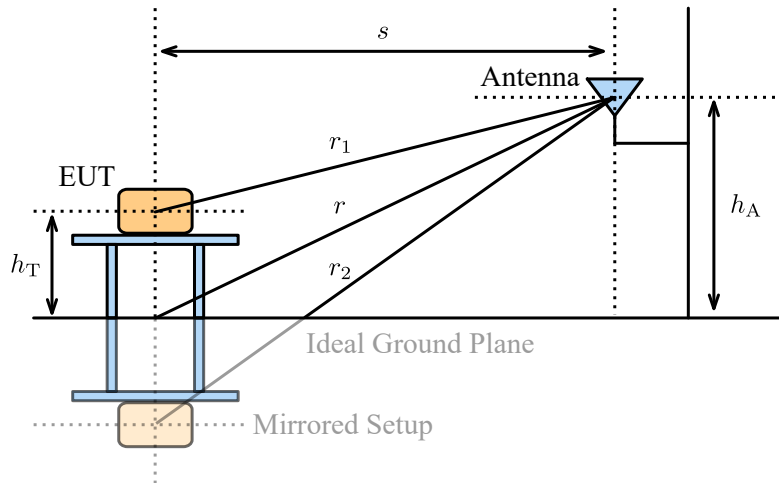


**Fig. 2.5:** Mirrored EUT scenario modeling the reflecting ground plane in an SAC.

### 2.1.2 Equivalent Far Field Representation

Usually, radiated emission limits are not specified explicitly for TEM cells. As suggested in *DIN EN 61000-4-20*, the results have to be transformed to conventional test chambers. In the following, the total radiated power estimate, derived in the previous section, is used to formulate an equivalent free space representation according to an SAC from Fig. 2.5. The basis assumption for this approach is to model the EUT in the SAC with an ideal dipole. In [19], the radiation pattern of a short dipole, symmetric over the radial angle  $\phi$ , is described in dependence of the spherical elevation angle  $\theta$  by:

$$E_{\theta} = \frac{\eta_0 k_0}{4\pi} I dl \sin \theta \frac{e^{-jk_0 r}}{r}, \quad (2.15)$$

where  $r$  denotes the observations distance,  $dl$  is the dipole's length, and  $I$  is the respective current amplitude defined in the middle. Integrating the energy density over a spherical envelope, covering the dipole, gives the total radiated power:

$$P_0 = \frac{1}{2} \int_{\phi=0}^{2\pi} \int_{\theta=0}^{\pi} \frac{|E_{\theta}|^2}{\eta_0} r^2 \sin \theta d\theta d\phi = \frac{\eta_0 \pi}{3} I^2 \left( \frac{dl}{\lambda} \right)^2 \quad (2.16)$$

where  $\eta_0 = 377 \Omega$ . Because of far field approximations, imaginary power exchanges subside and only the real power component remains. Reformulating (2.15) with (2.16) allows to eliminate  $I dl$  with  $P_0$  leading to:

$$E_{\theta} = 30 \sqrt{\frac{P_0}{10}} \sin \theta \frac{e^{-jk_0 r}}{r}. \quad (2.17)$$

In an SAC, the EUT is placed over an infinitely extended ground plane causing reflections of the emitted signal. To model this scenario analytically, the equivalent dipole source is mirrored according to Fig. 2.5. The height scan with the receiving antenna is performed in vertical and horizontal polarization mode. Maximum coupling with the EUT occurs if the dipole source is polarized in the same direction as the antenna. Thus, these two certain cases are taken into

account for calculating the radiated electric field strength at the measurement distance  $s$ . With (2.17), it is possible to superpose the mirrored dipole sources for the two different cases:

$$E(r_1, r_2) = 30\sqrt{\frac{P_0}{10}} \cdot \begin{cases} \left( \frac{e^{-jk_0 r_1}}{r_1} - \frac{e^{-jk_0 r_2}}{r_2} \right) & \text{Hor. pol.} \\ \left( \frac{s^2}{r_1^2} \frac{e^{-jk_0 r_1}}{r_1} + \frac{s^2}{r_2^2} \frac{e^{-jk_0 r_2}}{r_2} \right) & \text{Vert. pol.} \end{cases} \quad (2.18)$$

The parameters  $r_1$  and  $r_2$  refer to the absolute distances between the EUTs and the receiving antenna. As EMI measurements intend to find the maximum emitted field strength, the worst case points of the antenna height scan are considered only and are further denoted for simplicity reasons with  $g_{\max}$  reducing (2.18) to:

$$E_{\max} = 30\sqrt{\frac{P_0}{10}} g_{\max}. \quad (2.19)$$

Using the total radiated power definition from (2.12) and the relation  $V_i^2/Z_0 = |b_{0i}|^2$  allows to formulate an analytical expression for transforming TEM-cell-based measurements to an SAC with (2.19) by:

$$E_{\max} = g_{\max} \frac{60k_0}{e_{0y}} \sqrt{\frac{\sum_{i=1}^3 V_i^2}{Z_0}}. \quad (2.20)$$

The factor  $g_{\max}$  may be modified to satisfy different chamber types as well. By neglecting the secondary terms in (2.18), it is possible to eliminate ground reflections as in an FAC.

### 2.1.3 Usable Test Volume

The dipole moment based description of the EUT's radiation pattern from Sec. 2.1.1 underlies significant standardized restrictions. In particular, the presented model is limited to frequencies below 1 GHz. As the opening angle of radiation patterns may become relatively small for higher frequencies, an EUT rotation scheme with much finer steps has to be performed. Furthermore, the field homogeneity of the cell has a significant impact on the simplified multipole approximation. If the excited TEM field pattern does not cover the EUT uniformly, higher order terms may be necessary to achieve a sufficient accuracy of the analytical model. Simply put, the EUT must be electrically small and considerably smaller than the TEM cell's cross section. To hold the specified restrictions of *DIN EN 61000-4-20*, the EUT's maximum dimension must be  $d_{\max} \leq \lambda_{\min}/10$ . As in this thesis *CISPR* band C/D shall be addressed, ranging between 30 MHz–1 GHz,  $\lambda_{\min} = c_0/f = 30$  cm. It is implied by the standard, that small EUTs mainly consist of radiations sources with dipole characteristics only [18]. Hence, it is allowed to further relax this criteria to  $d_{\max} \leq \lambda_{\min}$ .

The uniform test-volume (UTV) of a TEM cell defines a cubic space in which fully-compliant measurements can be performed. As the EUT is rotated during characterization, it must be covered entirely by the defined space. Besides limitations of the analytical model, the TEM cell itself impacts the maximum EUT size and thus the UTV. Because of constructional caused bending edges, higher order modes are excited and perturb the intended TEM wave. This behavior further aggravates when loading the cell with a test object. It is therefore recommended to limit the EUT size to a third of the septum height  $d_{\max} \leq h_s/3$ , see Fig. 2.4 [39, 40].

To better understand the discussed problems, the impact of higher order modes is investigated by characterizing the electric field distributions in an open TEM cell, see Fig. 2.6. Therefore, the cell from [20] was used which has been designed by the author of this thesis. Details on the

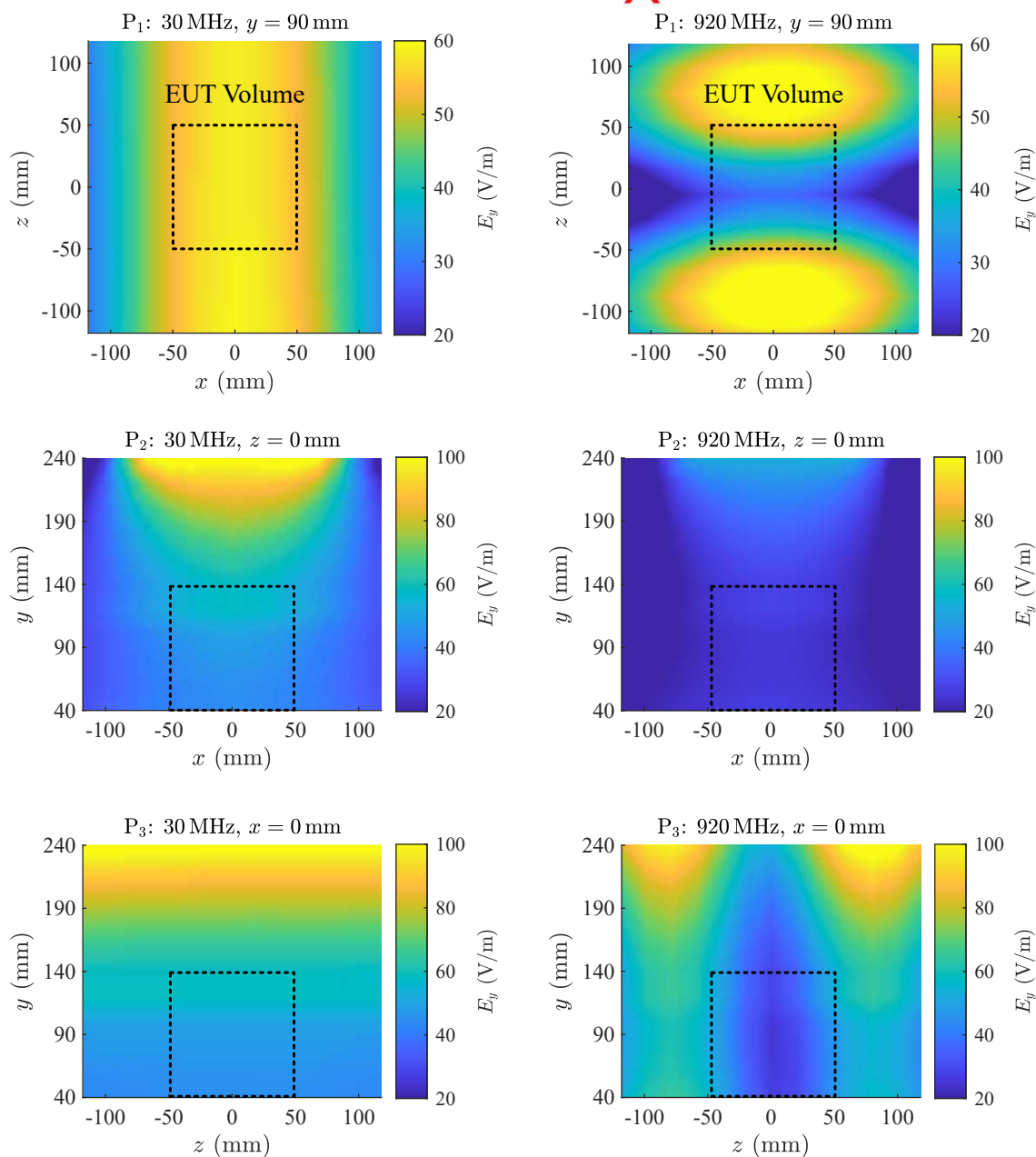
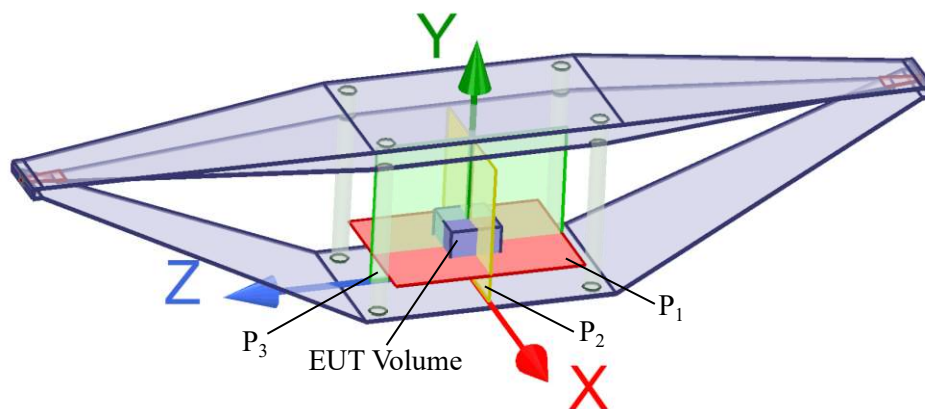


**Fig. 2.6:** Electric field strength  $E_y$  in vertical direction for different cross sections of the TEM cell from [20] (top) at 30 MHz (left) and 920 MHz (right), measured with a field probe.

measurement setup can be found in App. A. With a field probe, the vertical field component, i.e.,  $E_y$ , was measured along the cross sections  $P_1$ ,  $P_2$ , and  $P_3$  for two different frequencies. For the experiment, a continuous wave (CW) signal generator was used to stimulate the TEM cell. It is assumed that a dipole radiator (EUT) excites the same field pattern as an externally applied CW stimulus. In general, reciprocity is violated due to loading the cell, albeit to a negligible extent if the mentioned restrictions are held.

On the left hand side of the graph, the vertical field strength for a stimulus of 30 MHz is visualized. Obviously, the cut planes show a highly homogeneous field pattern in favor with a dominant TEM mode, uniformly covering the cubic UTV with an edge length of 10 cm. On the right hand side, the stimulus frequency is increased to 920 MHz. Some part of the energy couples into higher order modes leading to resonances in the test volume. Usually, it is the  $TE_{10}$  mode which has the lowest cutoff frequency next to the TEM mode. The cell's cross section decreases in size approaching the coaxial connection launcher. Thus, higher order modes are below cutoff at some point and are reflected causing a standing wave pattern. For the investigated frequencies, only the TEM mode is able to propagate in coaxial cables connecting the cell to an EMI receiver. Due to the reduced output power, radiated emission tests are inaccurate at resonant frequencies.

Even if the geometrical dimensions of a waveguide allow for higher order mode propagation, it is not sure that they are excited. Besides the typical excitation sources, e.g., field diffraction at bending edges and finite conductance of the material, EUT cabling is a serious problem. Peripheral connections of an EUT routed outside the TEM cell can cause resonances of high quality factor. Hence, long cables exiting the defined test volume are not allowed in a compliant measurement setup.

## 2.2 Concept Analysis of the EMI Receiver

In general, EMI receivers have a lot in common with classic spectrum analyzers. The main purpose is to perform frequency scans with a narrowband filter over a certain bandwidth. As EMI measurements are strongly involved with the detection of broadband transients, dedicated receivers incorporate specific adjustments in the analog receiver frontend to tackle inherent challenges more efficiently. To guarantee comparability of the measurement results among different instruments, specified filter bandwidths and detectors are used for signal analysis. The measurement accuracy of fully compliant instruments is verified by a black-box approach in accordance to *CISPR 16-1-1*. This test scenario shall represent the characterization of a worst case EUT, confronting the receiver with highly demanding linearity requirements. Goal of this norm is to ensure the unrestricted use, independent of the applied test method or EUT, which is in general not given for a classic spectrum analyzer.

### 2.2.1 Generic Receiver Elements

For describing the most important elements of an EMI receiver, a generic block diagram, depicted in Fig. 2.7, is used. Probably the most important part in the analog signal path is the preselector. As test devices may produce broadband transients with high amplitudes, potentially saturating the mixer, massive preselector filterbanks are used to reduce the bandwidth and thus, the amplitude of occurring impulses. Because of the high number of different frequency bands in EMC testing, the preselector has to cover large bandwidths making professional EMI receivers rather expensive. The filterbank is composed of fixed and tracking bandpass filters having bandwidths from a few kilohertz going up to 200 MHz [41, 42]. To protect the analog frontend from permanent damage through high voltage spikes, commonly, a secondary input foreseen with power limiters is available to safely level the received signal using subsequent attenuators. The

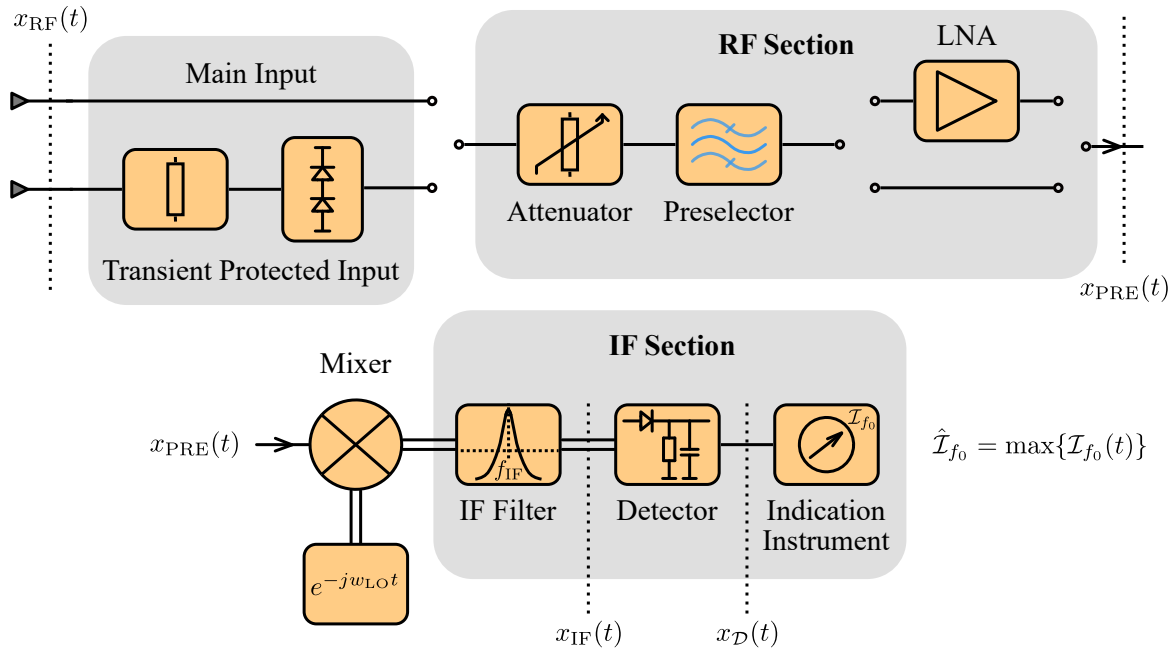


**Fig. 2.7:** Generic block diagram of an EMI receiver in accordance to the analytically derived signal model. Complex signals are indicated by two parallel connection wires.

functional blocks in the analog signal path preceding the LNA introduce a significant path loss, affecting the overall sensitivity. Investigating the noise floor of professional EMI receivers with activated LNA, i.e., Keysight Technologies' *MXE N9038A* and R&S' *ESR26*, an overall noise figure (NF) of 10–15 dB can be expected at the main input, indicating that this design parameter is less critical for such instruments.

To define an analytic signal path model describing the frequency scan and detection processes, the received signal denoted by  $x_{\text{RF}}(t)$  is used for upcoming derivations. After passing the radio frequency (RF) section, the signal reads:

$$x_{\text{PRE}}(t) = x_{\text{RF}}(t) * h_{\text{PRE}}(t). \quad (2.21)$$

In  $h_{\text{PRE}}(t)$ , relevant conversion gains and phase dependencies including the mixer are taken into account. The frequency conversion is modeled with a complex representation of the signal using the Hilbert transform  $\mathcal{H}\{\cdot\}$ . By mixing  $x_{\text{PRE}}(t)$  to the desired intermediate frequency (IF), where the analysis filter  $h_{\text{IF}}(t)$  is centered in complex baseband, gives:

$$\begin{aligned} x_{\text{IF}}(t) &= \frac{1}{2} \{ [x_{\text{PRE}}(t) + j\mathcal{H}\{x_{\text{PRE}}(t)\}] e^{-j2\pi(f_0 - f_{\text{IF}})t} \} * h_{\text{IF}}(t) \\ &= \frac{1}{2} \{ x_{\text{A}}(t) e^{-jw_{\text{LO}}t} \} * h_{\text{IF}}(t). \end{aligned} \quad (2.22)$$

It shall be noted that this approach was chosen as it refers to the simple homodyne receiver architecture which the most low-cost SDRs are based on. For performance critical reasons, traditional EMI receivers, e.g., Keysight Technologies' *MXE N9038B*, utilize several mixer stages (super heterodyne architecture) decreasing the vulnerability against undesired signal leakage and spurious emission. In former times, when the implementation of digital signal processing into hardware was in its infancy, the IF section was realized in the analog domain referring to

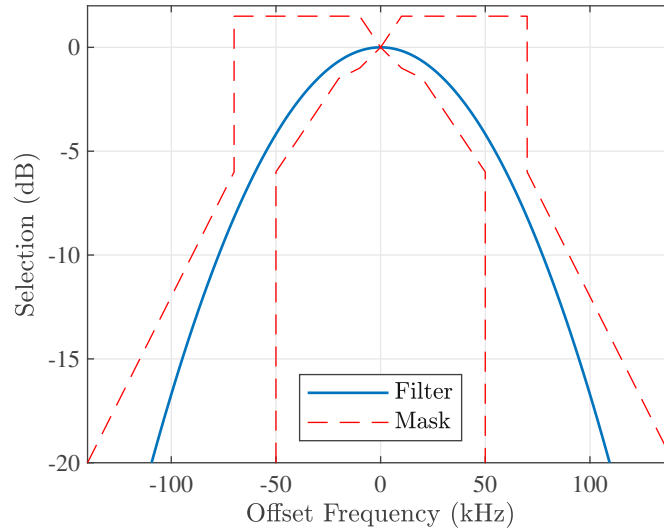


**Fig. 2.8:** IF filter response of (2.24) fulfilling the spectral mask specified in *CISPR 16-1-1*.

a real-valued signal representation. The complex notation is still applicable to such receivers by utilizing the bandpass representation of the IF signal with  $f_{\text{IF}} \neq 0$ . In contrast to swept spectrum analyzers, the receiver is tuned to a frequency of interest  $f_0$  to weight the signal  $x_{\text{IF}}(t)$  over a certain time period. This is also called a stepped sweep, allowing an accurate evaluation of transient signals by parking the local oscillator (LO). As a last step in the depicted receiver chain, the IF signal is passed through the detector  $\mathcal{D}(x(t))$  and the indication instrument  $h_{\mathcal{I}}(t)$ , resulting in the maximum:

$$\hat{\mathcal{I}}_{f_0} = \max\{\mathcal{I}_{f_0}(t)\}, \quad \mathcal{I}_{f_0}(t) = x_{\mathcal{D}}(t) * h_{\mathcal{I}}(t) = \mathcal{D}(x_{\text{IF}}(t)) * h_{\mathcal{I}}(t). \quad (2.23)$$

The IF filter of an EMI receiver must fulfill certain properties specified in *CISPR 16-1-1*. In particular, the bandwidth is defined by a relative selectivity of  $-6$  dB and the frequency response must satisfy a given spectral mask, see Fig. 2.8. For *CISPR* band C/D, the 6-dB bandwidth is  $B_6 = 120$  kHz. Although several characteristic filter types may be used, it is common practice to implement an IF transfer curve of Gaussian shape. The characteristic shape of a Gaussian filter preserves in time and frequency domain. A mathematical description of the impulse response, centered at 0 Hz, may be defined with:

$$h_{\text{IF}}(t) = 2\sqrt[4]{\pi}B_6 \exp(-2\sqrt{\pi}(B_6t)^2) \quad \circ \bullet \quad H_{\text{IF}}(f) = \exp\left(-\sqrt{\frac{\pi^3}{4}}\left(\frac{f}{B_6}\right)^2\right). \quad (2.24)$$

The normalized equivalent noise ( $B_{\text{N}}$ ) and impulse ( $B_{\text{I}}$ ) bandwidths are defined by:

$$B_{\text{N}} = \int_{-\infty}^{\infty} |H_{\text{IF}}(f)|^2 df = 90.3 \text{ kHz}, \quad B_{\text{I}} = \int_{-\infty}^{\infty} |H_{\text{IF}}(f)| df = 127.7 \text{ kHz}. \quad (2.25)$$

These bandwidth definitions are very helpful for RF-link budget calculations which are made in the following chapter. The impulse bandwidth may be used to obtain the peak output power response to an idealized Dirac impulse with voltage spectral density  $v\tau$  by  $P_{\text{I}} = (v\tau B_{\text{I}})^2 / (2Z_0)$ . In relation to thermal noise with a power spectral density of  $N_0$ , DR definitions for transient

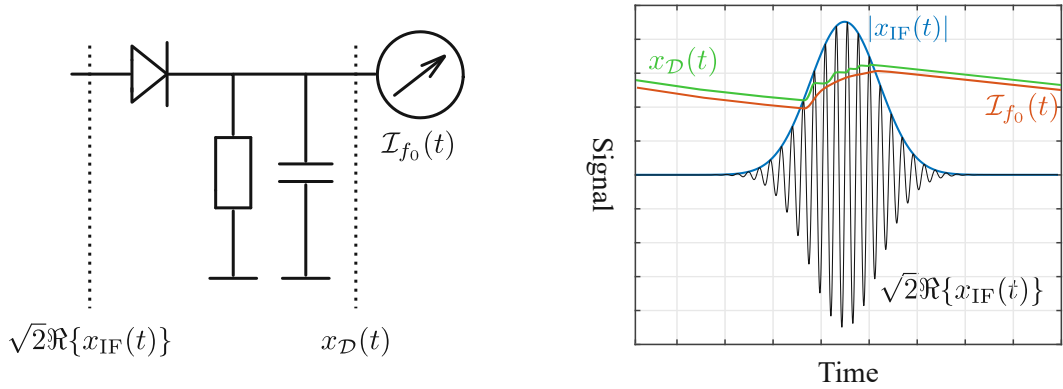


**Fig. 2.9:** Visualization of the direct envelope quasi-peak detector circuit (left) and the transient response (right).

signals can be made by accessing the noise power output of a filter via  $P_N = N_0 B_N$  and using  $DR = P_I/P_N$ .

There are four main detectors which are used for EMI measurements: peak, quasi-peak, average (AV), and AV-RMS. Taking typical radiated emission norms for the target use case of this thesis into account, e.g., *CISPR 32*, the most important detectors in *CISPR* band C/D are the peak and the quasi-peak. At the same time, these two detectors refer to the minimum and worst case requirements for EMI receivers in terms of frontend linearity and signal acquisition. Because of the mentioned aspects, the focus is put on these two detectors throughout this thesis.

The working principle of the peak detector is easily explained as it holds the maximum of  $|x_{IF}(t)|$  over the entire recording time, simplifying  $\hat{\mathcal{I}}_{f_0} = \max\{|x_{IF}(t)|\}$ . In contrast, the intrinsic quasi-peak detector is more sophisticated as it requires to evaluate the bandpass representation  $\sqrt{2}\Re\{x_{IF}(t)\}$  with different charging and discharging time constants, see Fig. 2.9. If the input signal of the detector exceeds the output level, the diode is conducting and charges the circuit with  $\tau_c = 1$  ms. When the input signal falls below the output level, the diode blocks and the circuit is discharging with  $\tau_d = 550$  ms. These time constants refer to a characteristic RC-circuit of first order described by the transfer function  $H_{LPF}(s) = (1 + sRC)^{-1} = (1 + s\tau)^{-1}$ . The step response of  $H_{LPF}(s)$  reaches 63% of the stationary output at  $t = \tau$ . As the bandpass signal of  $x_{IF}(t)$  oscillates with  $|f_{IF}| > 0$  Hz, the charging constant must be modified to achieve the desired effective step response. Eventually, the intrinsic quasi-peak detector can be described with:

$$x_{\mathcal{D}}(t) = \begin{cases} \sqrt{2}\Re\{x_{IF}(t)\} * h_{LPF}(t) & x_{\mathcal{D}}(t) \leq \sqrt{2}\Re\{x_{IF}(t)\} \\ x_{\mathcal{D}}(t_0)e^{-\frac{t-t_0}{\tau_d}} & x_{\mathcal{D}}(t) \stackrel{t=t_0}{>} \sqrt{2}\Re\{x_{IF}(t)\} \end{cases} \quad (2.26)$$

where  $h_{LPF}(t)$  denotes the impulse response of the RC charging circuit and  $t_0$  is the time when the diode starts to block. As this definition performs signal rectification and weighting within one circuit, this realization is called direct envelope quasi-peak detector. An alternative approach is the envelope quasi-peak detector which generates  $|x_{IF}(t)|$  before passing  $\mathcal{D}(x)$ . It is shown in [43] that significant amplitude inaccuracies occur by using the envelope, making compensation techniques necessary. By inserting a second pole in the charging circuit with an inductance in line with the diode, the resulting error is sufficiently reduced. Later in Sec. 2.2.3, it will be shown that the envelope approach has significant advantages when analyzing the signal in discrete

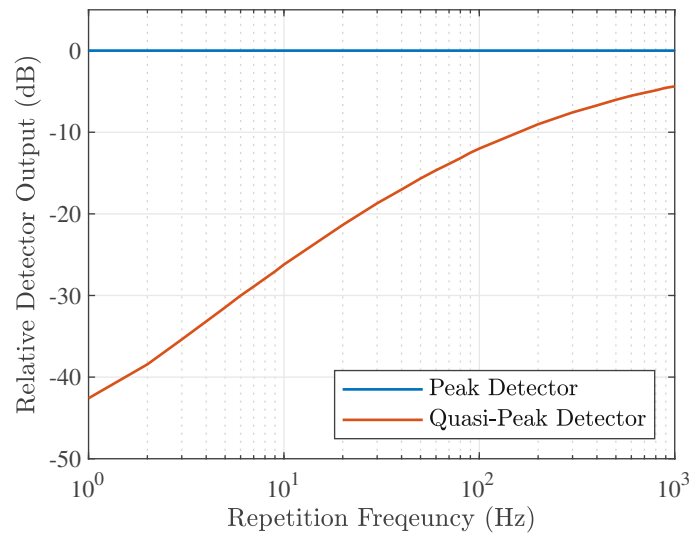


**Fig. 2.10:** Relative detector outputs for recurrent impulses in *CISPR* band C/D.

time domain. In particular, the required computational resources are lower than for the original detector as it is easier to process the signal's envelope than its bandpass representation.

The indication instrument in Fig. 2.9 is a critically damped mechanical meter which can be described by the transfer function of a harmonic oscillator:

$$H_I(s) = \frac{w_0^2}{s^2 + 2\vartheta w_0 s + w_0^2}, \quad (2.27)$$

where  $w_0 = 2\pi/T_M$  and  $T_M = 100$  ms denotes the mechanical time constant of the freely oscillating system. By adjusting the coefficient  $\vartheta$ , the meter gets damped such that the step response has an overshoot above the stationary output of maximum 5%. It is assumed that the detector and the indication instrument are sufficiently decoupled, allowing for this separate analysis.

For constant envelope signals, all mentioned EMI detectors indicate the same power level. The main idea of the quasi-peak detector is to weight recurrent impulses giving seldom events less strength. The response to periodically repeating impulses in comparison to the peak detected value is given in Fig. 2.10. The idealized description (2.26) can be rewritten by a differential equation as well. Unfortunately, the solution for an arbitrary signal is involved with computational expensive approximations. In [44], the response of an idealized direct envelope quasi-peak detector and the indication instrument is investigated using an universal approximation, based on a net charge analysis of the detector circuit. The work elaborates in detail on the response to recurrent impulses and thermal noise. It is shown that the minimum quasi-peak detector output is up to 43.5 dB below the peak power reached for isolated transient events. To ensure linear operation of the receiver within this indication range, the overload factor is defined  $OVF = 43.5$  dB referring to a maximum compression from linear gain of 1 dB for all elements preceding the detector [1].

For thermal noise, it is shown in [44] that the quasi-peak detector amplifies the RMS power level by  $G_N = 5$  dB. Regarding the peak detector, it is theoretically impossible to define a noise gain as the amplitude distribution function may reach infinite values if the observation time is extended sufficiently. However, in [45], it was demonstrated that an average noise gain of  $G_N = 10$  dB is a useful estimate for noise floor comparisons of different EMI detectors.

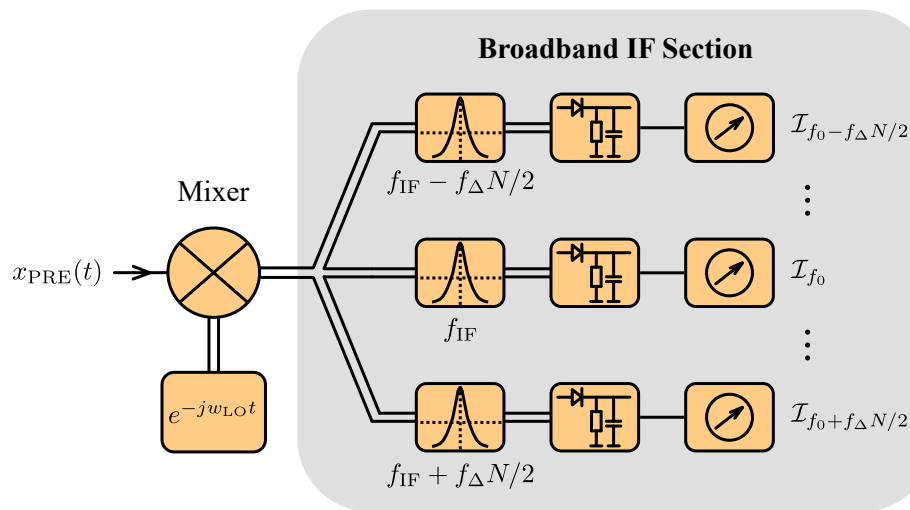


**Fig. 2.11:** Broadband extension of the IF section performing simultaneous signal detection over multiple independent paths.

In some cases, it is necessary to analyze a certain frequency  $f_0$  for several seconds to detect seldom signals in a radiated emission measurement. If the signal's bandwidth extends in addition over a large frequency range as well, it might become a lengthy exercise to investigate all significant frequencies having only a single IF path available. Therefore, it is of high interest to extend the IF section with multiple parallel detection circuits, as depicted in Fig. 2.11. Using this architecture allows to analyze  $N$  frequencies, centered equidistantly with  $\Delta_f$  around  $f_0$ , while the LO is kept parked. The resulting simultaneous signal analysis bandwidth, however, is limited by the preselector filterbank used in the EMI receiver. It will be shown in Sec. 2.2.4 that state-of-the-art receivers utilize advanced analog frontends, getting by without a narrowband preselector, exploiting the benefits of path parallelization even more efficiently.

## 2.2.2 Suitability of Software-Defined Radios

In the current section, the suitability of SDRs as an EMI receiver is analyzed from a system level perspective. State-of-the-art realizations often feature multiple independent inputs and outputs (MIMO). For the sake of simplicity and throughout this thesis, the investigation of one receive path is focused. Within Sec. 2.2.4, advanced EMI receiver frontends making use of multiple receive paths are discussed for inspiring future works on the applicability of MIMO capable SDRs to EMC measurements.

An isolation of a typical receive path architecture and required peripherals is given in Fig. 2.12. Within the RF section, the SDR is tuned to a certain frequency of interest and samples the downconverted signal with an analog-to-digital converter (ADC). In the target price range below 2k€, the analog frontend is usually based on a homodyne topology, besides a few exceptions, achieving sampling rates below 100 MSa/s. To preserve versatility, the analog frontends are typically not equipped with preselector paths or a transient protected input as EMI receivers are. In addition, for the most applications a high sensitivity is desirable which is contradictory referring to classic analyzers, see Sec. 2.2.1. After sampling, the digitized signal is forwarded to further signal processing blocks usually realized in an ASIC/FPGA. Possible functions of this section reach from simple ADC data stream serialization to real-time operations, e.g., calibration routines, automatic gain control, or decimation. Then, the processed samples are sent

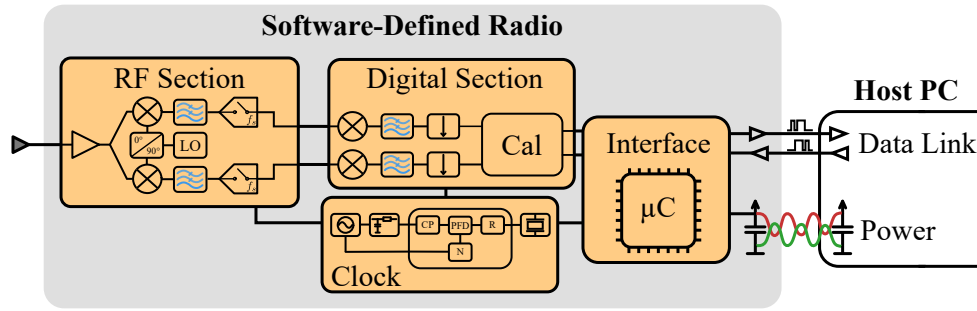


**Fig. 2.12:** Blockdiagram of a generic SDR connected to a host PC.

continuously to the host PC, via a USB or an Ethernet interface, where the data can be saved and modified. The benefit of SDRs is that the measurement data can be pre-processed, saving computational resources of the host, and recordings of arbitrary length can be made as long as sufficient memory is available. For the mentioned sampling rates, the data volume of a standard PC is large enough for typical recording lengths of radiated emission measurements ( $\leq 15$  s).

In the low-cost domain, USB interfaces are used most of the times to provide a data link and a power supply to the SDR at the same time. The maximum available power over one USB port is rather low ( $\sim 2.5$  W). Depending on the application, an external power supply may become necessary to ensure system stability during energy critical tasks.

Obviously, neither the IF section of the generic EMI receiver from Fig. 2.7 is yet implemented in the SDR, nor can this be done in the analog domain. As the downconverted signal is digitized by the ADC, the detection process must be transferred into the discrete time domain, which is done in Sec. 2.2.3. But beforehand, the basic operating principles of a homodyne-based receiver are examined, focusing on necessary configurations utilized in this thesis and performance critical aspects.

### The Homodyne Receiver

The frequency conversion of a homodyne SDR applies to the derived signal path model from (2.23) incorporating one single mixer stage. The complex signal representation is achieved by superposition of two orthogonal paths, named in-phase (I) and quadrature (Q), according to:

$$x_I(t) - jx_Q(t) = \{x_{\text{PRE}}(t)[G_I \cos(w_{\text{LO}}t + \phi_I) - jG_Q \sin(w_{\text{LO}}t + \phi_Q)]\} * h_{\text{AAF}}(t). \quad (2.28)$$

While  $x_{\text{PRE}}(t)$  refers to the signal in front of the mixer stage, the constant factors  $G$  denote the gain of the respective paths from the mixer outputs to the ADC inputs, see Fig. 2.13. The resulting mixing products at  $\pm 2w_{\text{LO}}$  are filtered out by  $h_{\text{AAF}}(t)$  yielding the complex IF signal representation in discrete time domain sampled equidistantly with  $T_s$  ( $x[k] = x(kT_s)$ ):

$$x_{\text{IF}}[k] = x_{\text{BB}}[k] * h_{\text{IF}}[k] = (x_I[k] - jx_Q[k]) * h_{\text{IF}}[k]. \quad (2.29)$$

If the gain and phase parameters of the LO are equal such that  $G_I = G_Q$  and  $\phi_I = \phi_Q$  hold, (2.29) equals the idealized EMI receiver model with one main restriction. Because of the sampling process, the analysis bandwidth of the downconverted signal is limited from  $-f_s/2$  to  $f_s/2$ , where  $f_s = 1/T_s$ . Furthermore, ideal quantization and negligible aliasing effects are assumed. The minimalistic hardware setup and the low-costs bring this receiver a widespread popularity having one major advantage over heterodyne schemes. As image frequencies are suppressed by

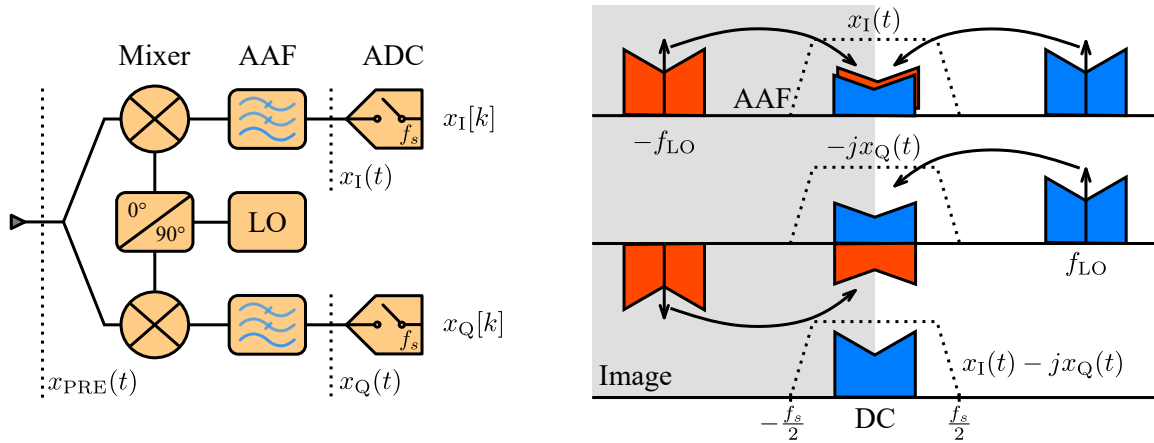


**Fig. 2.13:** Generic description of a homodyne receiver (left) and the downconverted signal represented in frequency domain (right).

superposition of two orthogonal channels, there is no need for an additional mixer stage or image filtering.

### IQ Imbalances

Because of manufacturing process tolerances, the gain and phase parameters of the signal paths I and Q cannot be perfectly matched. This leads to signal distortion through image frequency leakage. Out-of-the-box, the suppression of image frequencies is usually not satisfactory and requires an additional compensation. One possible solution is to calibrate the receive path with a loop-back test [46, 47]. Many SDRs incorporate one or more transmitter sections which can be utilized to generate a certain test stimulus and directly forward it to the receiver. One of the main challenges of this approach is to compensate any imbalances imposed by the stimulus. After estimating the phase offset  $\alpha$  and the gain imbalance  $G$  of the I and Q paths, the sampled data can be corrected by:

$$x'_I[k] = x_I[k] \sec(\alpha) e^{-j\frac{\alpha}{2}} \quad x'_Q[k] = x_Q[k] \sec(\alpha) e^{j\frac{\alpha}{2}} \quad (2.30)$$

$$x''_I[k] = x'_I[k] G'_I = x'_I[k] \frac{G}{2} \quad x''_Q[k] = x'_Q[k] G'_Q = x'_Q[k] \frac{2}{G}. \quad (2.31)$$

The differential offset  $\alpha = \phi_I - \phi_Q$  is applied by a phasor, normalized with  $\sec(\alpha)$ , rotating the in-phase and quadrature components in opposite directions. The gain error is compensated by factorization with the relative difference  $G/2$ . This simple approach neither takes frequency nor linearity dependencies into account. For large IF bandwidths, a worse image frequency suppression must be expected [48]. The anti-aliasing filters (AAFs) may have slightly different cutoff frequencies and thus, especially at the band edges, higher image frequency distortion occurs. Moreover, in case of high DR signals, nonlinearities can further degrade the loop-back calibration due to AM-AM and AM-PM conversion. There are approaches pursuing an adaptive IQ imbalance cancellation to improve the loop-back method [49]. But required information on the implementation in an individual SDR is not always made accessible by manufacturers.

### DC Offset

Homodyne receivers have the advantage that the usable ADC bandwidth extends from  $-f_s/2$  to  $f_s/2$ , being twice as high compared to a similar heterodyne concept. Because of unwanted effects, e.g., self mixing and nonlinearities, a DC component is produced and leads to distortion in

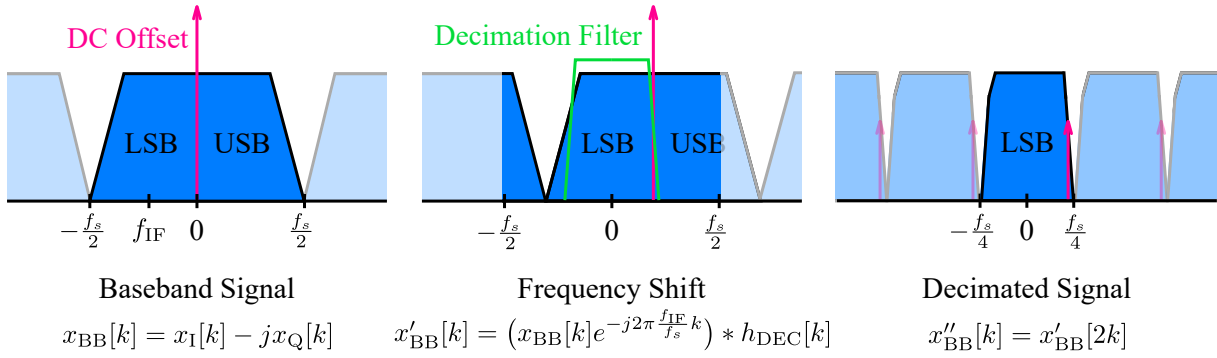


**Fig. 2.14:** Low-IF signal processing procedure in discrete time domain to access the LSB of the sampled signal for  $f_{\text{IF}} = -f_s/4$ .

complex baseband. Mixers have a finite isolation between the RF input and the LO port. Hence, the LO carrier leaks into the receiver output and is reflected due to impedance mismatches of connected equipment. The reflected signal is then downconverted to 0 Hz which is called self mixing. Integrated semiconductor elements, e.g. gain blocks or mixers, are in general nonlinear. A simple analytic system description can be found, e.g., with a Taylor series expansion [50].

$$y(t) = \sum_{i=1}^{\infty} a_i x^i(t) = \underbrace{a_1 x(t)}_{\text{Linear}} + \underbrace{a_2 x^2(t)}_{\text{2nd order}} + \underbrace{a_3 x^3(t)}_{\text{3rd order}} + \dots \quad (2.32)$$

The series is described by the linear term, multiplied by the small signal gain, and higher terms of even (2, 4, ...) and odd (3, 5, ...) order. Usually, the coefficients' magnitude  $|a_i|$  decay with increasing order. Especially the even order terms produce DC components contributing to the self mixing problem. Even if the receiver is operated with a signal of relatively small amplitude, the approximation of (2.32) indicates the generation of nonlinear distortion, changing the DC offset depending on the input signal. A typical compensation technique for a varying DC component is achieved by subtracting a constant offset estimate from the sampled data in discrete time domain [51, 52]:

$$x_{\text{I}}'''[k] = x_{\text{I}}''[k] - \frac{1}{N} \sum_{n=k_0}^{k_0+N} (x_{\text{I}}'' * h_{\text{DC}})[n] \quad x_{\text{Q}}'''[k] = x_{\text{Q}}''[k] - \frac{1}{N} \sum_{n=k_0}^{k_0+N} (x_{\text{Q}}'' * h_{\text{DC}})[n]. \quad (2.33)$$

The DC offset estimate takes place in the sum, representing an averaging window shifted in time if  $k$  elapsed a certain amount of increments. To suppress higher frequency components, the samples are filtered beforehand by the lowpass filter  $h_{\text{DC}}[k]$ . In addition to the described digital compensation, some homodyne receivers make use of analog biasing circuits at certain receiver stages to further decrease the DC component. These routines are often running per default in SDRs and have limited configuration possibilities.

### Low-IF Configuration

Because of the DC offset and the implemented compensation techniques, it is difficult to accurately measure a signal at 0 Hz in complex baseband. Furthermore, the receiver sensitivity degrades for low frequencies as  $1/f$ -noise increases the noise power level significantly. Assuming that IQ imbalances can be calibrated sufficiently, it is thus advisable to use only one sideband of the signal spectrum by setting  $f_{\text{IF}}$  between  $0 \text{ Hz} < |f_{\text{IF}}| < f_s/2$ , also called low-IF configuration.

By decimating the downconverted signal, the usable bandwidth can be processed more efficiently, see Fig. 2.14. This is especially beneficial when multiple detector paths are parallelized as for the broadband IF approach. Firstly, the sampled baseband signal  $x_{\text{BB}}[k]$  is shifted in frequency domain by  $f_{\text{IF}}$  centering the lower sideband (LSB) around 0 Hz. Then, the signal is convolved with a decimation filter  $h_{\text{DEC}}[k]$ , providing half the bandwidth  $f_s/2$ , leading to  $x'_{\text{BB}}[k]$ . After discarding half the samples equidistantly  $x''_{\text{BB}}[k] = x'_{\text{BB}}[2k]$ , only the LSB remains for subsequent detector paths. The spectrum repeats periodically around multiples of the decimated sampling rate, i.e.,  $f_s/2$ , due to periodicity implication in discrete time domain.

While several SDRs provide decimation out-of-the-box, this task can be easily implemented on the host PC as well. Moreover, the sampling rate can be reduced more than it was demonstrated, if the application allows or requires to. In reality, decimation filters and AAFs show a finite decay of their frequency response causing aliasing. Hence, a roll-off factor has to be taken into account decreasing the usable analysis bandwidth of the effective sampling rate.

### 2.2.3 Digital IF Implementation

As SDRs quantize the downconverted signal using an ADC, the entire IF section from Fig. 2.7 must be implemented digitally for signal detection. This has the consequence, that effects coming along with finite time resolutions must be considered. In what follows, the complex baseband signal, derived for a homodyne-based SDR in (2.29), is taken into account for further investigations.

#### Single Frequency Metering

It is started with the basic EMI receiver conducting signal detection using a single IF path. Discretization and normalization of the Gaussian analysis filter from (2.24), which is necessary to access  $x_{\text{IF}}[k]$ , results in:

$$h_{\text{IF}}[k] = \frac{\exp(-2\sqrt{\pi}(B_6/f_s k)^2)}{\sum_{n=-N/2}^{N/2-1} \exp(-2\sqrt{\pi}(B_6/f_s n)^2)} \quad -\frac{N}{2} < k \leq \frac{N}{2} - 1, \quad (2.34)$$

where  $N$  denotes the length of the filter. Subsequent elements in the IF section can be transferred to discrete time domain by simply applying the bi-linear  $z$ -transform. This transformation has the main benefit of preserving system stability, if given in continuous time domain representation. By use of  $s = 2f_s(1 - z^{-1})/(1 + z^{-1})$ , the indication instrument  $H_{\mathcal{I}}(s)$  and the quasi-peak detector's charging circuits  $H_{\text{LPF}}(s)$  are modeled with infinite impulse response (IIR) systems defined by:

$$H(z) = \frac{b_0 + b_1 z^{-1} + \dots + b_{N-1} z^{1-N}}{1 + a_1 z^{-1} + \dots + a_{N-1} z^{1-N}}. \quad (2.35)$$

The coefficients of  $H(z)$  can be directly used for calculating the output signal  $y[k]$  for a given stimulus  $x[k]$  using the difference equation:

$$y[k] = b_0 x[k] + b_1 x[k-1] + \dots + b_{N-1} x[k-N+1] - a_1 y[k-1] - \dots - a_{N-1} y[k-N+1]. \quad (2.36)$$

The signal feedback of  $y[k]$  in IIR filters is an obstacle when implementing them in systems (FPGA/ASIC) with limited amplitude quantization step resolutions. However, this approach is commonly adopted in state-of-the-art EMI receivers and has been tackled successfully in [53].

The impulse response  $h_{\text{IF}}[k]$  is the shortest possible event and requires to sample  $x_{\text{IF}}[k]$  with sufficient time resolution to satisfy a maximum amplitude error of  $\pm 1.5$  dB [1]. As the peak

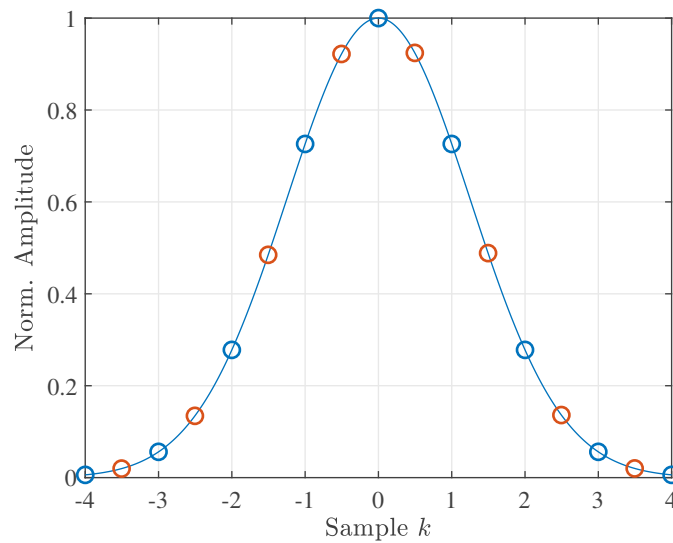


**Fig. 2.15:** Visualization of the amplitude uncertainty problem due to sampling the IF filter's impulse response  $h_{\text{IF}}[k]$  with finite time resolution.

detector evaluates the signal envelope, the worst case amplitude error occurs if the samples are centered symmetrically around the global maximum of  $h_{\text{IF}}[k]$ , see Fig. 2.15. The corresponding measurement uncertainty  $\epsilon_t$  can be calculated by:

$$\max\{\epsilon_t\} = 20 \log_{10} \exp \left( 2\sqrt{\pi} \left( \frac{B_6}{2f_s} \right)^2 \right) \quad (2.37)$$

and holds  $|\epsilon_t| \leq 1.5$  dB for  $f_s \geq 275$  kHz. This derivation also holds true for the envelope quasi-peak detector, including the indication instrument, as the bandwidths of the used circuits are far below the derived sampling rate. For the direct envelope quasi-peak, the IF filter response oscillates with  $|f_{\text{IF}}| > 0$  Hz which requires to increase the sampling rate substantially. As this is involved with a higher computational effort, the direct envelope approach is not implemented in modern receivers.

### Broadband IF Approach

Next, the parallelization of multiple detector paths, as depicted in Fig. 2.11, in time discrete domain is investigated for an improved frequency scan speed. By use of the well known short-time Fourier transform (STFT) based approach, it is possible to implement the convolution of  $x_{\text{BB}}[k]$  with multiple filters  $h_{\text{IF}}[k]$ , centered at different IFs, efficiently and exploit the low-IF bandwidth, provided by the SDR [54].

To explain this technique, an infinitely long sequence of the decimated low-IF signal ( $x_{\text{BB}}[k] = x''_{\text{BB}}[k]$ ) from Fig. 2.14 is assumed. This sequences is multiplied with a window function  $w[k]$ , shifted relative to  $x_{\text{BB}}[k]$  by multiples of  $R$  samples. For each multiplication, the time discrete Fourier transform is computed, defined by the matrix:

$$\underline{X}[m, n] = \sum_{k=-\infty}^{\infty} x_{\text{BB}}[k] w[k - mR] e^{-j \frac{2\pi}{N} nk} \quad (2.38)$$

where  $m$  and  $n$  denote the respective time and frequency indices.

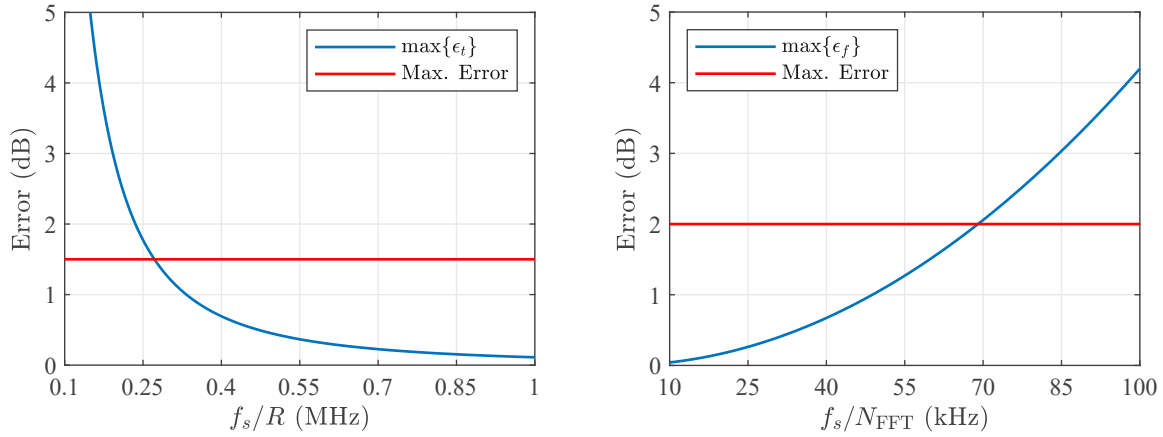


**Fig. 2.16:** Maximum amplitude uncertainty in time domain (left) and frequency domain (right) for the IF filter definition from (2.34) using the STFT-based analysis approach.

A multiplication of the two signals  $x_{\text{BB}}[k]w[k]$  in time domain corresponds to a convolution in frequency domain, similar to the operating principle of a swept spectrum analyzer. Hence, to retrieve the desired frequency response of the IF filter from Fig. 2.8 in the spectrum of  $\underline{X}[m, n]$ ,  $h_{\text{IF}}[k]$  must be used as a window function. Due to the Gaussian shape, signal components located far apart from the local maximum of  $h_{\text{IF}}[k = 0]$  are strongly attenuated. In general, this is no problem for CW signals, but short transient events might get missed if not covered appropriately. To accurately capture the spectrum of impulses, the window must be shifted by  $R$  over the sampled time domain signal such that a certain amount of overlap exists.

As the computation of infinitely long sequences is not possible, (2.38) must be modified. In particular, the arbitrary long time sequence  $x_{\text{BB}}[k]$  is split into consecutive segments, each of length  $N$ , before multiplying it with  $h_{\text{IF}}[k]$ . If  $\log_2 N$  is a positive integer, the spectrum can be computed very efficiently also known as the fast Fourier transform (FFT). For further derivations, the FFT is used with a sequence length denoted by  $N_{\text{FFT}}$ . The analytic description of this procedure can be found in:

$$\begin{aligned} \underline{X}_{\text{IF}}[m, n] &= \mathcal{F}\mathcal{F}\mathcal{T}\{x_{\text{BB}}[k]h_{\text{IF}}[k + mR]\} \\ &= \begin{bmatrix} x_{\text{IF}}[0, -N_{\text{FFT}}/2] & \dots & x_{\text{IF}}[0, N_{\text{FFT}}/2 - 1] \\ x_{\text{IF}}[R, -N_{\text{FFT}}/2] & \dots & x_{\text{IF}}[R, N_{\text{FFT}}/2 - 1] \\ x_{\text{IF}}[2R, -N_{\text{FFT}}/2] & \dots & x_{\text{IF}}[2R, N_{\text{FFT}}/2 - 1] \\ \vdots & \vdots & \vdots \end{bmatrix}. \end{aligned} \quad (2.39)$$

Each of the columns (m) in  $\underline{X}_{\text{IF}}$  stand for a separate IF path running at the effective sampling rate of  $f'_s = f_s/R$ . The frequency bins (n) are separated equidistantly by  $f_s/N$ . Due to the finite time and frequency resolutions, certain operating conditions must hold to fulfill the amplitude errors required by *CISPR 16-1-1*.

The required sampling rate has been already defined and can be directly applied to the current case by introducing  $f_s = f'_s/R$  in (2.37). Due to the finite frequency resolution of the FFT, the measurement of narrowband signals, i.e, CW tones, underlies significant amplitude deviations if not located directly on a bin  $n$ . This problem is also known as the picket-fence effect [55]. Applying (2.39) on a CW gives  $\underline{X}_{\text{IF}}[m, n] = H_{\text{IF}}[n - N_{\text{CW}}]$  which is the frequency response of the window function centered around the tone. Hence, equivalent to the problem depicted in

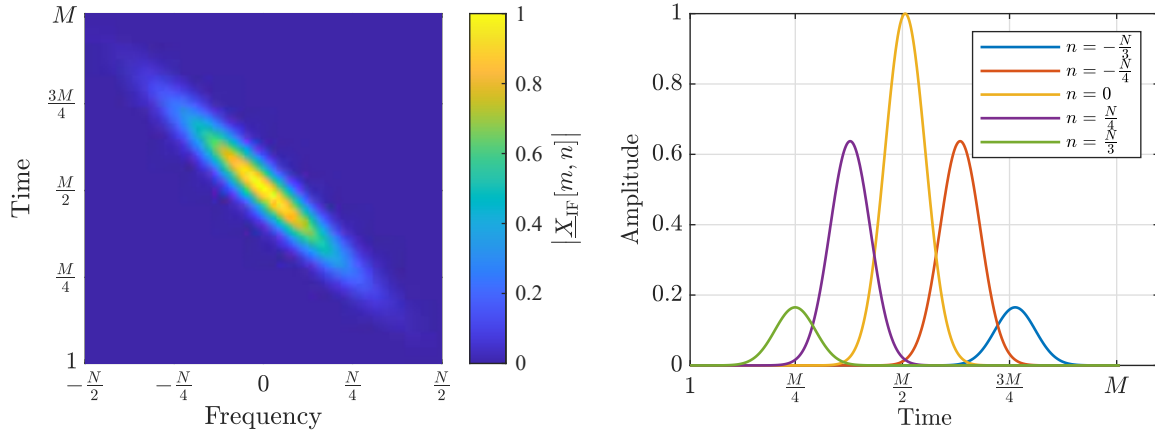


**Fig. 2.17:** Visualization of an impulse amplitude over time and frequency using the STFT-based method (left) and the time domain signal of certain frequency bins (right).

Fig. 2.15, the maximum amplitude error in frequency domain can be calculated by centering the grid of  $n$  symmetrically around the global maximum of  $H_{\text{IF}}[n]$ . The resulting error is given by:

$$\max\{\epsilon_f\} = 20 \log_{10} \exp \left( \sqrt{\frac{\pi^3}{4}} \left( \frac{f_s}{2N_{\text{FFT}}B_6} \right)^2 \right), \quad (2.40)$$

must hold  $|\epsilon_f| \leq 2$  dB, and directly affects the required window length  $N_{\text{FFT}}$ .

The maximum amplitude errors in time and frequency domain for the IF filter definition from (2.34) is evaluated in Fig. 2.16. For fulfilling the mentioned error bounds, the effective sampling rate must not be smaller than 270 kHz and the frequency resolution should be kept well below 70 kHz. In *CISPR 16-2 TR*, this method is reported and given full compliance [56]. Further deviations of this signal analysis approach, such as, spectral leakage, are considered to be negligible if the Gaussian window is used and the mentioned requirements are met [57, 58]. Throughout this thesis, the broadband signal analysis scheme is termed STFT.

Now, a simple example of (2.39) is went through by analyzing a single broadband impulse, see Fig. 2.17. While on the left hand side the evaluation of  $|\underline{X}_{\text{IF}}|$  is shown, the right hand side depicts certain columns of  $\underline{X}_{\text{IF}}$  over time. The resolutions  $f_s/R$  and  $f_s/N_{\text{FFT}}$  are chosen far above the derived amplitude uncertainty requirements and cause a negligible error. It can be clearly seen that each frequency bin represents an IF path according to the continuous time representation from Fig. 2.11. Each FFT bin output is followed by a detector and an indication instrument, implemented with the bi-linear z-transform. As the peak detector simply evaluates the signal envelope, the maximum amplitude is accessed by  $\hat{\mathcal{I}}_{f_0 \pm n\Delta_f} = \max\{|\underline{X}_{\text{IF}}[m, n]|\}$ . Regarding the quasi-peak detector definition from (2.26), the real-valued bandpass representation of  $\underline{X}_{\text{IF}}$  must be derived. This is a cumbersome task as the complex baseband signal must be resampled and shifted in frequency. Furthermore, it was discussed that the IF signal must be highly oversampled to achieve the required detector accuracy. Due to the mentioned aspects, the direct envelope detector is neither used for single frequency metering nor for the STFT-based approach in this thesis.

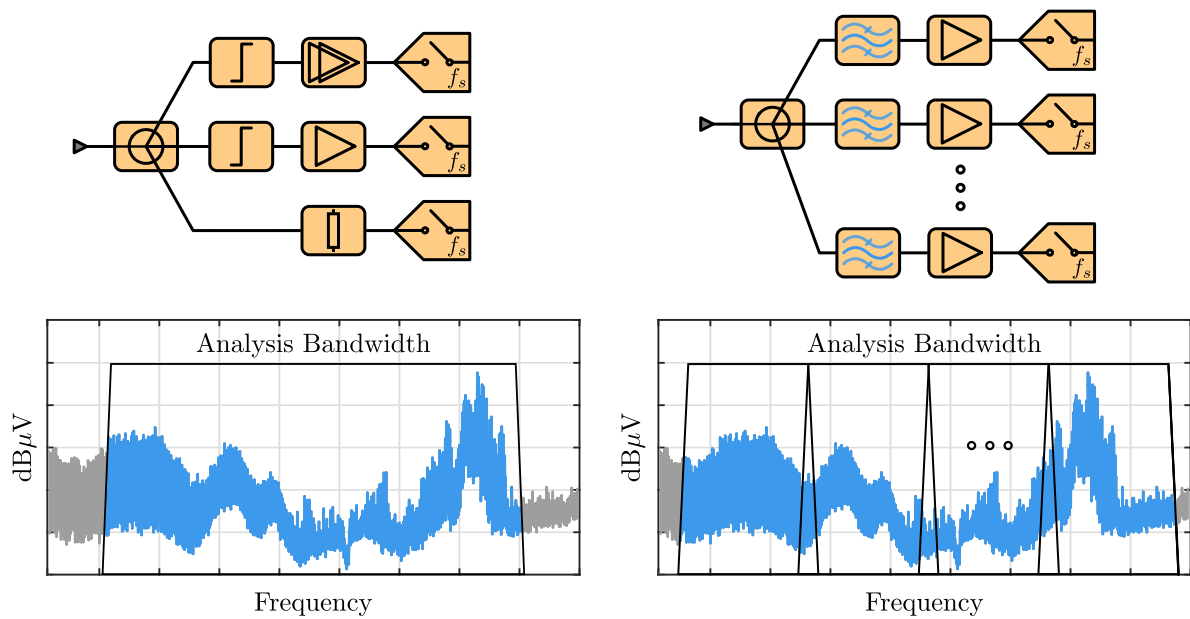


**Fig. 2.18:** Advanced receiver concepts: Gauss Instruments (left) and Rohde & Schwarz (right).

## 2.2.4 Broadband Receiver Frontends

It was discussed in Sec. 2.2.1 that EMI receivers make use of massive preselection filterbanks to avoid saturation of the analog frontend through high amplitude transients. As the preselector limits the bandwidth of the STFT-based signal analysis concept and thus the frequency scan time speed, popular manufacturers developed new receiver concepts providing sufficient linearity over large frequency ranges.

With the availability of giga-sample ADCs, it became possible to sample *CISPR* bands up to 1 GHz directly without the necessity of frequency conversion. The problem of this approach is the limited DR which was at the time of writing this thesis in the range of:

$$\text{DR} = 6.02 \text{ dB} \cdot \text{ENOB} + 1.76 \text{ dB} \cong 48 \text{ dB} \quad (2.41)$$

for an 8-bit ADC. Although, the quantization noise level decreases for the defined IF filter with  $10 \log_{10}(B_N/f_s)$ , not every detector can be operated appropriately. To achieve full compliance, three simultaneously sampling ADCs have been added with a power splitter in [9], according to Fig. 2.18 (left). The receive paths have different gains to increase the overall DR of the samplers. The amplitude ranges of the ADCs are overlapping to ensure that no quantization gap occurs. As the foreseen amplifiers have a limited input power rating, they are protected by RF power limiting diodes. During recovery from high voltage spikes, the overloaded paths are blind and such limiters cause strong signal reflections leading to erroneous measurement results. The recovery time of such protection diodes is up to a few nanoseconds. To reduce inherent path couplings, an unconditionally matched limiter design is used. The initial idea of this frontend was to enable EMI measurements in conjunction with a giga-sample oscilloscope having multiple channels available. Unfortunately, the memory depth of such instruments is rather limited and further signal processing on a host PC is required. Hence, the frontend was equipped with giga-sample ADCs and real-time processing units enabling frequency scan bandwidths of up to 685 MHz [59]. The inventors of this approach raised a company which is known under Gauss Instruments.

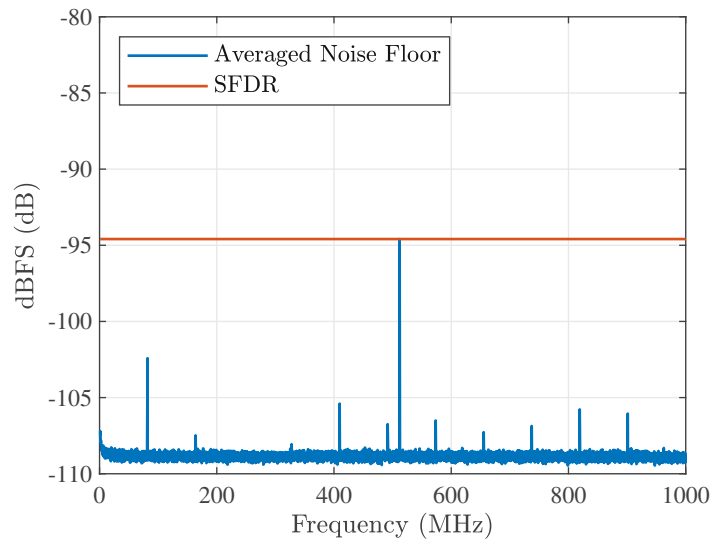


**Fig. 2.19:** Noise floor over frequency of the *RFSoc* at full sampling rate with terminated input. The indicated signals are relative to the full-scale power level (dBFS).

The direct competitor in this market is Rohde & Schwarz. Their newest receiver achieves a frequency scan bandwidth of up to 970 MHz, which is the total *CISPR* band C/D, by parallelization of up to eight ADCs having separate preselectors, see Fig. 2.18 (right) [60]. Details on the suppression of out-of-band reflections caused by the preselector paths are not available and therefore sketched by a power splitter.

Just as classic super heterodyne receivers, both presented topologies incorporate an additional mixer-based frontend to cover frequencies above 1 GHz. While legacy analyzers, e.g., Keysight Technologies' *MXE N9038B*, achieve DRs for broadband impulses of up to 55 dB in the IF section, the new concepts promise numbers of up to 100 dB.

In comparison, low-cost homodyne SDRs achieve sampling rates of up to 100 MSa/s. Even though several receiver inputs are often available, it is rather unusual that they can be tuned independently. Hence, an increase of the analysis bandwidth with multiple inputs tuned to different frequencies is not accessible using a single device. Even if the limited analysis bandwidth has to be accepted, a potentially successful strategy to increase the DR of a low-cost SDR can be found by the approach from Gauss Instruments. As this technique requires application specific RF power limiters, additional effort in signal processing, and calibrations, a careful benefits vs. costs analysis must be made taking other solutions into account.

A promising alternative to tackle broadband EMI measurements is the *RFSoc* from Xilinx featuring four independent RF ADCs with sampling rates of up to 4096 MSa/s at a resolution of 12 bit [61]. This high performance is achieved by cascading several time-interleaved 12-bit ADCs. The main drawback of this architecture is that interleaving spurs due to mismatches of the cascaded samplers limit the spurious free dynamic range (SFDR). Because of slightly different transfer characteristics, coupling effects, or imperfect synchronization in time domain, spurs appear in the spectrum at multiples and fractions of the sampling rate of a single ADC. To visualize these effects, the noise floor of a single receive path, terminated with a  $50\ \Omega$  load, has been measured by the author and depicted in Fig. 2.19. As the budget for a development board incorporating the *RFSoc* lies far above the target price range of 300 €–2 k€, further investigations are not carried out in this thesis.

---

# SDR Performance Evaluation

---

Goal of this chapter is to investigate the out-of-the-box performance of SDRs as an EMI receiver in *CISPR* band C/D. The research on this topic is introduced by analyzing available devices from a system level perspective. For delimiting potentially suitable SDRs, certain receiver requirements are derived in accordance to relevant norms and brought into context with common datasheet specifications.

Based on the gained knowledge, an SDR is chosen for a rigorous analysis performing standardized testing procedures. For the verification, TEM cells are taken into account as target pre-compliance test method. Compliance of the chosen device is analyzed out-of-the-box aiming to identify performance limitations regarding the peak and quasi-peak detectors. With the empirical results, further performance improvements shall be initiated and worked out in this thesis.

A summary of the following content has been presented to the public in [28] © 2022 IEEE and [29]. Revised text passages and graphs have been directly adopted from these publications.

### 3.1 SDR Selection

The high interest in universally applicable receivers emerged a large variety of different SDRs. The most relevant and popular examples have been listed in ascending order with respect to their budget in Tab. 3.1. It can be directly observed that specifications scale with costs considering, e.g., the receiver topology, sampling/streaming rates, or ADC resolutions. It is to be noted that the AAF bandwidth definition refers to complex baseband representation. Due to low-IF configuration, the usable AAF bandwidth reduces by half for homodyne-based receivers, see Sec. 2.2.2. Henceforth, these bandwidths are defined in single sideband notation.

Starting from the left hand side with the USB dongle Airspy *Mini*, the entry-level of low-cost devices is represented having remarkable features, e.g., a 12-bit ADC and a streaming bandwidth to the host PC of up to 10 MSa/s. For approximately twice the budget, the *HackRF One* and the *LimeSDR* are available. Similar to the latter device, the *USRP B200mini* is based on a single transceiver chip which is used in many other SDRs as well, e.g., Analog Devices *PlutoSDR* or Nuand *bladeRF micro 2.0*. Although these SDRs have the same RF hardware implemented, they are differing in the number of signal in-/outputs, data post processing capabilities, and manufacturers' support. For instance, the *bladeRF micro 2.0* provides the same analog frontend as the *USRP B200mini* but incorporates a different RF chip version foreseen with an additional receive and transmit path, delivering the same MIMO capabilities as the *LimeSDR*. Due to worse customer and software support, the *bladeRF micro 2.0* is much cheaper starting from about 500 €, though, more signal streams can be covered. Hence, SDRs with the same performance

**Tab. 3.1:** Popular SDRs of different budget and capabilities. The specifications for the *USRP X310* is given in conjunction with a single frontend, i.e., the *TwinRX*. AAF bandwidth definition refers to complex baseband taking both sidebands into account.

SDR	<i>Mini</i>	<i>HackRF One</i>	<i>LimeSDR</i>	<i>USRP B200mini</i>	<i>USRP X310</i>
<b>Company</b>	Airspy	Great Scott Gadgets	Lime Microsystems	Ettus Research	Ettus Research
<b>Topology</b>	Homodyne 1 RX	Heterodyne 1 RX & 1 TX Simplex	Homodyne 2 RX & 2 TX Full Duplex	Homodyne 1 RX & 1 TX Full Duplex	Super Heterodyne up to 4 RX
$f_{LO}$	24 MHz to 1.7 GHz	1 MHz to 6 GHz	100 kHz to 3.8 GHz	52 MHz to 6 GHz	10 MHz to 6 GHz
$f_s$	20 MSa/s	20 MSa/s	160 MSa/s	61.44 MSa/s	200 MSa/s
<b>AAF Bandwidth</b>	8 MHz	20 MHz	75 MHz	56 MHz	80 MHz
<b>ADC Resolution</b>	12 bit	8 bit	12 bit	12 bit	14 bit
<b>ENOB</b>	9 bit	7 bit	9 bit	n.a.	11 bit
<b>Clock Accuracy</b>	0.5 ppm	20 ppm	1 ppm	1 ppm	2.5 ppm
<b>Interface</b>	USB 2	USB 2	USB 3	USB 3	1G/10G Eth.
<b>Streaming Bandwidth</b>	10 MSa/s	20 MSa/s	61.44 MSa/s	61.44 MSa/s	25 MSa/s (1G) 200 MSa/s(10G)
<b>Budget</b>	180 €	370 €	450 €	1,200 €	11,000 €

as the *USRP B200mini* are in the budget range of the *LimeSDR*. One major advantage of the single transceiver chip based SDRs over the *HackRF One* is that they are already equipped with real-time processing units (FPGAs) allowing on-the-fly operations on the sampled data before streaming it to the host. The last example is the *USRP X310* having a modular concept that allows to utilize up to four different receiver frontends (boards). By use of two 10G Ethernet interfaces, high data rates can be streamed simultaneously to the host PC. As the budget for this SDR in conjunction with one *TwinRX* board is already around 11 k€, this category stands for high-performance equipment and is thus not further investigated in this thesis.

It is rather uncommon that precise RF performance measurements regarding the matching, image-rejection, or linearity are made available by manufacturers. When it comes to choose an SDR for a certain application, the mentioned performance parameters are often limited to those given in Tab. 3.1. Hence, it is very important to break down the receiver requirements into such generic parameters.

Goal of the current section is to investigate the suitability of the mentioned SDRs as an EMI receiver according to the golden standard for fully-compliant equipment, i.e., *CISPR 16-1-1*, using rudimentary datasheet specifications. In particular, it is elaborated on the requirements regarding LO specific parameters, i.e, tuning range, frequency accuracy, and stability. Afterwards, the most critical test cases for EMI receivers are analyzed and brought into context with different analog frontend concepts and potential performance limitations. After carefully weighting the advantages and disadvantage of the mentioned receivers, one SDR is chosen for a detailed analysis.

### 3.1.1 Tuning Range and Accuracy

As *CISPR* band C/D is the target frequency range in this work, the SDR must be tunable such that this frequency range  $30 \text{ MHz} \leq f_0 \leq 1 \text{ GHz}$  can be investigated yielding  $\hat{\mathcal{I}}_{f_0}$  with the desired detector. The frequency conversion of the generic EMI receiver is described in (2.22) with a complex phasor using  $x_{\text{LO}}(t) = \exp(-j\omega_{\text{LO}}t) = \exp(-j2\pi(f_0 - f_{\text{IF}})t)$ . Thus,  $f_{\text{IF}}$  must be chosen such that with  $f_{\text{LO}}$  the entire *CISPR* band C/D is covered. The IF may be varied within the usable bandwidth of the upper or lower sideband in low-IF configuration, limited by the AAF, see Fig. 2.13. In addition, the absolute frequency accuracy of  $f_0$  must be  $\epsilon_{f_0} = \pm 2\%$  [1]. Even though, the clock precisions of the listed SDRs from Tab. 3.1 show far better numbers, the frequency step resolution of the utilized LOs may have a significant impact on the overall frequency accuracy. All of the listed devices utilize fractional phase-locked loops (PLLs) achieving a frequency resolution of the LO below 1 MHz. As this maximum offset fits well into their AAF bandwidths, this error can be compensated by shifting the sampled complex baseband signal in frequency domain. As in *CISPR 16-1-1* no further requirements on the receiver phase noise are specified, it can be concluded that the mentioned SDRs can be tuned with sufficient accuracy over the entire *CISPR* band C/D. If the frequency offset is compensated digitally, the limited LO step resolution is a minor problem. To terminate the discourse on tuning range and frequency accuracy requirements, it is to be noted that the lower bands *CISPR* band A and B are also accessible with most of the listed SDRs. As *CISPR* band E extends from 1 GHz to 18 GHz, this frequency range is inaccessible and remains reserved for professional receivers so far.

### 3.1.2 Test Signal Considerations

In principal, *CISPR 16-1-1* specifies two signals to verify compliance of an EMI receiver. These are: a CW tone and a broadband impulse with an extremely large bandwidth of more than 1 GHz. With the tone, the receiver is investigated in terms of distortion through undesired effects, e.g., image frequency leakage or intermodulation products. To verify this, the receiver is tuned to a certain frequency  $f_0$  for measuring a single tone  $x_{\text{RF}}(t) = \cos(2\pi f_0 t)$ . Then, the tone is set to different frequency spots of interest  $f_{\text{RF}} \neq f_0$  with equal amplitude to determine if the relative suppression  $s$  is larger than or equal to 40 dBc:

$$s = 20 \log_{10} \frac{\hat{\mathcal{I}}_{f_0|f_{\text{RF}}=f_0}}{\hat{\mathcal{I}}_{f_0|f_{\text{RF}} \neq f_0}} \geq 40 \text{ dBc}. \quad (3.1)$$

This test must be fulfilled for each detector. The analog receiver frontend usually provides sufficient DR to exploit the full-scale amplitude range of the ADC if measuring narrowband signals. Hence, the sampler is the subject of investigation to crosscheck if the suppression from (3.1) can be measured. A simplified approach to estimate the available DR for a CW signal is to assume that the quantization noise is white as it was done in (2.41), see Sec. 2.2.4. Because of the flat spectral density and uncorrelatedness, the quantization noise power level decreases after applying the *CISPR* compliant IF filter with:

$$\text{DR}_{\text{CW}} = 6.02 \text{ dB} \cdot \text{ENOB} + 1.76 \text{ dB} + 10 \log_{10} \frac{f_s}{B_{\text{N}}^{\text{CISPR}}}. \quad (3.2)$$

Through the detector dependent noise gain, the calculated DR further reduces by  $G_{\text{N}}^{\text{PD}} = 10 \text{ dB}$  for the peak detector and by  $G_{\text{N}}^{\text{QPD}} = 5 \text{ dB}$  for the quasi-peak detector. Thus, the maximum required DR to verify the CW requirements is up to 50 dB. In Fig. 3.1, (3.2) is evaluated for different effective number of bits (ENOBs). Obviously, the desired 50 dB are already possible to

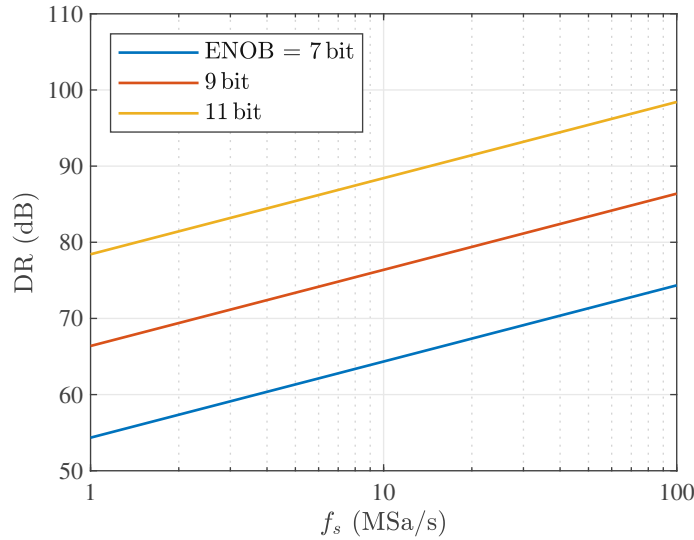


**Fig. 3.1:** Available DR using an idealized ADC for measuring a single CW tone.

measure with an ADC having an ENOB of 7 bit and a minimum sampling rate of 1 MSa/s which is no problem for the SDRs listed in Tab. 3.1. It shall be emphasized that the available DR of ADCs may degrade due to spurious emission. Especially for signal levels which are relatively low compared to the full-scale swing, nonlinear distortions have to be expected. This problem becomes less significant for ADCs with a high resolution [62]. However, the behavior of such distortion effects is highly individual depending on the implemented sampling technique and complexity. The analytical modeling of these effects for state-of-the-art ADCs is involved with a great effort and even with a detailed knowledge on the realization, the support of simulations is inevitable [63, 64]. Due to the mentioned aspects, the simplified analytical performance estimations are supported with empirical characterizations later in this chapter.

By use of the impulse bandwidth, introduced in Sec. 2.2.1, it is possible to estimate the available DR for transient signals. To do so, (3.2) is extended accordingly:

$$\text{DR}_I = 6.02 \text{ dB} \cdot \text{ENOB} + 1.76 \text{ dB} + 20 \log_{10} \left( \sqrt{\frac{f_s}{B_N^{\text{CISPR}}} \frac{B_I^{\text{CISPR}}}{2B_I^{\text{AAF}}}} \right). \quad (3.3)$$

The impulse bandwidth of the AAF in front of the ADCs depends on the filter characteristic and order. In the *HackRF One*, *LimeSDR*, and *USRP B200mini*, Butterworth filters of third order are implemented which are linked to  $B_I = 1.35B_3$  where  $B_3$  denotes the traditional 3-dB bandwidth definition. Furthermore, their AAFs are variable in bandwidth allowing to suppress strong in-band interference. For the remaining SDRs, i.e., *Airspy Mini* and *USRP X310*, the AAF characteristic is not mentioned and is assumed in further calculations to be a Butterworth filter of third order as well. In Fig. 3.2, (3.3) is evaluated over the ratio between sampling rate and AAF bandwidth. As the AAF filters are static for the *Mini* and *USRP X310*, the available DR is concentrated on a single point at maximum sampling rate. For the other SDRs with tunable filters, the achieved DR increases, the higher the oversampling ratio gets. The trace for the *USRP B200mini* also represents the *LimeSDR* as these two receivers have quite similar ADC performance numbers. Obviously, the medium budget devices strongly benefit from a higher DR in comparison to the high-performance category by decreasing the AAF bandwidth. To ensure

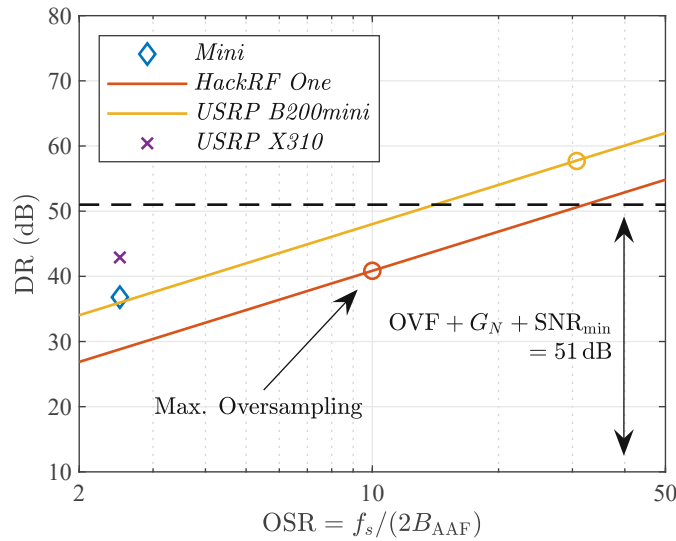


**Fig. 3.2:** Available DR using an idealized ADC for measuring broadband impulses.

that the AAF's frequency response has a negligible effect on the IF filter, the 3-dB bandwidth shall not be smaller than  $B_{AAF} \geq 8B_6^{CISPR} \cong 1$  MHz. Hence, the maximum oversampling ratio  $OSR = f_s / (2B_{AAF})$  is achieved for the *HackRF One* at  $OSR = 10$  and at  $OSR = 30.72$  for the *USRP B200mini* and the *LimeSDR*. In Sec. 2.2.1, it was discussed that the quasi-peak detector has a weighting range equal with the overload factor (OVF) of 43.5 dB. This definition can be directly translated into the necessary DR: The minimum readout for the quasi-peak detector is reached for isolated transients. The maximum measurement uncertainty in this case is  $\pm 2$  dB, which requires a minimum SNR of 2.5 dB. Hence, the necessary DR for compliant quasi-peak detection results in the superposition of  $OVF + G_N + SNR_{min} = 51$  dB. It can be directly seen in Fig. 3.2 that only the *LimeSDR* or the *USRP B200mini* are presumably capable enough to achieve this value. As a consequence of variable AAFs, this kind of SDRs fit best this OVF requirement considering the analytical investigations. Regarding the peak detector, the OVF must be slightly larger than one, strongly reducing the needed DR. The minimum SNR, however, must be high enough to safely detect a system overload. By increasing the receiver's input attenuation from A to B dB, the readings must hold:

$$20 \log_{10} \frac{\hat{I}_{f_0|B \text{ dB}}}{\hat{I}_{f_0|A \text{ dB}}} \leq (A - B) \text{ dB} \pm 0.5 \text{ dB}. \quad (3.4)$$

In Fig. 3.3, the expected amplitude deviation for a signal with  $|x_{IF}(t)| = \text{const.}$  superposed with Rayleigh distributed noise is evaluated. Taking 68% of the possible noise amplitudes centered around the signal's mean into account, i.e., denoted with the  $\sigma$ -trace, a minimum DR of 20 dB is required to hold (3.4) using an attenuation difference of  $B - A = 6$  dB. As the amplitude deviation requirement is still fulfilled for the  $3\sigma$ -trace with a 3-dB attenuator, a DR of 20 dB is assumed to be satisfactory for peak detector measurements which is possible for all of the investigated SDRs.

While for CW signals it was assumed that the analog receiver frontend preserves sufficient DR to make use of the ADCs' full-scale resolution, this premise does not hold for broadband transients. In particular, the utilized impulses to verify compliance of an EMI receiver are

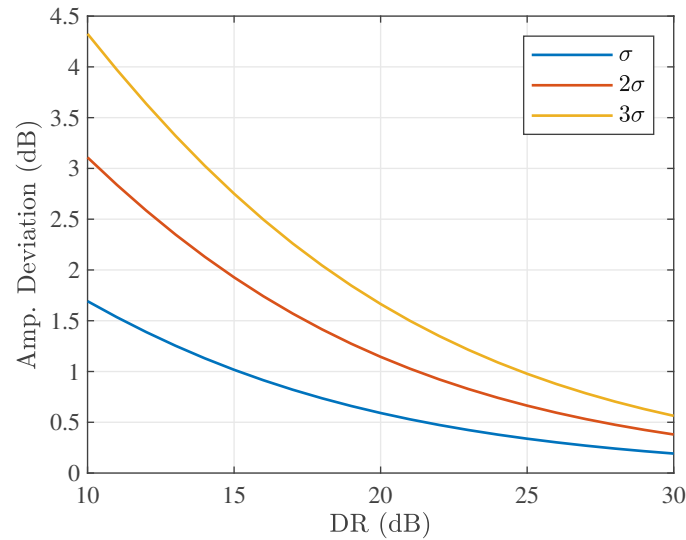


**Fig. 3.3:** Estimated measurement uncertainty using the peak detector for different standard deviation ( $\sigma$ ) intervals of thermal noise.

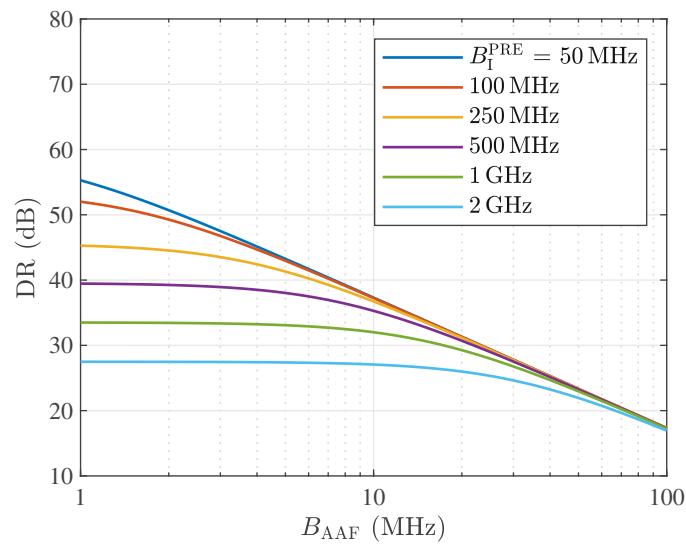


**Fig. 3.4:** Broadband DR limitations of a typical analog frontend incorporated in an SDR for different preselector bandwidths.

generated with pulse forming networks achieving amplitudes of up to 73 V over a time of 300 ps. Due to these extremely short events, the impulse has a flat power spectral density in frequency domain far beyond 1 GHz. This means that the analog receiver frontend is exposed to much higher peak power levels at the broadband RF input than the ADC which is limited in bandwidth by the AAF. As the datasheets of the implemented transceiver chips from the *LimeSDR* or *USRP B200mini* are lacking of information regarding their compression levels, the maximum input power rating  $P_{\max}$  and the full-scale power level of the ADC  $P_{\text{FS}}$  are utilized for further investigations. In general, SDRs have a configurable gain which is distributed over several stages in the receiver chain. To use full-scale resolution of the ADC at constant input power, the overall gain can be calculated by:

$$G = P_{\text{FS}} - P_{\max} + 20 \log_{10} \frac{B_{\text{I}}^{\text{PRE}}}{B_{\text{I}}^{\text{AAF}}}, \quad (3.5)$$

where  $B_{\text{I}}^{\text{PRE}}$  denotes the impulse bandwidth of the preselector at the RF input. The total noise power of the system can be modeled as a superposition of a thermal and quantization caused component using:

$$P_{\text{N}} = 10 \log_{10} \left[ \left( \frac{\Delta^2}{12Z_0} + G \frac{kT_0}{2} \text{NF} \right) B_{\text{N}}^{\text{CISPR}} \right]. \quad (3.6)$$

The quantization noise is defined by the least significant bit voltage of the ADC via  $\Delta = \sqrt{8Z_0 P_{\text{FS}}}/2^{\text{ENOB}}$ . In combination with the NF of the receiver frontend, the available DR in dependence of the preselector and the AAF bandwidth can be accessed:

$$\text{DR}_{\text{I}} = P_{\text{FS}} + 20 \log_{10} \left( \frac{B_{\text{I}}^{\text{CISPR}}}{2B_{\text{I}}^{\text{AAF}}} \right) - P_{\text{N}}. \quad (3.7)$$

To demonstrate the theoretically achievable DR of such an analog receiver frontend, (3.7) is evaluated for:  $P_{\max} = 0$  dBm,  $P_{\text{FS}} = 4$  dBm,  $\text{NF} = 10$  dB,  $f_s = 61.44$  MSa/s and  $\text{ENOB} = 9$  bit, which are typical values for the SDRs *LimeSDR* or *USRP B200mini* [51, 65]. In Fig. 3.4, it is shown that the preselector bandwidth must be drastically reduced to achieve the desired DR of 51 dB for the quasi-peak detector. The depicted results indeed justify the use of massive preselector filterbanks in EMI receiver frontends, discussed in Sec. 2.2.1. Furthermore, it is shown that especially for large input bandwidths, it is useless to further reduce the AAF bandwidth at a certain point as the analog frontend is in saturation otherwise. This behavior is essentially important to evaluate the maximum achievable DR versus analysis bandwidth for finding the optimum operating conditions when using the STFT-based analysis scheme. As the DR requirement of 20 dB for the use of the peak detector is easily achieved, broadband signal detection is presumably possible using the *LimeSDR* or the *USRP B200mini*. Evaluating (3.7) for the other SDRs from Tab. 3.1 indicates their applicability to peak detector measurements as well.

### 3.1.3 Decision for the *USRP B200mini*

Because of the benefits coming along with variable AAFs, the focus in this thesis is put on SDRs supporting this feature, i.e., *HackRF One*, *LimeSDR*, and *USRP B200mini*. Especially promising are the *LimeSDR* and the *USRP B200mini* as they are potentially capable to achieve the DR requirements for quasi-peak detector measurements. Both SDRs are based on single chip receivers, further denoted by RFIC, enabling a simple integration into other systems. While the *LimeSDR* is based on the RFIC *LMS7002M* from Lime Microsystems, the *USRP B200mini*

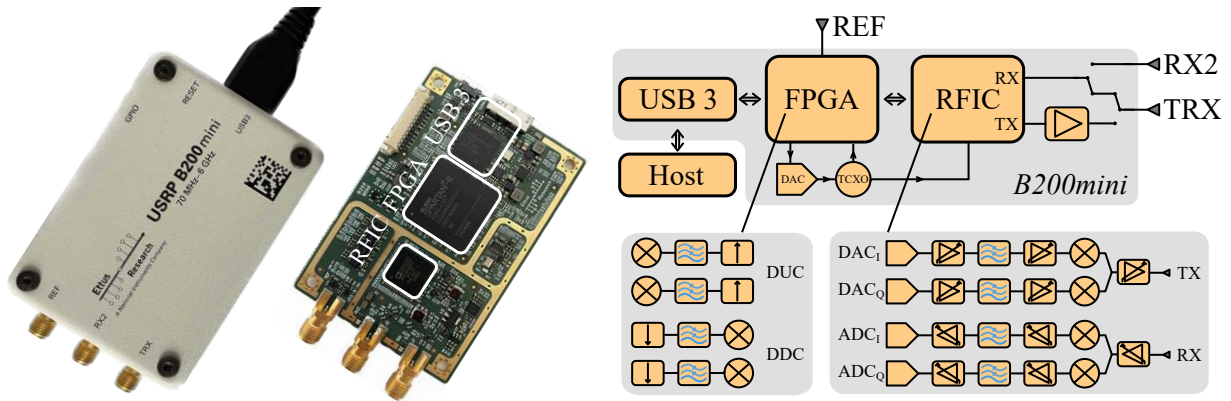


**Fig. 3.5:** Visualization of the *USRP B200mini* with enclosure (left), unboxed (middle), and a blockdiagram describing the main functionalities (right).

incorporates the RFIC *AD9364* from Analog Devices. Currently, Analog Devices and Lime Microsystems are the most relevant competitors in this segment. During corona crisis an immense backlog in chip production forced the company Lime Microsystems to discontinue the *LimeSDR*. Even so, a lot of manufacturers, e.g., Nuand, moved away from the RFIC *LMS7002M* before the pandemic already and utilized the RFIC series *AD936x* from Analog Devices instead. Because of the relatively low available DR provided by the 8-bit ADC in the *HackRF One* and the precarious availability of the *LimeSDR*, it was decided to rigorously investigate the capabilities of the *USRP B200mini* as an EMI receiver.

The *USRP B200mini*, see Fig. 3.5, incorporates the RFIC *AD9364* from Analog Devices featuring full duplex operation using a single receive and transmit path which can be tuned independently. Either the receive or the transmit path can be routed to the *TRX* port via two semiconductor switches. In duplex mode, the receiver is accessed via *RX2* and the transmitter via *TRX*. To increase the transmit power, an additional gain block is foreseen, enabling levels in the range of 10 dBm [66]. Both paths are purely homodyne with three configurable gain stages and Butterworth AAFs of third order tunable between 0.75 MHz–56 MHz<sup>1</sup>. Analog to digital conversion and vice-versa is performed with 12-bit continuous time delta-sigma samplers of third order. The RFIC *AD9364* is connected to an FPGA featuring a digital down (DDC) and upconversion (DUC) unit for the receive and transmit path respectively. In the next block, the digital data is exchanged over a USB 3 interface allowing a total streaming rate between the host and the SDR of up to 61.44 MSa/s. It is possible to connect peripherals to the SDR via a high speed GPIO port. Additionally, the *USRP B200mini* can be synchronized to an external 10 MHz or a pulse-per-second reference. This feature is essential for measurements in conjunction with additional equipment.

Although the focus in this thesis is put on the receiver side of the *USRP B200mini*, the available transmit path allows to generate complex modulations and thus, also an amplitude modulation of a single tone. The latter aspect is needed for radiated immunity tests where the EUT is exposed to a modulated electric field. As for TEM cells rather low power levels are required to achieve field strengths which are commonly in the range of 3–10 V/m, the *USRP B200mini* potentially offers a complete concept for EMC pre-compliance purposes.

<sup>1</sup>If applying the low-IF configuration from Sec. 2.2.2 for avoiding the characteristic DC offset of homodyne receivers, the available AAF bandwidth defined in complex baseband reduces by half.

Besides highly versatile analog hardware provided by the RFIC *AD9364*, the FPGA's DDC/DUC units may be extended with customized applications. Due to real-time operation, it would be of great use to implement the STFT-based signal processing scheme from Sec. 2.2.3 for saving computational resources and data storage.

In conclusion, the *USRP B200mini* represents currently for state-of-the-art SDRs with homodyne transceiver topology featuring the desired variable AAFs. Not merely, the presumably sufficient DR available for quasi-peak detector measurements are highly beneficial for the application as an EMI receiver, also the foreseen FPGA makes this kind of SDR to an interesting subject for research on embedding real-time signal processing.

## 3.2 Continuous Wave Analysis

It was discussed that compliant receivers have to fulfill one main requirement for CW signals. The suppression of unwanted signal components interfering at the IF through, e.g., any kind of leakage or intermodulation, must be at least 40 dBc, see (3.1). Hence, it is to investigate if the *USRP B200mini* provides sufficient performance in terms of DR and spurious emission to verify this requirement. To do so, the SDR is tuned to a certain frequency measuring a CW tone which is swept over power until full-scale resolution of the ADC is reached. The available DR is accessed by comparing the measured noise power to the CW level using the RMS detector:

$$\hat{\mathcal{I}}_{f_0} = \sqrt{\frac{1}{T_{\text{rec}}} \int_{t=t_0}^{t_0+T_{\text{rec}}} |x_{\text{IF}}(t)|^2 dt}. \quad (3.8)$$

The power level accuracy of a common CW source underlies significant tolerances. Besides absolute inaccuracies due to, e.g., thermal drifting, relative deviations occur because of internally changing attenuator settings when sweeping over a large power range. One solution to improve the accuracy is to level the source with a power meter embedded in a control loop, see Fig. 3.6. The CW tone is fed through a bandpass filter, tuned to  $f_0$ , and fed back via a 6-dB splitter to the power meter  $\text{PM}_1$  monitoring the signal level. If the deviation from the target value is within  $\pm 0.02$  dB, the power search is aborted. For the utilized power meter an accuracy of  $\pm 0.25\%$  may be expected [67]. Neglecting deviations through setup caused mismatches, the achieved overall accuracy is dominated by the power meter itself outperforming the tolerance of the incorporated CW source which is in the range of approx.  $\pm 1$  dB [68]. The aim of the bandpass is to filter out unintended harmonics potentially interfering with the DR measurement. After the 10-dB attenuator, two signal paths can be configured via SPDT RF switches. To compensate the path loss, a second power meter  $\text{PM}_2$  is connected at the end of the setup. After calibration, the SDR is exchanged with  $\text{PM}_2$  to perform the power sweep. The two different paths differing in insertion loss are utilized to operate  $\text{PM}_1$  at optimum conditions. To achieve the specified accuracy in a reasonable measurement time, the utilized power meter must be exposed to power levels above  $-40$  dBm. Hence, for the target power sweep ranging from  $-80$  dBm to the SDR's maximum power rating of 0 dBm, the setup is switched to the 40-dB path for power levels smaller than  $-40$  dBm and to the 0-dB path for higher values. To eliminate uncertainties through frequency drifting, the SDR and the CW source are synchronized to the same reference clock at 10 MHz.

The results of the power sweep for the *USRP B200mini* over different gain settings is given in Fig. 3.7. For the measurement, the SDR was tuned to  $f_0 = 750$  MHz at  $f_{\text{IF}} = -12$  MHz,  $f_s = 56$  MSa/s, and an AAF bandwidth of 22.5 MHz making recordings with a length of  $T_{\text{rec}} = 100$  ms. During the noise floor characterization, the SDR was disconnected from the setup and terminated with a  $50 \Omega$  load. The power sweep was aborted 10 dB above full-scale reading of the ADC. It is obvious from Fig. 3.7 that sufficient DR is available to verify the

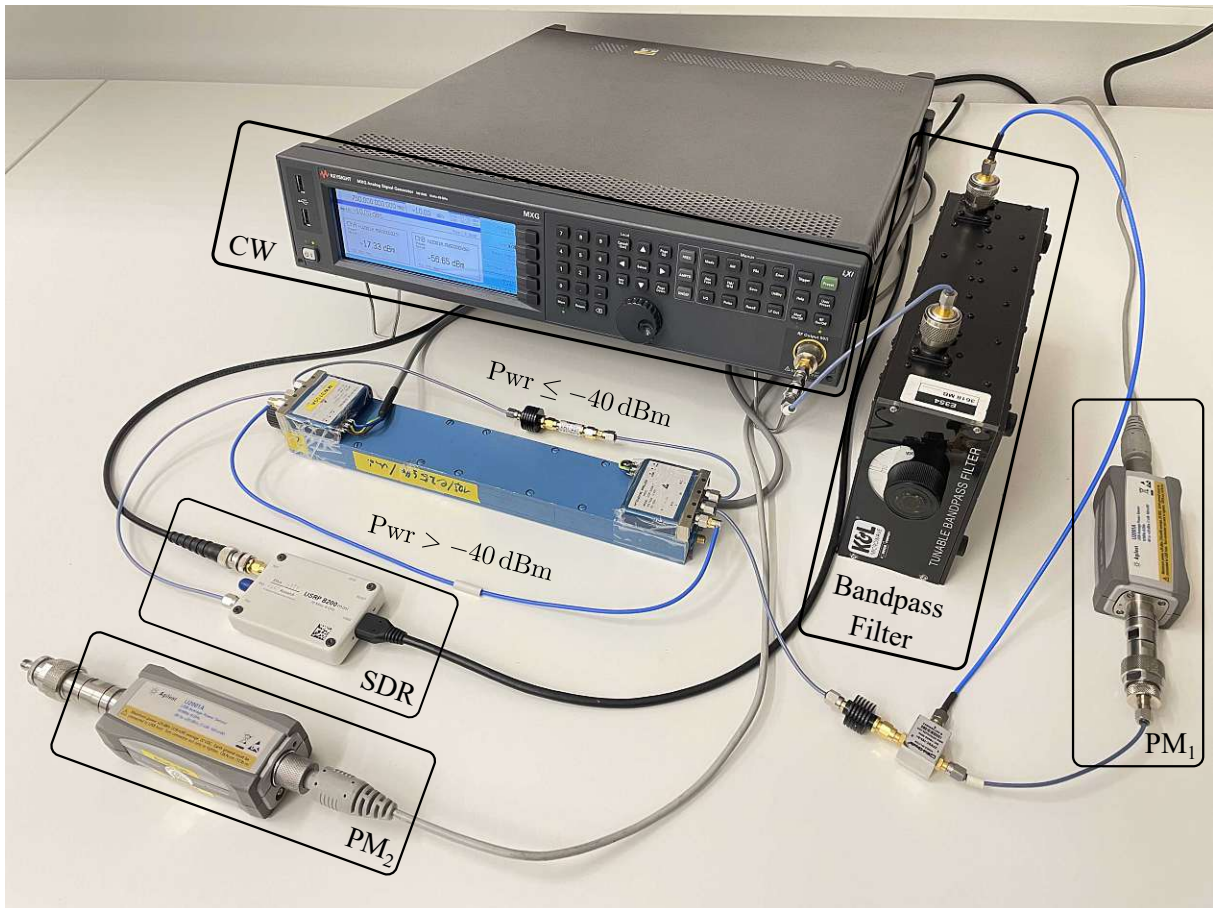
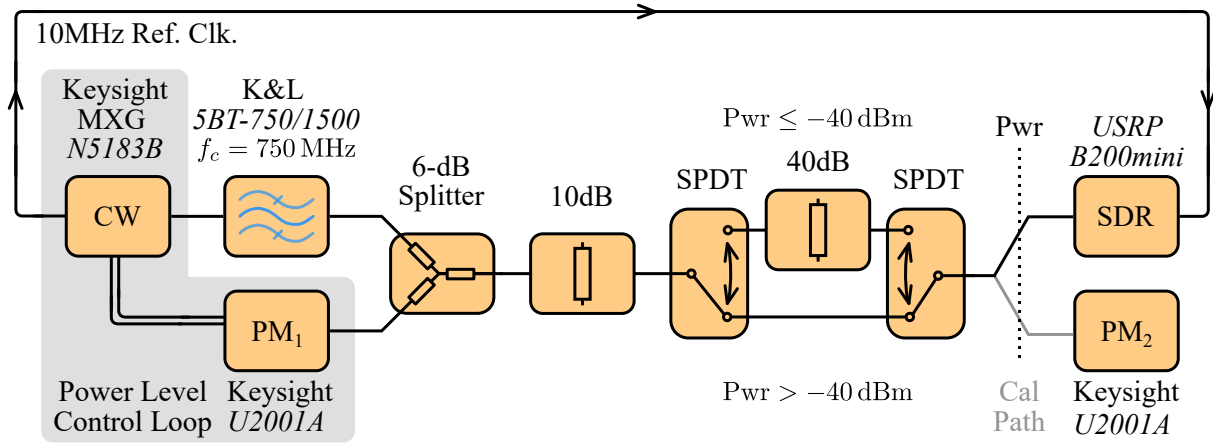
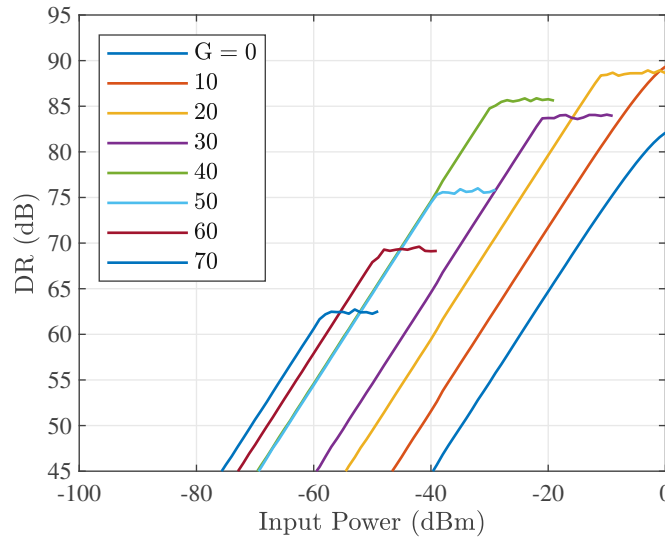


Fig. 3.6: Measurement setup for CW analysis of the SDR *USRP B200mini*.



**Fig. 3.7:** Measured DR for CW signals over input power at different gain settings:  $f_0 = 750$  MHz,  $f_{IF} = -12$  MHz.

40-dBc requirement for CW signals. It is to be noted that the gain settings are unitless and only approximately translate into relative gain differences in decibel. The three different gain stages of the RFIC *AD9364* are mapped to the adjusted settings by an optimized lookup table, supplied by the manufacturer. Gain settings above 50 show a strongly decreasing DR as thermal noise exceeds the quantization noise level. The traces for  $G = 40$  and  $50$  overlap as only the last amplifier in the receiver chain is adjusted which has no effect on the overall sensitivity. Assuming the quantization noise to be white, it is possible to estimate the ENOB of the ADC by using:

$$\text{ENOB} = \frac{\text{DR}_{\text{CW}} - 1.76 \text{ dB} - 10 \log_{10}(f_s/B_N^{\text{CISPR}})}{6.02 \text{ dB}}. \quad (3.9)$$

The gain settings between 10–20 show the largest DR and give an ENOB of approx. 10 bit.

The DR measurement has been carried out at a single frequency and a predefined IF. To investigate DR performance influences for a different IF, the noise power relative to the full-scale reading of the ADC is analyzed at constant LO frequency, i.e.,  $f_{LO} = 762$  MHz, in Fig. 3.8. The spike at 0 Hz indicates the characteristic DC offset of homodyne receivers. For frequencies approaching half the sampling rate, i.e., 28 MHz, the noise power increases which is typical for delta-sigma ADCs. Due to dominance of thermal noise at higher gain settings, the quantization noise lobes disappear. Obviously, spurs appear at different frequencies depending on the gain setting. Hence, the IF has to be chosen carefully to avoid signal distortion and a reduced DR. For instance, the best spurious performance is achieved at  $G = 30$ . As the noise shaping lobes cause a negligible decrease of the DR up to 22 MHz, the measurements from Fig. 3.7 apply in this specific scenario for an IF range of  $0 \text{ Hz} < |f_{IF}| \leq 22 \text{ MHz}$ .

By this example, it has been demonstrated that the *USRP B200mini* offers sufficient DR to verify the *CISPR* requirement of CW signals at a static LO configuration. The results indicate that the SDR performs best at gain settings between 10–40. As the DR is a decisive parameter for the application as an EMI receiver, this gain range is further investigated. The CW tone tests have to be performed over the entire *CISPR* band C/D. To enable measuring the desired frequency range, the bandpass filter in the CW measurement setup from Fig. 3.6 is removed.

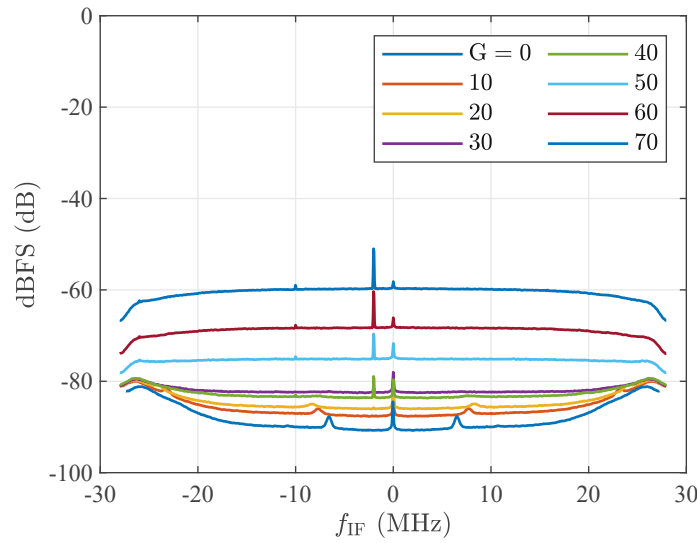


**Fig. 3.8:** Noise power measurement over  $f_{IF}$  at different gains and  $f_{LO} = 762$  MHz.

Furthermore, only the 0-dB path is utilized as the interference suppression measurements are ideally made close to the full-scale level of the SDR's ADC to achieve accurate results.

### 3.2.1 Out-of-Band Carrier Suppression

In *CISPR 16-1-1*, mainly three different CW suppression measurements are mentioned. As the complexity of these tests depend on the receiver topology, the relevant tests for homodyne-based SDRs are investigated. It was discussed in Sec. 2.2.2 that component tolerances and manufacturing imperfections cause interference through signal content located at image frequencies. The RFIC *AD9364* uses an internal calibration routine to improve intrinsic IQ imbalances. It can be directly seen from the noise power measurement in Fig 3.8 that the IF should be kept between 2 MHz–22 MHz for best performance. The required LO tuning range to cover the complete *CISPR* band C/D is thus between 52–1002 MHz. Over the entire LO tuning range, the suppression of images:

$$s_{IM} = 20 \log_{10} \frac{\hat{\mathcal{I}}_{f_0|f_{RF}=f_0}}{\hat{\mathcal{I}}_{f_0|f_{RF}=f_0-2f_{IF}}}, \quad (3.10)$$

was verified to be larger than 75 dB, see Fig. 3.9. In addition to this, the suppression of RF-IF leakage:

$$s_{IS} = 20 \log_{10} \frac{\hat{\mathcal{I}}_{f_0|f_{RF}=f_0}}{\hat{\mathcal{I}}_{f_0|f_{RF}=f_{IF}}}, \quad (3.11)$$

was measured and depicted by an additional trace. As the results are well above the required 40 dBc, this part is considered to be fulfilled. It shall be recapitulated that all measurements in this section have been performed at constant IF, i.e.,  $f_{IF} = -12$  MHz, and using the RMS detector from (3.8). Furthermore, gain dependencies have not been depicted as no significant performance changes occurred at the gain range of interest between 10–40.

Downconversion spurs are a severe problem for homodyne receivers. Frequency content located at LO harmonics interferes in baseband with the fundamental conversion product. This behavior further aggravates as LO harmonics are intentionally produced to increase the DR of the mixer

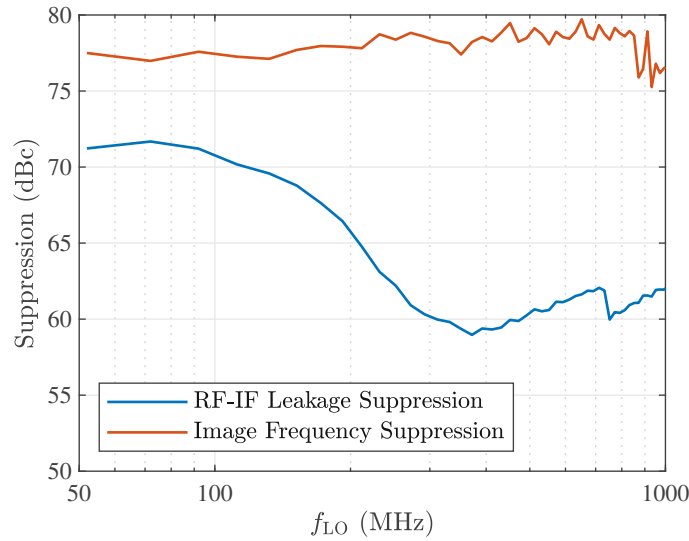


**Fig. 3.9:** RF-IF leakage and image frequency suppression over LO frequency.

using a rectangular signal [69]. The suppression is measured by setting the interfering tone to integer multiples of the LO according to:

$$s_{\text{MP}} = 20 \log_{10} \frac{\hat{\mathcal{I}}_{f_0|f_{\text{RF}}=f_0}}{\hat{\mathcal{I}}_{f_0|f_{\text{RF}}=n f_{\text{LO}} \pm f_{\text{IF}}}}, \quad (3.12)$$

where the positive sign of the IF stands for the image frequency. The suppression is depicted in Fig. 3.10. It can be seen that especially odd order modulation products cause the most problems. Furthermore, maximum interference occurs for tones located at multiples of the image frequency for  $n = 3$  and  $7$ . Obviously, the *CISPR 16-1-1* norm is not achieved. This problem can be mitigated by a preselector, filtering out frequency content at LO harmonics. The main downside of this approach is that a large amount of filters is required for sufficient suppression, especially at low tuning frequencies. Further investigations towards the linearity of the frontend must be made to evaluate how much bandwidth reduction is required if broadband impulses want to be measured.

### 3.2.2 Sensitivity and Spurious Emission

To derive the required receiver sensitivity for TEM cells, the far field transformation algorithm from Sec. 2.1.2 must be reformulated. The maximum emitted field strength  $E_{\text{max}}$  of an EUT measured in an SAC at a distance of  $s = 10$  m is specified in *CISPR 32* with  $30 \text{ dB}\mu\text{V}/\text{m}$  between  $30\text{--}230$  MHz and with  $37 \text{ dB}\mu\text{V}/\text{m}$  between  $230\text{--}1000$  MHz<sup>2</sup>. Assuming an empty cell simplifies the summation of the orthogonal EUT positions to  $\sum_{i=1}^3 V_i^2 = 3V_{\text{N}}^2$  where  $V_{\text{N}}$  denotes

<sup>2</sup>The mentioned field strength is defined for *class-B* devices representing end-consumer products. Industrial applications are categorized as *class-A* EUTs which are allowed to emit 10 dB higher field strengths.

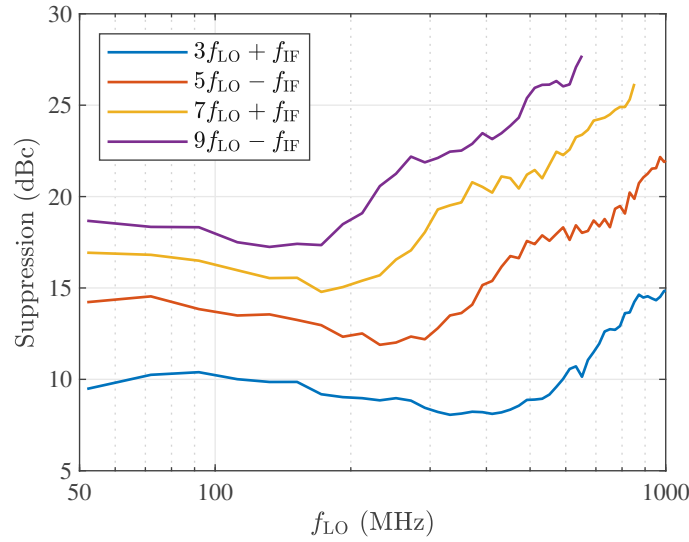


**Fig. 3.10:** Suppression of downconversion products due to frequency content located at  $f_{RF} = nf_{LO} \pm f_{IF}$ .

the measured thermal noise voltage. Applying these assumptions allows to reformulate (2.19) expressing the noise power in terms of the specified maximum electric field by:

$$P_N = 20 \log_{10} \left( \sqrt{\frac{1}{3}} \frac{E_{\max} \epsilon_{0y}}{60k_0 g_{\max}} \right). \quad (3.13)$$

With (3.13), the maximum noise power not exceeding the  $E_{\max}$  constraint is defined. In *CISPR 16-2-3*, the norm on radiated emission measurement methods, it is specified that the system noise floor must be 6 dB below  $E_{\max}$  while the EUT is de-energized [70]. Furthermore, in *CISPR 16-1-1*, it is stated that the maximum signal error due to spurious emission of any kind must be in within  $\pm 1$  dB. To meet these two requirements an additional margin has to be considered, further denoted with  $SNR_{\min}$ . In case of thermal noise,  $SNR_{\min} = 6$  dB. If spurious emissions coincide with the signal of interest, an  $SNR_{\min} \leq 19$  dB may become necessary depending on the signals phases.

The peak detector has the highest noise gain among all detectors and is thus taken into account to investigate the worst-case sensitivity of the *USRP B200mini* over frequency. Therefore, the broadband IF analysis technique from Sec. 2.2.3 is utilized with an FFT bandwidth of 10 MHz, a frequency resolution of 1 kHz, and a window overlap in time domain of 90 %, satisfying the requirements for a compliant frequency scan [56]. To ensure that also seldom transient events are captured, the recording time was set to 1 s. In Fig. 3.11, the results for different gain settings are depicted. The trace of the noise floor requirement was calculated for the TEM cell from [20] having a septum height of 300 mm and an analytic field factor of  $e_{0y} = 18 \sqrt{\Omega}/m$ . The results indicate that the gain must be set at least to 20 for achieving the first margin which requires the noise power level to be 6 dB below the derived limit  $P_N$  from (3.13). Obviously, frequency spurs occur in the spectrum below 100 MHz having a maximum of  $-78$  dBm at gain setting 20. As this spur slightly violates the 19 dB margin in case of coincidence with the signal of interest, one is best advised to keep the gain at setting 30 for a compliant frequency scan.

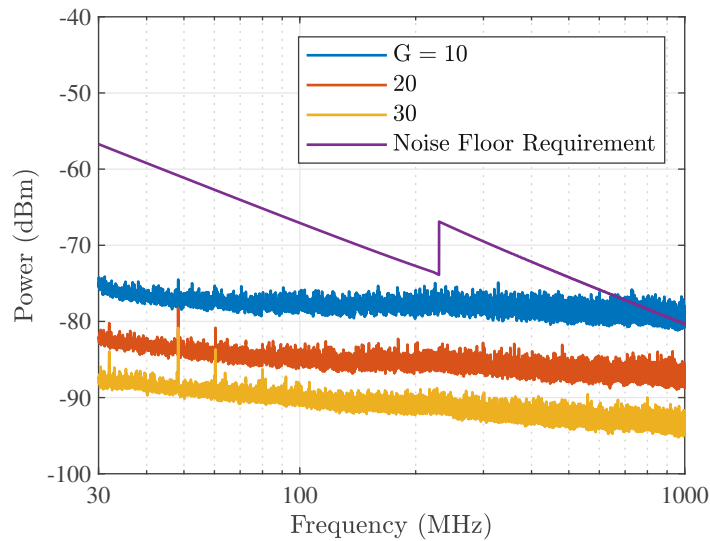


**Fig. 3.11:** Peak detected noise floor over *CISPR* band C/D for different gain settings.

### 3.2.3 Matching

If no attenuation is inserted at the receiver input, *CISPR 16-1-1* requires a voltage standing wave ratio (VSWR) below 2:1. The matching of the *USRP B200mini*, depicted in Fig. 3.12, did not change for the investigated gain settings 10–40. Out-of-the-box, the matching slightly fails between 400–800 MHz. The additional measurement error through the mismatch is rather small and can be neglected for pre-compliance purposes. However, the norm is still fulfilled if the VSWR is smaller than 1.2:1 for an attenuation at the receiver input larger than 10 dB. As this VSWR corresponds to a return loss (RL) of approx. 20 dB, it is easily possible to achieve compliance using a forced match. For gain setting 30, see Fig. 3.11, the degraded sensitivity would be still sufficient to perform compliant tests after inserting a 10-dB attenuator which is matched sufficiently.

## 3.3 Transient Analysis

Measuring *CISPR* impulses is the most challenging verification test for EMI receivers in terms of linearity and DR. The impulses are generated with a pulse forming network achieving voltage levels of up to 73.3 V and bandwidths easily exceeding 1 GHz. Even though, it seems to be unlikely that such broadband signals occur in reality, this approach represents a worst case scenario ensuring compliant linearity of the receiver without prior knowledge of an arbitrary EUT. Goal of this section is to investigate the broadband performance of the *USRP B200mini* out-of-the-box, focusing on optimum configurations and available DRs.

It is common practice in *CISPR 16-1-1* to characterize the impulse source's output power over frequency using a fully compliant EMI receiver. In addition, a CW source is adjusted such that the same level is indicated at  $f_0$ . Measuring and comparing these two calibrated signals with an unknown receiver, i.e., the SDR, allows to easily identify signal compression then. The characterization setup intended for broadband impulse measurements is depicted in Fig. 3.13. Mainly, the setup can be split into two parts: the signal sources (left) and the receivers (right). While the CW generator is again leveled with a power meter as in Fig. 3.6, the coherent impulse

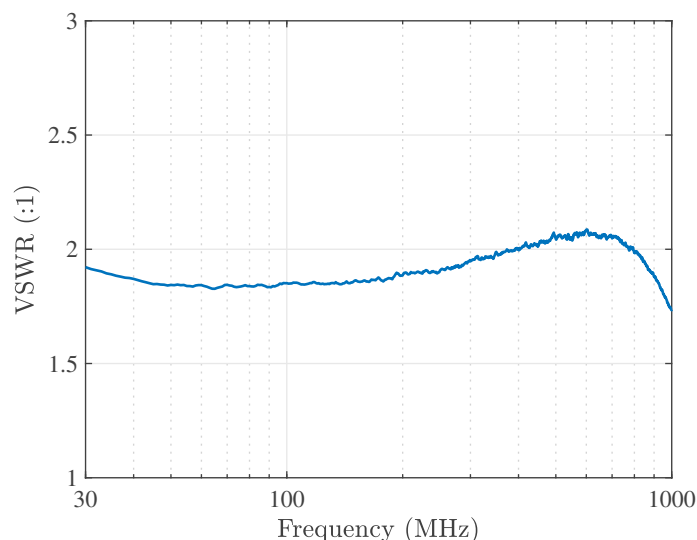


**Fig. 3.12:** VSWR of the *USRP B200mini* measured at the input connector *RX2*.

source block incorporates several instances which are discussed in the subsequent section. The SPDT switch on the right hand side is routed to the EMI receiver during calibration of the CW source according to the peak detected impulse power level. After calibration, the SPDT switch is routed to the SDR for measuring the two signals, accessible via the first RF switch.

To avoid interferences through unintended downconversion products, the SDR is foreseen with a preselection filter covering *CISPR* band C/D. Applying this modification still preserves the broadband scenario and allows CW compliant measurements for LO frequencies down to 375 MHz. The actual configuration shall represent a common pre-compliance case where an unknown EUT is investigated over a limited frequency range using a single preselector, e.g., a lowpass filter.

### 3.3.1 Coherent Detection of *CISPR* Pulses

The impulses generated by *CISPR* compliant sources are almost of rectangular shape. Usually, semiconductor switches cannot be used to achieve the required rise times and voltage levels. Hence, mechanical switches, i.e., reed contacts, are implemented in the pulse forming network. The working principle is based on a short coaxial cable connected to a DC source on the one side and to the switch on the opposite side. During open state of the mechanical switch, the cable is charged by the DC source to a certain voltage level. After closing the switch, the stored energy in the cable discharges via the output of the source and connected equipment. The impulse duration is defined by the cable length and is usually in the range of 300 ps. There are some drawbacks of such sources which must be considered to get accurate measurement results: Firstly, the output impedance of the source depends on the switch state and can be seen as a total reflect in open conditions. Secondly, mechanical reed contacts produce a significant amount of jitter. Hence, it is impossible to generate transients at defined time instances synchronized to external instruments. Lastly, reed-contacts also produce amplitude jitter causing a measurement error in the sub-decibel range. While the matching problem can be solved with a forced match, see the 10-dB attenuator applied to the impulse source output in Fig. 3.13, the remaining errors require more effort to be solved. To reverse the synchronization problem, it was decided to

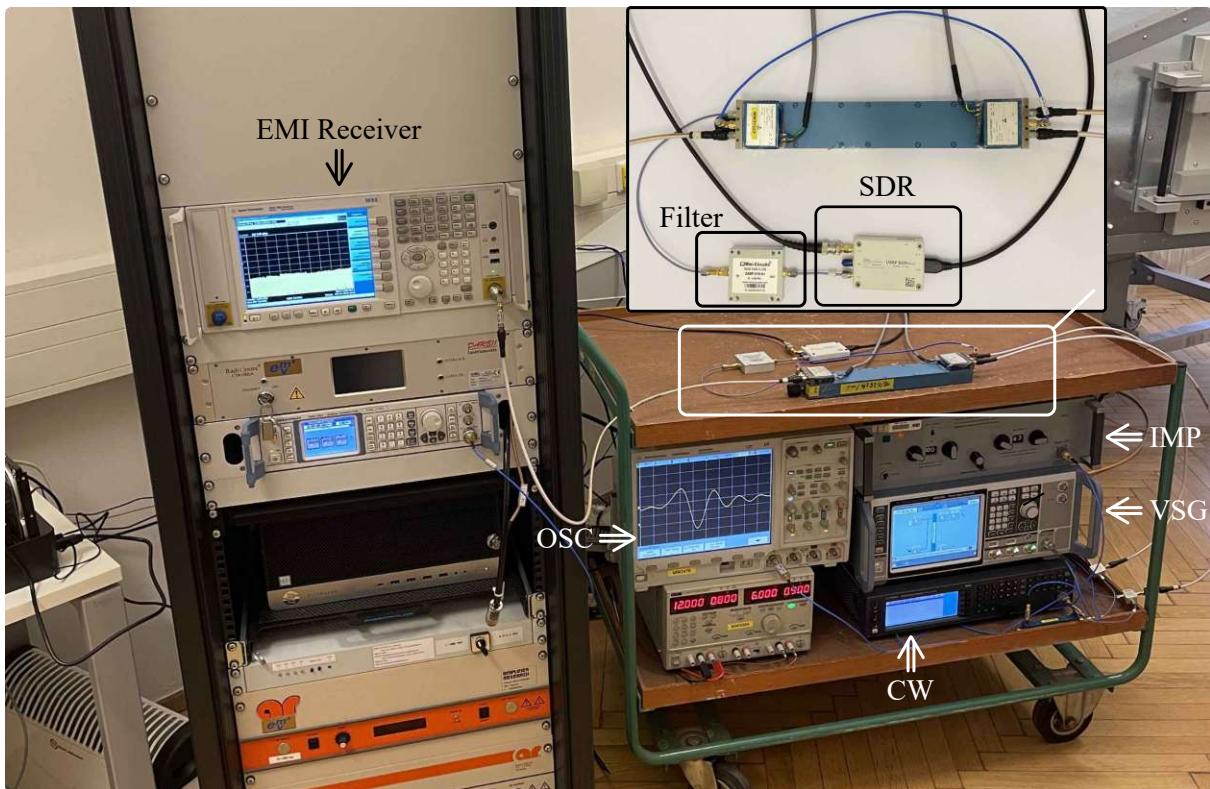
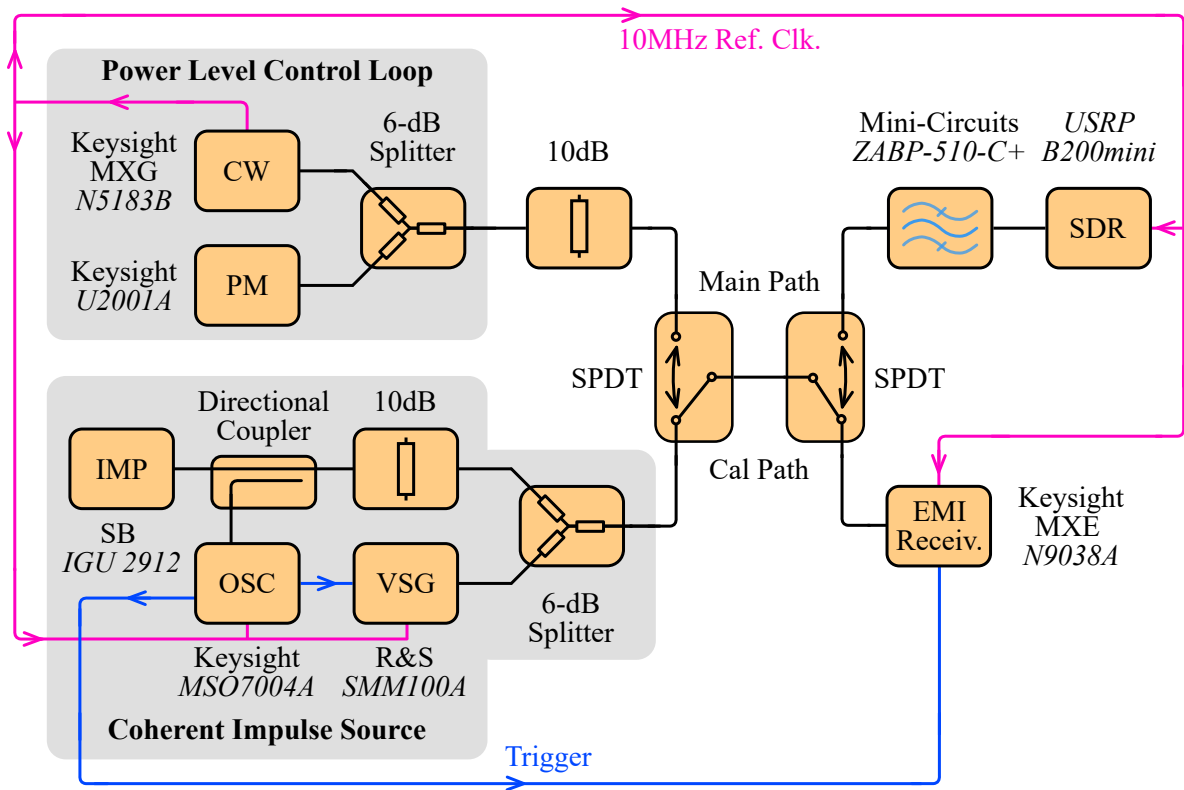
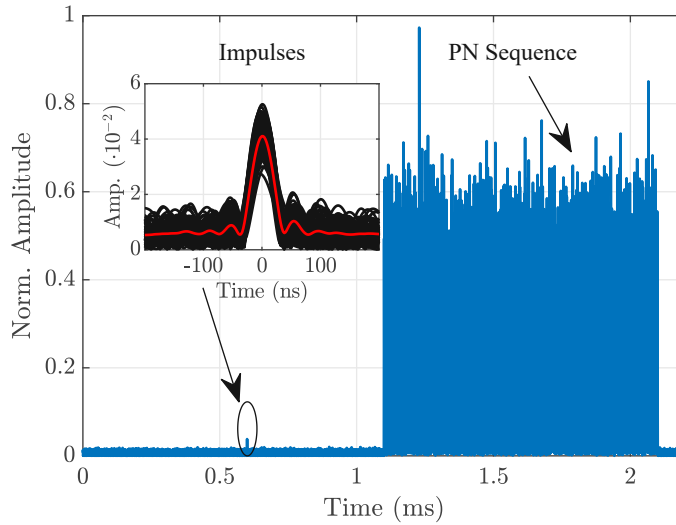


Fig. 3.13: Measurement setup for broadband linearity analysis of the SDR *USRP B200mini* measuring *CISPR* impulses.



**Fig. 3.14:** Coherent overlay of measured *CISPR* impulses followed by the PN sequence.

create a trigger signal by monitoring the periodically repeating impulses of the output using an oscilloscope. Each detected transient forces the EMI receiver to start a recording. As the time delay between the trigger signal coming from the oscilloscope and the received impulse is constant, the jitter problem in time domain is solved and several impulse traces can be averaged reducing the amplitude jitter as well to a negligible extent. The remaining measurement uncertainty is dominated by thermal noise due to averaging the signal's envelope. As the fully-compliant EMI receiver provides excellent linearity and sufficient DR ( $\gg 30$  dB) by using its preselector filterbank, this effect is considered to be a minor problem.

By now, the impulses can be measured accurately using the EMI receiver for calibration purposes. As the *USRP B200mini* does not provide any external trigger input, a software-based method has been developed as a work-around. During characterization of the SDR, a vector signal generator (VSG) is triggered by the oscilloscope injecting a correlation sequence  $\gamma(t)$  right after the impulse  $\delta(t)$ , see Fig. 3.14, with amplitude  $\alpha_i$  resulting in the expression:

$$x(t) = \sum_{i=1}^N \alpha_i \delta(t - \tau_i) + \gamma(t - \tau_i - \Delta_t) e^{j(\omega_{LO}t + \phi_{VSG})}. \quad (3.14)$$

After recording a time sequence with the SDR, including several events  $N$ , the corresponding baseband signal results in:

$$\begin{aligned} x_{BB}(t) &= G \{ [x(t) * h_{PRE}(t)] e^{-j(\omega_{LO}t + \phi_{SDR})} \} * h_{AAF}(t) \\ &\cong G [x(t) e^{-j(\omega_{LO}t + \phi_{SDR})}] * h_{AAF}(t) \\ &\cong G \sum_{i=1}^N \alpha_i h_{AAF}(t - \tau_i) e^{-j(\omega_{LO}\tau_i + \phi_{SDR})} + \gamma(t - \tau_i - \Delta_t) e^{j(\phi_{VSG} - \phi_{SDR})}. \end{aligned} \quad (3.15)$$

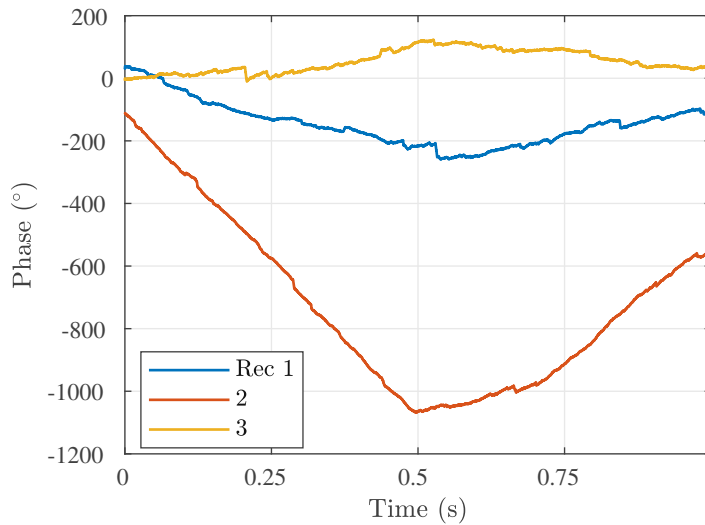


**Fig. 3.15:** Phase drift over time of a single tone measured at  $f_0 = 500$  MHz.

It is possible to locate the transients in (3.15) by correlating the baseband signal with the original pseudo noise (PN) sequence using the expectation operator  $\mathcal{E}\{\cdot\}$  according to:

$$\begin{aligned} R(t) &= \mathcal{E}\{\gamma(t+t')x_{\text{BB}}^*(t')\} \\ &= c \sum_{i=1}^N \delta(t - \tau_i - \Delta_t) e^{j(\phi_{\text{VSG}} - \phi_{\text{SDR}})}, \end{aligned} \quad (3.16)$$

where  $c$  denotes a constant taking the SDR's gain  $G$  and the correlation gain, depending on the PN sequence length, into account. The constant time delay between the impulse and the correlation sequence allows for a coherent overlay of multiple traces. For reasons of simplicity, the superposition of the baseband signal with noise has been omitted. Furthermore, in (3.16), it is assumed that the AAF's impulse response has no impact on the correlation peak which is satisfactory for envelope averaging in the time discrete domain where  $f_s \cong 2B_{\text{AAF}}$ .

Besides the enhanced measurement accuracy achieved by averaging, the developed setup offers another significant advantage for the broadband characterization of the SDR. It has been demonstrated in Sec. 3.1.2 that the achievable DR may be below 30 dB. To identify the compression limit of the *USRP B200mini*, a power sweep starting from an even lower indication  $\hat{I}_{f_0}$  has to be performed. As the measured transients are then close to the noise floor of the SDR, it is beneficial to know the true location of the peak amplitude value. To achieve accurate results even at a negative SNR, complex averaging is the means of choice as it allows to decrease noise power uncertainties by  $N^{-1}$ . Unfortunately, this approach requires a constant phase relationship between the detected events of (3.16) which the *USRP B200mini* does not provide. Measuring the phase of a single CW tone at  $f_0 = 500$  MHz over a recording length of 1 s obviously depicts the occurring problem in Fig. 3.15. Even though, the SDR shares the same reference clock with the signal generator, the phase of the tone is drifting over time significantly. One might get the impression that the phase drift is rather low as the observation time is quite long. However, the visible discontinuities impede an accurate phase alignment if occurring between the PN sequence and the impulse. As a consequence of these phase instabilities, the signal's envelope  $|x_{\text{IF}}(t)|$  is taken for averaging impulses to characterize the *USRP B200mini*.

The VSG has a finite response time to the asynchronous trigger signal coming from the oscilloscope. As the internal baseband signal generator operates at a clock rate of 600 MSa/s, the expected jitter can vary in the range of one sample causing a maximum uncertainty of  $\max\{\epsilon_t\} = 1.7$  ns. The resulting averaged IF signal envelope follows:

$$\begin{aligned} \overline{|x_{\text{IF}}(t)|} &= \frac{G}{N} \sum_{i=1}^N |\alpha_i h_{\text{AAF}}(t \pm \epsilon_{ti}) * h_{\text{IF}}(t)| \\ &\cong \frac{G}{N} \sum_{i=1}^N |\alpha_i h_{\text{IF}}(t \pm \epsilon_{ti})|. \end{aligned} \quad (3.17)$$

It has been shown in Sec. 2.2.3 that a time resolution of 1 MHz is already sufficient to achieve an amplitude error below 0.2 dB using the defined *CISPR* filter from (2.24). As the jitter achieved by the vector signal generator has a far better performance than this resolution, the time uncertainty  $\epsilon_t$  plays a subordinal role for envelope averaging.

### 3.3.2 Broadband Performance

To investigate the broadband performance of the *USRP B200mini*, a power sweep is performed to identify available DRs and compression limits. Therefore, the SDR is tuned to  $f_0 = 500$  MHz adopting the same IF and sampling rate configurations from the CW analysis section Sec. 3.2:  $f_s = 56$  MSa/s,  $f_{\text{IF}} = -12$  MHz. It has been demonstrated in Sec. 3.1.2 that the available DR is strongly limited for a broadband preselector at the SDR input. As the inserted filter has an impulse bandwidth of 720 MHz, there is no benefit from AAF bandwidth reduction due to linearity limitations of the analog frontend. Hence, to obtain the maximum resolution of the ADC, the AAF bandwidth is not changed, remaining at 22.5 MHz. The power sweep is performed over a range of 20 dB investigating different gain settings in Fig. 3.16. In the averaging process, up to 1000 traces have been superposed. The dashed lines indicate the theoretical DR curve over input power for the case of a linearly increasing signal and additive complex white Gaussian noise. As reference point for the alignment with measured traces, the DR values at 6 dB input power have been used. Obviously, gain setting 30 provides the highest DR with a 1-dB compression limit at 23 dB. For setting 40, the OVF could not be identified as the receiver frontend was already too far in compression for fitting a linearly increasing trace. It has been refrained from absolute power level specifications on the x-axis as the pulse amplitudes depend on the actual system bandwidth changing along the receiver chain. What cannot be obtained from the measurement results is that the SDR's analog frontend does not provide sufficient linearity to use full-scale resolution of the ADCs, for none of the investigated gain settings.

In *CISPR 16-1-1*, it is required to verify the detector accuracy by comparing the calibrated CW tone with the belonging impulse signal. The absolute error of this procedure over the achieved DR is given in Fig. 3.17. While the solid lines denote the amplitude error between the CW tone and the impulse (CW-IMP), the dashed lines stand for the error regarding the impulse level deviation from the approximated linear traces of Fig. 3.16. The absolute error of the CW-IMP measurement must be below 1.5 dB, which is reached later than for the 1-dB compression level from linear gain.

The offset between the traces mainly comes from impedance mismatches, spurious emission, and thermal drifting. As the input impedances of the EMI receiver used for calibration and the SDR are different, an absolute measurement uncertainty occurs. Although this problem has been improved by forced matching of the signal sources, it cannot be fully avoided. As the impulse forming network changes its matching due to switching, the calibration and equalization

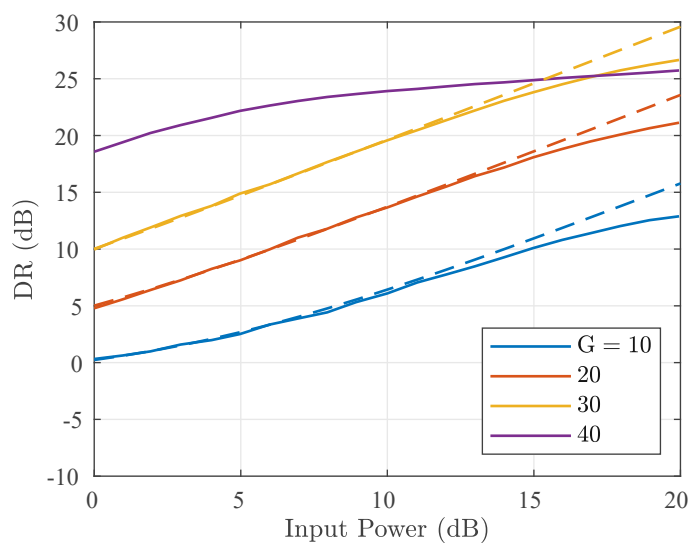


**Fig. 3.16:** Measured DR for *CISPR* impulses over input power at different gain settings:  $f_0 = 500$  MHz,  $f_{IF} = -12$  MHz.

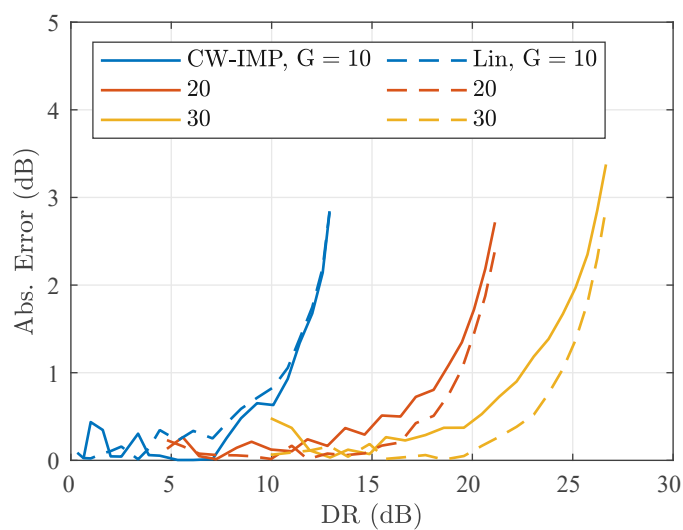


**Fig. 3.17:** Absolute error evaluation according to *CISPR 16-1-1* in comparison to compressions from linear gain.

of multiple reflections is a nontrivial task. Furthermore, the CW tone is very close or even below the least significant bit voltage of the SDR's ADC. At low resolutions, nonlinear effects in form of spurious emission impede an accurate measurement of the CW tone. Due to the relatively large bandwidth of the IF filter, the signal envelope suffers from modulation products close to the fundamental carrier. It shall be emphasized that several other sources may produce interference, sometimes of intermittent occurrence, buried in the noise floor and thus they are hard to detect and describe. In addition to the mentioned measurement accuracy limitations, there is one more effect to consider. The impulse source has no temperature compensated level control implemented and the power meter monitoring the CW output power underlies also uncertainties through thermal drifting.

Knowing that the mentioned problems are included in the error bound of *CISPR 16-1-1*, one can see that the usable DR is up to 23 dB at gain setting 30. As the settings 10 and 20 have a worse sensitivity at almost the same compression level and the linearity degrades significantly for a gain of 40, there is no benefit from using those for radiated emission testing. This is in favor with the required receiver sensitivity for the target TEM cell from [20], see Sec. 3.2.2. As the derived DR for peak detector measurements is achieved as well, it can be concluded that the *USRP B200mini* can be used for pre-compliance purposes if an appropriate preselector is applied for suppressing downconversion spurs in the desired frequency range. Regarding the quasi-peak detector, however, the available DR is insufficient to exploit the full weighting range if measuring recurrent impulses. The CW-IMP measurement trace from Fig. 3.17 must be performed for the quasi-peak as well at an impulse repetition rate of 100 Hz. In this scenario, the quasi-peak detector indicates 12 dB less than the peak detector and has a smaller noise gain at the same time. The achieved  $OVF = 23 \text{ dB} - \hat{T}_{f_0|100\text{Hz}} - G_N = 6 \text{ dB}$  is presumably sufficient to weight repetition rates down to 100 Hz. More information on detector performance evaluations are given later in Ch. 5.

---

## Improving the Performance

---

The most problematic performance limitations of the *USRP B200mini* comprise a rather low DR for broadband impulses as a test stimulus and signal distortions through downconversion spurs. This leads to *CISPR* norm violations and impedes accurate EMC measurements.

The downconversion spur problem can be solved with a preselector, suppressing frequency content located at LO harmonics of the SDR. Especially at lower tuning ranges, several different filters are needed to fulfill signal distortion requirements as multiple LO harmonics reach into the target *CISPR* band C/D. Even if the downconversion spur problem can be solved with this approach, there is still the insufficient DR which must be improved for making compliant impulse measurements with the quasi-peak detector possible. As this requires to drastically reduce the impulse bandwidth at the receiver input, regardless of the tuning frequency, the amount of necessary filters increases even more, making this filterbank approach less practical.

In what follows throughout this chapter, a hardware-based solution in form of an analog frontend extension to the SDR is analyzed for solving the mentioned problems. The goal is to enable compliant pre-compliance measurements with a low-cost SDR-based receiver, utilizing a TEM cell as test method.

The content of this chapter is mainly based on the author's own work from [29, 30] and [71] © 2023 IEEE. Revised text passages and graphs have been directly adopted from these publications.

### 4.1 Benefits of a Heterodyne Design

The most obvious way making the entire *CISPR* band C/D accessible to the *USRP B200mini* is to use an upconversion stage. In conjunction with the SDR, this creates a heterodyne frequency conversion architecture which is widely used by most professional receivers. Mixing up the signal of interest to a static center frequency and filtering it with a narrowband bandpass shall reduce the downconversion spur problem and the impulse bandwidth of which the SDR is exposed to, see Fig. 4.1.

The use of spectrum analyzers without a preselection filterbank for EMC measurements is treated in *CISPR 16-1-1 Annex J*. It is discussed that the linearity is in principal insufficient to achieve the required overload factor (OVF) for quasi-peak detector measurements. Especially, if an LNA is used in front of the first mixer stage, see Fig. 2.7, the available DR is considerably degraded. Standard mixers usually have their compression level in the same range as the pre-amplifier. Due to the additional gain, the mixer cannot cover the increased input power and sensitivity at the same time. For the specific use case of a TEM cell, it has been shown in Sec. 3.2.2 that the receiver noise floor is a less critical performance requirement. Furthermore, the analog

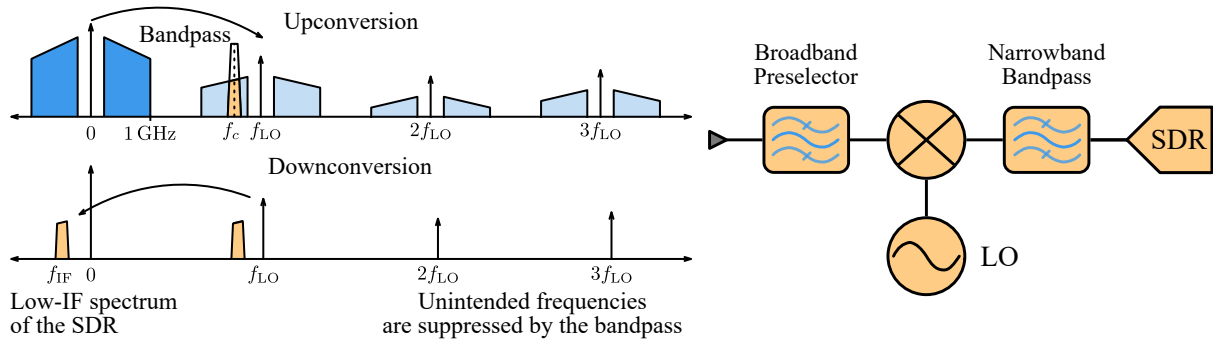


**Fig. 4.1:** Visual description in frequency domain (left) of the target upconversion stage (right), connected to the SDR *USRP B200mini*.

frontend of generic spectrum analyzers is often designed for very large frequency ranges making design compromises inevitable regarding sensitivity, linearity, and spectral purity. Thus, it is focused on the research question if the required OVF can be achieved by a pre-amplification-less upconversion stage, customized for radiated emission measurements in *CISPR* band C/D.

Combining the homodyne SDR with an upconversion stage requires to modify the analytical frequency conversion description of (2.22). Due to adding a mixer stage with a bandpass filtered output, the signal at the SDR input may be redefined by:

$$x'_{\text{PRE}}(t) = 2[x_{\text{PRE}}(t) \cos(2\pi|f_c \pm f_0|t)] * h_{\text{BP}}(t) \quad (4.1)$$

where  $h_{\text{BP}}(t)$  denotes the narrowband filter,  $f_c$  the respective center frequency, and the  $\pm$  sign indicates if the lower or upper sideband is converted. Applying the Hilbert transform yields the analytic representation of the upconverted signal:

$$x'_{\text{A}}(t) = x'_{\text{PRE}}(t) + j\mathcal{H}\{x'_{\text{PRE}}(t)\}. \quad (4.2)$$

The connected SDR is tuned to the static center frequency for downconverting the bandpass filtered output:

$$x_{\text{IF}}(t) = \frac{1}{2}\{x'_{\text{A}}(t)e^{-j2\pi(f_c - f_{\text{IF}})t}\} * h_{\text{IF}}(t). \quad (4.3)$$

Ideally, the bandpass suppresses any frequency content apart from  $f_c \pm B_{\text{BP}}/2$  where  $B_{\text{BP}}$  denotes the filter bandwidth. If the AAF covers the upconversion stage's frequency response such that  $B_{\text{AAF}} \cong B_{\text{BP}}/2$ , unintended downconversion products by the *USRP B200mini* are presumably less of a problem and meet *CISPR* requirements. Due to nonideal suppression of out-of-band signals by the filter, however, leakage cannot be fully avoided. This can be improved by shifting  $f_{\text{IF}}$  vs.  $f_c$  such that no higher order mixing product spur interferes with  $x_{\text{IF}}(t)$ .

Even though, the discussed mixing products may be also reduced with preselection filters at the SDR's input, the impulse bandwidth must be reduced significantly to about  $B_{\text{I}}^{\text{PRE}} = 50$  MHz for achieving the required DR for quasi-peak detector measurements, see Fig. 3.4. Hence, for covering the entire *CISPR* band C/D continuously, more than 20 filters are required. To keep the receiver sensitivity in an acceptable range, such costly filterbanks are usually realized with RF relays switches for routing the incoming signal via a certain preselector to the SDR. Besides various other disadvantages regarding the realization, the overall financial budget estimate for such a development was about two to four times higher than for a suitable upconversion stage and hence not further pursued.

**Tab. 4.1:** Examples of high dynamic range mixer specifications.

Name	<i>LTC 5510</i>	<i>SYM-30DHW+</i>	<i>T3-07M</i>
<b>Company</b>	Analog Devices	Mini-Circuits	Marki Microwave
<b>Topology</b>	Double-Balanced	Triple-Balanced	Triple-Balanced
<b><math>P_{1dB}</math></b>	11 dBm	14 dBm	20 dBm
<b>IIP<sub>3</sub></b>	23 dBm	26 dBm	32 dBm
<b>NF</b>	11 dB	6.5 dB	8 dB
<b><math>f_{RF}</math></b>	1 MHz–6 GHz	5 MHz–3 GHz	1 MHz–7 GHz
<b><math>f_{IF}</math></b>	1 MHz–6 GHz	5 MHz–1.5 GHz	1 MHz–4 GHz
<b><math>f_{LO}</math></b>	1 MHz–6.5 GHz	5 MHz–3 GHz	1 MHz–7 GHz
<b>Budget</b>	12 €	15 €	300 €

## 4.2 Feasibility Analysis of an Upconversion Stage

In a pre-amplification-less design, the mixer is the first element determining the receiver performances regarding the sensitivity, linearity, and compression level. Going through the performance parameters of available mixers from different manufacturers indicates that ring-diode based topologies offer the highest DRs [72]. Probably, the most commonly known converter is the double-balanced mixer using a set of four diodes (diode quad) to multiply the incoming signal (RF) with the LO and shifting it to a desired IF. The ports of this structure are decoupled by transformer networks in general. To achieve a DC IF response, however, the circuit is often modified with a diplexer, making an overlap in frequency of the RF and IF ports impossible. Extending the double-balanced mixer with a second diode quad, an evolved structure, called triple-balanced converter, has been developed [73]. The in-/outputs are fully decoupled and allow broadband mixing regardless of overlapping RF, IF, and LO frequency bands. Furthermore, triple-balanced converters outperform older topologies as they are promising a higher linearity and suppression of intermodulation products [74]. To obtain optimum performance, it is necessary to overcome the forward voltage of the diodes and operate them in push-pull mode, requiring a high LO power level. In general, diode-ring-based mixers achieve the best linearity and the highest DR when using a rectangular signal as LO. Assuming an infinitely short rise time leads to a Fourier series expansion of the LO stimulus with odd order components only. Thus, frequency conversion products of odd-even, even-odd, and even-even order ( $n f_{RF} \pm m f_{LO}$ ) are suppressed. In reality, this behavior cannot be fully retrieved simply because of imperfections in the diodes' switching behavior and LO signal generation. Another drawback of this approach is the strongly increased system bandwidth which is necessary to cover a sufficient number of LO harmonics. As the budget increases the higher the bandwidth gets, this technique is only applicable to low-cost developments if relatively low LO frequencies need to be tuned.

As it is the intention to design an upconversion stage without an LNA, the mixer is determining the NF. Typically, ring-diode based mixers have a conversion loss of about  $L \cong 7$  dB in the addressed frequency range of CISPR band C/D. Assuming that the NF is equivalent to conversion losses, it is possible to estimate the required compression level for compliant quasi-peak detector measurements:

$$P_{1dB} = -174 \text{ dBm/Hz} + \text{NF}_{|dB} + \text{DR}_{\text{QPD}|dB} + 20 \log_{10} \frac{B_I^{\text{PRE}}}{B_I^{\text{CISPR}}} \sqrt{B_N^{\text{CISPR}}}, \quad (4.4)$$

where  $DR_{QPD} = 51$  dB was derived analytically in Sec. 3.1.2. Evaluating (4.4) for a preselector impulse bandwidth of 1 GHz and a total NF of 10 dB gives a compression level of 14.4 dBm. The increased NF shall take path losses of additional components and striplines into account. To remember, the addressed TEM cell has a septum height of 300 mm and allows a NF of up to 25 dB for compliant measurements. There are several mixers on the market presumably achieving the desired sensitivity and compression level. To mention a few of them, the decisive performance parameters of three different converters are listed in Tab. 4.1. Directly comparing the mixers from Analog Devices and Mini-Circuits indicates the higher available DR of the triple-balanced topology by taking their NFs and compression levels into account. The main benefit of the double-balanced converter *LTC 5510* comes along with full integration in a single chip including an LO driver reducing circuit complexity and budget. However, it is obvious from the DR calculations that the Analog Devices chip cannot be used without a further impulse bandwidth reduction at the mixer input. In contrast, the *SYM-30DHW+* provides the desired compression level at an even lower NF for a budget of approx. 15 €. The performance parameters are specified for an LO power level of 17 dBm. As this level may be increased up to 20 dBm and the compression level of ring-diode mixers scales with LO power, an even better performance can be expected. If still more DR wants to be achieved, the *T3-07M* mixer from Marki Microwave can be used. The outstanding performance reflects in the price which is about 20 times higher. Furthermore, an expensive LO driver circuit is needed to fully exploit the mentioned performance parameters which further increases design costs significantly. As the triple-balanced mixer from Mini-Circuits is the best compromise in terms of achievable DR and budget, it was decided to take this converter into account for further investigations.

#### 4.2.1 Implementation Considerations

As a first step, an evaluation board was designed aiming to build a complete upconversion stage including filtering and amplification to analyze which performance may be expected of such a system. Due to a missing nonlinear model of the mixer, a simulation based analysis was not followed. To enable an easy and low-cost manufacturing process, mostly off-the-shelf components on a standard four-layer *FR4* substrate have been used, see Fig. 4.2. For initial verification purposes, the LO signal has been applied by an external source to decouple the measurement results from parasitic influences of an on-board LO.

The mixer input is bandpass filtered covering a frequency range of  $20 \text{ MHz} \leq f_{\text{PRE}} \leq 1 \text{ GHz}$  and having an impulse bandwidth of  $B_{\text{I}}^{\text{PRE}} = 720 \text{ MHz}$ . Aim of the preselector is to limit the bandwidth for broadband impulse measurements and to reduce vulnerability against nonlinear distortions located out of *CISPR* band C/D. Investigating the harmonic table of the utilized mixer gives a first impression which frequency conversion products are the most critical. In Tab. 4.2, the intermodulation distance (IMD) between the fundamental and higher order conversion products are given according to  $nf_{\text{RF}} + mf_{\text{LO}}$ , where  $f_{\text{LO}} = 1532.5 \text{ MHz}$ ,  $f_{\text{RF}} = 1502.5 \text{ MHz}$ ,  $P_{\text{RF}} = -1 \text{ dBm}$ , and  $P_{\text{LO}} = 17 \text{ dBm}$ . Obviously, the first table row indicates the strongest unintended modulation products. These can be avoided at the output, centered around  $f_c$ , by mixing up the lower sideband, i.e.,  $f_{\text{LO}} = f_c + f_0$ . In addition,  $f_c$  must be chosen such that multiples of  $\cos[2\pi m(f_{\text{LO}} + f_c)t] \cdot x_{\text{PRE}}(t)$  do not interfere with  $x'_{\text{PRE}}(t)$ , see (4.1). Simply put, the preselector's frequency response must suppress any out-of-band signal with at least 40 dB at frequencies of  $m f_{\text{LO}} - f_c$ .

Due to the good availability of SAW filters with an  $f_c$  of 1090 MHz, a solution satisfying these needs has been found with an output bandwidth to 2 MHz. The bandwidth has been chosen that small for minimizing linearity requirements of the connected receiver which is used to verify the upconversion stage. An LNA is placed right after the mixer for keeping the system's NF

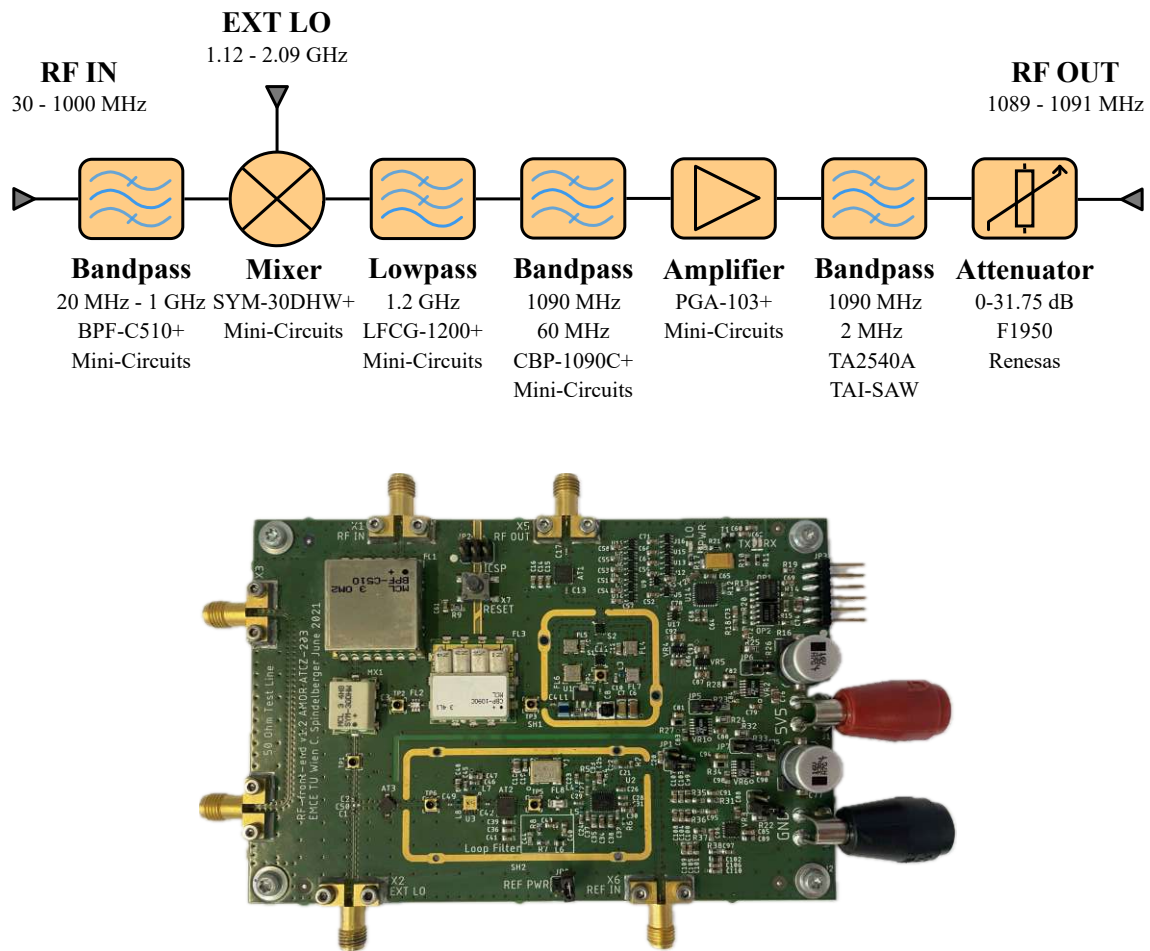


**Fig. 4.2:** Initial upconversion stage design showing the block diagram (top) and the realization (bottom).

**Tab. 4.2:** Harmonic table of the used mixer *SYM-30DHW+* from Mini-Circuits.

IMD (dBc)	$m \cdot f_{LO}$						
	1	2	3	4	5	6	7
$n \cdot f_{RF}$	0	36	14	55	25	36	47
1	63	63	66	54	58	66	60
2	60	80	60	78	67	78	71
3	> 93	> 93	> 93	> 93	> 93	> 93	> 93

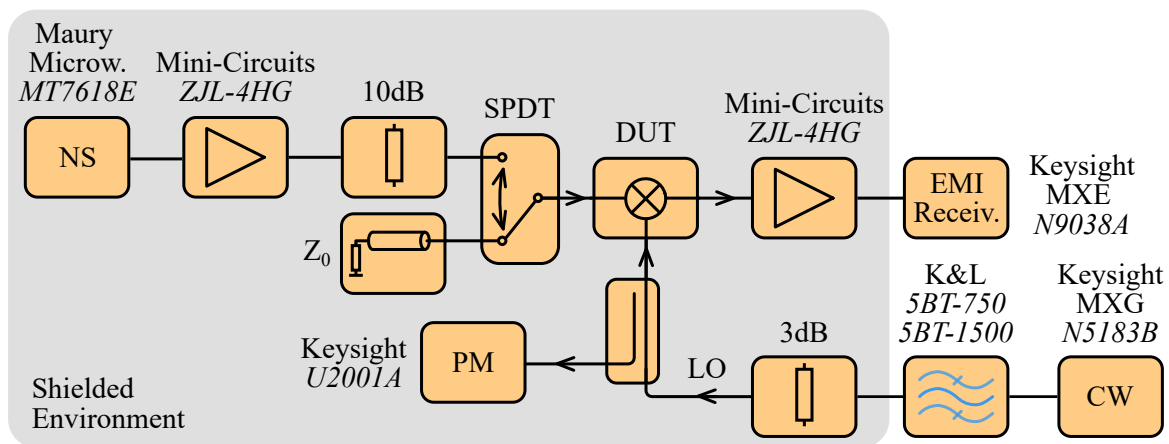


**Fig. 4.3:** Noise figure measurement setup situated in a shielded environment, i.e., a GTEM cell, performing the Y-factor method.

as low as possible. The bandpass filter preceding the LNA has a bandwidth of 60 MHz and is used to reduce the peak amplitude of broadband transients potentially driving the amplifier into saturation. Furthermore, a lowpass has been added to compensate insufficient suppression by the bandpass at multiples of  $f_c$ . At the end of the chain, a digitally-stepped attenuator is implemented for leveling the signal coming from the output of the 2 MHz SAW filter. This feature is essential for operating connected measurement equipment at optimum gain configurations. For verification purposes, the LO has been generated with a bandpass filtered CW source having a constant output power level. As the LO tuning range is between  $f_{LO} = f_c + f_0 = 1.12\text{--}2.09$  GHz, the use of a rectangular signal driving the mixer was not applicable. Because of bandwidth limitations by the RF and LO ports, higher order harmonics cannot be covered and thus, no performance improvement can be expected in comparison to a CW stimulus.

The realized prototype has been foreseen with additional bandpass filters of higher bandwidths and an on-board LO. These units have been implemented to evaluate component and layout specific performances which were needed for further design iterations, discussed later in Sec. 4.3.

#### 4.2.2 Design Criteria Evaluation

Next, the performance of the initial upconversion stage design is analyzed. The system's NF has been characterized using the well known Y-factor method [75]. As the mixer was affected by interference through mobile communication and DVB-T base stations in close vicinity, it was decided to situate the measurement setup in a shielded environment, i.e., a GTEM cell Teseq 500, see Fig. 4.3. To achieve a reasonable accuracy of the system's NF, it was necessary to modify the standard measurement setup. Usually, the noise source (NS) is directly connected to the DUT while the receiver is measuring the noise power output in turned on (hot) and off (cold) conditions of NS. The performance of a noise source is described by the excess noise ratio (ENR), defining the output power relative to the thermal noise power density  $kT_0$  at room temperature. Performing the Y-factor method requires to calibrate the receiver's NF. To achieve an appropriate measurement accuracy, the ENR of the NS shall be 5 dB higher than the NF of the DUT which is a common rule of thumb assumption [76]. As the expected NF of the upconversion stage may be in the range of 10–15 dB and the conversion gain is rather low around 0–5 dB, it was necessary to increase the ENR, i.e., 15 dB. To do so, the noise source was connected to a gain block with about 17 dB gain. Subsequently, a 10-dB attenuator was applied ensuring an RL of

the combination in excess of 20 dB. The gain block causes an increase of the thermal noise power output also in turned off conditions of NS. To obtain the desired cold noise power output, a  $50\ \Omega$  termination has been introduced. Switching between the amplified NS and the load increases the ENR by 7 dB. The measurement setup allows to choose between hot and cold output power conditions using an SPDT switch. For lowering thermal influences on the  $50\ \Omega$  termination, a coaxial cable with a length of 30 cm has been introduced making thermal heat dissipation by the constantly energized coils in the switch a minor problem.

The new hot noise power output has been calculated by determining the NF and the gain of the connected amplifier in combination with the attenuator. As the receiver was placed outside the shielded environment and long coaxial cables were used to connect, an additional gain block has been introduced to overcome cable losses and a reduced sensitivity. Regarding the LO, an external CW source was applied and leveled using a power meter sensing the tone via a directional coupler. To exclude influences on the NF measurement by phase noise of the CW source coupling into the IF path of the upconversion stage, tunable bandpass filters have been used to filter the LO signal. The absolute measurement uncertainty of the used setup has been analyzed in accordance to [76]. The derived uncertainty lies within a range of  $\pm 0.5$  dB which is considered to be acceptable for an expected system NF of more than 10 dB.

While the linear S-parameter measurements are a straightforward task using a network analyzer, it is the relatively high compression level of triple-balanced mixers that requires setup modifications. The utilized mixer has by specification a 1-dB compression level of at least 14 dBm which exceeds the output power of a common network analyzer. To overcome this, the internal signal source was routed via an external amplifier, see Fig. 4.4. By inserting a 6-dB attenuator, potential damage of the network analyzer shall be avoided due to the high gain of the amplifier. The internal receiver  $R_1$  is used for leveling the output power and has been foreseen with a 20-dB attenuator compensating the increased signal power. As for a narrowband signal it is likely that the LNA of the upconversion stage is driven into saturation or even destroyed, the 1-dB compression level has been measured at a surface mount connector directly after the mixer output. The network analyzer ports and the external CW source generating the LO signal have been calibrated using a power meter. During the compression level measurement, the receiver  $R_1$  is used to level the output power independent on the matching of the DUT. In this setup, the LO source power level was calibrated only once as the temperature of the environment was controlled by an air condition and the remaining thermal drift over the short measurement time period was considered to be negligible.

The measurement results comprising the NF, compression level, and S-parameters, are depicted in Fig. 4.5. S-parameter port definitions relate to: RF IN (port 1) and RF OUT (port 2), see Fig. 4.2. Usually, the sensitivity of mixers is specified as double or single sideband NF. These two terms distinguish the cases whether lower and upper sidebands of the upconverted thermal noise overlap in frequency domain or not. As the preselector avoids this overlap due to suppressing image frequency content reaching into the IF band, the measured NF refers to the double sideband definition. If the conversion gain of the mixer may be assumed constant over frequency, it is possible to derive the NF for the single sideband case by simply adding 3 dB. The results indicate a maximum NF of 12 dB and a compression level of up to 15 dBm which is slightly below the desired DR of analytical calculations from (4.4). Furthermore, there is obviously a problem with the matching of the upconversion stage. Remembering Sec. 3.2, *CISPR 16-1-1* allows a maximum VSWR of 2:1 or an RL of 10 dB if no input attenuation is applied. Even though, forced matching the upconversion stage would solve this problem, the measured values deviate significantly from manufacturer specifications. The mismatch could be traced to a layout problem regarding an underestimated impact of the parasitic capacitance, introduced by the large pads of the mixer's package.

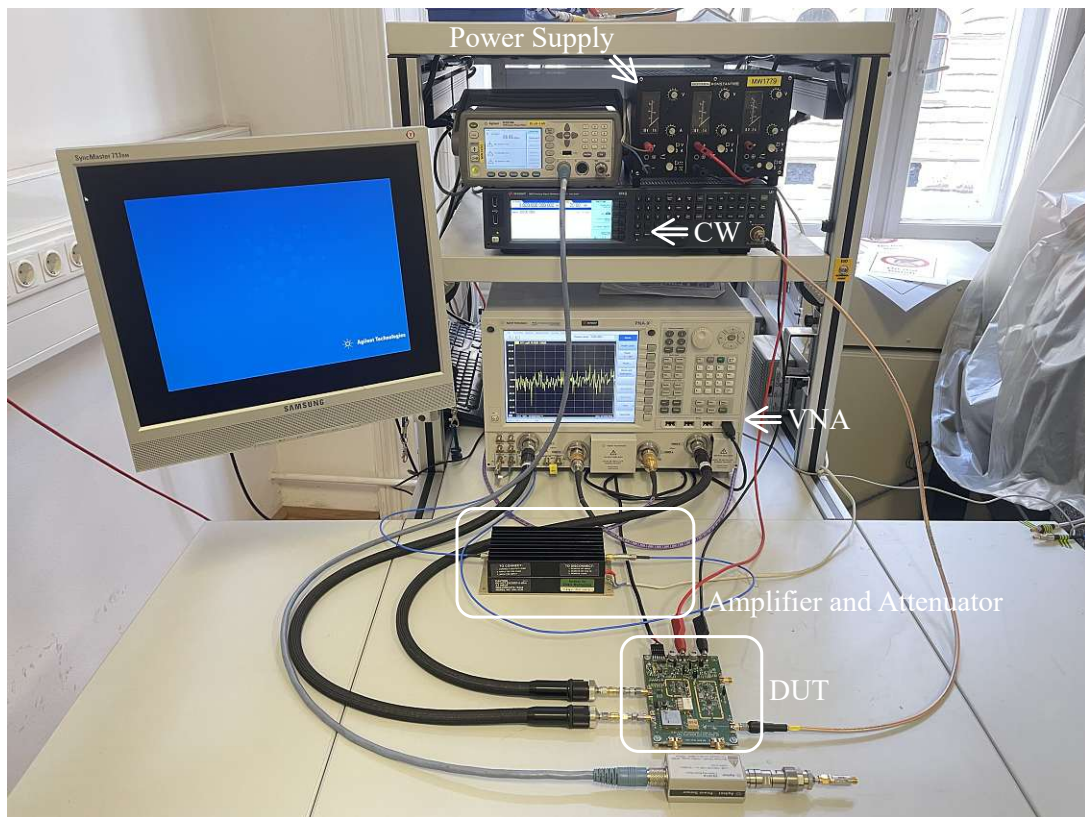
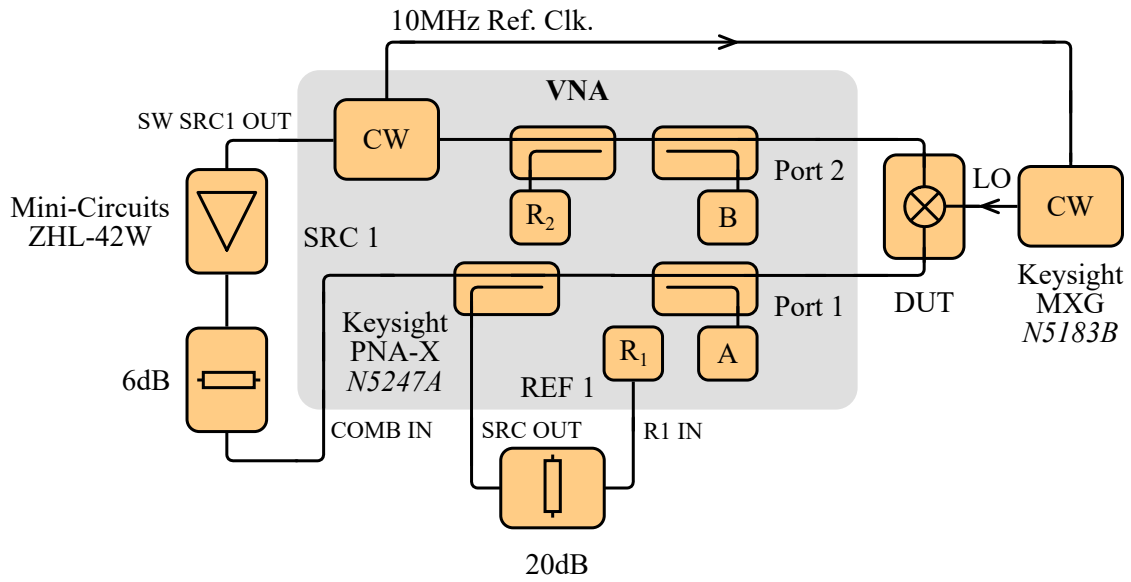
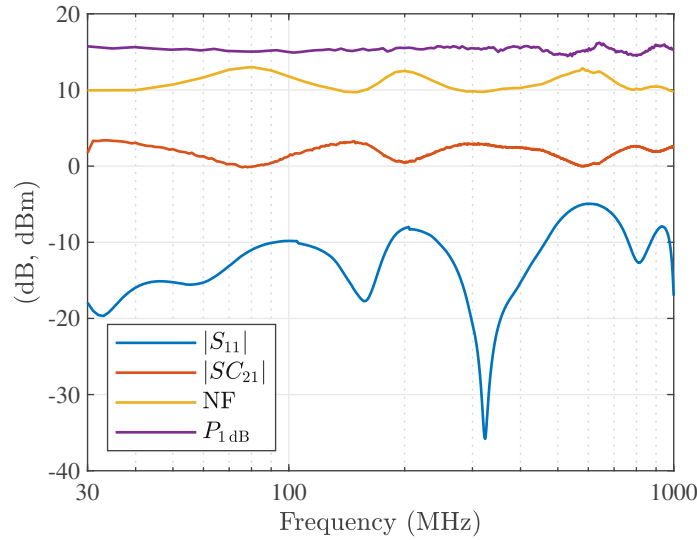


Fig. 4.4: Modified network analyzer setup for S-parameter and 1-dB compression measurements.



**Fig. 4.5:** Prototype performance over frequency measured at  $f_c = 1090$  MHz,  $P_{LO} = 20$  dBm.

The focus of the transmission line design was put on the IF section where the highest frequencies occur. As the prototype contains a lot of different components, strongly varying in package size, a compromise had to be found regarding the transmission line dimensioning and PCB layer stack-up. The rather low height distance between the RF signal and ground layer, i.e.,  $250\ \mu\text{m}$ , caused a large capacitance at the mixer's pads and thus, the resonant behavior of the matching. In general, it was found out that the mixer is sensitive to load mismatches. Applying a broadband match directly at the mixer output improved the RL and conversion gain ripple significantly. The directly connected bandpass filters represent a mismatch at out-of-band frequencies impeding the RL optimization of the presented frontend even with perfectly matched transmission lines. The upconversion stage showed the best performance for an LO power of 20 dBm. At lower values, the conversion gain decreased and the NF increased which is undesired as the performance is already quite close to the calculated design parameters.

Regarding the CW requirements of *CISPR 16-1-1*, a single tone was swept over the entire frequency range of the preselector to identify critical modulation products and feedthrough effects. The RF-IF suppression:

$$s_{IS} = 20 \log_{10} \frac{\hat{\mathcal{I}}_{f_0|f_{RF}=f_0}}{\hat{\mathcal{I}}_{f_0|f_{RF}=f_c}} \quad (4.5)$$

was violating the 40-dBc criteria at certain tuning frequencies. Although, the isolation of triple-balanced mixers is usually above 40 dBc, the requirement was failed by up to 3 dB. As the roll-off of the preselector is not sharp enough at 1.09 GHz, one possible solution is to shift  $f_c$  even higher. Besides the slightly insufficient RF-IF isolation, mixing products of

$$s_{MP} = 20 \log_{10} \frac{\hat{\mathcal{I}}_{f_0|f_{RF}=f_0}}{\hat{\mathcal{I}}_{f_0|f_{RF}=|f_c \pm m f_{LO}|/n}} \quad (4.6)$$

have been analyzed and non of them were in excess of 40 dBc. In case of  $f_{RF} = n|f_c \pm f_{LO}|$ , only a few frequencies have been investigated. As the harmonics of a common CW source are typically 30–40 dBc below the fundamental tone interfering at  $f_c$ , it was necessary to filter the

tone for verifying this certain *CISPR* requirement. The measured modulation products could be correlated with the specified  $IIP_2$  and  $IIP_3$  levels of the mixer. As long as CW tones below 0 dBm are measured, the 40-dBc requirements are fulfilled. Due to the additional conversion gain of the upconversion stage, the input power must be even reduced to prevent a connected SDR from permanent damage.

### 4.2.3 LO Signal Generation

By now, the upconversion stage has been tested with an external LO source under ideal conditions due to filtering the signal with tunable bandpass filters. As the stage is designed for operation in conjunction with a low-cost SDR, the LO signal must be generated by another source to create a standalone measurement solution. The *USRP B200mini* has a transmitter output working in a frequency range between 50 MHz–6 GHz achieving power levels of up to 14 dBm. Hence, it is obvious using the transmitter with an additional gain block for stimulating the upconversion stage. Because of on-chip couplings between the receive and transmit paths, this approach had to be dropped. Harmonics of the generated LO signals caused a significant leakage driving the ADCs of the SDR into saturation at several frequency configurations. As the required LO tuning range is quite large to cover *CISPR* band C/D and the effort of analyzing if all unintended spurs can be avoided by simply shifting the IFs of the receiver and transmitter was unjustifiable, this approach has not been pursued any further. Consequently, an on-board LO solution needs to be implemented which is part of the following section.

## 4.3 Final Prototype Design

The main problems of the initial upconversion stage design can be concluded by the following five points:

1. Insufficient impedance matching of  $|S_{11}|$
2. RF-IF isolation test violates the 40-dBc criteria
3. Impulse bandwidth of the preselector  $B_1^{\text{PRE}}$  is too large
4. On-board LO signal generation is missing
5. System shielding required

While the points 1–3 are crucial for complaint radiated emission testing, points 4–5 are highly desired to be solved enabling stand alone measurements in conjunction with an SDR and robustness against interference. To tackle the mentioned problems, a redesign of the upconversion stage was made, see Fig. 4.6 and Tab. 4.3. The main changes, except insignificant component replacements, are discussed hereinafter.

**Ad 1)** The matching shall be improved by an increased stack-up height between the pads of the mixer package and the ground layer. To keep the transmission line dimensions for routing small components effectively, the ground layer is cut out locally and the reference potential is provided by the next ground layer beneath. Due to the increased height, it is possible to decrease parasitic capacitances of large components and an improved matching of the upconversion stage is to be expected.

**Ad 2)** To increase the RF-IF isolation of the design, it was decided to choose a bandpass filter with a higher center frequency. Due to a good availability of SAW filters at  $f_c = 1227$  MHz and the high suppression of the preselector at this frequency, the IF section has been modified accordingly,

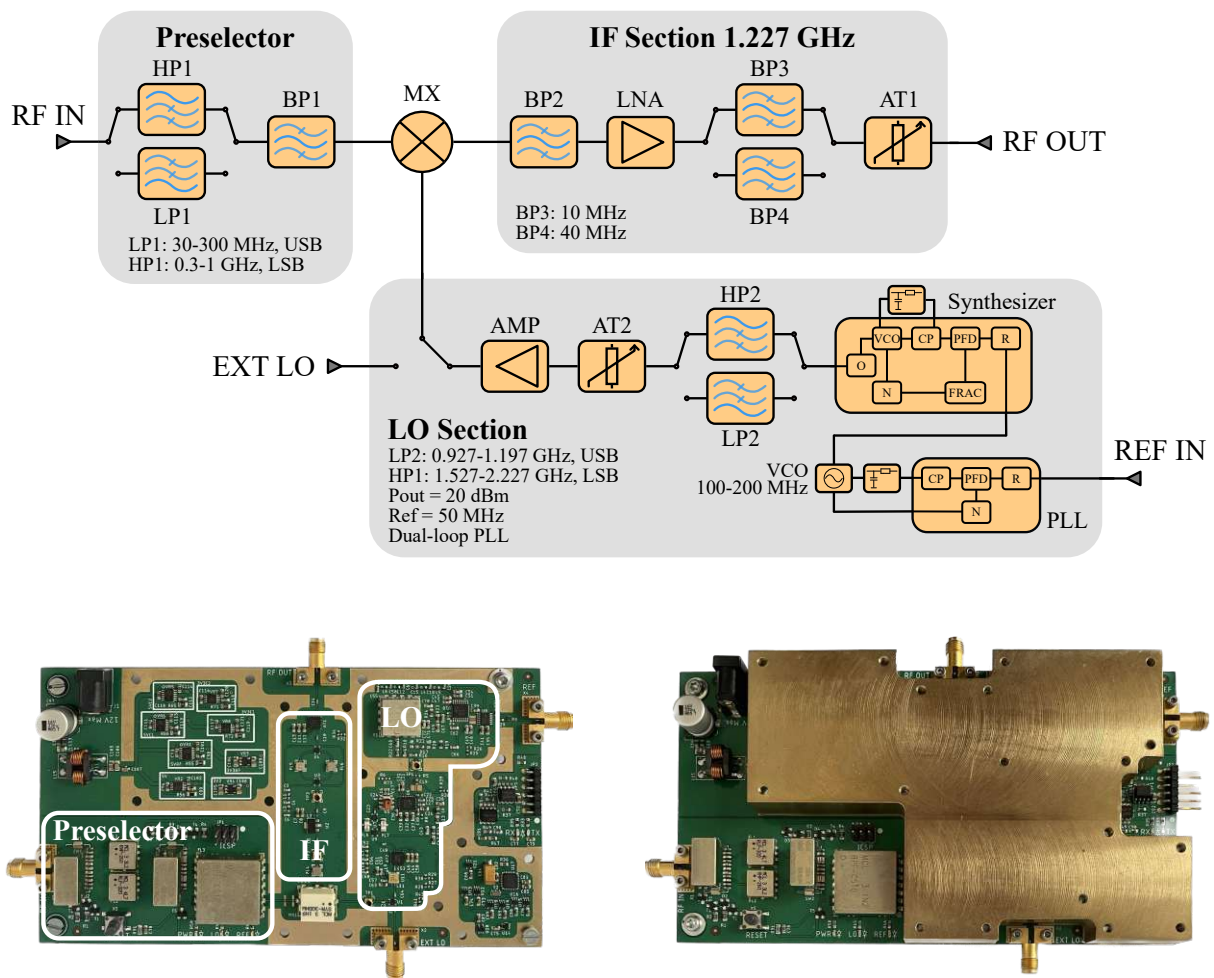


**Fig. 4.6:** Redesigned upconversion stage: Block diagram (top) and the realization with and without a brass shielding (bottom).

**Tab. 4.3:** Key component list of the redesigned upconversion stage.

Name	Part Number	Manufacturer
LP1	<i>RLP-320+</i>	Mini-Circuits
HP1	<i>RHP-260+</i>	Mini-Circuits
BP1	<i>BPF-510C+</i>	Mini-Circuits
MX	<i>SYM-30DHW+</i>	Mini-Circuits
BP2/4	<i>TA1227BB</i>	Tai-Saw
LNA	<i>TQP3M9009</i>	Qorvo
BP3	<i>TA1228BB</i>	Tai-Saw
AT1/2	<i>F1950</i>	Renesas
LP2	<i>LFCN-1000+</i>	Mini-Circuits
HP2	<i>HFCN-1500+</i>	Mini-Circuits
PLL	<i>ADF4002</i>	Analog Devices
Synthesizer	<i>LTC6948-2</i>	Analog Devices

guaranteeing an isolation larger than 40 dBc. In the redesign, it can be chosen between two different IF filters, having a usable bandwidth of 10 MHz and 40 MHz. The additional IF path has been added for the STFT-based signal analysis approach for reducing frequency scan times. Recapitulating the theoretically achievable DR for impulses from Fig. 3.4 indicates that the output bandwidth is low enough for compliant quasi-peak detector measurements in conjunction with the SDR.

**Ad 3)** It was mentioned that the achieved DR is quite close to the calculated limits of (4.4). To introduce an additional margin, the preselector is extended with two more filters reducing the impulse bandwidth and covering *CISPR* band C/D separately. This change has a further advantage regarding the norm *CISPR 16-1-1*. In general, the OVF is defined for the entire *CISPR* band C/D with a value of 43.5 dB for the quasi-peak detector. Strangely in fact, the required weighting range in band D has been reduced to an impulse repetition rate of 10 Hz, in the actual revision of the norm. As the required OVF decreases then by 17.5 dB to fulfill quasi-peak detector accuracies, there is less DR required for compliant radiated emission testing in band D. Therefore, it is beneficial covering these two bands separately for performing compliant measurements. Moreover, the added lowpass filter enables frequency conversion of the upper sideband in band C which has been identified to be advantageous regarding the mixer's linearity. The lowpass filter reduces the impulse bandwidth in front of the mixer to 270 MHz in band C increasing the DR up to 8.5 dB when measuring broadband *CISPR* impulses. In band D, the impulse bandwidth is reduced to 630 MHz yielding a negligible increase in DR of 1.2 dB.

**Ad 4)** The relatively high power level of the LO, i.e., 20 dBm, poses high demands on the phase noise performance, spurious emission, and signal isolation on a PCB level. Implementing a dual-loop synthesizer enables the avoidance of unintended coupling effects due to inevitable circuit layout imperfections and inherent frequency spurs. To synchronize the upconversion stage with peripheral equipment, an external reference clock has to be provided. Due to the high frequency resolution of the used components and versatile tuning options, the required absolute frequency accuracy of  $\pm 2\%$  is considered to be fulfilled. As the upper sideband is taken for frequency conversion in band C and the center frequency of the IF section has been changed, the LO is now operated at the following tuning ranges: 0.927–1.197 GHz in band C and 1.527–2.227 GHz in band D.

**Ad 5)** The used mixer is prone to over-the-air couplings causing interference in the IF section with the fundamental conversion product. This shall be improved by a metal shielding enclosing sensitive parts of the upconversion stage.

### 4.3.1 Transfer Characteristics

The network analyzer setup from Fig. 4.4 was used to measure the transfer characteristics of the redesigned upconversion board. The S-parameter port definitions are: RF IN (port 1) and RF OUT (port 2), see Fig. 4.6. Due to potential saturation of the amplifier and thermal destruction of the implemented SAW filters, the compression limit has not been measured using a CW tone. Later in this section, the available DR of the upconversion stage is verified by use of *CISPR* impulses for characterizing the broadband performance.

The S-parameter measurements are depicted in Fig. 4.7. Obviously, the ground layer cutout has improved  $|S_{11}|$ , though, still failing the matching requirement of *CISPR 16-1-1* around 380 MHz. As the utilized mixer is sensitive to load mismatches introduced by the IF filter BP2, this behavior may be avoided if the LNA changes position with BP2, providing a broadband match to the mixer output. The downside of this approach is that LNAs do not have the necessary compression level to handle the output power of such mixers. The minimum required NF for measurements with the target TEM cell from [20] may be up to 25 dB. Hence, applying a

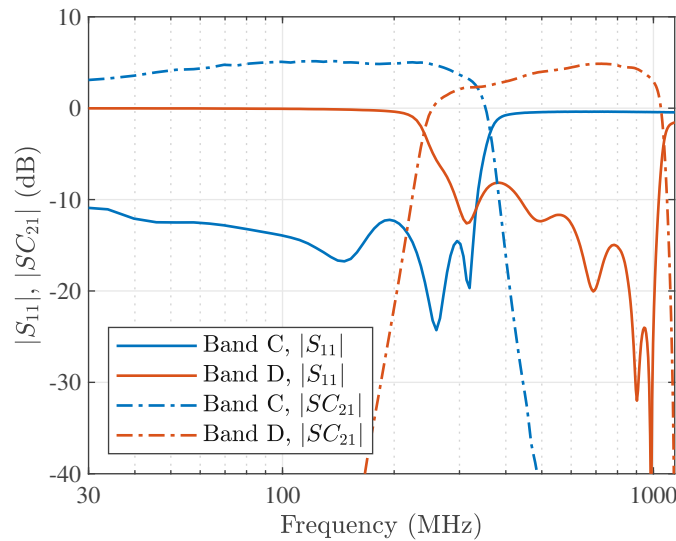


**Fig. 4.7:** Conversion gain and matching of the redesigned upconversion stage having the 40-MHz path configured.

forced match at the RF input by use of a 10-dB attenuator is easily possible while preserving the necessary sensitivity at the same time. Comparing the conversion gain  $|SC_{21}|$  of the initial design, see Fig. 4.5, with the redesign shows that the ripple has been reduced in the new design significantly. In addition, the IF response of the upconversion board is depicted in Fig. 4.8. The impulse bandwidths of the two different IF paths are 20 MHz and 67 MHz, respectively calculated with (2.25).

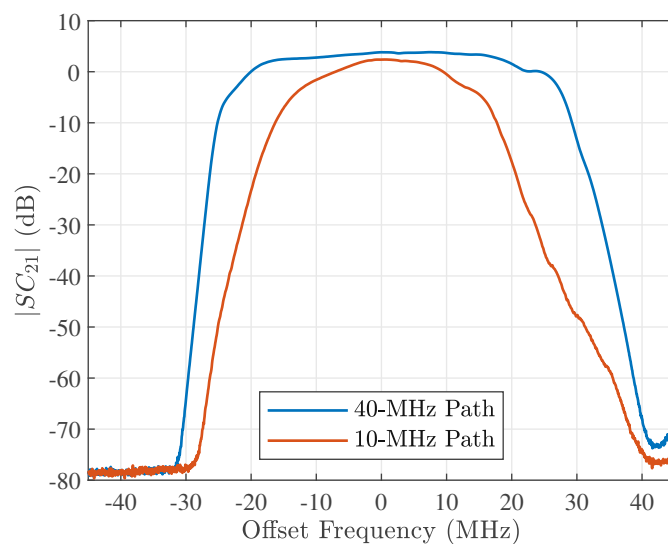


**Fig. 4.8:** IF response of the redesigned upconversion stage,  $f_c = 1227$  MHz.

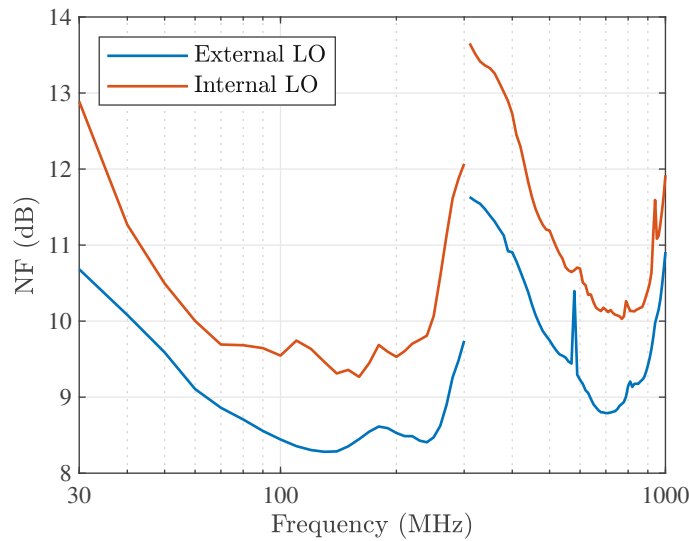


**Fig. 4.9:** NF of the redesigned upconversion stage measured with internal and external LOs.

### 4.3.2 Sensitivity and LO Design

The LO design for high DR mixers is a crucial task regarding spurious emission and system sensitivity. In general, phase-locked loops (PLLs) are used to drive the mixer by creating a desired frequency  $f_{LO}$  from a constant reference source  $f_{REF}$ . The working principle is based on a feedback loop which controls the output frequency of a voltage controlled oscillator (VCO) by comparing the instantaneous phases of the applied reference and a fractional part of the fed back VCO signal [77]. The section in a PLL monitoring the phase alignment is called phase frequency detector (PFD) and can be considered as a simple comparator. Depending on the signals phases, the PFD forces a charge pump (CP) to in-/decrease the tuning voltage supplied to the VCO. The CP is operated at the same frequency as the PFD and thus, spurious emissions occur, repeating periodically relative to the LO carrier. These spurs may distort the upconverted signal due to insufficient isolation between the mixer's LO and IF ports or parasitic coupling effects on the PCB and over-the-air as well. The mentioned problems further aggravate due to the high required LO power level, i.e., 20 dBm, for driving the triple-balanced mixer. Usually, the PFD can only be operated at integer fractions  $R$  of the applied reference source. To avoid CP spur leakage into the IF path for a given LO frequency, the relation  $f_{LO} \pm n f_{REF}/R \neq f_c$  must hold where  $n$  is an integer. Evaluating possible spurs for common references, e.g., 10 MHz, and the target LO frequency range indicates that leakage is inevitable for a static  $f_{REF}$ . To solve this problem, a dual-loop synthesizer has been implemented in the redesigned upconversion stage. With a first PLL, integer multiples of the externally applied source are generated between a frequency range of 100–200 MHz. With the gained freedom of changing the clock frequency supplied to the main synthesizer's PFD, distortions through CP spurs are avoided.

Another important aspect is the phase noise performance of the LO. Especially, the wideband noise floor, dominated by the VCO, can decrease the available DR of a mixer due to feedthrough from the LO into the IF port. For achieving the relatively large LO power level, a high gain is required potentially amplifying the wideband phase noise in excess of the thermal noise floor of the upconversion stage. This effect shall be minimized by additional low and highpass filtering at the main synthesizer output for suppressing phase noise contributions in the IF range. The

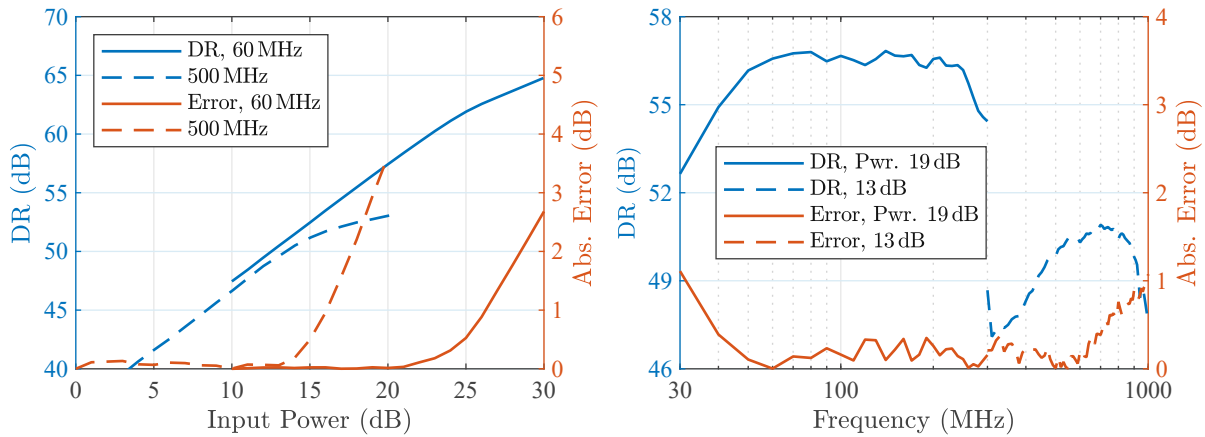


**Fig. 4.10:** Broadband DR of the upconversion stage measuring *CISPR* impulses: power sweep at constant frequency (left) and frequency sweep at constant power (right). The absolute error was evaluated by  $|\hat{\mathcal{I}}_{f_c|CW} - \hat{\mathcal{I}}_{f_c|IMP}|$ .

subsequent attenuator is utilized to level the output power of the gain block to the desired 20 dBm. Intentionally, the filtering was applied before the amplifier to provide a broadband match to the mixer for avoiding load mismatch effects.

To verify the implemented concept, the achieved system sensitivity has been characterized to compare the performances using internal and external LO configurations, see Fig. 4.9. The measurements have been carried out with the setup from Fig. 4.3. Regarding the internal configuration, the LO's output power level has been calibrated using a power meter. The results show that the external LO measurements are in the same range as for the initial prototype. Using the internal LO decreases the sensitivity by approx. 2 dB. The degraded NF can be mainly explained by the thermal noise amplification through the last gain block AMP in the LO section. Even though, the wideband phase noise is suppressed by the preceding filters, thermal noise leaks into the IF band due to insufficient LO-IF isolation. The visible spurs in band D are caused by interference from LTE and DVB-T base stations in close vicinity coupling into peripheral cables, connected to the shielded setup.

### 4.3.3 Broadband Performance

So far, DR requirements have been described with CW stimulus based parameters using the 1-dB compression level. Even though, this parameter gives an initial insight in system capabilities, it lacks of information regarding distortions for broadband signals. To close this gap, the impulse measurement setup, explained in Sec. 3.3, is utilized to identify relevant indication limits regarding *CISPR* impulses. Firstly, the calibration path is used to characterize the impulse source over frequency and power. Subsequently, the CW tone is leveled to the equivalent peak impulse power level indicated by the EMI receiver. Afterwards, the upconversion stage is inserted right in front of the receiver for measuring the calibrated signals at the output RF OUT, centered around  $f_c = 1227$  MHz. In Fig. 4.10, the available DRs of the two individual preselector paths are depicted. On the left hand side, the upconversion stage was tuned with the internal LO to two different frequencies, i.e.,  $f_0 = f_c - f_{LO} = 60$  MHz and  $f_0 = f_{LO} - f_c = 500$  MHz, for

performing a power sweep. The DR is calculated analytically for the 120-kHz filter of (2.24) by taking the stage's conversion gain, NF, and peak output power level into account:

$$\text{DR} = \hat{\mathcal{I}}_{f_c|\text{IMP}} - [-174 \text{ dBm/Hz} + 10 \log_{10}(\text{NF}_{f_0} |SC_{21}|_{f_0} B_N^{\text{CISPR}})]. \quad (4.7)$$

Insertion losses between the upconversion stage and the EMI receiver have been calibrated for the indicated peak power values  $\hat{\mathcal{I}}_{f_c|\text{IMP}}$ . Obviously, the preselector path for *CISPR* band C achieves a higher DR due to the reduced impulse bandwidth. The deviation from linear gain is measured by comparing the detected peak power level with the calibrated CW tone using  $|\hat{\mathcal{I}}_{f_c|\text{CW}} - \hat{\mathcal{I}}_{f_c|\text{IMP}}|$ . The 1-dB compression limit is reached at a DR of 62 dB and 52 dB respectively in band C and D. In principal, both preselector paths achieve the desired 51 dB, required for the quasi-peak detector. However, the compression level changes over frequency. On the right hand side of Fig. 4.10, the achieved DR and error over frequency is depicted at a constant impulse power level. It can be directly seen that the power level must be reduced by a few decibel to keep the error through compression smaller than 1 dB. This causes a reduced available DR at the lower and upper limits of *CISPR* band C/D. While in band C, the DR is in excess of the derived quasi-peak detector requirements, band D is slightly below the 51 dB. As the weighting range has been reduced in the actual version of *CISPR 16-1-1* for this frequency range by 17.5 dB, the upconversion stage is assumed to be compliant [1].

## 4.4 Enhancements

The performance of the designed upconversion stage has been verified in satisfaction to *CISPR 16-1-1* requirements. Now, the development is tested in conjunction with the *USRP B200mini*, investigating if sufficient DR can be achieved for compliant peak and quasi-peak detector measurements. In addition, it is elaborated on operating limits in terms of available analysis bandwidths for speeding up frequency scan times.

### 4.4.1 Available Dynamic Ranges

Out-of-the-box, the broadband DR of the *USRP B200mini* for measuring *CISPR* pulses is limited to about 25 dB, see Sec. 3.3. It was shown with Fig. 3.16 that the best performance is achieved at gain setting 30. While at a higher setting, i.e., 40, the linearity of the SDR frontend strongly degraded, settings 10–20 showed a comparable compression level but a worse sensitivity. Due to saturation of the SDR's receiver frontend, it was impossible to exploit the full DR of the ADCs, even not with the optimum gain setting. As the impulse bandwidth is now strongly reduced by the bandpass filtered output of the upconversion stage, the full ADC DR should be accessible. To verify this, the measurement setup from Fig. 3.13 is used to characterize the SDR in conjunction with the redesigned upconversion stage. The stage's internal LO is tuned such that the frequency content at  $f_0 = 60$  MHz is upconverted to the center frequency of the bandpass filter  $f_c = 1227$  MHz, according to  $f_{\text{LO}} = f_c - f_0 = 1167$  MHz. At the upconversion stage output, the *USRP B200mini* is directly connected. The 40-MHz bandpass path is configured for exposing the SDR to *CISPR* impulses extending over the entire AAF bandwidth. Besides one exception, all settings of the SDR, regarding the sampling rate, AAF bandwidth, etc., have been adopted from Sec. 3.3. Only the IF has been changed to  $f_{\text{IF}} = -500$  kHz which is necessary for further performance verification measurements if smaller AAF bandwidths are needed. The RMS jitter introduced by the upconversion stage was verified to be in the range of a few picoseconds and is thus negligible for averaging the measured impulses according to (3.17).

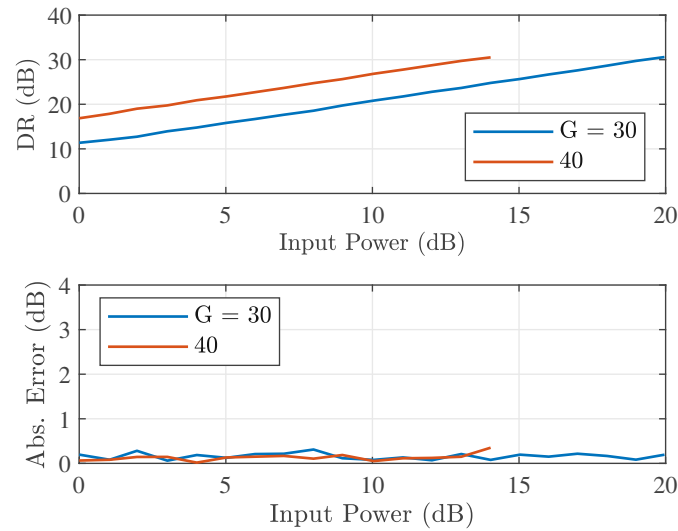


**Fig. 4.11:** Broadband DR of the SDR-based receiver at  $f_0 = 60$  MHz,  $f_{IF} = -500$  kHz, and full AAF bandwidth. The absolute error was evaluated relative to a linearly increasing trace fitted to the measurement data.

The measurement results of a power sweep at different gain settings is depicted in Fig. 4.11. As in Sec. 3.3, the absolute error has been evaluated by use of a linearly increasing trace, fitted to the measurement data. Obviously, the DR traces grow linearly with increasing impulse power ending at 30 dB where full-scale readings of the ADCs are reached. During this sweep, the absolute measurement error is close to 0 dB indicating linear operation of the SDR. The gain settings have been chosen such that the noise floor of the upconversion stage was measurable with the SDR. This was reached at setting 30 where also the highest DR was available. In addition, gain setting 40 was tested to further increase the overall system sensitivity for measurements close to the noise floor. These two settings are analogous to configuration options of professional receivers where the user can decide between a low IF gain setting with best linearity performance and a high IF gain setting where low SNR signals are covered with a higher precision. To conclude, sufficient DR for compliant peak detector measurements is available for both gain settings at maximum AAF bandwidth.

By now, it has been demonstrated that the entire ADC DR is accessible at full AAF bandwidth, i.e., 22.5 MHz. Next, the available DR shall be increased by tuning their cutoff frequencies to a lower value. Due to the decreased peak power at the ADC, the power sweep may be further extended to higher levels. As discussed in Sec. 3.1.2, the AAF bandwidth should not be smaller than 1 MHz to resolve the IF envelope  $|x_{IF}(t)|$  compliantly. Hence, the cutoff frequency of the *USRP B200mini*'s lowpass filters is tuned to the respective limit for measuring the maximum available DR at a single frequency spot, i.e., 60 MHz, see Fig. 4.12. The measurement has been carried out for gain settings 30 and 40 at the two different IF path configurations of the upconversion stage, denoted by  $B = 40$  MHz and  $B = 10$  MHz. As expected, the high IF gain setting traces, i.e.,  $G = 40$ , reach the 1-dB compression level earlier than for setting 30. The best performance is achieved for the low IF gain setting using the 10-MHz IF path. It should be noted that only for this configuration, the full ADC reading was exploited before running into saturation of the SDR's analog frontend. Moreover, the black dashed trace on the left hand side highlights the maximum input power level of the upconversion stage not exceeding the 1-dB

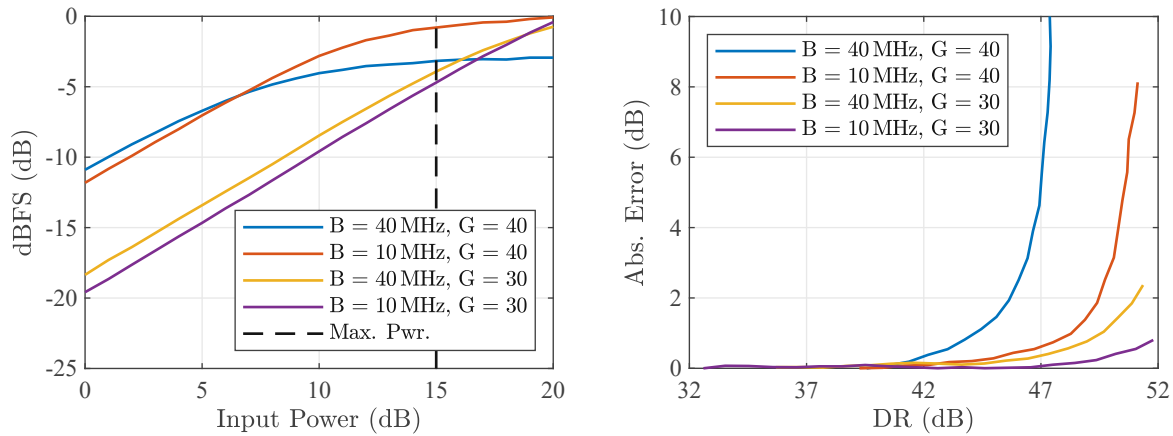


**Fig. 4.12:** Broadband DR of the SDR-based receiver at  $f_0 = 60$  MHz,  $f_{IF} = -500$  kHz, and minimum AAF bandwidth. The absolute error was evaluated relative to a linearly increasing trace fitted to the measurement data.

compression limit over the frequency range of *CISPR* band C. Even though, the power level may be increased beyond this point at certain frequencies, it must be reduced for lower tuning ranges close to 30 MHz, see Fig. 4.10. This means that the required DR of 51 dB for quasi-peak detector measurements can be in principal fulfilled but not over the entire frequency band. The maximum input power level for *CISPR* band D is 6 dB below the black dashed trace of Fig. 4.12. As the required DR in this frequency range is 38 dB, which is easily achieved for both depicted gain settings, band D requirements are considered to be fulfilled.

#### 4.4.2 Available Analysis Bandwidths

Assuming the case of measuring broadband impulses which do not achieve full-scale resolution of the ADC at minimum AAF bandwidth, it might be of interest to increase the analysis bandwidth for speeding up the frequency scan time by using the STFT, see Sec. 2.2.3. By taking the quantized peak amplitude from the power sweep measurement of Fig. 4.12 into account, it is possible to calculate an equivalent bandwidth of the AAF which leads to full-scale resolution of the ADC. As reference, the lowpass filter configuration at  $B_{\text{ref}}^{\text{AAF}} = 1$  MHz cutoff frequency is used. From this definition on, the equivalent bandwidth is defined using:

$$B_{\text{eq}}^{\text{AAF}} = \frac{B_{\text{ref}}^{\text{AAF}}}{\text{dBFS}_{\text{lin}}}. \quad (4.8)$$

The IF responses of the upconversion stage and the SDR are not perfectly flat. Hence, these calculations give an estimate only and require additional verification measurements for precise values. Furthermore, (4.8) does not hold if the SDR's AAF bandwidth is in a similar range as the bandpass filters of the upconversion stage. The calculated bandwidth values, taking the ADC readout (dBFS) up to a compression of 1 dB from linear gain into account, are depicted in Fig. 4.13. While peak detector measurements are already possible at full AAF bandwidth, the quasi-peak detector represents the bottleneck in terms of measurement speed. The required DR for measuring isolated transients in band C is only achieved for the minimum AAF cutoff frequency of 1 MHz which is 22.5 times smaller than for the peak detector. In band D, the

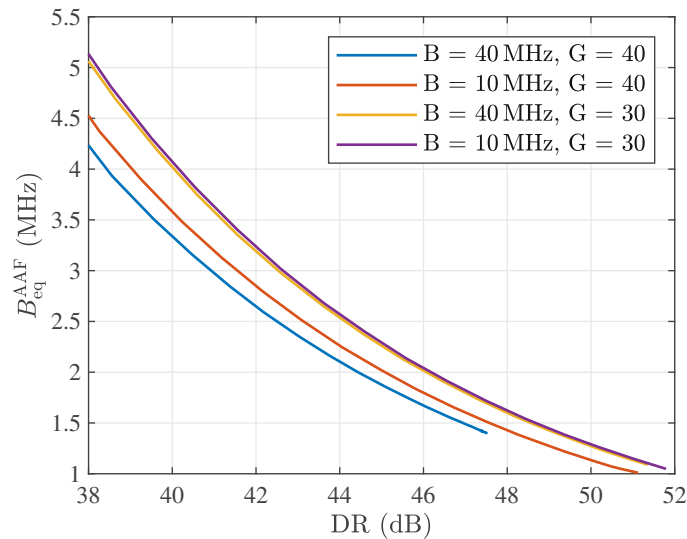


**Fig. 4.13:** Analytically calculated AAF bandwidths vs. DR of the SDR-based receiver.

required DR is 38 dB and allows for an  $B_{\text{eq}}^{\text{AAF}}$  of up to 5 MHz. Due to the mentioned influences through bandwidth dependencies, the graph has not been evaluated below a DR of 38 dB.

#### 4.4.3 Discussion of Further Improvements

It has been demonstrated that the upconversion stage fulfills the DR requirements for compliant quasi-peak detector measurements in *CISPR* band C/D. However, in conjunction with the *USRP B200mini*, the available DR decreases due to the added noise power and limited compression level by the SDR. While in band D, the overall system performance is considered to be sufficient, in band C, it is not possible to cover the full quasi-peak detector weighting range at tuning frequencies below 40 MHz.

The DR problem between 30–40 MHz could be solved by either improving the system's sensitivity or compression level. For the developed setup, the NF can only be improved by increasing the SDR's gain. However, it has been demonstrated that the *USRP B200mini* has an insufficient linearity to exploit the ADC's DR at higher gain settings, i.e.  $G = 40$ . For the redesigned upconversion stage, an SAW filter of quite narrowband bandwidth specifications has been used. The achieved roll-off of available filters for the target center frequency ( $f_c = 1227$  MHz) was not as sharp as for the initial design ( $f_c = 1090$  MHz). The IF responses of the initial and updated designs are compared in Fig. 4.14. The filter centered around 1090 MHz reduces the impulse bandwidth, the SDR is exposed to, further by approx. 6 dB. Due to the lower peak power, it is presumably possible to use gain setting 40 of the *USRP B200mini* without running into saturation by the analog frontend. The improved system sensitivity shall sufficiently increase the DR for quasi-peak detector measurements even at low tuning frequencies. As the initial design had problems with an insufficient RF-IF isolation, it was decided to choose a higher center frequency of the IF section. Unfortunately, it was not possible to find a filter off-the-shelf with a similar transfer characteristic at 1227 MHz. Hence, the design of a customized bandpass filter is considered to be future work for exploiting the available DR of the upconversion stage more efficiently.

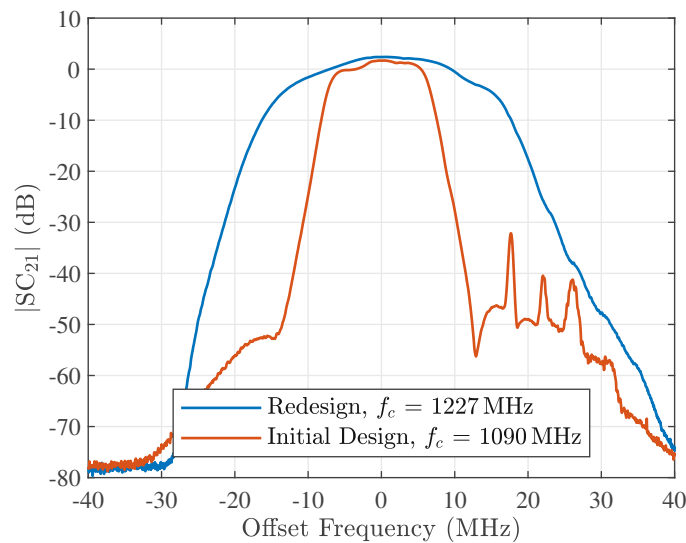


**Fig. 4.14:** IF response comparison of the designed upconversion stage versions.

For improving the compression level of the system, a possible solution may be found with an additional preselector covering the problematic frequency range. This would allow to increase the input power level for broadband impulses and compensating for the reduced DR achieved by the upconversion stage. The implementation of an additional preselector path is more expensive than a customized SAW in general. Moreover, this method implies that the SDR dominates the system's overall NF which holds for the tested gain setting 30.

## 4.5 Gain Control

From the presented results, it is obvious that the analysis bandwidth must be significantly reduced for exploiting the full DR of the quasi peak detector, limiting the frequency scan time severely. A potential solution for improving the system speed could be the application of an automatic gain control (AGC) somewhere between the upconversion stage's output and the SDR's ADC. The idea is to increase the AAF bandwidth and avoiding inherent ADC clipping by a time dependent attenuation of impulse amplitudes. In turn, an AGC could be also used to overcome the degraded DR of the SDR at high gain settings. Due to the improved system sensitivity, the full weighting range of the quasi peak detector gets presumably accessible at critical tuning frequencies of the upconversion stage. As for EMI measurements the absolute amplitude information is crucial, it is necessary to recover the true signal envelope after or during a recording. Moreover, leveling short transients occurring over a few ten nanoseconds only is in general difficult as it requires coherent information about the AGC's gain and appropriate calibrations. In the upcoming sections, a certain AGC type and equalization technique is presented allowing to accurately level broadband impulses without the loss of amplitude information. Because of the focus on low-cost measurement solutions of this thesis, the goal was to implement a standalone solution coming by without complex calibrations.

The following content is based on [71] © 2023 IEEE, which is the output of a collaborative work. While I have performed the system design, feasibility analysis, measurement data evaluation, and major editorial reviews, the first author wrote the manuscript, supported me with verification measurement setups, and coding tasks.

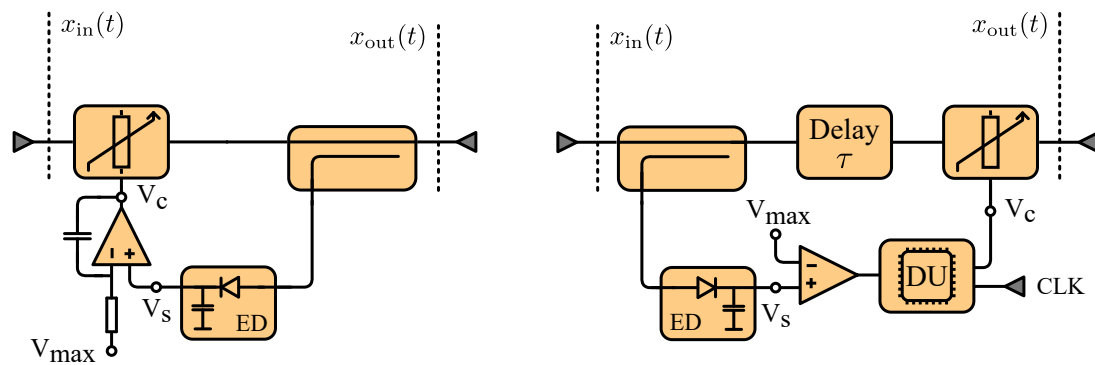


**Fig. 4.15:** Blockdiagram of a classic analog feed back AGC (left) and a digital feed-forward approach (right).

#### 4.5.1 Application of a Feed-Forward AGC

Exploiting the full DR of an ADC is always beneficial in terms of nonlinear distortions and amplitude accuracy [62]. In data link applications, the time behavior of the received signal is often unknown and may have strong amplitude fluctuations due to communication channel effects, e.g., fading. For improving the SNR of the quantized signal on average, it is common practice to dynamically adjust the receiver gain depending on the actual signal level. Traditionally, active gain control is achieved by use of a feedback loop, see Fig. 4.15 (left). In the schematic example, a voltage variable attenuator is biased such that the signal level is close to the full-scale reading  $V_{max}$  of the ADC. The biasing is realized by an integrator evaluating the actual signal level  $V_s$ , provided by an envelope detector (ED), relative to  $V_{max}$ . The rise time of the control signal  $V_c$  is limited by the RC-circuit of the amplifier which ensures stability of the entire system and a biasing signal which the attenuator is able to follow. This approach works well for scenarios where relatively long time sequences need to be sampled. Due to the finite response time of the attenuator and the limited bandwidth of the feedback loop, it is impossible to level broadband impulses. The *USRP B200mini* provides an on-chip AGC which may be used for signal leveling [52]. However, the response time is in the milliseconds range and thus not applicable to short transient signals. A possible solution to compensate these delays can be found if knowledge about the amplitude of the received signal envelope is given. This can be achieved if the feedback loop is transformed into a feed-forward loop, see Fig. 4.15 (right). This structure utilizes a delay line for detecting an ADC overload in advance and adjusting the path loss before an impulse approaches the attenuator at  $t = \tau$ . The digital unit (DU) gets triggered by the comparator and delays  $V_c$  in accordance to  $\tau$ . Advantageous of DU is that no filtering of the decision signal  $V_c$  is required, enabling a fast response time, and digitally controlled attenuators may be utilized, coming by without an analog biasing circuit. Due to a-priori knowledge of an ADC overload, the control signal can be pre-computed and initiated coherent with the provided clock reference. Having information about the AGC's attenuation, synchronized to the sampled data, allows for posterior reconstruction of the leveled signal which is required for EMC measurements.

#### 4.5.2 Signal Reconstruction

Information about absolute power levels is essential for EMC measurements. Hence, it is necessary to accurately reconstruct the leveled signal after quantization for further analysis in the digital domain using, e.g., the peak or quasi-peak detector. The discussed feed-forward AGC approach shall represent a performance improvement of the *USRP B200mini* in combination with the

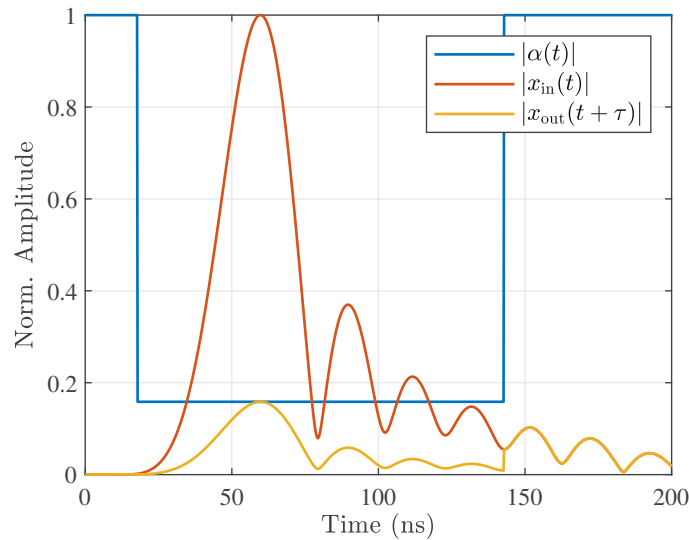


**Fig. 4.16:** Time domain excerpt of the downconverted signals used in (4.10).

upconversion stage. Henceforth, the stage's bandpass filtered output signal going into the AGC is denoted with  $x_{\text{in}}(t)$ . Multiplying this signal with the time dependent attenuation  $\alpha(t)$  yields the output of the AGC which is connected to the SDR:

$$x_{\text{out}}(t) = x_{\text{in}}(t - \tau)\alpha(t). \quad (4.9)$$

The result of this multiplication is then downconverted into complex baseband according to:

$$\begin{aligned} x_{\text{BB}}(t) &= (x_{\text{in}}(t - \tau)\alpha(t)e^{-jw_{\text{LO}}t}) * h_{\text{AAF}}(t) \\ &= (x_{\text{out}}(t)e^{-jw_{\text{LO}}t}) * h_{\text{AAF}}(t). \end{aligned} \quad (4.10)$$

An example of an impulse passing through this system is depicted in Fig. 4.16. As a test signal, the normalized time domain response of the upconversion stage, having the 40-MHz path configured, is taken. The attenuator and the comparator are generated using rectangular signals of infinitely fast rise times. In excess of a certain signal level threshold, i.e.,  $\text{th} = -16$  dB, the digitally stepped attenuator gets triggered and changes from 0 dB insertion loss to 16 dB. To ensure stability during  $|x_{\text{in}}(t)| < \text{th}$ , the comparator signal is elongated by at least three clock cycles of the synchronized SDR, where  $1/f_s = 17.9$  ns. The delay  $\tau$  has been chosen such that  $\alpha(t)$  is already active before the impulse approaches the attenuator. This is essential to reduce frequency spreading which is discussed hereinafter. After sampling, the signal reads  $x_{\text{BB}}[k] = x_{\text{BB}}(kT_s)$ . For signal reconstruction, it is necessary to dispose of the time dependent gain variations by  $\alpha(t)$ . Due to the multiplication in (4.9), firstly,  $x_{\text{BB}}[k]$  must be deconvolved with the inverse of the AAF:

$$h_{\text{AAF}}^{-1}[k] = \mathcal{F}\mathcal{F}\mathcal{T}^{-1}\left\{\frac{1}{H_{\text{AAF}}(e^{j\theta})}\right\} \quad (4.11)$$

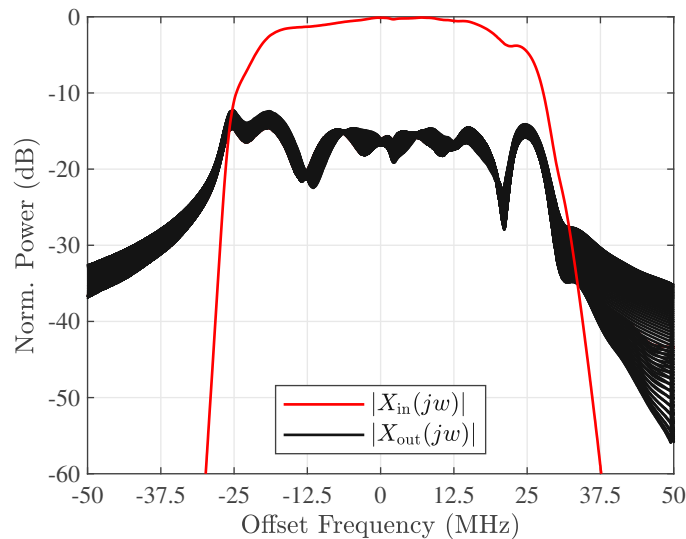


**Fig. 4.17:** Spectral broadening due to the finite trigger response time of DU to asynchronously detected events,  $f_c = 1227$  MHz.

where  $H_{\text{AAF}}(e^{j\theta}) = \mathcal{FFT}\{h_{\text{AAF}}[k]\}$ , before equalizing the attenuator's influence<sup>1</sup>. Afterwards, the reconstructed signal is again convolved with  $h_{\text{AAF}}[k]$  resulting in the new baseband signal:

$$x'_{\text{BB}}[k] = \frac{x_{\text{BB}}[k] * h_{\text{AAF}}^{-1}[k]}{\alpha[k]} * h_{\text{AAF}}[k]. \quad (4.12)$$

In general, this equalization technique refers to the well known zero-forcing principle requiring perfect knowledge of the two functions  $\alpha[k]$  and  $h_{\text{AAF}}[k]$  for optimum performance. Potential pitfalls impeding this approach are summarized below.

1. Due to fast switching times by the attenuator, the signal spectrum of  $x_{\text{in}}(t)$  gets broadened. The finite time resolution of the SDR's ADC limits the observable signal bandwidth, i.e.,  $f_s = 56$  MSa/s. Hence, information about spreaded frequency content located out of this band gets lost. To solve this, the attenuation time can be extended until the ringing of the depicted impulse response has subsided. However, signal content might get lost in noise during this time requiring further evaluation if this is acceptable.
2. The digital unit DU must save information about the monitored attenuator control stimulus to enable a posterior reconstruction of  $\alpha[k]$ . As the power detector triggers DU asynchronously to the reference clock, a maximum jitter between  $\alpha(t)$  and  $x_{\text{in}}(t)$  of one clock cycle occurs. This changes the spectrum of the attenuated signal which is demonstrated in Fig. 4.17 for a jitter  $t_j$  varying between  $-\Delta_t/2 \leq t_j \leq \Delta_t/2$ , where  $\Delta_t = 1/f_s = 17.9$  ns. The resulting spectra are visualized as an overlay in comparison to the undistorted spectrum. Due to the different frequency spreadings, it is obvious that the reconstructed signal underlies an amplitude uncertainty over frequency which cannot be calibrated.
3. Zero-forcing poses high demands on the DR of the receiver. Even though, if the sampling rate of the SDR may be extended sufficiently to cover the spreaded frequency content and

<sup>1</sup>The inverse  $h_{\text{AAF}}^{-1}[k]$  can only be computed if  $H_{\text{AAF}}(e^{j\theta})$  has no zeros. As the AAF in the *USRP B200mini* shows a finite suppression within the investigated bandwidth, this problem is negligible.

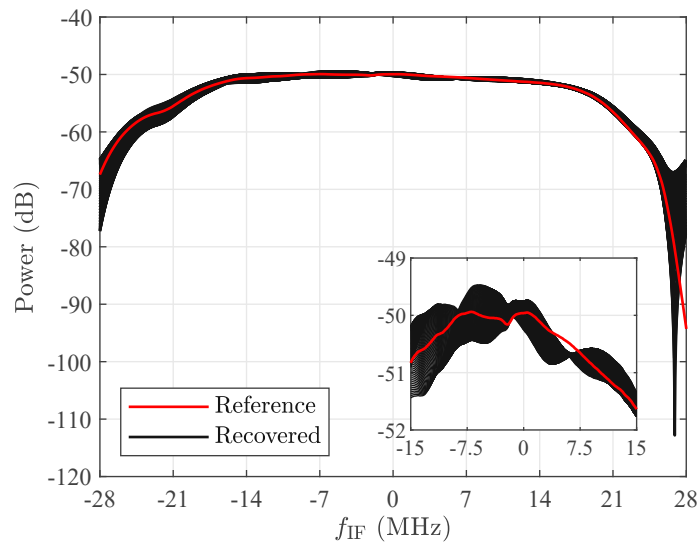


**Fig. 4.18:** Recovered signal spectrum taking the timing uncertainty into account.

$h_{\text{AAF}}[k]$  is perfectly known, there is still the characteristic noise amplification problem. Due to the limited DR of the SDR's frontend and ADC, the noise increases after zero-forcing at frequencies where the AAF suppression is high. Consequently, it comes to an over estimation of the spreaded frequency content buried in noise corrupting signal reconstruction.

To investigate the accuracy of the discussed feed-forward AGC approach, a simulation is performed, reconstructing the signal from Fig. 4.16 in accordance to (4.12). The AAF is modeled with a Butterworth filter of third order having a 3-dB bandwidth of 22.5 MHz. Furthermore, the rectangular attenuator response, which is coherent with the SDR's ADC clock, is decimated to the baseband sampling frequency  $f_s$  for getting  $\alpha[k]$ . Afterwards, the signal is processed by the *CISPR* filter for gaining the peak detected power over  $f_{\text{IF}}$ . The recovered signal, taking the asynchronous trigger delay into account, is compared to the undistorted impulse response in Fig. 4.18. It can be seen that the amplitude uncertainty requirement of *CISPR 16-1-1*, which is  $\pm 1.5$  dB, between  $|f_{\text{IF}}| \leq 15$  MHz is fulfilled. Consequently, a prototype is built to verify the simulation.

### 4.5.3 System Design

In what follows, the implementation of the target feed-forward AGC is discussed. A block diagram and a corresponding picture of the realized setup are given in Fig. 4.19 and Fig. 4.20 respectively. The signal coming from the upconversion stage  $x_{\text{in}}(t)$  is divided via a 6-dB splitter into two paths feeding a power detector, indicating potential ADC overloads, and the main signal path producing  $x_{\text{out}}(t)$ , which is further processed by the SDR. The digital control unit is implemented in the SDR's FPGA having the same clock reference as the RFIC incorporating the ADCs. Recording coherent information of the attenuator control signal  $V_c$ , which is synchronous to the ADC clock, enables signal reconstruction in a post processing step on the host PC. Below, the functional blocks are discussed more in detail.

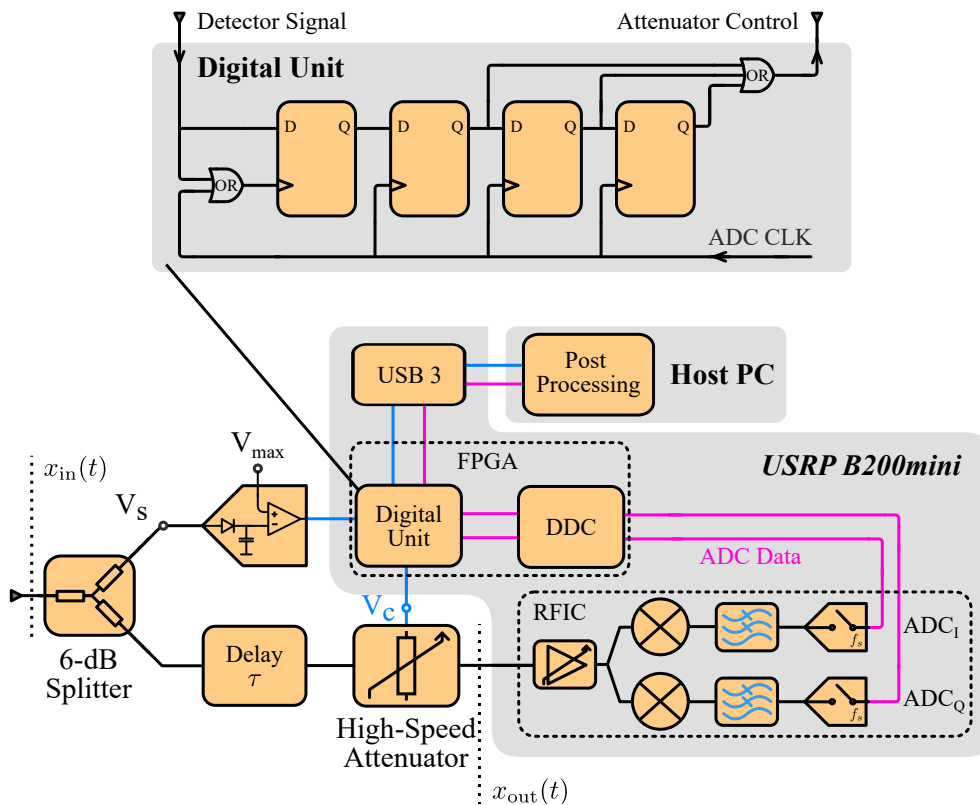


Fig. 4.19: Block diagram of the feed-forward AGC implementation approach [71] © 2023 IEEE.

### Attenuator and Detector

To satisfy the timing constraints of the simulation, a FET based digitally-stepped attenuator *AT-232-PIN* from Macom is used. By specification, this device needs 12 ns for changing the path loss from 0 to 16 dB. As the transition speed is well within one sample of the SDR, it is possible to model  $\alpha[k]$  using a rectangular signal, as it was done in the simulation.

For the a-priori ADC overload indication, the power detector *LTC5564* from Analog Devices is used. The selection of this component bases on the required demodulation bandwidth which is up to 75 MHz and thus in satisfaction with the upconversion stage's 40-MHz IF path. In addition, the detector features a digital output which is directly fed into the SDR via the GPIO ports of the FPGA where the digital unit is implemented for triggering the attenuator.

As the attenuator and power detector required additional electrical circuits, e.g., biasings and single-ended to differential conversion, it was decided to implement the respective building blocks on a single PCB, see Fig. 4.20.

### Digital Unit

As the *USR P B200mini* incorporates an FPGA with GPIO pins, it is possible to handle the tasks of the digital unit right on the device. These tasks involve recording of ADC overload events indicated by the power detector and triggering of the attenuator for leveling the impulses. In particular, the detector signal is processed by a concatenation of D-latches which is magnified in the top of the block diagram. Potential overloads are clocked into the FPGA asynchronously by the first latch which overtakes any event coming from the power detector. The next three latches are used to lengthen the attenuator control signal to at least three clock cycles, as it was done in the simulation. With the amount of latches right after the asynchronous detection, the

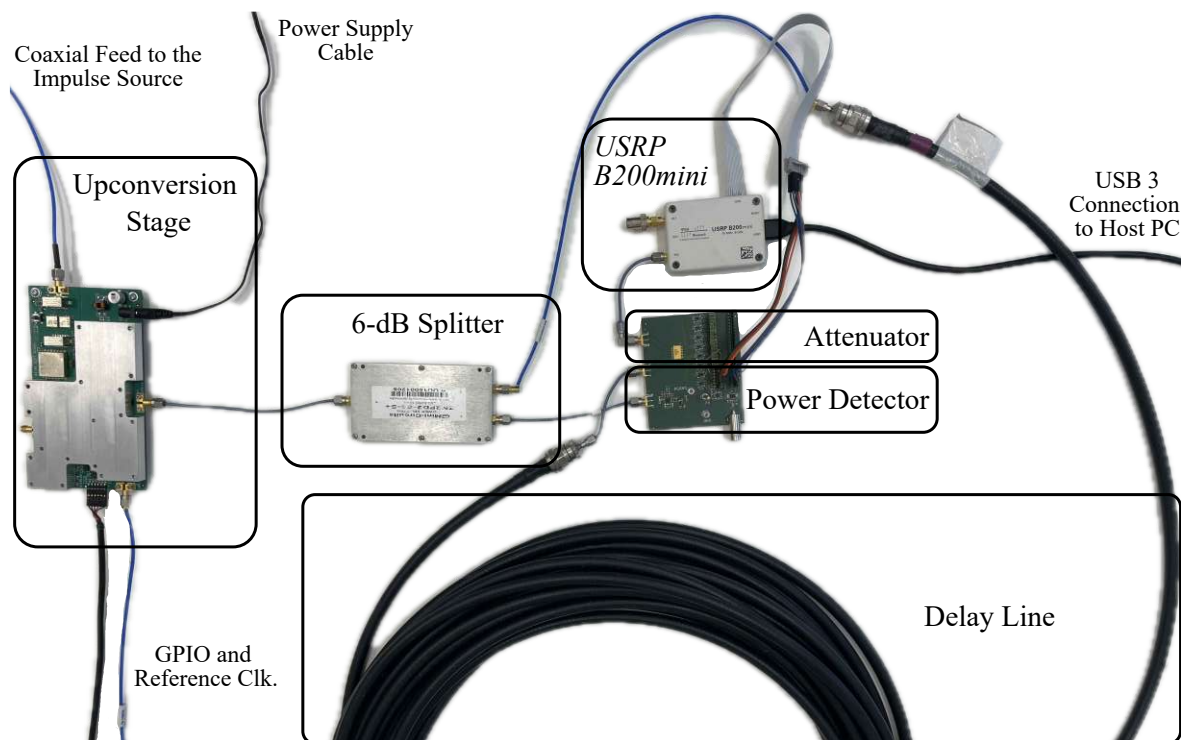


**Fig. 4.20:** Measurement setup for characterizing the feed-forward AGC.

attenuator control signal can be adjusted to the propagation delay of the setup. The stimulus  $V_c$  is forwarded to the host PC coherently with the ADC data.

### Delay Line

In general, every kind of element may be used which produces sufficient propagation delay to compensate response times of the system. For the developed AGC, a response time of approx. 70 ns had to be expected. In addition, it is desired to have constant transfer characteristics and low dispersion effects in the frequency range of interest to avoid additional calibrations.

For demonstration purposes, an appropriate delay line has been found by a 30 m long RF cable introducing a group delay of approx. 150 ns. As this is a quite bulky solution, the idea was to use an SAW-based delay line instead for miniaturization purposes. Unfortunately, this idea had to be dropped due to vague estimated delivery delays of dual-use products during the Ukraine conflict. As acoustic filters have problems with signal dispersion effects, suitability investigations of such delay lines are considered to be future work.

### 4.5.4 System Verification

As a next step, the discussed system from Fig. 4.19 is verified in conjunction with the upconversion stage measuring *CISPR* impulses. The realized setup is depicted in Fig. 4.20 without the impulse source which was directly connected to the receiving aperture. For leveling the maximum amplitude, not clipping the ADC's full-scale voltage  $V_{\max}$ , the AGC was set to 16 dB path loss. Afterwards, the power detector threshold was adjusted such that the attenuator switches between 0 dB and 16 dB if the signal envelope, coming from the upconversion stage's output, is more than  $V_{\max} - 16$  dB.

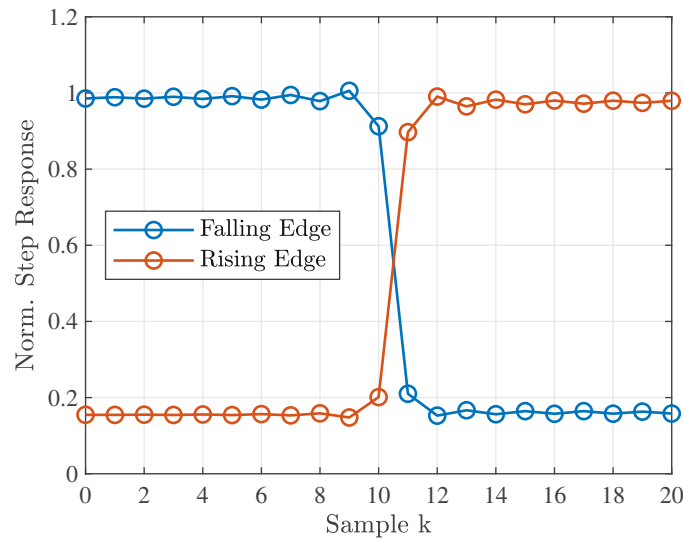


**Fig. 4.21:** Normalized step responses of the attenuator for modeling  $\alpha[k]$  at  $f_s = 56$  MSa/s [71] © 2023 IEEE.

For signal reconstruction according to (4.12), information about  $h_{\text{AAF}}[k]$  and  $\alpha[k]$  is mandatory. These two parameters are extracted by performing a two-step calibration procedure.

Firstly, the AAF response is characterized by measuring a PN sequence, generated with a VSG, which is correlated with the original signal in complex baseband for obtaining the normalized impulse response of the SDR [78]. The accuracy of this approach can be controlled by the length of the sequence in time domain. Due to the phase stability problem of the *USRP B200mini*, it is necessary to repeat this measurement several times with a relatively short correlation signal, e.g., 1 ms. Otherwise, the correlation fails if the sequence is made too long. To gain  $h_{\text{AAF}}[k]$ , 1000 sequences have been averaged.

Secondly, the attenuator is calibrated. The transfer characteristics of the *AT-232-PIN* are assumed to be constant over the frequency range of the 40-MHz IF path which was verified with an S-parameter measurement in advance. The transient response, however, is characterized by measuring a single tone and alternating the AGC's path loss repeatedly to gain information about the rising and falling edges, see Fig. 4.21. The depicted transitions have been measured with a tone located at  $f_{\text{IF}} = -1$  MHz in complex baseband of the SDR and a switching frequency of 10 kHz. Larger offset frequencies have been investigated as well but did not lead to success due to an unsymmetrical attenuation in frequency domain of the tone's amplitude modulated spectrum. In addition, the signals have been deconvolved with  $h_{\text{AAF}}^{-1}[k]$  as it is required for (4.12). A further aim of this measurement is to calibrate state dependent changes of the transfer characteristics during switching. Because the attenuator responds almost within one sample, modeling  $\alpha[k]$  using a rectangular signal, as it was done in the simulation, is possible. Due to the changing group delay of the attenuator at different gain settings, the function is complex valued.

It shall be emphasized that the step response of the *USRP B200mini* introduces a significant amount of ringing. The time domain signal of clipped impulses gets lengthened over dozens of samples and may interfere with consecutive signals causing an amplitude uncertainty. Hence, for recalculating the attenuated signal, the equalization step is mandatory as the rectangular signal assumption of  $\alpha[k]$  is violated otherwise.

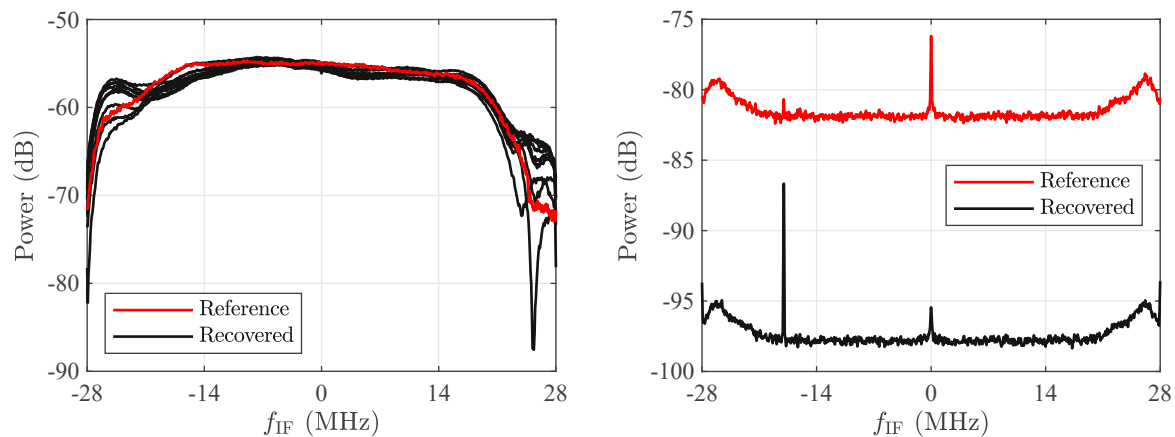


**Fig. 4.22:** Measurement results of the AGC over  $f_{IF}$  indicating peak detected impulse spectra (left) and the RMS noise power spectra (right) [71] © 2023 IEEE.

To test the created setup from Fig. 4.20, a sequence of ten impulses was measured and processed according to (4.12). The peak detected spectrum of each transient has been computed with the STFT-based method and is depicted in Fig. 4.22. Besides the time overlap of the FFT window, i.e., 99%, the remaining settings for signal analysis have been adopted from Sec. 3.2.2. In comparison, the same sequence has been measured with constant attenuation at 16 dB visualized as reference trace. To reduce the impact of thermal noise, the reference impulse spectrum has been averaged. The recovered traces show a similar behavior as in the simulation and stay within the allowed amplitude error bound of  $\pm 1.5$  dB within  $|f_{IF}| \leq 14$  MHz. The increased amplitude uncertainty of the spectrum close to  $|f_{IF}| = 28$  MHz originates from a slightly different time offset between  $\alpha(t)$  and  $x(t)$  for the measurement and specific aliasing effects by the SDR. Simulations have shown that the amplitude accuracy can be improved if the attenuation time interval is lengthened. Moreover, the RMS noise power level is shown for the two different operating conditions. One can see that the SNR is increased by approximately 16 dB in active state of the AGC. The frequency spur around  $-18$  MHz originates from the upconversion stage and is almost completely buried in noise for the reference trace.

To conclude, the application of a feed-forward AGC has been successfully demonstrated. Impulses with a bandwidth of more than 40 MHz have been leveled and recalculated, fulfilling error bounds of *CISPR 16-1-1*. Hence, either the available DR at constant AAF bandwidth can be enhanced by up to 16 dB or the SDR's available AAF bandwidth may be increased by a factor of up to 6.3 at constant DR (see Sec. 4.4), if the overall measurement tolerances allow to. Due to the simple recalibration procedure, it is possible to implement the presented approach directly into the *USRP B200mini*'s FPGA. Currently, the delay line was realized by a 30 m long RF cable. Instead of the cable, it might be possible to utilize SAW delay lines fitting into small SMD packages for reducing the AGC's size. Regarding the applicability of this alternative approach, further investigations of signal distortion through inherent dispersion effects need to be done and is considered to be future work.

---

## System Verification

---

Within this chapter, the measurement accuracy of the designed system comprising the *USRP B200mini* and the upconversion stage is investigated. This task is treated in three sections: At the beginning, the detector performances are analyzed according to *CISPR 16-1-1* measurement methods. In a next step, the applicability of the broadband IF signal processing architecture using the STFT is tested for evaluation of potential frequency scan time savings. Furthermore, the radiated emission spectrum of a test EUT is characterized using a low-cost TEM cell which has been specifically designed for this thesis by the author. The same EUT is investigated in three different accredited EMC measurement halls and one fully-compliant GTEM-cell-based setup. Comparing these measurement results shall give an impression how well the designed setup works, performing compliance estimates in advance. Lastly, it is went trough an overall budget estimate of the used measurement solution to evaluate the relevance and justification of this thesis.

The content of Sec. 5.3 is an excerpt of the author's publications [20, 29] and contains revised text passages and graphs.

### 5.1 Classic Single Frequency Metering

The classic EMI receiver, depicted in Fig. 2.7, has one detector path implemented and stays tuned to a single frequency  $f_0$  until a certain dwell time has elapsed. Even though, the scan time is considerably slower than for the STFT-based approach where multiple detector paths can be parallelized, the accuracy is higher as no amplitude error due to windowing take effect.

For measuring the entire DR of the quasi-peak detector with the developed SDR-based receiver requires to reduce the AAF bandwidth of the *USRP B200mini* to 1 MHz. In this configuration, only one detector path can be used to guarantee that the measured signal envelope is not limited by the transfer characteristics of the SDR. Hence, only single frequency metering is possible if even isolated transients want to be detected with the quasi-peak detector.

In what follows, it is concentrated on the developed measurement solution performing the classic EMI receiver operating principle. In particular, it shall be investigated if compliant quasi-peak detector measurements are feasible which has been pursued throughout this thesis extensively.

#### 5.1.1 Detector Implementation

While the peak detector is easily implemented by capturing the maximum signal envelope, the quasi-peak detector is a more sophisticated topic. Several works have been published on the

implementation using different approaches. The results of these publications indicate that each technique achieves different accuracies at the expense of system complexity and computational effort. It is shown in [43] that even the intrinsic direct-envelope detector, see Sec. 2.2.1, shows significant deviations from the ideal and analytically derived response curve, specified in *CISPR 16-1-1*. Due to the lower computational effort, it is preferred to compute the signal envelope before passing the quasi-peak detector. In [53], a real-time applicable method is presented, applying this technique. Due to weighting the signal envelope, larger errors from the ideal response occur. The author of [43] compensates this problem by modeling the charging circuit of the quasi-peak detector with a second order lowpass filter. As this approach achieved the best compromise between accuracy and computational effort, it was decided to utilize this implementation for upcoming measurements. In accordance to (2.26), the envelope  $|x_{\text{IF}}(t)|$  is now weighted with the lowpass filter  $h_{\text{LFPF}}(t) \circ \bullet H_{\text{LFPF}}(s) = w_0^2 / (s^2 + 2\vartheta w_0 s + w_0^2)$ :

$$x_{\mathcal{D}}(t) = \begin{cases} |x_{\text{IF}}(t)| * h_{\text{LFPF}}(t) & x_{\mathcal{D}}(t) \leq |x_{\text{IF}}(t)| \\ x_{\mathcal{D}}(t_0) e^{-\frac{t_0-t}{\tau_d}} & x_{\mathcal{D}}(t) \stackrel{t=t_0}{>} |x_{\text{IF}}(t)| \end{cases} \quad (5.1)$$

where the damping  $\vartheta = 6$ ,  $w_0 = 2\pi/\tau_c$ , and  $\tau_c = 0.35$  ms. The parameters of the indication instrument from (2.27) were adjusted to  $\vartheta = 12$  and  $T_{\text{M}} = 130$  ms for fulfilling *CISPR* requirements. The parameter adaptation of  $T_{\text{M}}$  and  $\tau_c$  is a convenient way to compensate occurring detector deviations. It is clearly stated in *CISPR 16-1-1 Annex H* that no verification measurements on these parameters are conducted. Only, certain error bounds of absolute and relative accuracy measurements, testing the EMI receiver as a whole system, must be met which are treated hereinafter.

### 5.1.2 Absolute Accuracy

In *CISPR 16-1-1*, the absolute detector accuracy is verified by comparing the detected impulse power level with a calibrated CW signal which shall cause the same indication level. This measurement must be performed at a defined power level yielding the indication  $\hat{\mathcal{I}}_{f_0} = 60$  dB  $\mu\text{V}$ . The peak voltage at the *CISPR* impulse source output is about 73.3 V in this test case. To prevent the upconversion stage from permanent damage, the signal is attenuated appropriately at the preselector input<sup>1</sup>. The allowed deviation between the two measurements must fulfill  $\epsilon = |\hat{\mathcal{I}}_{f_0|\text{CW}} - \hat{\mathcal{I}}_{f_0|\text{IMP}}| \leq 1.5$  dB over the entire *CISPR* band C/D. As the impulse's bandwidth extends over the complete band, this verification measurements has a secondary benefit as it indicates the impact of modulation products or saturation effects impeding accurate measurements.

All detector characterization measurements in this section were performed with the setup from Fig. 3.13 with the only difference that no correlation sequences were injected as no averaging was performed. During calibration, the CW power level was adjusted to the peak detected impulse level and the EMI receiver's specific IF impulse bandwidth has been compensated. By definition, the quasi-peak detector must indicate 12 dB less than the peak detector at an impulse repetition rate of 100 Hz. Hence, for verifying the absolute accuracy of the quasi-peak detector, this number is subtracted from  $\hat{\mathcal{I}}_{f_0|\text{CW}}$ . The measured detector accuracies over frequency and different gain settings are depicted in Fig. 5.1. For single frequency metering, the SDR configurations from Sec. 4.4 have been adopted:  $f_s = 56$  MSa/s,  $B_{\text{AAF}} = 1$  MHz,  $f_{\text{IF}} = -500$  kHz, and  $f_{\text{LO}} = f_c - f_{\text{IF}}$ . To preserve optimum linearity of the SDR, the 10-MHz bandpass filter path of the upconversion stage was used. For minimizing the influence of thermal noise, the measurements were performed

<sup>1</sup>Even though, professional receivers incorporate a transient protected input, preventing from permanent damage if such high voltage peaks occur, the signal still must be attenuated to avoid a system overload.

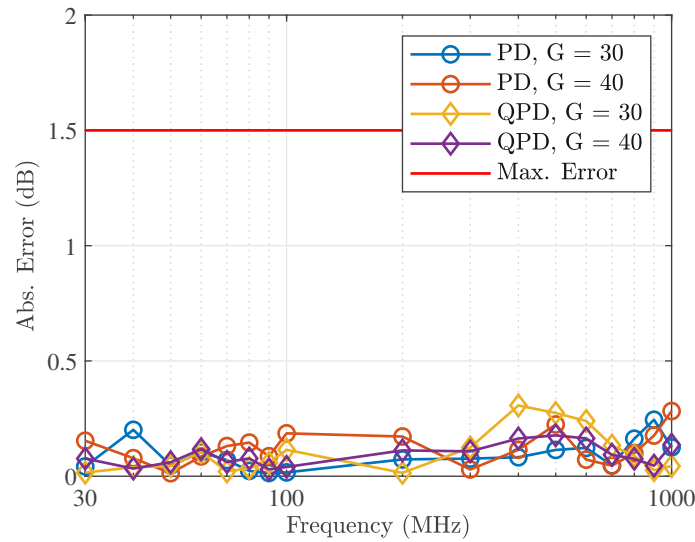


**Fig. 5.1:** Absolute detector accuracy  $\epsilon$  of the peak and quasi-peak detector over frequency.

at an SNR larger than 35 dB. It can be seen from the graphs that the detector deviations are well within the allowed error bound of 1.5 dB.

### 5.1.3 Relative Accuracy

Concerning the quasi-peak detector, the response to recurrent impulses must hold certain error boundaries depending on the repetition rate  $f_{\text{rep}}$ . To verify this, the impulse source power level is adjusted such that the 1-dB compression level of the receiver is reached. This shall indicate the achieved overload factor (OVF). Next, the quasi-peak detected level is measured at  $f_{\text{rep}} = 100$  Hz representing the reference value  $\hat{I}_{f_0|100\text{Hz}}$ . Then,  $f_{\text{rep}}$  is reduced to specified frequencies and the detected value is compared according to  $\hat{I}_{f_0|f_{\text{rep}}} - \hat{I}_{f_0|100\text{Hz}}$ . The measurement results of this procedure and the allowed error bounds are visualized in Fig. 5.2 and Fig. 5.3 for gain setting 30 and 40 respectively. The measurement setup configurations have been adopted from the previous measurements on the absolute accuracy. For demonstration purposes, the upconversion stage has been tuned to certain frequencies covering the spots of largest and lowest DRs. To remember, in *CISPR* band C (30 MHz–300 MHz), it is necessary to detect even isolated transients appropriately. While in band D (300 MHz–1 GHz), a repetition rate of 10 Hz is already sufficient. One can see from Fig. 5.2 that the relative responses match *CISPR* requirements well with one exception. The 30 MHz trace fails for  $f_{\text{rep}} < 2$  Hz and requires an additional preselection filter to accurately weight an isolated transient. Therefore, the lowpass *SLP-90+* from Mini-Circuits, having a bandwidth of 90 MHz, was applied directly at the upconversion stage input. The corresponding trace, now fulfilling the requirements, is denoted with "30 MHz filt.". It can be obtained from the graphs that the achieved weighting range is best in *CISPR* band C when using gain setting 30 while in band D both settings may be used to achieve the required OVF.

The quasi-peak detector accuracy depends on the individual implementation which must solely fulfill some relatively large error bounds which are up to  $\pm 2$  dB. To uncouple performance verifications from this detector, the available DR of the low-cost measurement system is compared to a professional EMI receiver, i.e., Keysight Technologies *MXE N9038A*, fully complying with *CISPR 16-1-1*. The averaged signal envelopes at maximum indication level of the receivers,

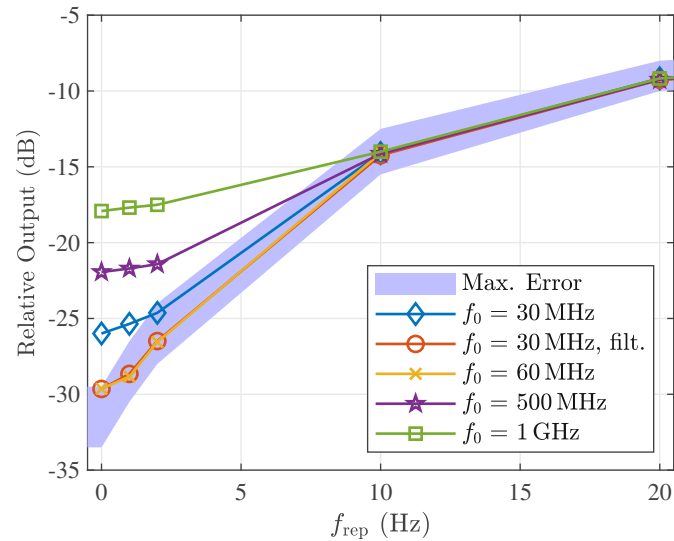


**Fig. 5.2:** Relative accuracy of the envelope quasi-peak detector at gain setting  $G = 30$ .

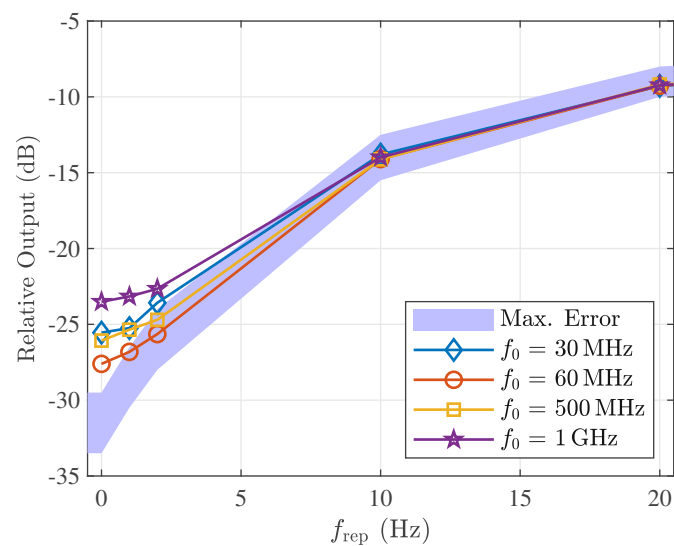


**Fig. 5.3:** Relative accuracy of the envelope quasi-peak detector at gain setting  $G = 40$ .

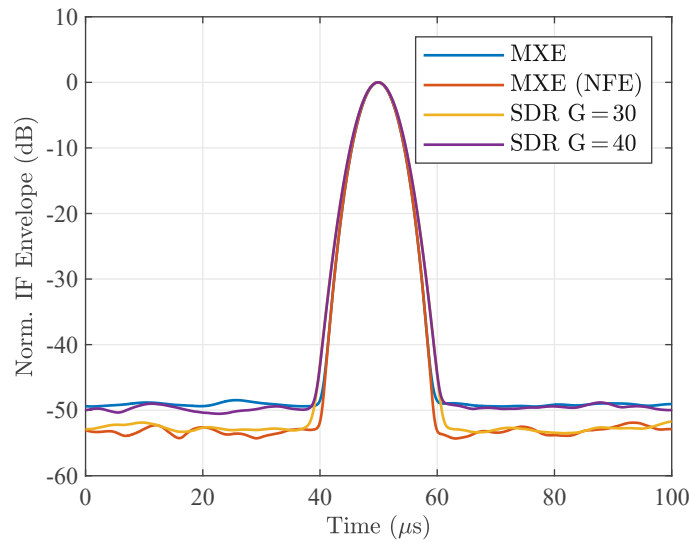


**Fig. 5.4:** Available DR comparison with fully-compliant EMI receiver Keysight Technologies MXE *N9038A*.

measuring *CISPR* impulses, are depicted in Fig. 5.4 for  $f_0 = 60$  MHz. The MXE achieves a DR of 50 dB and 53 dB with a digital noise reduction technique, denoted by the manufacturer with noise figure extension (NFE). These values match with the performance of other EMI receivers well which has been demonstrated in [9]. Coincidentally, the traces measured with the *USRP B200mini* overlap with the ones of the MXE. Hence, it can be concluded that the SDR-based setup achieves a comparable OVF as equipment been certified with full compliance of *CISPR 16-1-1*.

#### 5.1.4 Overload Detection

A system overload occurs if the receiver is exposed to signal levels which are above its 1-dB compression level. It is a difficult task to identify the section of a receiver chain being in saturation, especially, if unknown transient signals must be measured. For the SDR-based measurement setup, the most obvious way to identify an overload is the signal level indicated by the ADC at full sampling rate. When performing single frequency metering, the AAF bandwidth is pretty low and the maximum signal level delivered by the ADC cannot be used anymore as a system overload indicator unrestrictedly. While the identification of CW signals in excess of the usable indication range is an easy task, it has been shown in Fig. 4.12 that the *USRP B200mini* can be driven into saturation easily before reaching full-scale reading of the ADC when measuring *CISPR* impulses using gain setting 40. Hence, even if the achieved DR for quasi-peak detector measurements are better over frequency using the high IF gain setting, one is better advised to use the low IF gain to prevent from wrong measurement results. In this configuration, the 1-dB compression level of the total system equals the full-scale indication of the SDR's ADC allowing a reliable estimate of a system overload in case of broadband impulses. Another approach to close the gap between the 1-dB compression level and the full-scale level of the ADC when using the high IF gain setting is to increase the AAF bandwidth in accordance to Fig. 4.13.

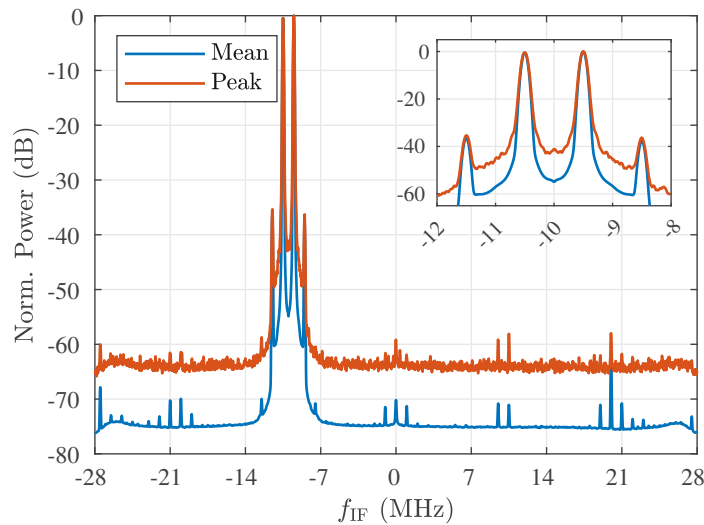


**Fig. 5.5:** Intermodulation distortion measurement using a two-tone with a distance of 1 MHz.

## 5.2 Broadband IF Capabilities

When performing a radiated emission test, it is common practice to conduct a fast initial pre-scan using the peak detector for finding critical frequency spots, potentially violating the defined emission limit. Afterwards, these spots are remeasured over long recording times ( $T_{\text{rec}} \geq 1$  s) taking secondary detectors into account, e.g., the quasi-peak. It has been shown in Sec. 4.4 that the SDR-based setup achieves sufficient DR for peak detector measurement even at full AAF bandwidth having the 40-MHz IF path of the upconversion stage configured. Hence, by use of the STFT-based signal analysis method, which was elaborated on in Sec. 2.2.3, the frequency scan time presumably can be improved significantly during the pre-scan in comparison to single frequency metering. Goal of this section is to investigate the suitability of the built SDR-based setup regarding this measurement technique.

### 5.2.1 Spectral Purity

The CW requirements and the achieved DR of the *USRP B200mini* have been investigated thoroughly in Sec. 3.2. However, when performing signal detection over multiple IF streams simultaneously, frequency spurs of arbitrary source may impede an accurate pre-scan. To investigate the spectral purity in terms of narrowband signals, a two-tone measurement was performed, see Fig. 5.5. The upconversion stage was tuned to 1 GHz, having the 40-MHz IF path activated. Furthermore, the SDR was configured to  $f_s = 56$  MSa/s,  $B_{\text{AAF}} = 22.5$  MHz,  $G = 40$ , and  $f_{\text{LO}} = f_c$ . For signal analysis using the STFT, the full ADC bandwidth has been taken into account with a window overlap of 90% and a bin resolution of 1 kHz. The signal envelope was leveled 3 dB below full-scale reading of the ADC at a tone distance of 1 MHz. Besides image frequencies, the main part of visible spurs is caused by nonlinearities of the analog receiver frontend. The largest frequency spurs are close to the two-tone and originate from a nonlinearity of third order. On the upper right, the two-tone signal is magnified for giving an insight into the phase noise performance of the system. It can be directly seen that the peak detected noise floor between the tones is limited to  $-40$  dBc, although, the IF filter selectivity would go below this level. The measurement has been repeated without the upconversion stage leading to the same

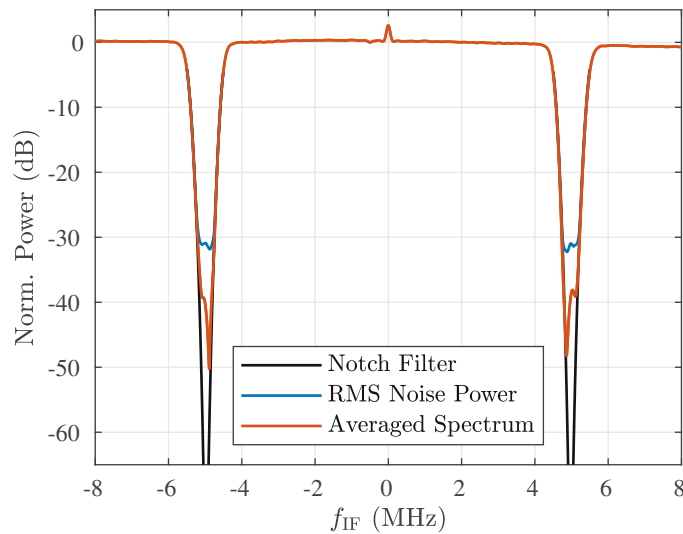


**Fig. 5.6:** Spectral regrowth measurement using a notch filtered impulse.

results indicating that the phase noise performance is dominated by the *USRP B200mini*. At full AAF bandwidth, i.e., 22.5 MHz, it has been demonstrated that the available DR for impulses is limited to approx. 30 dB. Reducing the two-tone power such that this indication range is achieved decreases the nonlinear modulation products and the phase noise to a negligible extent. Furthermore, there are no phase noise requirements mentioned in *CISPR 16-1-1* as it is desired to find the maximum radiated power instead of a small carrier buried in noise.

In case of recurrent impulses, multiple intermodulation spurs are generated in the IF section, adding up on a periodic frequency grid. To investigate the signal distortion at maximum DR, a broadband impulse, extending over the complete ADC bandwidth, is measured. By filtering the impulse with a narrowband bandstop filter, a certain amount of frequency content is suppressed which allows to identify any kind of spectral regrowth in the notch. As the upconversion stage provides DRs well above 50 dB, signal distortion amounts mostly to the SDR when performing peak detector measurements and using the applied configurations mentioned above. Due to the reduced indication range and the limited output bandwidth of the upconversion stage, it is possible to generate impulses with a vector signal generator (VSG). This has the advantage, that unwanted effects of the classic *CISPR* impulse source, e.g., jitter of amplitudes or over time, can be eliminated which improves the measurement accuracy. Furthermore, the transmitted signal can be of arbitrary shape as it is generated in discrete time domain and then stored in the VSG for playback. The signal is repeated several times for averaging the signal spectrum received by the SDR, see Fig. 5.6. The black trace shows the ideal impulse spectrum which was designed in discrete time domain. In blue, the RMS noise floor power is shown when no signal is present and in red, the averaged impulses are visualized. The signal phase of the measured transients have been aligned at maximum SNR in time domain which allowed to perform complex averaging, resulting in a higher sensitivity. Because of the phase instability of the *USRP B200mini*, it was not possible to retrieve the ideal notch response lower than  $-50$  dB by performing a single point phase alignment. Anyhow, it can be clearly seen, that no significant modulation spurs are produced within the desired indication range.

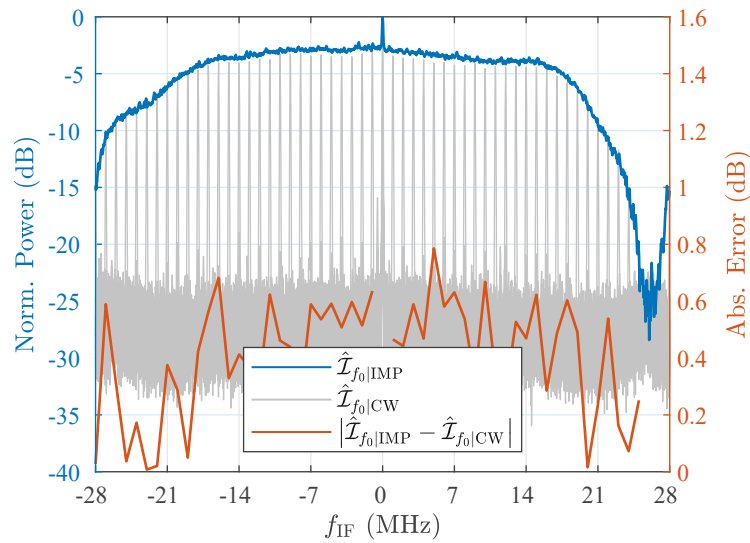


**Fig. 5.7:** Peak detected spectra of absolute calibration procedure and the corresponding amplitude error over frequency  $f_{IF}$ .

### 5.2.2 Usable Analysis Bandwidth

The absolute calibration test from Sec. 5.1.2 is now performed over the entire IF bandwidth of the *USRP B200mini*. Using a VSG for this characterization has an essential benefit over the measurement procedure made before. As the CW signal and the impulse come from the same source, the calibration is much easier and the influence of impedance mismatches when using two different sources can be neglected. Moreover, in discrete time domain, the indicated impulse and the CW spectra can be ideally adjusted to each other. The IF filter response used for calibration is then perfectly known and does not need any further compensations after the measurement. As mentioned before, the signal accuracy is improved as the amplitude jitter problem of reed-contact based impulse sources does not play a role for VSGs. The test sequence consists of a CW tone conducting a stepped frequency sweep between  $-28 \text{ MHz} \leq f_{cw} \leq 28 \text{ MHz}$  with a step size of 1 MHz and a dwell time of 1 ms. After this sweep, an impulse is transmitted which is flat over the entire IF bandwidth of the SDR. These two signal sequences are repeated continuously. The max hold peak detected spectra over 20 sequences and the absolute error between the CW and impulse power level over frequency are given in Fig. 5.7. From the results, it can be concluded that the absolute measurement error does not change significantly over the bandpass response of the upconversion stage. In addition, the error  $|\hat{\mathcal{I}}_{f_0|IMP} - \hat{\mathcal{I}}_{f_0|CW}|$  is well below the allowed error bound of 1.5 dB. However, aliasing limits the effective analysis bandwidth of the SDR. This effect can be seen on the right hand side of the graph, where a fraction of the measured impulse spectrum from  $f_{IF} < -28 \text{ MHz}$  leaks into  $\hat{\mathcal{I}}_{f_0|IMP}$ . To be on the save side regarding *CISPR 16-1-1* requirements, only 80 % of the acquired sampling rate should be used to hold the 40-dBc requirement for CW signals.

In low-IF configuration of the SDR, only the lower or upper sideband of the depicted spectrum is used. Decimating the sampling rate by a factor of  $M = 2$  allows then an effective analysis bandwidth of  $ABW = 0.8f_s/M = 22.4 \text{ MHz}$ . As the filter response of the upconversion stage has a usable bandwidth of up to  $B = 40 \text{ MHz}$ , the calculated ABW can be achieved by setting the



**Fig. 5.8:** Realized test EUT: top view (left), bottom view (middle), and side view (right).

IF of the SDR such that the flat response part coincides with the decimated spectrum. Taking (4.3) into account, the relation

$$\left| f_{\text{IF}} \pm 0.8 \frac{f_s}{2M} \right| \leq \frac{B}{2} \quad (5.2)$$

must hold to achieve the desired performance.

Conducting a frequency scan with the STFT-based method over *CISPR* band C/D at an ABW of 22.4 MHz requires to perform  $970 \text{ MHz} / 22.4 \text{ MHz} \cong 44$  recordings. To achieve compliance when using the 120-kHz filter from (2.24), a frequency step size of at least  $\Delta_f = 70 \text{ kHz}$  is necessary, see Fig. 2.16. Hence, in case of single frequency metering, a total amount of  $970 \text{ MHz} / 70 \text{ kHz} \cong 13,858$  recordings must be made. For a dwell time of 1 ms, the frequency scan time can be reduced from 13.9 s to 44 ms if exploiting the broadband IF approach. It shall be emphasized that relevant LO lock times, which might further increase the gained time savings, have not been considered in this calculations.

A further advantage of the broadband signal analysis approach is that system overloads can be easily detected. Independent of the used gain setting, at full AAF bandwidth, the ADC's full-scale level is reached much earlier than the system's 1-dB compression limit. Thus, the quantized signal can be easily leveled by using the attenuator implemented in the upconversion stage.

### 5.3 Performance Comparison Against Accredited Test-Houses

As the target use case of the SDR-based receiver is to perform radiated emission measurements in *CISPR* band C/D, the developed setup is tested in conjunction with a low-cost TEM cell in accordance to *CISPR 32*. By characterizing a test EUT using the far field transformation algorithm from Sec. 2.1.2 and comparing the results to accredited EMC test houses using different test sites, the reliability of such a low-cost system for estimating compliance in advance shall be demonstrated. The used cell has been designed by the author of this thesis and characterized in accordance to the relevant norm *DIN EN 61000-4-20*, see App. A.

To perform a radiated emission test, an EUT fitting in the uniform test-volume (UTV) of the used TEM cell has been designed, see Fig. 5.8. On a PCB with a size of 10 cm by 10 cm, different electronic systems have been implemented which are typical for commercial products in the IoT sector. These systems include: a brushed DC motor, an LCD display, a class-D audio amplifier, buck and boost converters, and serial interfaces. Focus during the selection process was to cover a large variety of different interference sources emitting disturbances (dis-)/continuously. It was worked closely together with EMC consultants to identify critical components and to

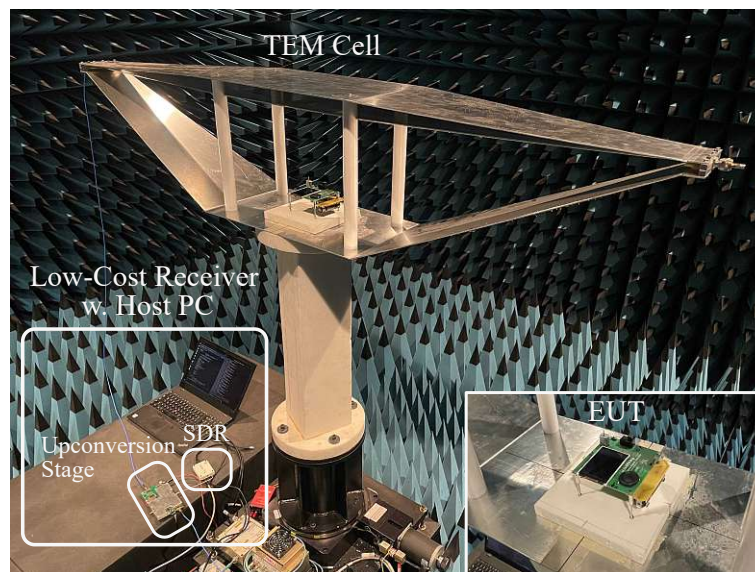


**Fig. 5.9:** Low-cost measurement setup placed in an anechoic chamber. In the lower right, the test EUT is magnified.

embed common layout mistakes which often lead to certification fails. For instance, the brushed DC motor is a common worst case test-object as brush sparking causes impulses with a high peak power spreading their energy over a large frequency bandwidth [79]. The test EUT is fully battery-powered which is on the one hand, a fundamental criteria for a compliant radiated emission measurement using TEM cells, and on the other hand, typical for IoT products which are addressed in this thesis.

### 5.3.1 Pre-Compliance Setup

As the used TEM cell is laterally open and thus prone to interference from surrounding emission sources, e.g., mobile communication systems, the EUT was characterized in an anechoic chamber, see Fig. 5.9. To minimize field distortions in the UTV by metallic surfaces beneath the absorbers, the cell has been placed on a Rohacell foam support more than 60 cm apart, in accordance to *MIL-STD-462F RS105*. Usually, the UTV of a TEM cell is characterized with a field probe. An alternative, but also compliant, approach for verifying the measurement setup can be achieved by simply characterizing the losses of the TEM cell [18]:

$$|10 \log_{10} (|S_{11}|^2 + |S_{21}|^2)| \leq 1 \text{ dB.} \quad (5.3)$$

It is assumed that the losses of the cell are mainly caused by energy couplings into higher order modes which can cause resonances of the electric field in the UTV. To be compliant, the losses in loaded conditions (EUT inside) have to be smaller than 1 dB. This method is applicable to two-port cells only and is especially beneficial to crosscheck if the field homogeneity requirements are violated depending on the EUT's position. In Fig. 5.10, the losses in empty and loaded conditions are given. For the loaded trace, the maximum losses have been depicted including all possible EUT positions which are necessary for the far field transformation algorithm. While the empty cell complies with the requirement from (5.3), there are some critical resonances above 700 MHz which need to be taken into account when interpreting emission spectra at these certain

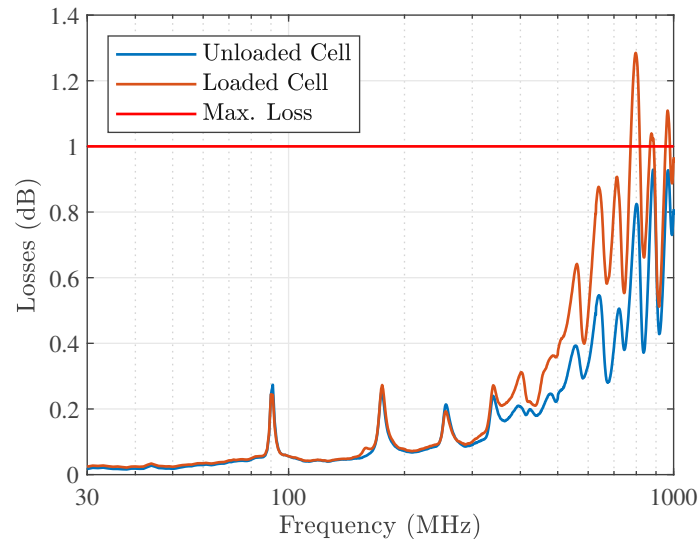


**Fig. 5.10:** Alternative criteria evaluation in unloaded and loaded conditions of the used low-cost TEM cell.

frequencies in loaded conditions. A detailed field homogeneity characterization of the UTV using a field probe, confirming the utilized loss criteria, can be found in App. A.

To calculate the equivalent electric field strength in far field conditions with (2.19), it is necessary to derive the field factor  $e_{0y}$  either by measurements with (2.13) or analytically according to (2.14). The calculated field factor values in the center of the UTV of the low-cost TEM cell and a professional Teseq 500 GTEM cell are compared to the measured values<sup>2</sup> in Fig. 5.11. As both cells strongly deviate from the calculated field factor over frequency, the measured values are taken into account for the free space transformation algorithm. It shall be emphasized, that the resonances of  $e_{0y}$  will lead to an over estimation of the noise floor if the emitted signal level falls below the receiver's sensitivity level.

### 5.3.2 Measurement Results Comparison

The low-cost measurement setup from Fig. 5.9 is now compared to three different accredited EMC test houses using a 3 m SAC, a 5 m SAC, and a 3 m FAC. In addition, measurements with a professional GTEM-based setup<sup>3</sup>, where full control of setup calibrations were accessible, have been made to identify uncertainties caused by limitations of the far field transformation algorithm or the cell itself. The repeatability and accuracy of different test sites has been investigated by a round robin test in [31] and [80]. Within these works, a measurement uncertainty of up to  $\pm 10$  dB has been experienced which may also be expected for the presented results.

As the participating EMC test-houses provided peak detected emission spectra only, the measurements with the low-cost setup have been carried out using the STFT approach providing sufficient DR for this detector. To guarantee a compliant measurement accuracy, the signal is

<sup>2</sup>The field factor has been characterized with a calibrated CW source and the field probe from App. A. Furthermore, the probe was placed in the central of the UTV ( $i = 2$ ,  $j = 5$  see Fig. A.3) measuring  $e_{0y}$  90 mm above the bottom conductor.

<sup>3</sup>The GTEM-based setup consists of the Teseq 500 cell and the EMI receiver MXE N9038A from Keysight Technologies, both given full compliance for the performed measurements and applicable EMC standards.

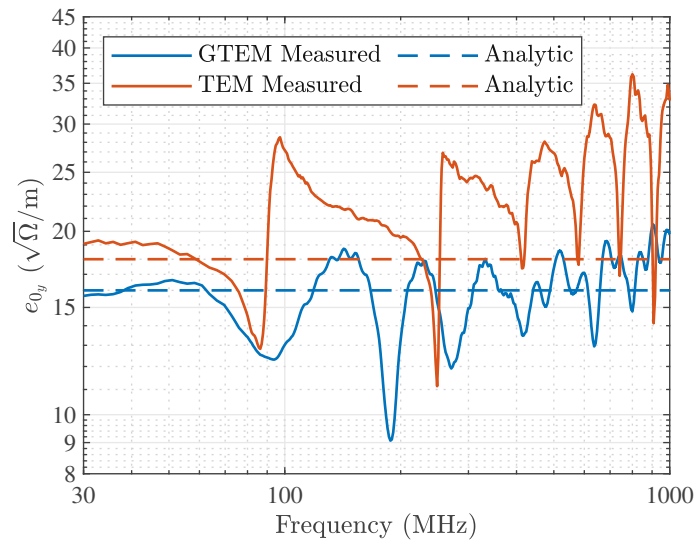


**Fig. 5.11:** Calculated vs. measured field factor of a Teseq 500 GTEM cell and the used low-cost TEM cell.

processed such that the frequency bin resolution is  $\Delta_f = 1$  kHz and the window overlap is 90 % at a sampling rate of  $f_s = 56$  MSa/s, see Sec. 2.2.3.

The transformation algorithm for (G-)TEM cells is a worst case model as it superposes absolute power values of three different EUT positions, see (2.19), aiming to preserve the maximum emission spectrum. In Fig. 5.12, the comparison of the emission spectra from different test-sites with the proposed low-cost setup is depicted. As an overlay of noisy spectra impedes the visibility of differences in field strength, the maximum peaks with a minimum separation of 1 MHz have been depicted to highlight the results. It was verified in advance that the output power of the TEM cell is not saturating the SDR-based receiver. It can be directly seen from all graphs that the TEM cell yields a higher field strength than the GTEM-based setup, although, the spectrum shape is quite similar up to 700MHz. According to [31], potential measurement uncertainty sources causing this offset are, e.g, the repeatability of the EUT, field homogeneity perturbations of the loaded cell, and thermal drifting of the setup. Above 700 MHz, resonances in the TEM cell cause an over estimation of the spectrum which was predicted in Fig. 5.10. The SACs show a relatively high spectrum amplitude compared to the FAC for frequencies between 30–50 MHz. In this range, maximum field strengths occurred for vertical polarization of the receiving antenna at a height of only  $h_A = 1$  m above the ground plane. Operating large EMI antennas that close to a reflecting surface influences their transfer characteristics and causes, in this case, a higher field strength. As the antenna height is kept constant at approx. 2 m in the FAC, the measurements show a better correlation with the TEM-based results. Besides test site, EUT, and transformation algorithm related deviations, the envelopes of the emitted spectra show a good agreement with the low-cost setup considering typical tolerances analyzed in the mentioned round robin tests. Hence, the feasibility of radiated emission testing has been further verified by carrying out a realistic test case, supplementary to *CISPR 16-1-1* procedures.

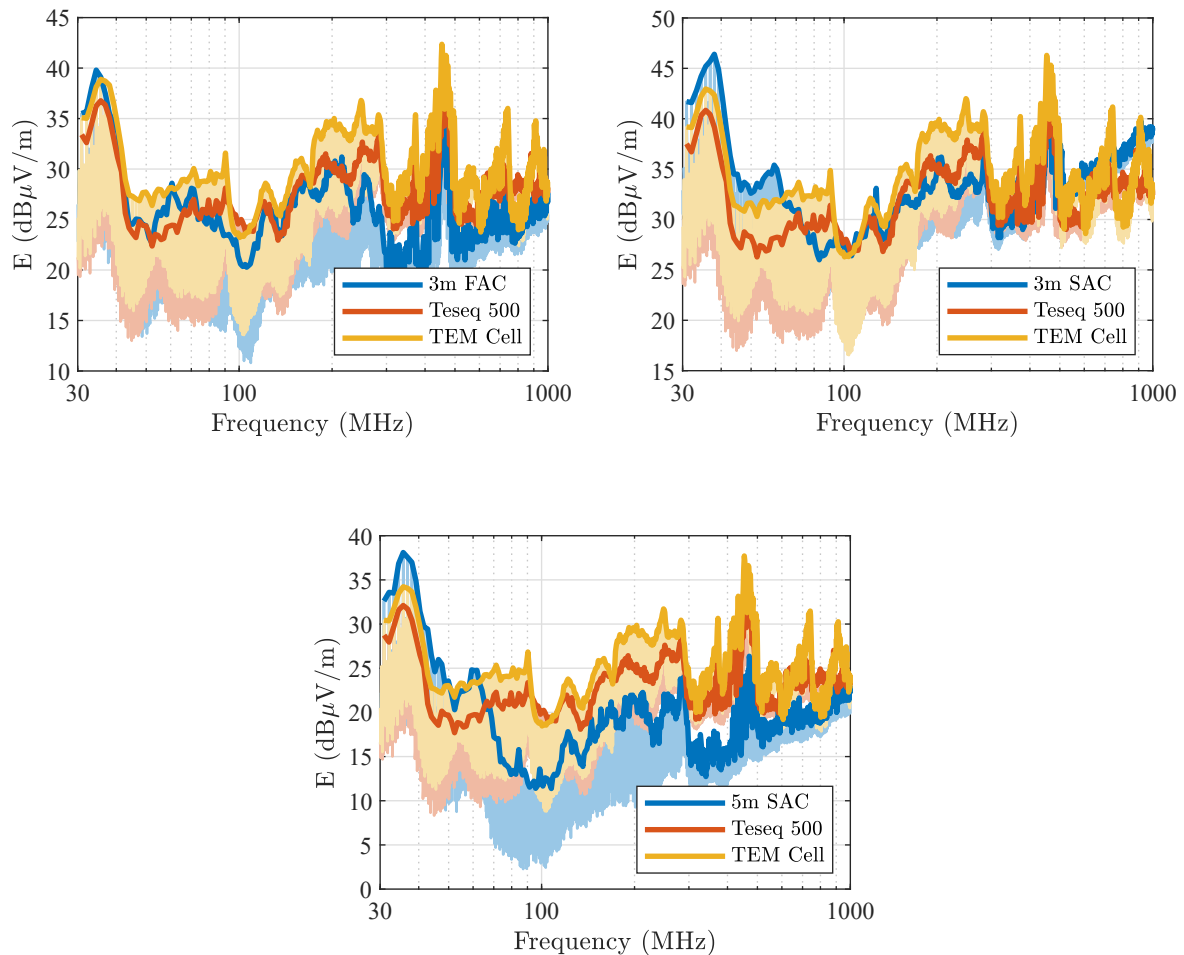


**Fig. 5.12:** Comparison of the radiated emission spectra from the 3 m FAC (top left), 3 m SAC (top right), and the 5 m SAC (bottom) with the measurements made using a Teseq 500 GTEM cell and the proposed low-cost setup. The results of the 5 m SAC have been transformed by the EMC test house to a hall with 10 m distance. The maximum field strength of the traces is emphasized by visualization of the spectrum peaks separated by at least 1 MHz.

**Tab. 5.1:** Overall budget estimate of the low-cost measurement system. Alternative or not mandatory options are denoted with \*. PCB assembly costs are derived for a single unit production size.

SDR-based receiver		TEM cell		Manufacturing	
<b>Upconversion stage</b>		<b>Metal sheets</b>		<b>PCB assembly</b>	
RF components	210 €	Al 3 mm	150 €	Assembly 50 €/pc.	50 €
Power units	90 €			Stencil	50 €
Passives	35 €	<b>Pillars</b>		Setup Costs	200 €
Peripherals	45 €	Teflon 35 mm	200 €		300 €
PCB	70 €	*Nylon	100 €		
*Shielding	345 €		100–200 €	<b>TEM cell</b>	
	450–795 €	<b>Connectors</b>		Assembly 100 €/h	200 €
		N-type	20 €		
<b>Possible SDRs</b>		<b>Mounting material</b>			
<i>PlutoSDR</i>	220 €	Screws etc.	75 €		
<i>bladeRF micro 2.0</i>	500 €				
<i>USRP B200mini</i>	1320 €				
	220–1320 €				
	665–2110 €		345–445 €		500 €
		<b>Total (excl. taxes)</b>			<b>1510–3050 €</b>

## 5.4 Overall Budget Estimate

After extensive functionality demonstrations, an overall budget estimate is made justifying the use of the low-cost measurement system instead of off-the-shelf available equipment. The required financial resources for building the used setup is split into three parts, see Tab. 5.1. Firstly, the material costs for the SDR-based receiver comprising the upconversion stage and a possible SDR are evaluated. Secondly, the material costs for the do-it-yourself TEM cell are analyzed and lastly, the manufacturing process is taken into account. The material prices are based on typical distributor quotations, e.g., Mouser, Digi-Key, or RS components, for a production size of a single prototype. As most of the components get cheaper with increasing sample size, this estimate shall cover a worst-case scenario. The PCB production and assembly is calculated for a single unit taking Asian providers into account. Due to the simple PCB fabrication of the upconversion stage, i.e., a four-layer *FR4* board holding standard design rules, European based companies, having their strengths when it comes to more complex designs, have not been considered.

By now, the upconversion stage has been used with a customized shielding, milled out of an Aluminum block. The costs of this part may be strongly reduced by use of a folded metal sheet or a conductive spray printed approach. When measuring emissions with an open TEM cell in laboratory conditions, the shielding makes even less sense to be used as interferences from various sources in immediate surroundings efficiently couple into the stripline, perturbing the measurement results. In case of accepting the enhanced susceptibility to interference, the material costs are 450 €. Within this thesis, the SDR *USRP B200mini* has been used for verification purposes as it has a well documented and tested user interface. However, other realizations

having the same analog receiver chip implemented exist for an even lower budget. The cheapest one is the *PlutoSDR* from Analog Devices. Although, the RF frontend is equivalent with the *USRP B200mini*, the streaming rate to the host PC is significantly lower as the data exchange is established via a USB 2 interface. This affects the frequency scan time of the receiver as a usable analysis bandwidth of approx. 16 MHz can be expected. The *bladeRF micro 2.0* is fully equivalent to the *USRP B200mini* except that this SDR features two independent receive and transmit paths. Hence, from a cost-benefit point of view, the *bladeRF micro 2.0* is the best choice. In conjunction with the upconversion stage, the total costs for the SDR-based receiver including the manufacturing are 1250 €. In [28], the low-cost spectrum analyzer *BB60C* from Signal Hound has been investigated in accordance to *CISPR 16-1-1* requirements. This receiver is available for a budget of 4 k€ and comes with a graphical user interface supporting a lot of different applications including EMC pre-compliance measurements. The measurement results in [28] indicate that the *BB60C* achieves a DR of only 20 dB, if measuring broadband *CISPR* impulses. Due to the limited DR it is difficult to identify a system overload and compliant quasi-peak detector measurements are impossible without additional preselection filtering. To the author's best knowledge, the cheapest EMI receiver given full compliance is the *N9000A* from Narda available for a budget starting from 18 k€. In direct comparison with the SDR-based receiver, which achieves similar DRs as professional equipment, the investment costs can be reduced by more than 14 times.

Regarding the TEM cell used throughout this thesis, the expected investment costs are 445 € for the material and 200 € for the assembly. The price can be further lowered by 100 € if Nylon sticks are used instead of PTFE as septum support. In the target frequency range between 30 MHz–1 GHz, Nylon has comparable RF characteristics to PTFE and thus, no significant changes of the field homogeneity are to be expected. Currently, the price of comparable open TEM cells on the market is about 1100 € but having a much lower septum height and consequently a smaller UTV [81]. Although, the used TEM cell from [28] allows to measure larger EUTs, the budget saving is lower than for the EMI receiver reducing the investment costs by a factor smaller than two. If frequencies above 1 GHz need to be tackled, an interesting open GTEM cell has been launched for a budget of 2245 € only [82].

To conclude, the low-cost measurement setup used in this thesis is available for a budget between 1510–3050 €. In particular, taking the *bladeRF micro 2.0* with a shielding-less upconversion stage and the TEM cell into account requires a budget of 1.9 k€, including assembly costs. This number lies in the price range required for renting an EMC measurement hall per day for a certification attempt which is one of the major goals of this thesis. Furthermore, it has been shown that the largest cost reduction was achieved for the EMI receiver. Due to the relatively low complexity and good availability of open TEM cells, investment savings by implementing a do-it-yourself cell are rather low.

---

# Conclusion and Outlook

---

In this thesis, the suitability of low-cost receivers for radiated emission measurements in *CISPR* band C/D (30 MHz–1 GHz) has been investigated. Because of their versatile hardware concepts and on-board signal processing resources, SDRs have been identified as a promising alternative to costly EMI receivers. The goal was to enable reliable pre-compliance measurements of battery-powered devices, typical for the IoT branch, utilizing a TEM cell as test method.

Based on analytical derivations and basic RF performance parameters, it has been demonstrated that SDRs with variable bandwidth AAFs have significant advantages in terms of DR which is a crucial parameter for EMC measurements. Such state-of-the-art devices lie in a price range between 300 €–2 k€ and mostly incorporate analog frontends of homodyne architecture, implemented in a single chip (RFIC). A widely used chip representing this category is the popular RFIC series *AD936x* from Analog Devices. Integrated receiver solutions are often used in conjunction with real-time capable signal processing units (FPGA) allowing for significant reductions of computational effort on the host PC. On the market, several comparable SDRs exist incorporating such a system architecture based on an RFIC and an FPGA. Many of these devices deploy the RFIC series *AD936x*, hence delivering the same RF performance, and differ mostly in the FPGA’s capabilities. The *USRP B200mini* represents for this category and was thus chosen for a rigorous analysis in this thesis.

A frequently applied radiated emission norm for battery-powered IoT devices is *CISPR 32*. By specification, two detectors are mandatory in the addressed frequency range, i.e., the peak and quasi-peak. The latter one represents for the highest requirements in terms of DR. In accordance to *CISPR 16-1-1*, the main device norm for EMI receivers, a black-box based approach has been pursued to investigate the performance of the *USRP B200mini* out-of-the-box. Specified testing methods and setups have been modified partly. To improve the measurement accuracy, e.g., a correlation based technique has been presented which allowed for time coherent averaging with the SDR having no external trigger input available. Goal of this evaluation was to explore weak spots of the receiver architecture, DR limitations, and optimum configuration settings.

By measuring different test stimuli, i.e., a CW tone and a broadband impulse, two major requirement violations have been identified. Firstly, the homodyne-based receiver frontend suffered from unintended downconversion contents located at  $f_{\text{dist}} = n f_{\text{LO}} \pm f_{\text{IF}}$  where  $n > 1$ . It was demonstrated that especially at low tuning frequencies  $f_{\text{LO}} < 600$  MHz, modulation products of third order  $n = 3$  are downconverted efficiently with about 8 dB less conversion gain than for the fundamental product  $n = 1$ . Although this problem may be solved with additional preselection filters, the SDR suffered from an insufficient DR of the analog frontend as well. In general, the *USRP B200mini* fulfilled the derived peak detector requirements but for the quasi-peak

detector, the preselector bandwidth must be drastically reduced for weighting recurrent impulses compliantly. By applying a broadband preselector covering *CISPR* band C/D and suppressing downconversion spurs down to frequencies of  $f_0 = 375$  MHz, it has been shown that the SDR achieves a DR of up to 23 dB at  $f_0 = 500$  MHz. Under these circumstances, 27 dB more are necessary to satisfy quasi-peak detector requirements. The frontend's compression level did not allow for resolving the full DR of the SDR's ADCs when measuring broadband impulses, even not at maximum bandwidth of the AAFs, i.e., 22.5 MHz. Consequently, the benefits from a reduced AAF cutoff frequency cannot be exploited out-of-the-box.

In a next step of this thesis, the identified performance limits of the *USRP B200mini* have been improved by certain hardware extensions. The main focus was put on developments which are low-cost, easy to replicate, and working stand-alone. For solving the downconversion spur problem and increasing the available DR of the SDR, a highly linear upconversion stage has been realized. The frequency content located in *CISPR* band C/D is mixed upwards to a certain IF, i.e.,  $f_c = 1227$  MHz, and filtered with a narrowband bandpass. Due to filtering, unintended conversion products located at  $f_{\text{dist}}$  are suppressed, solving the downconversion spur problem. Furthermore, the impulse bandwidth the SDR is exposed to, reduced in satisfaction with quasi-peak detector requirements. In particular, the full-scale reading of the implemented ADCs became accessible and the available DR was improved up to 52 dB by reducing the AAF bandwidth to 1 MHz. At full bandwidth, i.e., 22.5 MHz, a DR of up to 30 dB was available. With the presented measurement results, it has been demonstrated that compliant radiated emission tests are in principal possible with the *USRP B200mini*.

Key component of the upconversion stage is a triple-balanced frequency converter. With this kind of ring-diode based mixer, *CISPR 16-1-1* requirements have been fulfilled without the need for a costly preselector filterbank. It has been shown that the receiver's NF may be up to 25 dB for measurements in conjunction with the target TEM cell. As this number was easily achieved without any pre-amplification, the derived RF-link budget was held with at least two preselector paths covering *CISPR* bands C/D individually. However, in case of a different test environment requiring an LNA, the mixer needs several filters more at the preselector for measuring recurrent impulses compliantly with the quasi-peak.

The AAF bandwidth had to be drastically reduced, i.e., 1 MHz, for achieving quasi-peak detector requirements. As this limits the frequency scan speed of the system, the application of an AGC loop between the upconversion stage and the SDR has been investigated. To increase the AAF bandwidth and avoid ADC clipping at the same time, a feed-forward based AGC has been implemented. Due to a-priori knowledge of signal levels exceeding the ADC's full-scale voltage, it was possible to switch a digitally-stepped attenuator such that the increased peak power of impulses was compensated. With a simple algorithm and calibration procedure, the attenuated signal was recovered in discrete time domain. This allowed to increase the AAF bandwidth by a factor of 6.3 at the expense of a degraded amplitude accuracy. The introduced error was within the allowed error bound of  $\pm 1.5$  dB, specified by *CISPR 16-1-1*.

In case of a potential overload, the attenuator of the feed-forward AGC gets triggered by a routine implemented on the *USRP B200mini*'s FPGA, synchronized to the ADC clock. Due to the finite resolution of the time base, the attenuation over time jitters against asynchronously occurring impulses. This causes an amplitude error in the signal reconstruction procedure which cannot be calibrated. As a consequence, the feed-forward AGC can be used only if the overall amplitude error budget of the SDR-based receiver allows to. Especially for measurements close to the 1-dB compression level this might not be the case.

As a last step of this thesis, the measurement accuracy of the SDR-based receiver comprising the *USRP B200mini* and the upconversion stage was verified in accordance to *CISPR 16-1-1*, taking no setup modifications into account. With this final test, the derived requirements and the designed system's performance have been verified utilizing the peak and quasi-peak detector. It was focused on classic single frequency metering and modern STFT-based analysis techniques. Moreover, the receiver was tested in conjunction with a low-cost TEM cell measuring radiated emission spectra of a test EUT. The same EUT was characterized in three different accredited test houses. By comparing the results, a reliable compliance estimate in advance has been demonstrated.

For single frequency metering, it has been shown that the accuracies for both detectors was fulfilled and that the full DR of the quasi-peak detector was accessible. At low tuning frequencies, i.e.,  $f_0 = 30\text{ MHz} - 40\text{ MHz}$ , the upconversion stage's available DR degraded and required an additional preselector for measuring isolated transients.

For the broadband STFT-based analysis approach, the entire IF bandwidth of the SDR was analyzed. Due to the reduced available DR at full AAF bandwidth, only peak detector capabilities have been investigated. The spectral purity and detector accuracy of the SDR-based receiver have been verified to be sufficient within an indication range of 30 dB. The usable analysis bandwidth amounts to approx. 80% of the ADC's half sampling rate, i.e., 22.4 MHz. Due to detector path parallelization, the calculated frequency scan time can be reduced from 13.9 s to 44 ms in comparison to single frequency metering, taking a dwell time of 1 ms into account.

The radiated emission spectra of the test EUT measured with the low-cost setup showed a good agreement with the accredited test sites, taking typical uncertainty budgets into account. For investigating performance limitations of the used TEM cell, measurements with a professional GTEM cell have been conducted as well. The two emission spectra were only 2–3 dB offset from each other confirming preceding compliance verification results.

In conclusion, it can be said that compliant radiated emission measurements of battery-powered devices in *CISPR* band C/D using the low-cost SDR *USRP B200mini* are possible. Due to inherent problems of the homodyne-based frequency conversion architecture and DR limitations, however, an upconversion stage was necessary to achieve compliance using the peak and quasi-peak detector. The overall budget for the SDR-based receiver was estimated to be about 1.3 k€. In conjunction with the utilized TEM cell, the costs increase to 1.9 k€ including manufacturing costs. As this price lies well below of comparable professional instruments, the relevance of this work has been finally justified.

Future work on this topic may include the following tasks. The radiated emission measurements of the test EUT have shown in principal a good agreement with EMC test houses, taking typical uncertainties into account. As the utilized one-port far field transformation algorithm for TEM cells represents a worst case emission test due to neglecting phase terms of the EUT's radiation pattern, the transformed results were at some frequencies several decibel above the far field sites. By use of the second port, phase dependencies of the presented multipole expansion technique can be extracted to describe the detailed radiation pattern of an EUT, resulting in a higher accuracy. As the utilized RFIC series from Analog Devices provides chip versions with up to two receive paths, e.g., the *AD9361* which is used in the *bladeRF micro 2.0*, this approach may be applicable. However, it need to be investigated if the phase coherence and stability is sufficient to conduct this two-port measurement method. Furthermore, the open TEM cell is in general prone to interference which impedes an accurate pre-compliance measurement if not shielded. Having a second receive path available may be also used for active noise cancellation.

---

## References

---

- [1] *DIN EN IEC 55016-1-1: Specification for radio disturbance and immunity measuring apparatus and methods — Part 1-1: Radio disturbance and immunity measuring apparatus — (CISPR 16-1-1:2019)*. German. Sept. 2020.
- [2] *DIN EN 55032: Electromagnetic compatibility of multimedia equipment — Emission (CISPR 32:2015)*. German. Feb. 2016.
- [3] X. Chen, J. Tang, T. Li, S. Zhu, Y. Ren, Z. Zhang, and A. Zhang. “Reverberation Chambers for Over-the-Air Tests: An Overview of Two Decades of Research”. In: *IEEE Access* 6 (2018), pp. 49129–49143. DOI: 10.1109/ACCESS.2018.2867228.
- [4] R. Vogt-Ardatjew, U. Lundgren, S. F. Romero, and F. Leferink. “On-Site Radiated Emissions Measurements in Semireverberant Environments”. In: *IEEE Transactions on Electromagnetic Compatibility* 59.3 (2017), pp. 770–778. DOI: 10.1109/TEMC.2016.2623380.
- [5] *DIN EN IEC 61000-4-21: Electromagnetic compatibility (EMC) — Part 4-21: Testing and measurement techniques — Reverberation chamber test methods (IEC 61000-4-21:2011)*. German. Dec. 2011.
- [6] J. Yousaf, W. Nah, M. I. Hussein, J. G. Yang, A. Altaf, and M. Elahi. “Characterization of Reverberation Chamber - A Comprehensive Review”. In: *IEEE Access* 8 (2020), pp. 226591–226608. DOI: 10.1109/ACCESS.2020.3045028.
- [7] A. Kriz. “Calculation of antenna pattern influence on radiated emission measurement uncertainty”. In: *2008 IEEE International Symposium on Electromagnetic Compatibility*. 2008, pp. 1–7. DOI: 10.1109/IEMC.2008.4652052.
- [8] F. Krug and P. Russer. “The time-domain electromagnetic interference measurement system”. In: *IEEE Transactions on Electromagnetic Compatibility* 45.2 (2003), pp. 330–338. DOI: 10.1109/TEMC.2003.811303.
- [9] S. Braun and P. Russer. “A low-noise multiresolution high-dynamic ultra-broad-band time-domain EMI measurement system”. In: *IEEE Transactions on Microwave Theory and Techniques* 53.11 (2005), pp. 3354–3363. DOI: 10.1109/TMTT.2005.855745.
- [10] M. F. A. Rahim. “Evolution and trends of EMI receiver”. In: *2013 IEEE International RF and Microwave Conference (RFM)*. 2013, pp. 362–367. DOI: 10.1109/RFM.2013.6757285.
- [11] Adobe Stock, Audrius Merfeldas, Picture ID: #366624593. *Near field EMC scanning system*.
- [12] Adobe Stock, balipadma, Picture ID: #112314112. *EMC measurement with a near-field probe on a circuit board*.
- [13] M. Ma, M. Kanda, M. Crawford, and E. Larsen. “A review of electromagnetic compatibility/interference measurement methodologies”. In: *Proceedings of the IEEE* 73.3 (1985), pp. 388–411. DOI: 10.1109/PROC.1985.13164.

- [14] R. Laroussi and G. Costache. “Far-field predictions from near-field measurements using an exact integral equation solution”. In: *IEEE Transactions on Electromagnetic Compatibility* 36.3 (1994), pp. 189–195. DOI: 10.1109/15.305453.
- [15] B. Fourestie, Z. Altman, J.-C. Bolomey, J. Wiart, and F. Brouaye. “Statistical modal analysis applied to near-field measurements of random emissions”. In: *IEEE Transactions on Antennas and Propagation* 50.12 (2002), pp. 1803–1812. DOI: 10.1109/TAP.2002.807495.
- [16] E.-X. Liu, W.-J. Zhao, B. Wang, S. Gao, and X.-C. Wei. “Near-field scanning and its EMC applications”. In: *2017 IEEE International Symposium on Electromagnetic Compatibility & Signal/Power Integrity (EMCSI)*. 2017, pp. 327–332. DOI: 10.1109/IEMC.2017.8077889.
- [17] M. L. Crawford. “Generation of Standard EM Fields Using TEM Transmission Cells”. In: *IEEE Transactions on Electromagnetic Compatibility* EMC-16.4 (1974), pp. 189–195. DOI: 10.1109/TEMC.1974.303364.
- [18] *DIN EN IEC 61000-4-20: Electromagnetic compatibility (EMC) — Part 4-20: Testing and measurement techniques — Emission and immunity testing in transverse electromagnetic (TEM) waveguides (IEC 61000-4-20:2010)*. German. July 2010.
- [19] P. Wilson. “On correlating TEM cell and OATS emission measurements”. In: *IEEE Transactions on Electromagnetic Compatibility* 37.1 (1995), pp. 1–16. DOI: 10.1109/15.350235.
- [20] C. Spindelberger, G. Giannetti, and H. Arthaber. “Increasing the Test-Volume of Open TEM Cells by Using an Asymmetric Design”. In: *2022 Kleinheubach Conference*. 2022, pp. 1–4.
- [21] A. Al Takach, F. Ndagijimana, J. Jomaah, and M. Al-Husseini. “3D-Printed Low-Cost and Lightweight TEM Cell”. In: *2018 International Conference on High Performance Computing & Simulation (HPCS)*. 2018, pp. 47–50. DOI: 10.1109/HPCS.2018.00022.
- [22] M. Parvis, G. Perrone, and A. Vallan. “A precompliance EMC test-set based on a sampling oscilloscope”. In: *IMTC/2002. Proceedings of the 19th IEEE Instrumentation and Measurement Technology Conference (IEEE Cat. No.00CH37276)*. Vol. 2. 2002, 1197–1201 vol.2. DOI: 10.1109/IMTC.2002.1007128.
- [23] C. De Capua and C. Landi. “A digital measurement station for RF-conducted emissions monitoring”. In: *IEEE Transactions on Instrumentation and Measurement* 51.6 (2002), pp. 1363–1366. DOI: 10.1109/TIM.2002.808029.
- [24] A. A. Abidi. “The Path to the Software-Defined Radio Receiver”. In: *IEEE Journal of Solid-State Circuits* 42.5 (2007), pp. 954–966. DOI: 10.1109/JSSC.2007.894307.
- [25] Y. K. Kwag, J. S. Jung, I.-S. Woo, and M.-S. Park. “Modern Software Defined Radar (SDR) Technology and Its Trends”. In: *Journal of electromagnetic engineering and science* 14 (2014), pp. 321–328. URL: <https://api.semanticscholar.org/CorpusID:12437236>.
- [26] J. Marimuthu, K. S. Bialkowski, and A. M. Abbosh. “Software-Defined Radar for Medical Imaging”. In: *IEEE Transactions on Microwave Theory and Techniques* 64.2 (2016), pp. 643–652. DOI: 10.1109/TMTT.2015.2511013.
- [27] D. Neunteufel, S. Grebien, and H. Arthaber. “Indoor Positioning of Low-Cost Narrowband IoT Nodes: Evaluation of a TDoA Approach in a Retail Environment”. In: *Sensors* 22.7 (2022). DOI: 10.3390/s22072663. URL: <https://www.mdpi.com/1424-8220/22/7/2663>.

- [28] C. Spindelberger and H. Arthaber. “Out-of-the-Box Performance of popular SDRs for EMC pre-compliance Measurements”. In: *2022 International Symposium on Electromagnetic Compatibility – EMC Europe*. 2022, pp. 677–682. DOI: 10.1109/EMCEurope51680.2022.9901003.
- [29] C. Spindelberger and H. Arthaber. “Investigating the Potential of the Low-Cost SDR USRP B200mini as an EMI Receiver”. In: *IEEE Transactions on Electromagnetic Compatibility* (2023), pp. 1–14. DOI: 10.1109/TEMC.2023.3317731.
- [30] C. Spindelberger and H. Arthaber. “Improving the Performance of Direct-Conversion SDRs for Radiated Precompliance Measurements”. In: *IEEE Letters on Electromagnetic Compatibility Practice and Applications* 5.1 (2023), pp. 22–26. DOI: 10.1109/LEMCPA.2022.3227409.
- [31] A. Nothofer, D. Bozec, A. Marvin, M. Alexander, and L. McCormack. *The Use of GTEM Cells for EMC Measurements - Measurement Good Practice Guide No. 65*. 2018. URL: <https://eprintspublications.npl.co.uk/2771/1/mgpg65.pdf> (visited on 01/18/2024).
- [32] M. Koch. “Rigorous Analysis of TEM Cells”. Doctoral Thesis. Hannover: University of Hannover, 1998. ISBN: 3-8265-6017-5.
- [33] M. Arezoomand, M. Kalantari Meybodi, and N. Noori. “Design of a TEM cell using both multi-step and piecewise linear tapering”. In: *2016 8th International Symposium on Telecommunications (IST)*. 2016, pp. 571–574. DOI: 10.1109/ISTEL.2016.7881886.
- [34] W. Nolting. *Grundkurs Theoretische Physik 3*. 10., korrigierte und erweiterte Auflage. Berlin Heidelberg: Springer Spektrum, 2013. ISBN: 978-3-642-37904-8.
- [35] W. Stutzman and G. Thiele. *Antenna Theory and Design*. 3<sup>rd</sup>. Edition. Wiley, NY, 2013. ISBN: 978-0-470-57664-9.
- [36] G. H. Koepke and M. T. Ma. “A New Method for Determining the Emission Characteristics of an Unknown Interference Source”. In: *1982 IEEE International Symposium on Electromagnetic Compatibility*. 1982, pp. 1–6. DOI: 10.1109/ISEMC.1982.7567737.
- [37] R. Collin. *Field Theory of Guided Waves*. Second Edition. New York, USA: Wiley, 1991. ISBN: 0-87942-237-8.
- [38] P. F. Wilson and M. T. Ma. “Shielding-Effectiveness Measurements with a Dual TEM Cell”. In: *IEEE Transactions on Electromagnetic Compatibility* EMC-27.3 (1985), pp. 137–142. DOI: 10.1109/TEMC.1985.304277.
- [39] M. Heidemann and H. Garbe. “Using TEM waveguides according to the new IEC 61000-4-20”. In: *2003 IEEE International Symposium on Electromagnetic Compatibility, 2003. EMC '03*. Vol. 1. 2003, 457–460 Vol.1. DOI: 10.1109/ICSMC2.2003.1428290.
- [40] C. Groh, H. Garbe, and M. Koch. “Higher order mode behavior in loaded and unloaded TEM cells”. In: *1999 IEEE International Symposium on Electromagnetic Compatibility. Symposium Record (Cat. No.99CH36261)*. Vol. 1. 1999, 225–230 vol.1. DOI: 10.1109/ISEMC.1999.812899.
- [41] Keysight Technologies. *N9038A MXE EMI Receiver*. URL: <https://www.keysight.com/at/de/assets/9018-04935/technical-specifications/9018-04935.pdf> (visited on 01/18/2024).
- [42] Rohde & Schwarz. *ESR EMI Test Receiver*. URL: [https://scdn.rohde-schwarz.com/ur/pws/dl\\_downloads/dl\\_common\\_library/dl\\_brochures\\_and\\_datasheets/pdf\\_1/ESR\\_dat-sw\\_en\\_3606-7201-22\\_v0600.pdf](https://scdn.rohde-schwarz.com/ur/pws/dl_downloads/dl_common_library/dl_brochures_and_datasheets/pdf_1/ESR_dat-sw_en_3606-7201-22_v0600.pdf) (visited on 01/18/2024).

- [43] S. Linkwitz. “Realization of CISPR Quasi-Peak Detection Requirements with an Envelope Quasi-Peak Detector”. In: *1984 International Symposium on Electromagnetic Compatibility*. 1984, pp. 1–5. DOI: 10.1109/ISEMC2.1984.7568056.
- [44] D. B. Geselowitz. “Response of ideal radio noise meter to continuous sine wave, recurrent impulses, and random noise”. In: *IRE Transactions on Radio Frequency Interference RFI-3.1* (1961), pp. 2–11. DOI: 10.1109/RFI.1961.6541594.
- [45] R. L. Belding. “Receiver Measurements Near the Noise Floor”. In: *1986 IEEE International Symposium on Electromagnetic Compatibility*. 1986, pp. 1–8. DOI: 10.1109/ISEMC.1986.7568204.
- [46] E. S. Erdogan and S. Ozev. “Detailed Characterization of Transceiver Parameters Through Loop-Back-Based BiST”. In: *IEEE Transactions on Very Large Scale Integration (VLSI) Systems* 18.6 (2010), pp. 901–911. DOI: 10.1109/TVLSI.2009.2017542.
- [47] A. Nassery and S. Ozev. “An analytical technique for characterization of transceiver IQ imbalances in the loop-back mode”. In: *2012 Design, Automation & Test in Europe Conference & Exhibition (DATE)*. 2012, pp. 1084–1089. DOI: 10.1109/DATE.2012.6176656.
- [48] Y. Aoki, M. T. Dao, K. Min, Y. Hwang, Y. Kim, and S.-G. Yang. “1.4-GHz Bandwidth Frequency-Dependent I/Q Imbalance Calibration for 5G mmWave Communications”. In: *2019 IEEE MTT-S International Microwave Symposium (IMS)*. 2019, pp. 626–629. DOI: 10.1109/MWSYM.2019.8700941.
- [49] A. Schuchert, R. Hasholzner, and P. Antoine. “A novel IQ imbalance compensation scheme for the reception of OFDM signals”. In: *IEEE Transactions on Consumer Electronics* 47.3 (2001), pp. 313–318. DOI: 10.1109/30.964115.
- [50] M. Pozar David. *Microwave Engineering*. Fourth Edition. Wiley, NY, 2012. ISBN: 978-0-470-63155-3.
- [51] Lime Microsystems. *LMS7002M — FPRF MIMO Transceiver IC With Integrated Microcontroller*. URL: <https://limemicro.com/app/uploads/2017/07/LMS7002M-Data-Sheet-v3.1r00.pdf> (visited on 01/18/2024).
- [52] Analog Devices. *Reference Manual AD9364 (UG-673)*. URL: [https://www.analog.com/media/cn/technical-documentation/user-guides/ad9364\\_reference\\_manual\\_ug-673.pdf](https://www.analog.com/media/cn/technical-documentation/user-guides/ad9364_reference_manual_ug-673.pdf) (visited on 01/18/2024).
- [53] F. Krug and P. Russer. “Quasi-peak detector model for a time-domain measurement system”. In: *IEEE Transactions on Electromagnetic Compatibility* 47.2 (2005), pp. 320–326. DOI: 10.1109/TEMC.2005.847410.
- [54] P. Russer. “EMC measurements in the time-domain”. In: *2011 XXXth URSI General Assembly and Scientific Symposium*. 2011, pp. 1–35. DOI: 10.1109/URSIGASS.2011.6050792.
- [55] A. Oppenheim and R. Schaffer. *Zeitdiskrete Signalverarbeitung*. 3., durchgesehene Auflage. Berlin, Boston: Oldenbourg Wissenschaftsverlag, 1998. DOI: <https://doi.org/10.1515/9783486792966>.
- [56] *CISPR TR 16-3: Specification for radio disturbance and immunity measuring apparatus and methods — Part 3: CISPR technical reports (CISPR TR 16-3:2020)*. Tech. Rep. CISPR, Oct. 21, 2020. 299 pp.
- [57] S. Braun, A. Frech, and P. Russer. “CISPR specification and measurement uncertainty of the time-domain EMI measurement system”. In: *2008 IEEE International Symposium on Electromagnetic Compatibility*. 2008, pp. 1–4. DOI: 10.1109/ISEMC.2008.4652078.

- [58] M. Keller. *Comparison of Time Domain Scans and Stepped Frequency Scans in EMI Test Receivers*. URL: [https://scdn.rohde-schwarz.com/ur/pws/dl\\_downloads/dl\\_application/application\\_notes/1ee24/1EE24\\_1e\\_ESR\\_Time\\_Domain\\_Scan.pdf](https://scdn.rohde-schwarz.com/ur/pws/dl_downloads/dl_application/application_notes/1ee24/1EE24_1e_ESR_Time_Domain_Scan.pdf) (visited on 01/18/2024).
- [59] Gauss Instruments. *TDEMI Ultra, Best RF Performance and Lowest Noise Floor*. URL: [https://www.gauss-instruments.com/images/Datasheets/TDEMI\\_ULTRA\\_series\\_productcatalog.pdf](https://www.gauss-instruments.com/images/Datasheets/TDEMI_ULTRA_series_productcatalog.pdf) (visited on 01/18/2024).
- [60] Rohde & Schwarz. *ESW EMI Test Receiver*. URL: [https://scdn.rohde-schwarz.com/ur/pws/dl\\_downloads/dl\\_common\\_library/dl\\_brochures\\_and\\_datasheets/pdf\\_1/ESW\\_bro\\_en\\_3607-2810-12\\_v0800.pdf](https://scdn.rohde-schwarz.com/ur/pws/dl_downloads/dl_common_library/dl_brochures_and_datasheets/pdf_1/ESW_bro_en_3607-2810-12_v0800.pdf) (visited on 01/18/2024).
- [61] Xilinx. *Zynq Ultrascale+ RFSoc Datasheet: Overview*. URL: <https://docs.xilinx.com/v/u/en-US/ds889-zynq-usb-rfsoc-overview> (visited on 01/18/2024).
- [62] W. R. Bennett. "Spectra of quantized signals". In: *The Bell System Technical Journal* 27.3 (1948), pp. 446–472. DOI: 10.1002/j.1538-7305.1948.tb01340.x.
- [63] J. Engelen and R. Plassche. *Bandpass Sigma Delta Modulators*. Edition 1. New York, NY: Springer, 1999. ISBN: 978-0-7923-8698-8.
- [64] S. Rangan and B. Leung. "Quantization noise spectrum of double-loop sigma-delta converter with sinusoidal input". In: *IEEE Transactions on Circuits and Systems II: Analog and Digital Signal Processing* 41.2 (1994), pp. 168–173. DOI: 10.1109/82.281851.
- [65] Analog Devices. *AD9364 — RF Agile Transceiver*. URL: <https://www.analog.com/media/en/technical-documentation/data-sheets/ad9364.pdf> (visited on 01/18/2024).
- [66] Ettus Research. *RF Performance Measurements USRP B200mini*. URL: [https://kb.ettus.com/images/a/ae/B200mini\\_B205\\_RF\\_%20Performance\\_Data\\_20160119.pdf](https://kb.ettus.com/images/a/ae/B200mini_B205_RF_%20Performance_Data_20160119.pdf) (visited on 01/18/2024).
- [67] Keysight Technologies. *U2000 Series USB Power Sensors*. URL: <https://www.keysight.com/at/de/assets/7018-01515/data-sheets/5989-6278.pdf> (visited on 01/18/2024).
- [68] Keysight Technologies. *MXG X-Series Signal Generators*. URL: <https://www.keysight.com/at/de/assets/7018-04096/data-sheets/5991-3131.pdf> (visited on 01/18/2024).
- [69] E. Klumperink and A. Molnar. "Interference Robust, Flexible Radio Receivers in CMOS". In: *IEEE RFIC Virtual Journal* 6.6 (2014). DOI: 10.1109/RFICVJ.2017.0000006.
- [70] *CISPR 16-2-3: Specification for radio disturbance and immunity measuring apparatus and methods — Part 2-3: Methods of measurement of disturbances and immunity — Radiated disturbance measurements — (CISPR 16-2-3:2016)*. English. Sept. 2016.
- [71] D. Kalodikis, C. Spindelberger, and H. Arthaber. "A Feed-Forward Gain Control for Improving the Dynamic Range of the Receiver's ADC in EMC Measurements". In: *2023 International Symposium on Electromagnetic Compatibility – EMC Europe*. 2023, pp. 1–5. DOI: 10.1109/EMCEurope57790.2023.10274411.
- [72] S. Maas. *Microwave Mixers*. Second Edition. Artech House, 1992. ISBN: 978-0890066058.
- [73] M. F. and M. C. *Mixer basics primer — A tutorial for RF and microwave mixers*. Morgan Hill, CA, USA, 2010.
- [74] M. F. and M. C. *A tutorial on high linearity high IP3 RF and microwave mixers*. Morgan Hill, CA, USA, 2010.
- [75] G. H. Bryant. *Principles of Microwave Measurements*. Volume 5. IEE, UK, 1993. ISBN: 0-86341-296-3.

- [76] M. Leffel and R. Daniel. *THE Y FACTOR TECHNIQUE FOR NOISE FIGURE MEASUREMENTS*. 2021. URL: [https://scdn.rohde-schwarz.com/ur/pws/dl\\_downloads/dl\\_application/application\\_notes/1ma178/1MA178\\_5e\\_NoiseFigure.pdf](https://scdn.rohde-schwarz.com/ur/pws/dl_downloads/dl_application/application_notes/1ma178/1MA178_5e_NoiseFigure.pdf) (visited on 01/18/2024).
- [77] U. L. Rohde. *Microwave and Wireless Synthesizers — Theory and Design*. First Edition. Wiley, NY, 1997. ISBN: 0-471-52019-5.
- [78] L. Ljung. *System Identification: Theory for the User*. 2<sup>nd</sup>. Edition. Prentice Hall, NJ, 1999. ISBN: 978-0136566953.
- [79] T. North, K. Frazier, D. L. Sanders, and J. P. Muccioli. “Electromagnetic Compatibility of Direct Current Motors in an Automobile Environment”. In: *SAE Transactions* 114 (2005), pp. 116–129. ISSN: 0096736X, 25771531. URL: <http://www.jstor.org/stable/44682411> (visited on 01/18/2024).
- [80] J. Goedbloed and P. Beeckman. “Uncertainty analysis of the CISPR/a radiated emission round-robin test results”. In: *IEEE Transactions on Electromagnetic Compatibility* 46.2 (2004), pp. 246–262. DOI: 10.1109/TEM.2004.826892.
- [81] Tekbox. *TBTC0/1/2/3, OPEN TEM CELLS FOR EMC PRE-COMPLIANCE TESTING*. URL: <https://www.batronix.com/files/Tekbox/Datenblaetter/TEM-Cells-Datasheet-V14.pdf> (visited on 01/18/2024).
- [82] Tekbox. *TBGTc1, OPEN GTEM CELL FOR EMC PRE-COMPLIANCE TESTING*. URL: [https://www.batronix.com/files/Tekbox/Datenblaetter/TBGTc1\\_Manual.pdf](https://www.batronix.com/files/Tekbox/Datenblaetter/TBGTc1_Manual.pdf) (visited on 01/18/2024).
- [83] S. M. Satav and V. Agarwal. “Do-it-Yourself Fabrication of an Open TEM Cell for EMC Pre-compliance”. In: 2008. URL: <https://api.semanticscholar.org/CorpusID:32634743> (visited on 01/18/2024).
- [84] Hewlett-Packard. *Microwave mismatch error analysis, Application note 56*. 1967.

---

# TEM Cell Characterization

---

In this thesis, TEM cells have been declared as target test method as they offer a low-cost solution for EMC measurements. To provide a complete measurement setup in conjunction with the intended SDR-based EMI receiver, an open TEM cell has been designed by the author for this purpose, supported with 3D-EM simulations [20].

The usual approach to construct a TEM cell bases on the use of a stripline with symmetric geometry. The main drawback of this technique is the equal distance between the inner and outer conductors, limiting the available vertical space for the EUT and thus the uniform test-volume (UTV). Several works have been published, targeting the design of a symmetric TEM cell for pre-compliance measurements [21, 33, 83]. In accordance to the main norm for such waveguides, i.e., *DIN EN 61000-4-20*, a cubic UTV with an edge length of maximum 30 mm is achieved in the addressed frequency range of *CISPR* band C/D.

To increase the available UTV size, the benefits of an asymmetric stripline geometry have been exploited for the TEM cell utilized in this thesis, see Fig. A.1. Referring to *DIN EN 61000-4-20*, a cubic UTV with an edge length of 100 mm shall be achieved for measurements up to 1 GHz. During the development process, the focus was put on a design which is easy to build having limited manufacturing tools available and deploying low-cost material.



Fig. A.1: Picture of the developed asymmetric TEM cell from [20].

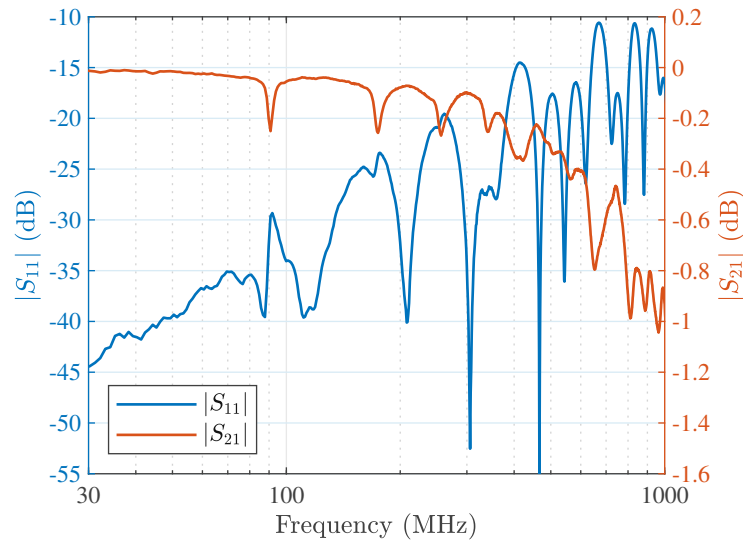


**Fig. A.2:** S-parameter measurement of the empty low-cost TEM cell from [20] placed in an anechoic chamber as in Fig. 5.9.

As TEM cells have two RF ports available, it is allowed to draw conclusions on the UTV size taking S-parameters and certain geometrical dimensions into account. This approach is based on superficial assumptions regarding field distributions in a wave guide. Goal of this chapter is to verify if these hold for the designed TEM cell and which performance can be expected.

The content of this chapter regarding the field homogeneity analysis and simulation-based data plots have been adopted from the author's own work [20].

## A.1 S-Parameters

Taking S-parameters into account for evaluating compliance of a given TEM cell bases on the assumption that each kind of losses amount to energy couplings into higher order modes. This criteria was evaluated in (5.3) for the developed low-cost cell. If the losses of the cell are below 1 dB in the desired frequency range, compliance in accordance to *DIN EN 61000-4-20* is given if the entire EUT, including cables, fits into a cubic UTV having an edge length  $l_{UTV} \leq h_s/3$  where  $h_s$  denotes the septum height, depicted in Fig. 2.4. The defined volume is located in the central of the cell, apart from the bottom conductor with a height offset of  $h_{UTV} \geq 0.05h_s$ .

The S-parameter measurements of the designed TEM cell is given in Fig. A.2. These values have been utilized in Sec. 5.3 for calculating the losses of the empty cell situated in the environment from Fig. 5.9. Besides a few critical frequencies in loaded conditions above 800 MHz, evaluating the loss criteria has indicated that the cell may be used for radiated emission measurements up to 1 GHz. In comparison to TEM cells incorporating a symmetric stripline, an  $l_{UTV}$  of 100 mm is achieved which is approx. three times higher.

It can be seen in Fig. A.2 that  $|S_{11}|$  stays below  $-10$  dB in the addressed frequency range of CISPR band C/D. The maximum absolute measurement uncertainty through the mismatches of the cell and a connected EMI receiver can be calculated with [84]:

$$\epsilon_{\max} = 20 \log_{10} \frac{1}{1 \pm |S_{11}^{\text{EMI}}| |S_{11}^{\text{TEM}}|}. \quad (\text{A.1})$$

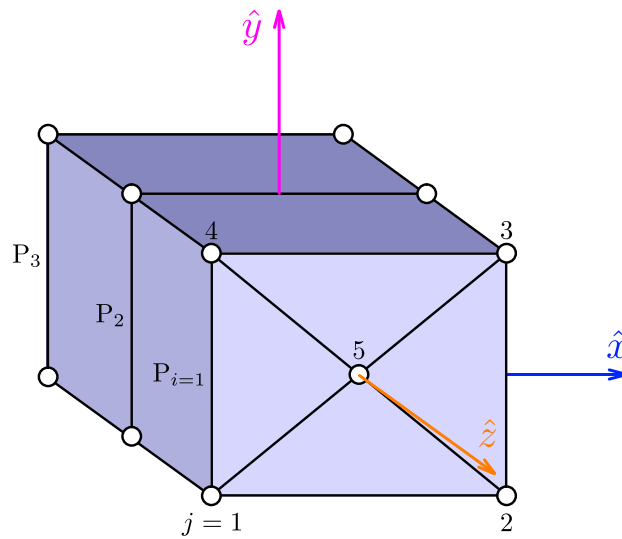


**Fig. A.3:** Definition of the cubic UTV placed in the central of a TEM cell.

Fully compliant receivers must have an  $|S_{11}| \leq -10$  dB. Taking the depicted measurements of the low-cost TEM cell into account, an uncertainty of  $|\epsilon_{\max}| < 0.83$  dB occurs.

The resonances of  $|S_{21}|$  indicate the excitation of unintended field modes, e.g., the  $TE_{10}$ . Due to energy couplings from the desired TEM mode into higher order modes, the amount of power measured at the cell's output port shrinks and thus reduces  $|S_{21}|$ . Even if the waveguide is operated below its certain cutoff frequency, where only TEM waves are able to propagate, disturbing patterns are excited due to constructional caused bending edges. In the test volume of the cell, they superpose with the TEM mode and cause field perturbations. In the subsequent chapter, the field homogeneity in the defined UTV is further investigated with a field probe. The goal is to verify if the used loss criteria holds for the developed TEM cell.

## A.2 Field Homogeneity

Characterizing the electric field distribution in the test volume of a TEM cell with a field probe is the method of first choice. It gives a detailed information about the individual field vector components and applies also to single-port-based GTEM cells. By stimulating the cell with a CW tone, the electric field is evaluated at the excited frequency taking certain points in the desired UTV into account. According to *DIN EN 61000-4-20*, the volume is cubic and investigated at points located on a five-star grid<sup>1</sup> which is visualized in Fig. A.3. In this description,  $\hat{z}$  stands for the longitudinal propagation direction of the TEM mode in the wave guide,  $\hat{y}$  points in vertical direction, and  $\hat{x}$  stands for the horizontal vector, directly adopted from Fig. 2.4. Each plane  $P_i$  and their respective points  $j$  are investigated separately.

In the far field transformation algorithm presented in Sec. 2.1.2, it is assumed that the TEM mode is dominant and only a field component of vertical direction  $\hat{y}$  occurs within the UTV. To verify if a TEM cell fulfills this assumption in satisfaction of standardized requirements, two main criteria must hold at the excited frequency for each plane  $P_i$  [18, 31]:

<sup>1</sup>The amount of grid points scales with the size of the investigated volume and must be increased for an  $l_{\text{UTV}} > 0.5$  m.

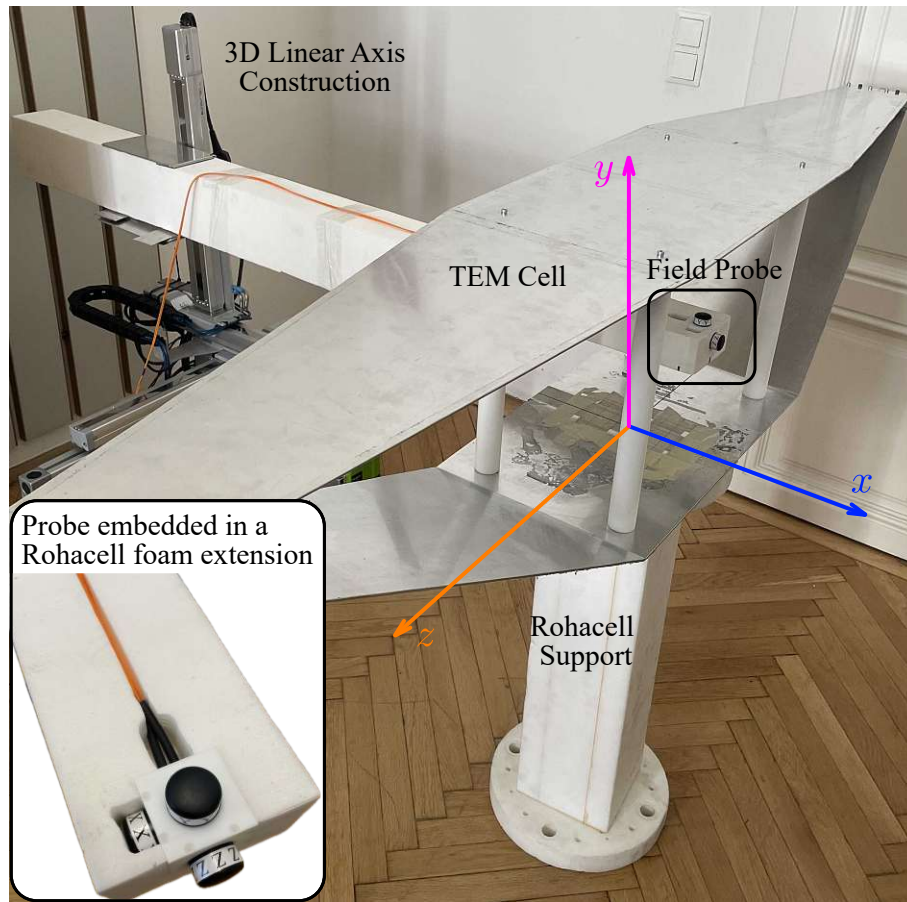


**Fig. A.4:** Automatized measurement setup for characterizing the field homogeneity of the developed TEM cell with a field probe.

1. The variation of the magnitude  $|\vec{E}_{ij}|$  is not larger than 6 dB for the points  $j$  in  $P_i$ . In this step, the point having the largest deviation is sorted out and is not considered.
2. The secondary field components  $E_{ij}^{(x)}$  and  $E_{ij}^{(z)}$  of the remaining points  $j$  in each plane  $P_i$  are 6 dB smaller than the respective magnitude  $|\vec{E}_{ij}|$ .

To verify these two points, the developed TEM cell from [20] has been characterized with a field probe. The settling time of such probes is rather slow and may cause significant idles times during a measurement. Hence, the field homogeneity has been characterized with an automatized setup utilizing linear axis variable in three dimensions. In particular, the *RadiSense 4* from Dare was used having three orthogonal monopoles implemented. The probe was embedded in a certain foam arm, mounted on the 3D variable linear axis. The corresponding measurement setup, depicted in Fig. A.4, holds the specified distances of the cell to any reflecting surface according to *MIL-STD 462F RS105*, i.e.,  $2h_s = 600$  mm. For minimizing field diffraction due to the used foam supports, a material from Rohacell was used promising a low relative dielectric constant similar to air. While on the left hand side a CW source is applied for stimulating the waveguide, on the right hand side the port is terminated with a  $50\ \Omega$  load. Both, the probe and the cell have been vertically aligned with a mechanic's level.

The setup alignment is verified by a horizontal sweep of the field probe along the cross section located in the middle of the TEM cell ( $z = 0$ ) at a constant height offset from the bottom

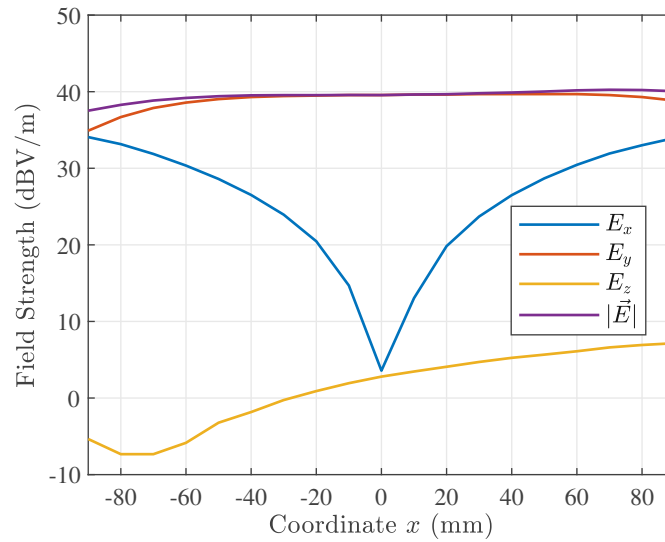


**Fig. A.5:** Horizontal sweep of the field probe along the TEM cell's cross section  $z = 0$  measured at the constant height of  $y = h_s/2 = 15$  cm and frequency of 30 MHz.

conductor, i.e.,  $y = h_s/2 = 15$  cm. From a simulation based model, it is known that the field homogeneity is high at an excitation frequency of 30 MHz and thus chosen accordingly. In Fig. A.5, the measured field vector components are depicted. Obviously, the magnitude  $|\vec{E}|$  and the vertical component  $E_y$  can be considered flat over the edge length of the target UTV reaching from  $x = -50$  mm to 50 mm. This indicates that vertical height deviations by the movable field probe support are negligible. In the central  $x = 0$ , the horizontal component  $E_x$  should be zero under ideal circumstances. Moreover, in dominance of the TEM mode, the longitudinal component  $E_z$  should be zero as well. Consequently, a probe misalignment would be directly visible in the secondary field components due to projections from  $E_y$  into  $E_x$  and  $E_z$ . As both are more than 30 dB smaller than the intended field, the construction is assumed to be sufficiently aligned. The tapering of the cell causes a spherical wave pattern which is not fully subsided in the uniform stripline section. Consequently, slight vertical height deviations along  $x$  reflect in a changing longitudinal field component.

With the automatized setup, the field homogeneity of the asymmetric TEM cell has been evaluated in accordance to the mentioned field requirements of *DIN EN 61000-4-20* on a specified frequency grid. The cubic UTV with an edge length of 100 mmeter was defined in the middle of the cell with a height offset of 40 mm from the bottom conductor. In Fig. A.6, the discussed field homogeneity criteria are evaluated for a 3D-EM simulation based model of the cell and the measured values.

In general, the field homogeneity indicators extracted from the measured values show a good agreement with the simulations. Occurring deviations may be explained by imperfections of the measurement environment in comparison to ideal conditions, i.e., an open radiation boundary. In addition, the field probe itself affects the measurement accuracy due to introduced field perturbations of the housing which has not been considered in the simulations. Further problems, but less significant, are the limited DR and linearity of the probe.

From the graphs it is obvious that the longitudinal component  $E_z$  causes the strongest distortion above 500 MHz. For the simulation, 0.3% of the investigated frequencies fail the second requirement and 1.3% for the measured ones. In total, a maximum amount of 3%

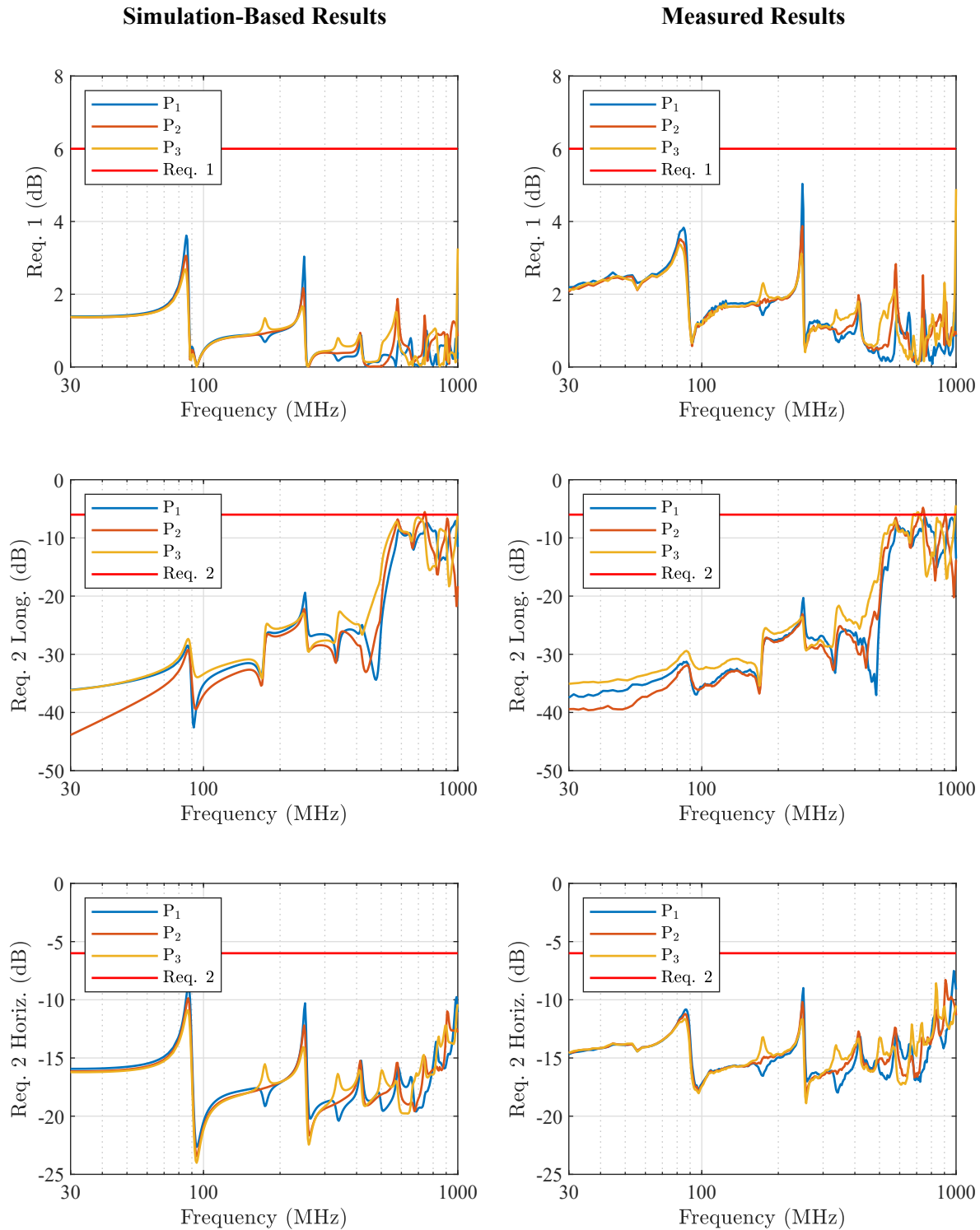


**Fig. A.6:** Field homogeneity criteria evaluation in accordance to *DIN EN 61000-4-20*. While on the left hand side, the simulation-based results are evaluated, the right hand side represents for the measured values. The y-axis of the plots denote the investigated criteria and the belonging field components. Longitudinal stands for the evaluation of  $E_{ij}^{(z)}/|\vec{E}_{ij}|$  and horizontal for  $E_{ij}^{(x)}/|\vec{E}_{ij}|$ . For the simulation and the measurement, 0.3% and 1.3% of the investigated frequencies are failing the second requirement respectively.

Die approbierte gedruckte Originalversion dieser Dissertation ist an der TU Wien Bibliothek verfügbar. The approved original version of this doctoral thesis is available in print at TU Wien Bibliothek.

is allowed for the used frequency grid and thus considered to fulfill the field homogeneity requirements of *DIN EN 61000-4-20* in *CISPR* band C/D.

Comparing the requirement violations of the field probe based results with the S-parameter based criteria indicates that the losses can be used in general to evaluate compliance of the measurement setup. Even though resonances are visible by use of the TEM cell's transfer characteristics, their impact on the field distortion in the UTV does not always reflect the same extent as for field homogeneity measurements. Especially for low frequencies below 300 MHz, occurring resonances are well below the 1-dB loss criteria, giving the impression of having a negligible impact on the measurement accuracy. The field data, however, shows that some of these resonances are already close to the 6-dB rule of the first field requirement. At higher frequencies, both methods correlate and allow for a reliable identification of norm violations and their respective frequencies. For the radiated emission measurement setup, utilized in this thesis, the field homogeneity requirements are fulfilled as the amount for violations is below 3%.